FACULTY OF SCIENCE
UNIVERSITY OF COPENHAGEN

Ph.D. Thesis

Application of cavity ring down spectroscopy to isotopic bio- geo- & climate-sciences

&

the development of a mid-infrared CRDS analyzer for continuous measurements of N_2O isotopomers

By:

David Morten Balslev-Clausen

Academic supervisors:
Prof. Dorthe Dahl-Jensen, Centre for Ice and Climate
Prof. Thomas Blunier, Centre for Ice and Climate
Prof. Minik Rosing, Nordic Centre for Earth Evolution

Submitted 01/07/2011

Abstract

This thesis conducts several explorations in applying sensitive optical spectroscopy methods to isotopic bio-geo-chemical and climate sciences.

A new mid-infrared cavity ring down spectrometer was successfully built. The analyzer measures the abundance of $^{14}N^{15}N^{16}O$ and $^{15}N^{14}N^{16}O$ relative to $^{14}N^{14}N^{16}O$ as well as the concentration of N_2O . The precision in δ-values has been demonstrated to reach below 0.5‰ for both isotopomers. The analyzer can help elucidating microbial N_2O dynamics in terrestrial ecosystems, perform monitoring of the atmosphere or to study climate history stored in ice cores air bubbles. Application to each of these fields is addressed in the presented thesis. The analyzer is easy to use, performs real time – continuous measurements and is a prototype for a coming product at Picarro Inc.

Another frontier work was on the application of CRDS, to measure Carbon-13 isotopic composition of rocks. Such measurements were made using a novel instrument from Picarro Inc. where CO_2 from a flash combustion oven is send into an isotopic CO_2 cavity ring-down spectrometer. Powdered rock samples containing kerogen or graphite were successfully analyzed by this method and it was found that rocks containing more than 0.5% TOC provides effective combustion and sufficient yield of CO_2 to obtain analytical precision of the Carbon 13/12 ratio. It was found that 1 mg of carbon correspond to a CO_2 concentration of 3000 ppm in the laser spectrometer. Measurements of USGS-24 graphite standards showed that the best precision was obtained for 1 mg to 2.5 mg of Carbon providing a precision of 0.05‰ in $\delta^{13}C_{VPDB}$. Successful inter comparison measurements with the mass spectrometric method, was made on samples straddling the SPICE isotopic excursion in a Cambrian Alum shale stratigraphic section.

Resumé

I denne afhandling er anvendelsen af optisk spectroskopi til anvendels inden for de biogeokemiske videnskaber blevet undersøgt.

En nyudvikling af et mid-infrarødt "cavity ring down" laser spektrometer er med success blevet udført. Spektrometeret kan måle isotop forholdet af $^{14}N^{15}N^{16}O$ og $^{15}N^{14}N^{16}O$ i forhold til $^{14}N^{14}N^{16}O$, samtidig med præcise målinger af N_2O koncentrationen. Instrumentets præcision i δ-værdi er blevet demonstreret til bedre end 0.5‰ for begge isotopomerer. Instrumentet kan hjælpe med at belyse mikro-organismers nitrifications processer i terrestriale økosystemer, til overvågning af atmosfæren, såvel som til måling af klima historie gemt i luft bobler der er insluttet i de polare iskapper. Alle disse anvendelses områder er blevet berørt under arbejdet og præsenteres i denne afhandling. Instrumentet er nemt at anvende, laver kontinuerte målinger med løbende data opdatering og er en prototype til et kommende produkt hos Picarro Inc.

Isotopforhold af Karbon-13 er blevet målt i klippestykker ved brug at en forbrændings ovn efter fulgt af en "cavity ring down" laser spektrometer der måler isotoper påCO_2. Knuste klippe prøver indeholdende kerogen og grafit blev målt med success og det blev konstateret at klippe prøver der indeholder mere en 0.5% TOC effektivt bliver brændt med tilstrækkelig CO_2 produktion til at opnå analytisk præcision for Karbon 13/12 forholdet. Det blev erfaret at 1 mg carbon svarer til en CO_2 koncentration på 3000 ppm i laser instrumentet. Målinger af grafit standarden USGS-24 viste at den bedste præcision blev opnået med prøver indeholdende 1 mg til 2.5 mg Karbon, hvorved en præcision på 0.05‰ in $\delta^{13}C$ blev opnået. En succesful sammenligning af målinger med tilsvarende masse spektroskopiske metode blev udført med prøver fra den stratigrafiske skiffer sektion i Alum, som spænder over den Kambriske SPICE ekskursion.

Acknowledgments

So many helped making this project a success and I am sure I will forget somebody but let it be known, that I was and am thankful of the support you gave me.

To my suppervisors: Dorthe, I thank you for accepting me as your Ph.D. student and allways having confidence that I would be able to manage my way through, however insane the situations sometimes were. Thomas, Thank you so much for your support and guidance in the lab and else where, and I appreciate the many great advices you have given me through the project. To Minik, I will write it in small letters, to keep it secret You make science fun. I hope nobody reads it.

Then I have to thank all the people at Picarro, for being really supportive during my stay in Sunnyvale. Special thanks goes to Alex Farinas for all the good lunchtimes, Sze Tan for your lecturing conversations, Mike Woelk for agreeing on this collaboration and being a good sport, Aaron for allways being honest and cheerful, John Hoffnagle for baring over with my inconveniences, Bruce, Tony, Hugo, Priah etc. etc. all for being a good friends and welcoming. But most of all I have to give an infinite thanks to Tania Pashkevich and Eric Crosson to whom I cannot express strongly enough what gratitude I feel for all the things you have done for me, in terms of academic and project advices as well as taking me in as full part member of your family. Thank you.

I also have to give very special thanks to Julia Rosen for the fun and awesome times during your visits here in Copenhagen. Star Wars pictographs will go into history. Thanks also goes to the other collaboration partners, Tais Dahl, Søren Christensen, Matthew Johnson and the rest of people in their groups. Special thanks to Ellen Chrillesen and Lene Bentzen for your great support with administration.

I would like to thank people at Centre for Ice and Climate and NordCEE, for support and all the people there for the great social environment, both in Copenhagen and in the field. An extra thanks goes to Christo Buizert, Sebastian Simonsen, Peter Sperlich, Christopher Stowasser, Vasileios Gkinis, Trevor Popp, Myriam, Sigfus, JP, Simon, Steff, Mads, HC, Mai, lone etc. etc. etc. etc.

Last but definitely not least, I would like to thank my family and friends for being patient and encouraging when this work was time consuming. And a special thanks to Annemette Lyng Svensson helping me with my english in this thesis.

David Balslev-Clausen
Copenhagen, July 2011

1 Preface

Managing the Ph.d. project – a view of the time line and circumstances

This section gives an overview of how this Ph.D. project was managed. The starting title of the project was "Application of Cavity enhanced optical frequency comb spectroscopy to perform measurements on greenhouse gases in the encaptured airbubles in ice cores from Greenland to determine the climate over the past 11,700 years" but was eventually evolved to the final title: "Explorations of using Cavity Ring-Down Spectroscopy to Bio-, Geo- & Climate-Science & Development of a Mid-IR CRDS analyzer for continuous measurements of N_2O isotopomers". The project was supervised and financed by Professor Dorthe Dahl Jensen, of the Center for Ice and Climate, a center of excellence funded by The Danish National Research Foundation located at the Niels Bohr Institute at University of Copenhagen.

Part of the financing of this Ph.D. project was provided by Minik Rosing at the Geological Museum at University of Copenhagen. This part of the project was based at the Nordic Center for Earth Evolution NordCEE, another center of excellence also funded by The Danish National Research Foundation. The goal of this part of the Ph.D. project was to apply laser spectroscopy methods in order to perform measurements on the 3.8 billion year old rock cores from ISUA in Greenland.

The project set out to build up a cavity enhanced optical frequency comb CEOFC spectrometer as developed in the group of Jun Ye in Boulder Colorado, [Thorpe, 2009], in which I participated as part of my master's thesis [Balslev-Clausen, 2007]. It was intended to modify this spectrometer and optimize it for measurements on air bubbles entrapped in ice cores. As the

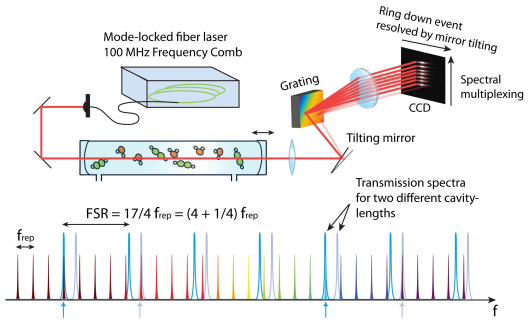

sample volume from the ice cores are significantly smaller than the sample availability from atmosphere, serious modifications to the 250 mL cell volume in the work of Thorpe [2009]; Balslev-Clausen [2007] would have to be made. The spectroscopy scheme of Thorpe [2009] required that the sample would be evacuated from the sample cell in order to capture the laser intensity, a scheme which is incompatible with the continuous flow system (CFA) to which the instrument was intended to be coupled onto. For this reason other comb spectroscopy methods were considered. In particular the work by Mandon et al. [2008, 2007a,b]; Picqué et al. [2007] was of great inspiration, as well as the Vernier comb spectroscopy by Gohle et al. [2007] was considered as alternative approaches. Through correspondences with Dr. Nathalie Picqué discussions were made on applying the technique of Mandon et al. [2008] but introducing a high finesse cavity instead of a single pass cell. Suggested by this author was also to make a vernier ring down comb spectrometer as depicted in Figure 1. However, these were very high risk projects and would most likely not turn out applicable to the ice core measurements within the time frame of this project. At the time of this correspondence, Dr. Nathalie Picqué had just established collaboration with the group of Nobel laureate Theodor Hänsch in Garching, Germany which they demonstrated the Cavity-enhanced dual-comb spectroscopy system published in Bernhardt et al. [2010].

No optical equipment was available at the Geophysical Department and the project as formulated was relying on collaboration with the group for "Ultra cold atoms and Quantum Optics" at the Niels Bohr Institute, from which I made my master thesis. In collaboration with Jan W. Thomsen and Jes O. Henningsen, (Quantum optics group) and Jan Hald and Jan Conrad Petersen from DFM (Dansih Fundamental Metrology, Lyngby DK) an application for additional funding was submitted to the "The Danish Research Council for Technology and Production Sciences" with the Title "Frequency comb technology for health and climate". This was rejected.

By this time it was May 2008 and it was not clear what directions should

be taken in order to build an instrument which could be applicable to the ice core measurements. A more simple approach was considered on encouragement by M. Thorpe from JILA which was to build a mid-infrared (single frequency) continuous wave cavity ring down spectrometer. This would provide higher sensitivity to the small volume of available sample as the molecular absorptions are orders of magnitude stronger in the mid-infrared. This would require optics for a very different wavelength region, with which limited experience was available in Copenhagen. Decisions had to be made soon as the budgeted money for the project had to be spent before the end of the first year. However, in June 2008 the situation took a drastic change as Thomas Blunier called the attention to the new line of products from Picarro Inc., a company in Silicon Valley which provide automated cavity ring down analyzers for gas concentration measurements and isotope measurements of water and carbon dioxide.

After a project status meeting in July 2008 (with the attending partners) it was decided that a negotiation should be made with Picarro Inc. in which it should be discussed if there were any attempts to push their technology from the near-infrared optical region to the mid-infrared. Based on a personal desire to develop a new analyzer and because Picarro Inc. had the necessary facilities and mutual plans to develop such an instrument, it was finally agreed upon that CIC would buy three analyzers (a water isotope, carbon isotope and CH4/CO2/H2O concentration analyzer), and that I should spend 6 months in California (as part of the change of environment program), to develop a novel mid-infra red cavity ring down system. In this way the implementation of applying the laser systems to ice core measurements could be initiated in parallel with development of a new laser instrument as stated in the project title. A solution of benefit to this author as well as to other students at CIC.

In the fall of 2008 technical considerations on which detection method should be applied were made, while laser and other components were ordered. Also in collaboration with Picarro Inc. a SBIR application was submitted with milestones for the project. In January 2009 the first visit to Picarro Inc. was made and during this first month important results with the first cavity were achieved in close collaboration with Eric Crosson. The full 6 month stay started in April 2009. At this time Eric Crosson had become the chief Technical officer (CTO) at Picarro Inc. and I was assigned as the PI of the project. Thorough progress on the spectroscopy was made in the first couple of months. Also an optoelectronic engineer was hired to help on the project in part time as well a mechanical engineer was part time assigned. There was serious concerns to whether the instrument would achieve the necessary performance. It was therefore decided to aim for a design which would be

very vibrationally and thermally stable. This was at the same time as Picarro was growing from 25 employees to 50 employees, and other important projects were going on, e.g. release of a new platform. So only limited access to the mechanical engineer was available, meaning that the necessary developments in the mechanical design were progressing too slowly, as this author did not have the necessary skills to perform the mechanical drawings and decision of materials. So in the fall of 2009 only a table top version of the instrument was realized, and only partly integrated between optics, electronics and software. As by now this had to be the foundation of this thesis it was decided to extend the stay for another three months, a decision which had to be repeated again in December 2009 extending the stay at Picarro Inc. to a full year. At the end of 2009 it became apparent that the rapid changes and the intense projects at the company, turned out to be a too big challenge to the mechanical engineer, resulting in several mistakes on the design, setting back the project by multiple months. At this point it was decided to change direction in terms of the instrument design to be less rigid and more flexible as suitable for a prototype, resulting in the final design described in part II. Finally in the spring of 2010 real progress was made nevertheless the instrument did not get ready for the NEEM field season 2010 and the instrument did not arrive in Copenhagen until November 1. Another month overlapping May and June 2010 was also spent at Picarro in order to instruct new employees on how to carry on with the setup[1].

July 2010 was spent at the NEEM ice core drilling site in Greenland. During the stay at NEEM the author was supervising the Picarro instruments running, making water isotope measurements and methane concentration measurements as part of the continuous flow analysis system deployed in the field. The author was also attending the water isotope measurements made with the Picarro instrument, sampling the ice chips from scraping in the preparation of the ice cores for the line scanner.

During the spring of 2010 Thomas Blunier and Ed Brook from Oregon state University established interest in using the nitrous oxide isotopomer analyzer to make measurements on a series of Antarctic Holocene ice core samples from Siple Dome, Antarctica. This ensured the great fortune of having Julia Rosen, a ph.d. student of Ed Brook, on visit at CIC for six months. Her support was crucial in succeeding with the presented ice core measurements, see chapter 4.

[1] I thank the whole Picarro-team for their persistent and energetic efforts, see acknowledgments.

During the fall of 2010 contacts with other groups interested in Nitrous Oxide was also established. The group of Matthew Johnson at the chemistry department was very helpful in applying ideas and concepts from the atmospheric chemistry aspect. At the Biological department Lars Lindgaard, Bo Elberling og Søren Christensen who has done experiments on estimating terrestrial emissions from the Rain forrest in Amazon, the thawing permafrost in Greenland and anthropogenic and agricultural areas in Europe. All were indispensable in bringing encouragement for the application of the analyzer, and for supplying the microbial samples for measurements presented in chapter 5.

While I was at Picarro an integration of the Picarro laser analyzer to a Costech front end combustion unit was realized. This sort of system was exactly what was in mind for the project at Geological Museum, and at Picarro rock samples were tested on the analyzer. This showed that the CM-CRDS system had sufficient performance for the purpose. Based on these measurements, at full CM-CRDS system was bought, and was installed at the Geological Musuem in October 2010. Next, running standards were chosen, a calibration scheme and dosing approach was established, and followed by a data series measurement of SPICE a Cambrian stratigraphy section of known isotopic values from mass spectrometer measurements. See Chapter 3

Although frequency comb spectroscopy was not employed within this work, more was achieved than if this had been the realized path, as many processes were parallelized during the eventual course of actions, enabling more implementation to application in the different contexts.

1.1 Planned publications

It is planned that three articles should be written on basis of the thesis work.

On the application of the CM-CRDS analyzer to rock samples and optimization of this, an article is planned to be submitted to Analytical Chemistry.
On the development of the mid infrared analyzer and performance of this, an article is also being planned but a journal has not been chosen yet.
On the application of the mid-infrared analyzer to measurements on Antarctic ice core samples, to which measurements still needs to be made during the fall of 2011.

A post doc. position has been granted to me for 2011, and it is planned to conduct the missing work over the fall of 2011.

1.2 Outline of thesis

The thesis is divided into two parts.

Part I – is about the application of CRDS in biogeosciences, with three main topics being the carbon-13 measurements on rock samples by flash combustion, second and third topic is on the application of CRDS to measurements of nitrous oxide isotopomers in ice core samples and in microbial nitrification and de-nitrification processes.

Part II – is about the extension of the crds technology to mid-infrared spectroscopy, in form of a automated nitrous oxide isotopomer analyzer. Careful considerations on the design are given and performance of the ananlyzer is presented at the end.

Contents

Part I

Applications of Cavity Ring Down Laser Spectroscopy to Bio-, Geo-, & Climate Science

2 Background

This chapter starts with section 2.1, giving an introduction on CRDS intended for biogeoscientist describing the most important knowledge of the system and it's limitations. Next, follows a short introduction to stable isotopes to motivate how cavity ring down spectroscopy (CRDS) can play a role in the investigations of biogeosciences.

2.1 Cavity ring down spectroscopy foundation and limitations

Cavity Ring Down Spectroscopy (CRDS) was first presented in 1988 by O'Keefe and Deacon [1988]. Since have hundreds of articles presented on advances and application of the method. This section presents the fundamental knowledge of CRDS which I would recommend to the bio or geo scientist getting involved with the details of CRDS. The knowledge in this section is widely presented in spectroscopy literature so only few references will be given. For further reference please consult section 6.2.

CRDS is a highly sensitive method of optical absorption spectroscopy. Absorption spectroscopy allows for chemical trace gas analysis, concentration measurements of molecules and can distinguish between isotopic variants, which allows for isotopic composition measurements.

2.1.1 Absorption spectroscopy

The foundation for these molecular concentration measurements is Beer-Lambert's law of optical absorption. The law quantifies the absorptance $A = 1 - I/I_0$ that a beam of light experiences when it traverses through a

gas. When light of wavelength λ and intensity I_0, travels a distance L through a gas (e.g. in a glass cell), the transmitted light will have the intensity

$$I(\lambda) = I_0(\lambda)\, e^{-\alpha(\lambda)L} \tag{2.1}$$

where the absorption coefficient $\alpha(\lambda)$ (often reported in cm^{-1}) quantifies the magnitude of the absorption per unit length, assuming the gas is homogeneous. The absorption coefficient $\alpha(\lambda)$ is specific for the gas composition, temperature and pressure. For mixing of gases α is linear. This means that when different gases with $\alpha_1(\lambda) \ldots \alpha_n(\lambda)$ are mixed, the resultant gas has the absorption coefficient $\alpha(\lambda) = \sum_i \alpha_i(\lambda)$. The different gases could be different atomic or molecular species e.g., N_2, O_2, H_2O, Ar, CO_2, Ne, CH_4, N_2O, CO, NO, NO_2 etc. The absorption spectrum α as a function of λ differs for each of these species, atomic and molecular.

Absorption occurs only at wavelengths that correspond to the transition energy between two quantum mechanical energy states of the absorber gas. These are called absorption lines. For optical wavelengths in the Ultra Violet and visible range, absorption typically originates from changes in the electronic energy state of the absorber. At longer wavelengths in the infrared, absorption is typically from changes in rotational and vibrational energy states of a molecule. These energy states depend on the masses, configurations and binding energies of the atoms in the molecule. The absorption spectrum for each of all the gas components mentioned above therefore differs from each other. Further more as the energy states of a molecule also depend on the atomic masses, isotopic variants of the same molecule may also be distinguished. An example of this is shown in figure 2.1.

2.1.2 Deriving the molecular concentration from the absorption

The molecular concentration of a species is proportional to the integrated area under its absorption feature i.e. the highlighted area in figure 2.1. These areas however do *not* generally scale with the same factor for different absorption lines. Not even for lines of the same species. Each absorption line is related to the concentration through the relation

$$\alpha_{i,l}(\lambda) = n\, S_{i,l}\, g_{i,l}(\lambda) \tag{2.2}$$

where n is the concentration of the absorber, $S_{i,l}$ is the absorption intensity of the absorption line, $g_{i,l}(\lambda)$ is the normalized spectral profile ($\int_{-\infty}^{\infty} g_{i,l}(\lambda)\, d\lambda = 1$) and index i and l indicate the molecule and specific absorption line. A database on $S_{i,l}$ and $g_{i,l}(\lambda)$ information is provided by Rothman et al. [2009],

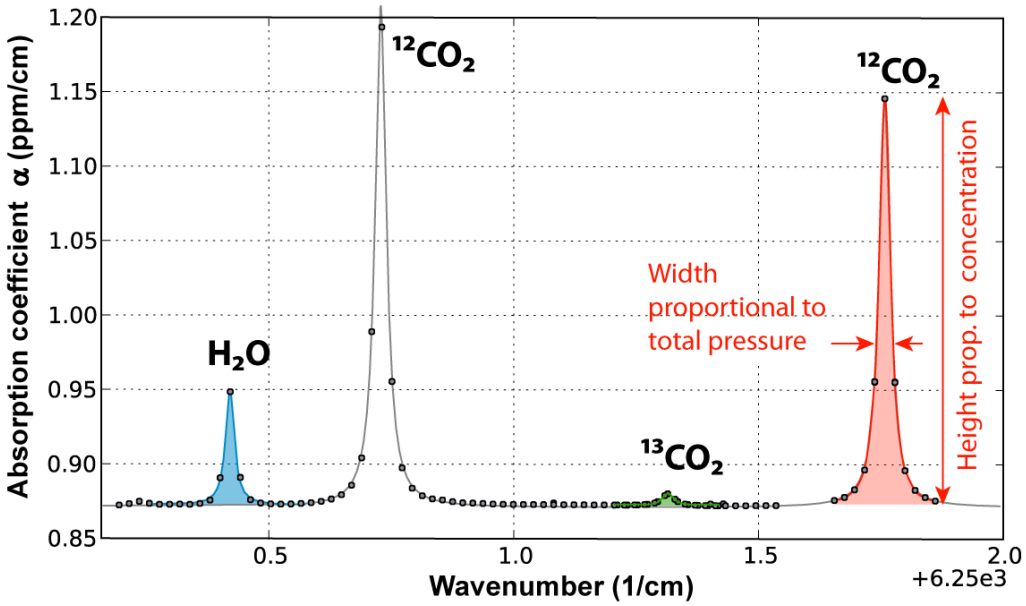

Figure 2.1: Spectrum applied by the CRDS analyzer used in chapter 3 to measure $\delta^{13}CO_2$. Highlighted with green area is the $^{13}CO_2$ absorption line and in Red $^{12}CO_2$. The magnitude of these areas quantifies their concentrations, from which the $\delta^{13}CO_2$ is calculated. Rather than wavelength the spectrum is plotted using wavenumbers $\tilde{\nu} = 1/\lambda$ which are typically more convenient numbers.

and further details on their calculation is presented in section 7.1. An important thing to note is that the magnitude (or height) of the absorption line-profile scales linearly with concentration. But the profile shape (including the height) is dependent on temperature, pressure and composition of the buffer gas. High precision CRDS analyzers therefore apply high precision temperature and pressure control of the environment of the sample gas, to provide good stability for the measurement. Special attention is also needed, if the same analyzer is used for measurements of a molecule being in a pure nitrogen solution and in an atmospheric mixture of nitrogen and oxygen.

When having samples of limited amounts, it may be convenient to lower the pressure. By lowering the pressure the peak height is roughly preserved but the width of the line is narrowed. This makes it harder for the spectrometer to target the peak and will eventually degrade performance. Most commercial analyzers operate around 150 to 200 mbar, but some go down to 20 mbar, and few even lower.

For trace gas analysis, α may be very small and attenuation by a single

pass through a gas cell can be essentially impossible to detect. To enhance the absorption, the light beam can be made to traverse the gas multiple times using mirrors. CRDS and other cavity enhanced methods bring this concept to its limit, using highly reflective mirrors (typically $> 99.99\%$) to create an effective path length which may be more than 10,000 times that of the gas cell length. In the following, the CRDS detection technique is described and in section 6.1 a comparison to the other cavity enhanced techniques is given.

2.1.3 The CRDS absorption measurement

A setup diagram for a CRDS analyzer is shown in figure 2.3. A tunable diode laser is targeted onto the optical cavity. This optical cavity consists of three optical mirrors which are aligned such that the laser beam forms a closed path on every round trip. The cavity is essentially opaque due to the high reflectivity of the mirrors (ca. 99.99%). But for wavelengths being an integer fraction of the cavity round trip, high transmission of power is possible because the oscillations of the incoming light matches phase with that circulating in the cavity, injected earlier by the same beam. In wavelength space this provide a grid $\lambda_m = L/m$ where L is the cavity round trip, m is an integer and λ_m is the wavelengths for which the laser will be on transmission resonance. The round gray data points in figure 2.1 fall exactly on such a transmission grid. The difference in light frequency between these transmission resonances is called the free spectral range denoted FSR $= L/c$. By changing the cavity length the transmission grid can be shifted such that any optical wavelength can be transmitted, see figure 2.2. The cavity length is changed by using a piezo electric actuator to move the position of a cavity mirror, see figure 2.3. This is an important attribute for targeting measurements at the peak of an absorption line. The continuous wave (cw) lasers commonly applied have an intensity spectrum which is much narrower than the spacing between the transmission modes of the cavity. So the laser is not automatically on

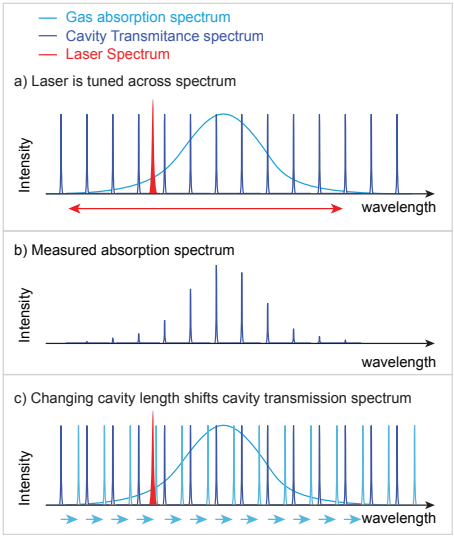

Figure 2.2: Spectra of cavity transmission and gas absorption. The gas absorption is sampled at the cavity transmission wavelengths. The latter can be shifted by changing the cavity length.

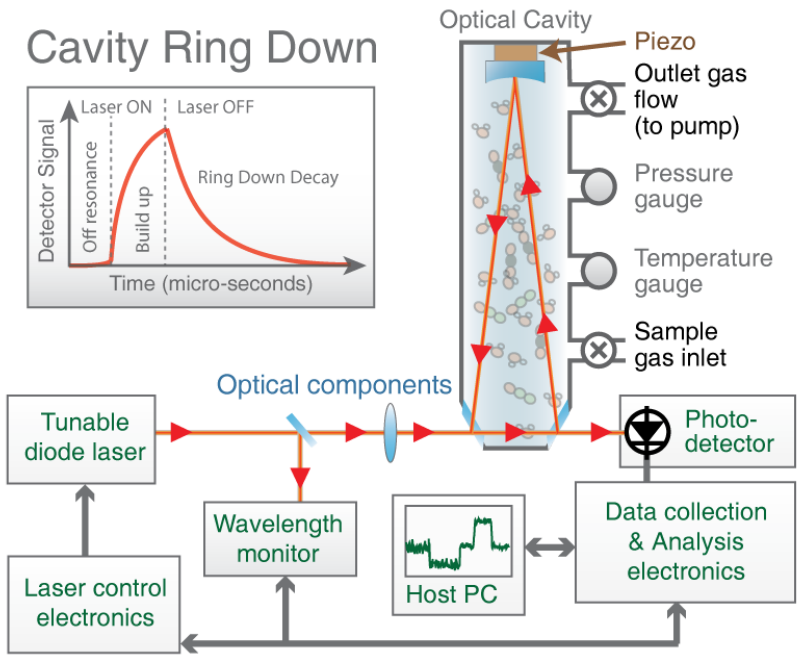

Figure 2.3: Diagram of the essential components in the CRDS analyzer.

resonance with the cavity.

In order to obtain resonance in practice, either the laser wavelength or the cavity length must be tuned, and generally both will be tuned, see Figure 2.2. The analyzer described in part II of this thesis, tunes the cavity length such that the transmission grid has a resonance at the peak of the absorption line of interest. The laser is then tuned over several free spectral ranges and the absorption at each resonance is measured to provide a spectrum such as shown in figure 2.1. [1]

To quantify the optical absorption, the CRDS analyzer performs a cavity ring down measurement, see plot in figure 2.3. A photo detector monitors the amount of light in the cavity. When laser and cavity are not on resonance no signal is detected. Once the laser hits resonance with one of the cavity modes, a transmission signal will build up stochastically. This is monitored by the electronics, and when the intensity reaches a preset threshold the electronics will turn off the laser, which happens in less than 100 ns. In the cavity, light is trapped between the mirrors and exhibits an exponentially decay in intensity (known as the cavity ring down) which may last for as

[1] In other systems the laser is tuned to the desired wavelength, and then the cavity length is rapidly swept to make a cavity modes sweep across the wavelength of the laser.

long as 40 µs or even more. The intra cavity laser power may be more than 10000 times higher than that exposed to the photo-detector. The entrapped light field loses power through the mirrors and due to prospective analyte absorbers. The more absorption is present in the cavity the faster the decay will be.

To extract the magnitude of cavity losses from the ring down signal, consider the following. The light intensity measured by the detector is directly proportional to the intensity circulating in the cavity and transmitted at the output mirror. The round trip time of light in the cavity, is typically on the order of a ns, which is much smaller than the typical response time of photo-detectors and thus not observed. The round trip time of light in the cavity is $t_{\mathrm{rt}} = L/c$ where L is the cavity round trip distance and c is the speed of light. In one round trip the light of intensity I will experience an absorptance A_c. This provides a rate equation for the intra cavity light intensity:

$$\frac{dI}{dt} = -\frac{A_c\, I}{L/c}\,. \tag{2.3}$$

which has the exponential decay solution

$$I(t) = I_0\, e^{-t/\tau}, \qquad \tau = \frac{L/c}{A_c} = \frac{1}{c\,\alpha_c} \tag{2.4}$$

where I_0 is the initial intensity, τ denotes the cavity ring down decay time, and α_c is the effective absorption coefficient pr. round trip in the cavity $\alpha_c = A_c/L$, the latter being the values that are plotted in figure 2.3. When the ring down decay is measured, an exponential fit is performed to find τ and thus α_c. Finally, a wavelength monitor is used to measure the exact wavelength of the laser at the time of the ring down event, so the absorption can be assigned accurately on the wavelength scale. This is basically all that is needed to run a CRDS analyzer and is summarized in the diagram of Figure 2.4.

It can be realized from the cavity round trip absorptance A_c, that the shaded areas of α_c really do correspond to that of the gas absorption α_g. This is seen by factoring A_c into the contributions from gas and mirror:

$$A_c = 1 - T_c = 1 - R_m^3\, e^{-\alpha_g L} \tag{2.5}$$

where T_c is the cavity round trip transmittance, R_m is the reflectance of the three mirrors and lastly the gas transmittance given by Beer-Lambertś law using the gas absorption coefficient α_g. Substituting $A_c = \alpha_c\, L$ and using the Taylor expansion $\ln(x) = x$ gives

$$\alpha_g = \alpha_c - 3(1 - R_m)/L \tag{2.6}$$

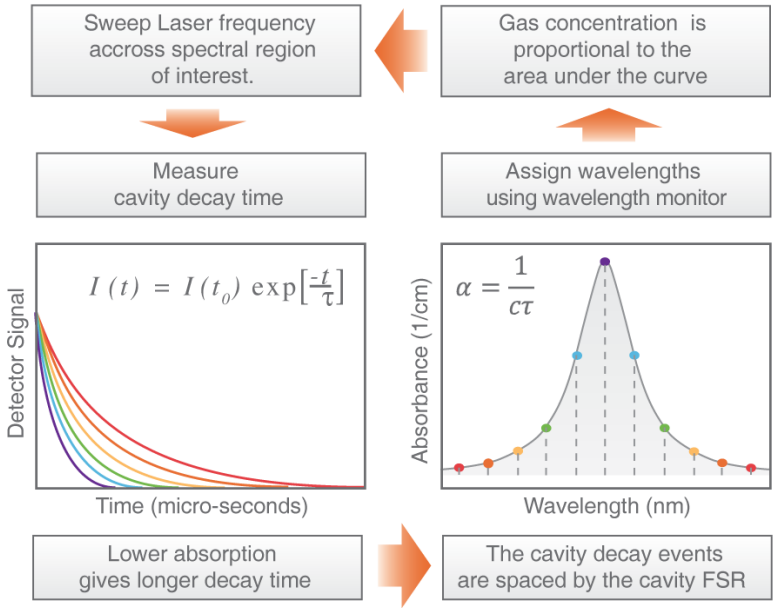

Figure 2.4: Basic procedure for using CRDS to measure gas concentrations. Start in upper left corner and follow the arrows. For further details see the text.

from which it is seen that α_c and α_g only differ by the empty cavity loss which is constant. Note that the area of the absorption peak is modulo the empty cavity baseline absorption. The baseline may be subtracted either by interpolating from parts of the spectrum without absorption or by measuring an empty cavity spectrum. The baseline absorption is never zero, because mirror transmissions and losses also contribute to the intra cavity round trip losses. This is realized by setting $\alpha_g = 0$:

$$\alpha_{c0} = (1 - R_m^3)/L, \qquad \text{for} \qquad \alpha_g = 0. \tag{2.7}$$

In terms of $\tau_0 = 1/c\alpha_{c0}$, this corresponds to the longest obtainable ring-down that can be measured from the cavity. For the current work, cavity ringdowns are recorded at 25 MHz. Thus, the longer the ring down time is, the greater is the number of sample points on the ring down curve. A better fit is therefore obtained for longer decay times, as there are more points for the exponential fit. High reflective mirrors giving a long ring down time, is therefore desired. The empty cavity, decay time is equivalent to the average life time of the light inside the cavity, which corresponds to an effective path length of $c\,\tau_0$. A cavity having $\tau_0 = 40\,\mu$s therefore has an effective path length of 12 kilometers.

When looking at dynamic range of concentration or isotopic measure-

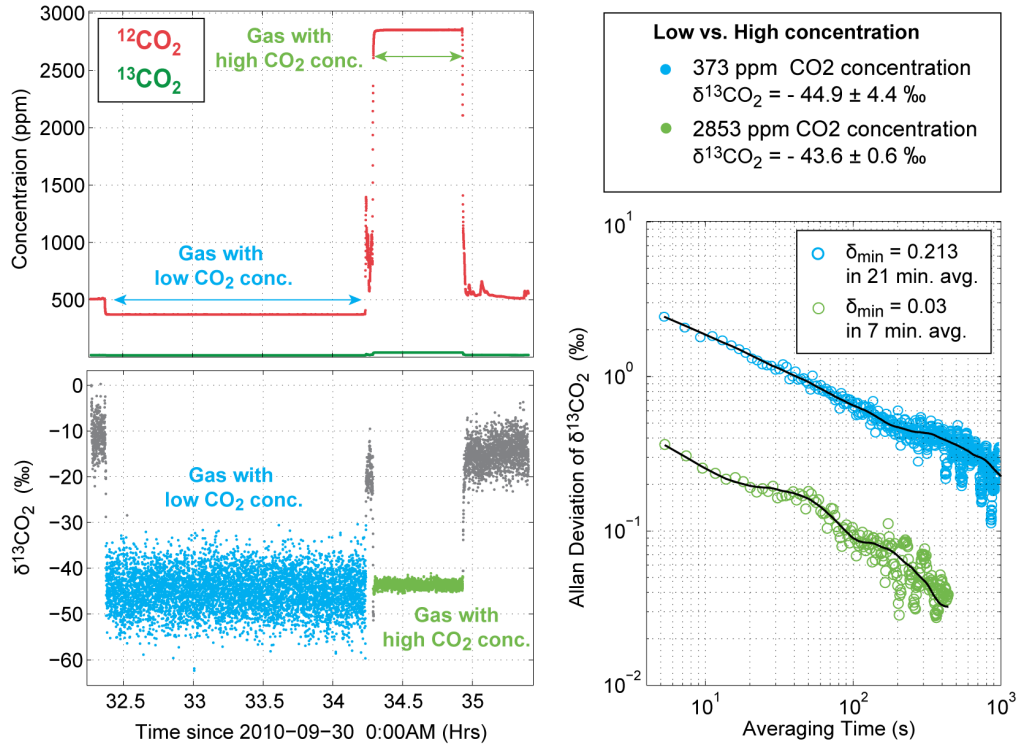

Figure 2.5: $\delta^{13}CO_2$ time series measurement of two gases with high and low CO_2 concentration using analyzer from chapter 3. To the right Allan plots are given for the isotopic sections of same color in the lower left plot.

ments as a function of mirror reflectivity, a long empty cavity decay time is also desired, as this provides a wider range of measurable concentrations. Further details on obtainable precision is presented in section 7.2.

One point from section 7.2 is that the precision of a weak absorber can be significantly improved by increasing the concentration of the absorber (Obviously – Making the absorption peak larger makes it easier to see.). This is in particularly helpful with low abundant isotopes, which often have very weak absorption profiles, that may be of comparable magnitude as to the baseline noise e.g. for the ^{13}C line in figure 2.1. An example of such an improvement is shown in Figure 2.5. The figure shows data taken with the analyzer used in chapter 3, where two gases having nearly the same $\delta^{13}CO_2$ but very different CO_2 concentrations are injected into the analyzer. By changing concentration from 373 ppm to 2853 ppm the precision in δ-value is improved from 4.4‰ to 0.6‰ (VPDB).

The CRDS method is a non destructive analysis, and so a measurement

can be repeated on the same sample as many times as desired, if the sample is kept statically in the cell. This provides the ability to improve precision by averaging repeated measurements expecting the standard error of mean to improve as $1/\sqrt{N}$ where N is the number of measurements. In practice analyzers are not perfectly stable and there is a limit to how many points can be used to improve the measurement. The Allan deviation presented in section A provides a measure of the precision that can be expected for a given averaging time. Figure 2.5 shows the Allan deviation calculated from the two $\delta^{13}CO_2$ isotope measurements at low and high concentration. As is typically the case these measurements show that the precision improvements follows a $1/\sqrt{t}$ relation with the averaging time t. Results in section 10.3 show examples where the precision does not keep improving for longer averaging times. This is the ultimate limit for the minimum detectable concentration or delta value. In Figure 2.5 the minimum detectable δ-value is limited by the extent of the sampled data, but it can be seen that the minimum must be less than 0.2‰ for the low concentration and 0.03‰ for the high concentration.

2.2 Stable isotopes

The most important elements in nature are considered to be Carbon, Hydrogen, Oxygen, Nitrogen and Sulfur. The stable isotopes of these elements (^{12}C, ^{13}C, ^{1}H, ^{2}H, ^{16}O, ^{17}O, ^{18}O, ^{14}N, ^{15}N, ^{32}S, ^{33}S, ^{34}S, and ^{36}S) provide a way of tracking their origin, sources and sinks in a chemical cycle. This is achieved through measurements and considerations of the isotopic molar concentration ratios and fractionation processes altering these.

The isotopic ratios are quantified by the molar concentration ratio $R_a = [a]/[A]$, where $[a]$ is the molar concentration of the heavy (less abundant) isotope and $[A]$ that of the heavy (the abundant) isotope, e.g. $[^{13}\mathrm{C}]/[\ ^{12}\mathrm{C}]$. Isotope ratios are typically small numbers and hard to quantify in absolute. Instead of reporting absolute isotope ratios, measurements are typically quantified with respect to a reference material (with known or decided isotpic-ratio $R_{\mathrm{reference}}$), and reported in form of the δ-value

$$\delta\, a = \left(\frac{R_{\mathrm{a}}}{R_{\mathrm{reference}}} - 1 \right) \times 1000\,[‰], \tag{2.8}$$

which is commonly stated in parts pr. thousand (‰) as indicated. For scientific comparisons of high accuracy, calibration of measurements is necessary in order to have comparable scales. The reference material for such a calibration must have well characterized properties and high degree of isotopic homogeneity. Reference materials and guidlines for these are provided by

national and international agencies like NIST[2], and IAEA[3]. Commonly used references for ^{13}C is the Vienna Pee Dee Belemnite (VPDB), for ^{18}O VSMOW (Vienna Standard Mean Ocean Water) and for ^{15}N the atmospheric composition of nitrogen isotopes is used.

Changes in the isotopic composition (fractionation processes) can be classified into several types, of which three important are: kinetic fractionation, equilibrium fractionation and mass-independent fractionation. These correspond to different chemical reactions. A fundamental principle of fractionation, is that the heavier isotopes is retarded due to its heavier mass.

Kinetic fractionation is related to fast irreversible, incomplete and unidirectional physical and chemical processes, i.e. $A \rightarrow B$. The kinetic fractionation is quantified in terms the *fractionation factor* $\alpha_{A\rightarrow B}$ and the more convenient *fractionation* $\varepsilon_{A\rightarrow B}$ defined by

$$\alpha_{A\rightarrow B} = \frac{k_a}{k_A} \quad \text{and} \quad \varepsilon_{A\rightarrow B} = \left(\frac{k_A}{k_a} - 1\right) \times 1000[‰] \tag{2.9}$$

where k_a and k_A are the reaction rates of the heavy and light isotope.

Equilibrium fractionation occurs in equilibrium reactions $C + D' \rightleftharpoons C' + D$ where C and D are two different chemical components and the $'$ denotes the location of the heavy isotope. An example of such a reaction is $H_2O^{18} + CO_2^{16} \rightleftharpoons H_2O^{16} + CO^{16}O^{18}$ which is the process used in mass-spectrometer measurements of $\delta^{18}O$ in water). the fractionation factor is then given by

$$\alpha_{C'+D\rightleftharpoons C+D'} = \frac{([a]/[A])_C}{([a]/[A])_D} = \frac{R_D}{R_C} \tag{2.10}$$

Equilibrium fractionation is typically smaller than kinetic fractionation and it depends strongly on the enrichments of the specific process. It origins from the mass dependence of translational, vibrational and rotational binding energies of the molecules. At equilibrium the isotopes are distributed according to minimization the these energies.

Mass-independent fractionation can be observed when considering more than two isotopic species such as ^{16}O, ^{17}O and ^{18}O or the isotopomers (see. definition below) of N_2O . It is generally expected that the fractionation of the heaviest isotope (e.g. ^{18}O) has double the magnitude as the fractionation for

[2]https://www-s.nist.gov/srmors/

[3]nucleus.iaea.org/rpst/ReferenceProducts/ReferenceMaterials/Stable_Isotopes/index.htm

the lighter isotope (e.g. ^{17}O) producing fractionations with $\delta^{17}O \approx 0.5 \times \delta^{18}O$ [de Groot, 2009, Ch. 6-9]. However photo dissociations processes such as stratospheric photolysis provide fractionations which deviates from this relation.

2.2.1 N_2O

N_2O is a linear molecule having it's oxygen molecule at the terminal position. This atomic configuration provides a difference on whether the N_2O molecule has a single ^{15}N atom located on the central or the terminal position in the molecule, see figure 2.6. This difference can be observed e.g. during photolysis from a UV source, and provide mass independent fractionation in the stratosphere, see section 4.1.3.2. Different nomenclature is applied in literature to distinguish isotopic molecular species. According to de Groot [2009] the following applies

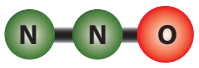

Figure 2.6: N_2O distinguishes between ^{15}N enrichment on central and terminal N position.

Isotopomers: Isomers having the same number of each isotopic atom but differing in their positions (e.g. $CH_2DCH{=}O$ and $CH_3CD{=}O$). The term is a contraction of "isotopic isomer".

Isotopoloques: A molecular entity that differs only in isotopic composition (number of isotopic substitutions), e.g. CH_4, CH_3D, CH_2D_2.

These terminologies are often not distinguished by authors and are often referred to simply as *isotopes of molecules*.

For the isotopomers of N_2O addressed in this work the following terminologies are often used in literature:

Formular	Kaiser & Röckmann	Yoshida et al.		
$^{15}N^{14}N^{16}O$	$^{1}\delta^{15}N$	$\delta^{15}N^{\beta}$	$\delta^{15}N_2O^{\beta}$	Terminal
$^{14}N^{15}N^{16}O$	$^{2}\delta^{15}N$	$\delta^{15}N^{\alpha}$	$\delta^{15}N_2O^{\alpha}$	Central

Two important quantities related to these are the Bulk and site-preference (SP) values defined by [Toyoda et al., 2008] as:

$$\delta^{15}N_{\text{bulk}} = (\delta^{15}N^{\alpha} + \delta^{15}N^{\beta})/2 \quad \text{and} \quad \text{SP} = \delta^{15}N^{\alpha} - \delta^{15}N^{\beta}. \tag{2.11}$$

2.2.2 Measurements of isotopes

The standard method for isotope ratio measurements is by isotope-ratio-mass-spectrometry (IRMS). Advantages of IRMS is the high precision and accuracy. Disadvantages is that they operate with high vacuum, is sample destructive and are easily contaminated.

For N_2O isotopes Rockmann et al. [2003b] achieve a reproducibility of ± 0.1 ‰ for $\delta^{15}N$ in N_2O , by using a combination of gas chromatography and IRMS. For the isotopomers $^{15}N^{14}N^{16}O$, and $^{14}N^{15}N^{16}O$ additional efferts is needed as IRMS cannot distinguish species of same mass directly. To determine the site-selective isotopic composition, the ^{15}N content of the NO^+ and N_2O^+ fragment and molecule ions of N_2O has to be analyzed [Brenninkmeijer and Rockmann, 1999]. For the isotopomers a precision of 0.05 ‰ has been achieved Röckmann and Levin [2005].

For CO_2 isotopes Werner et al. [2001] reported precisions of 0.012‰ for $\delta^{13}C$ and 0.019‰ for $\delta^{18}O$. However in inter-comparison between different labs these differences are often larger by an order of magnitude.

In this thesis it is examined how cavity ring down spectroscopy provides a competitive alternative to the mass spectrometers.

3

Using CRDS to measure δ^{13}C in rock samples from Greenland

During 2009 while the author was at Picarro Inc. the company developed an interface between a commercial combustion module (CM) and their isotopic carbon dioxide analyzer optimized for high concentrations. This provided an opportunity to examine the ability of measuring the carbon content of rock samples using CRDS. In October 2010 a CM-CRDS analyzer from Picarro Inc. was installed at the Geological Museum in Copenhagen. In this chapter I present the examinations of performance, memory effects and comparison with conventional Isotope Ratio Mass Spectrometry (IRMS).

3.1 Studying life conditions in the Archean eon using δ^{13}C measurements

Earth is considered to be 4.5 billion years (Ga) old Dalrymple [2001]; Manhes et al. [1980]. Through fossils it is known that life has existed for the majority of Earth's existence. These oldest known fossils date back 3500 Ma, and are considered to originate from photosynthetic cyano-like bacteria, Schopf and Packer [1987]; Schopf [1994]. The complexity of these life forms indicate that life must have evolved from even earlier times. Occurrence of fossils older than 3600 Ma are not know because supracrustal rocks older than this have undergone a high degree of metamorphosis, and the possible fossils in these rocks are therefore not preserved. Yet it has still been possible to make conclusions about the presence of life before 3600 Ma.

Rosing [1999] found indications that life existed $>$ 3700 Ma ago, by his findings that $2-5$µm graphite globules in the Isua supracrustal belt in West

Greenland, has isotopic depletion of ^{13}C with $\delta^{13}C_{PDB}$ ranging from $-10‰$ to $-19‰$. Earlier work by Schidlowski [1988] had shown similar indications and argued that such low delta values although modified by metamorphic reequilibration still represented the presence of Archean biogenic sedimentation, comparable to that of today.

From oxygen isotope inclusions in zircon grains it is suggested that oceans were formed 4.4 Ga ago Rosing et al. [2006]. Support that the Isua supracrustal belt contains remnants of an ocean similar to those of the present was given by Appel et al. [2001]. Hydrothermal systems are seeded by volcanoes and features of such are visible in the low strain zones of the ∼3.75 Ga part of the Isua Greenstone belt. In the primary features of mafic lavas with fine grained cooling rims and pillow breccias, a complex system of quartz veins and quartz globules is found. This system of veins and globules is interpreted as former gas vesicles which have been filled with quartz. Rare gaseous and aqueous inclusions are found in the globules showing remnants of methane and highly saline fluids of about 25wt.% NaCl. Appel et al. [2001] concludes that "the Isua pillow breccia preserves a record of an early Archaean sea-floor, methane-brine, hydrothermal system, which was operative at ca. 3.75 Ga. Overall similarities with fluids from present-day sea-floor alteration systems suggest that a number of conditions, notably the salinity of early Archean sea water, was not drastically different from today."

Banded iron formations (BIFs) are also present in the Isua Greenstone belt. The BIFs are believed to be sedimentations of iron that were dissolved in the Arcaean ocean. Fe^{+2} precipitate immediately when reacting with Oxygen, so it is believed that the oceans and atmosphere had very low concentrations of oxygen. Oxygen may have been formed by Oxygenic photosynthesis Rosing and Frei [2004] but anaerobic production of Iron oxide has been proven possible and Canfield et al. [2006] investigated the reaction rates necessary to be consistent with the carbon isotope records.

In order to confirm such dynamic considerations about these ancient oceans it is necessary to have a time series of data such as data deposited in chronological stratigraphies. In pursuit of such, the drilling of two rock cores through the sediment layers of the Isua Greenstone belt, was facilitated in 2008 by NordCEE and Minik Rosing. The two cores were drilled in a sedimentary section at two different locations in order to ensure replicate confirmation of the findings within the cores. The core depths measure roughly 80 m and 116 m, to include the full sedimentary rock section. Six 1 meter sections of the cores is shown in figure 3.1. Now remains a large number of measurements that need to be made on these cores. Measurements that may be done by the CM-CRDS analyzer.

Earlier it was thought that Earth was uninhabitable the first almost 1

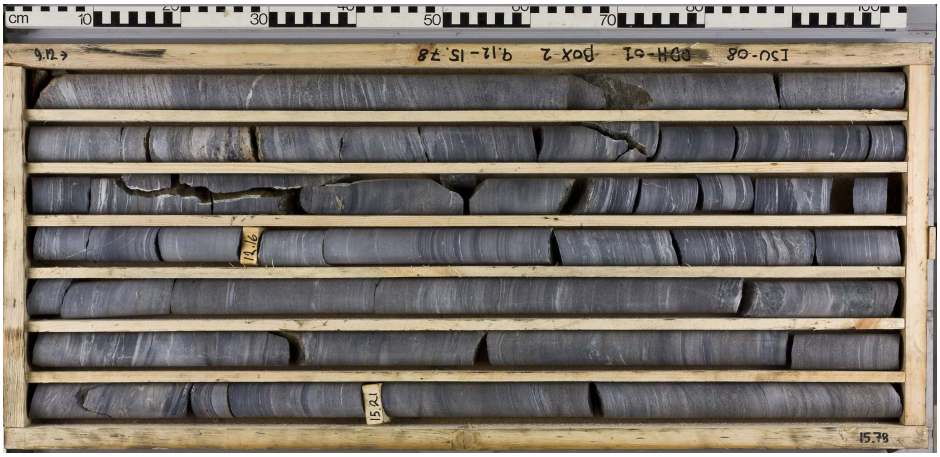

Figure 3.1: Seven sections of the Isua rock core each of 1 meter length.

billion years. With the findings from Isua, it is now suggested that life may have occurred almost from the beginning of Earth. This has led geologist to question the interaction between geochemical and biologic processes. Rosing et al. [2006] have suggested that the biosphere may have been an active player in the creation of Earth's continents, through considerations of the energy balance of Earth's internal heat production versus the much larger insolation from the Sun. The stratigraphic sedimentary layers at Isua provide a unique possibility of building a chronological story of events that occurred 3800 Ma ago, and the Carbon 13 isotopes may bring new insight to the extent, kind and dynamics of life during the Archean.

When Rosing [1999] documented the low δ^{13}C values in the Isua sedimentary rocks, he did this by grinding 5 to 10 cm^3 sedimentary sections and measuring the isotope composition of 2 g aliquots using mass spectrometry. He did this because previous studies Mojzsis et al. [1996] had shown large heterogenity of the graphite grain size with δ^{13}C variations of ~ 40 ‰ when studying with an ion microprobe. For the large number of samples needed to be studied in the Isua rock cores it is desired to have a robust semi automated simple system to perform the measurements. This work shows how the cavity ring down spectroscopy installed at NordCEE in Copenhagen provides a system which can measure δ^{13}C with 0.05‰ precision and very high accuracy which is essentially limited by the combustion system.

3.2 Analysis and Calibration of the CM-CRDS

3.2.1 Description of the analyzer

As the cavity ring down spectrometer only measures the isotope ratio of CO_2 the samples have to be converted into carbon dioxide. This is similar to the mass spectrometry methods. For this, the integrated CM-CRDS system provided by Picarro Inc. combines a Costech combustion module and a sample handling interface with the Picarro isotopic CO_2 analyzer. More details on the combustion module is presented in section 3.2.1.2.

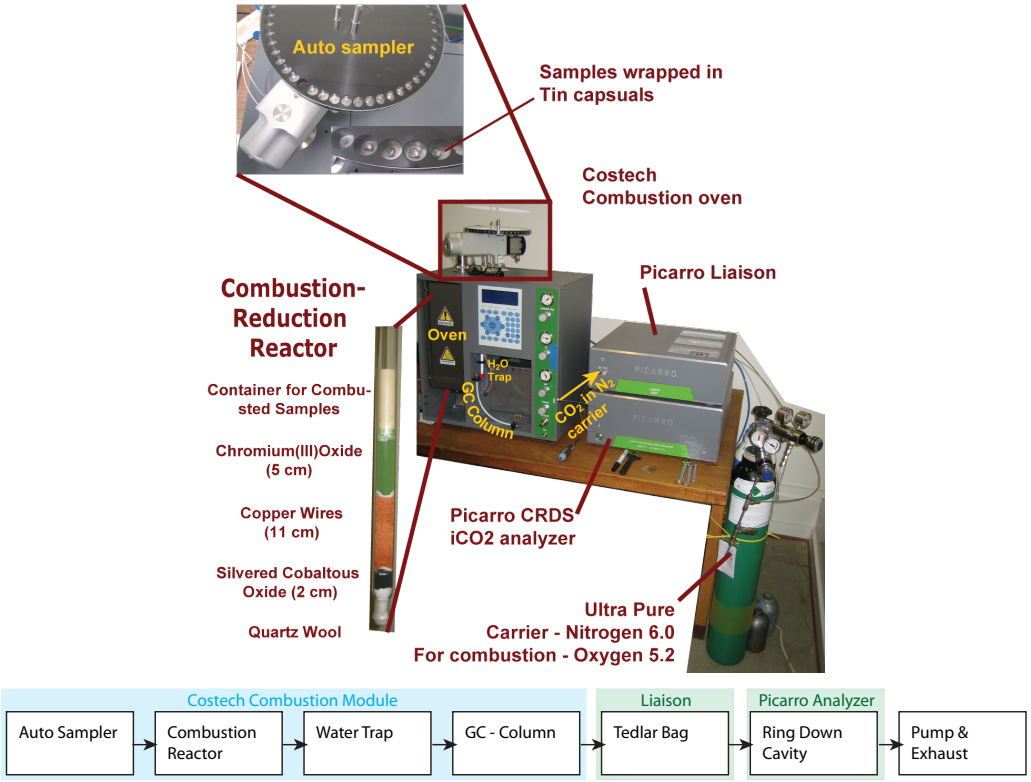

Figure 3.2: Top: Picture of the setup. Insets show closeup of the combustion/reduction reactor and autosampler. Bottom: Flow chart showing the processing of the sample. After the Combustion in the combustion reactor the sample is converted into CO_2 mixed in Nitrogen.

The system consists of six key parts.

1. An isotopic CO_2 CRDS analyzer – Picarro Inc. model G2121-i.
2. A diaphragm vacuum Pump – Supplied by Picarro Inc.
3. The Picarro Liaison – Universal Interface.

4. A combustion Module from Costech Analytical Technologies, Inc. equipped with an autosampler.

5. 99.9999% pure Nitrogen (grade 6.0)

6. 99.9992% pure Oxygen (grade 5.2)

The setup and sample processing is depicted in figure 3.2. The tin wrapped samples are placed into the autosampler on the top of the combustion module. The sample drops into the combustion/reduction tube which is continuously flushed with 80 mL/min of Nitrogen 6.0. Then a pulse of Oxygen is added which allows for the tin capsule to ignite and oxidize at 1600-1800 °C. Then carried by the Nitrogen the CO_2 flows down through the combustion reactor into a water trap (Magnesium Perchlorate), onward through a GC column and into a gas sampling bag where the sample is stored and mixed until the CRDS is ready. The CO_2 is then under steady flow carried through the cavity while being under very stable pressure and temperature conditions. The concentrations of $^{12}CO_2$ and $^{13}CO_2$ are averaged and an isotopic ratio is calculated. From the cavity the sample is exhausted through the vacuum pump. Figure 3.3 shows the elevated concentrations of CO_2 from consecutive combusted samples, between which the cavity is flushed with pure Nitrogen lowering the CO_2 to zero. Each measurement takes approximately 10 min including nitrogen flush time.

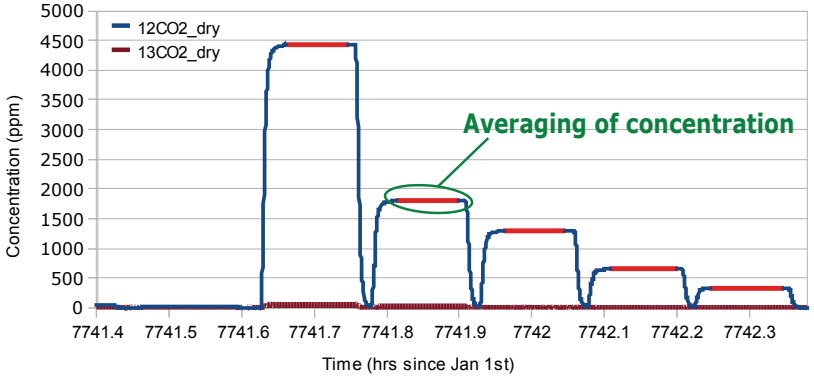

Figure 3.3: Plot of CO_2 concentration in cavity versus time. Highlighted in red is the part of each CO_2 pulse which is used to make an average value for isotopic ratio.

3.2.1.1 Liaison – Universal Interface

The gas sampling bag located in the Liaison serves two purposes: Ensuring a good mixing of the CO_2 isotopologues in the CO_2 pulse from the combustion

and to provides a steady CO_2 concentration when flown through the CRDS analyzer. Using gas sampling bags also provide an easy way of keeping a steady inlet pressure to the cavity. The Liaison has three gas sampling bags allowing that while one bag is being filled another is being diverted to the CRDS for measurement while the last is being flushed with pure Nitrogen to eliminate memory effects from the bags. This setup also enables the discrimination of memory effects from the combustion oven and from the Liaison itself, because these will show up differently with injections in the ring down cavity.

3.2.1.2 Running the Combustion Module

The Combustion Module works by the principle of flash combustion. The auto sampler drops the sample Tin capsule into to the Alumina Ash Crucible at the top of the reactor, see figure 3.2. In the 980 °C oven the Tin melts and penetrates into the sample. Then after 1-2 seconds a pulse of pure oxygen is added into the reactor, starting the flash combustion, which drives the local temperature around the sample to 1600 °C to 1800 °C. The sample is broken down into its elemental components; N_xO_y, CO_2, H_2O, SO_2, and excess Oxygen not used for the sample combustion.

According to the manual Saad [2010]: The chromium oxide catalyst in the combustion reactor ensures 100% conversion of the combustion products to the gases of interest. The excess oxygen is adsorbed by the copper wires, and any sulphur is retained by the silvered cobalt oxide[1] H_2O is retained by the magnesium perchlorate in the water trap. Since the CM uses pure Nitrogen as the carrier gas the only gas which will be measured is the CO_2.

However as will be shown in section 3.2.3 the Chromium(III)Oxide does not guarantee a complete oxidation for all types of samples.

3.2.2 Preparation of samples

1. The drill core is split with a diamond saw, cooled with water.

2. Sedimentary intervals of interest are selected and crushed and homogenized in either an agate mortar or an agate ball mill dependent on sample size.

3. Carbonate bearing samples are decarbonated by treatment with hot 2N HCl, followed by washing with MQ-water, and dried.

[1] Also the N_xO_y is reduced to N_2 by the copper wires.

4. Powdered samples are dosed on an electron scale and packed into small tin capsules, tightly folded to provide good contact between sample and tin.

5. Samples are loaded into the auto sampler, software is initiated and the rest is automated.

Proceedure for closing the tin capsule Using forceps, the top of the tin is capsule squeezed flat together. Grabbing the capsule on the top at either end, the ends are pushed toward the middle, forming a "Z" shaped fold. Holding the capsule at the top with a single tweezer, the top is pushed towards the bottom as to squeeze the bottom flat, creating a broad contact between sample and tin while holding the tweezer tightly to prevent any sample from escaping. Then using two forceps the top is folded folded over to seal the top and the whole capsule is pressed tightly together to form a spherical/cubical shape.

3.2.3 Minimizing memory effects from incomplete combustion

The first task with the analyzer was to calibrate it using known standards. However, the system was showing memory effect and the first three weeks more than 400 runs were used to diagnose and solve memory problems. Particular problems were caused by the NordCEE internal standard 1 (NIS-1, described in section **??**).

The impact of a combustion memory effect may be calculated using Keeling's Law of isotopic mixing. This states that when mixing of two gases of different isotopic composition the resultant isotope delta value may to first order be expressed as

$$\delta_m = \frac{c_b}{c_m}(\delta_b - \delta_S) + \delta_S \tag{3.1}$$

where c is molecular concentration, δ isotope delta value and subscripts S, b and m denotes sample, background and measured. The impact of a memory effect is in other words dependent on difference in isotope delta value of the samples being mixed by carry over. The shift in delta value is linearly dependent on the ratio between the concentration sample and carry over. So if a sample is measured at a concentration of 4000 ppm, but 1000 ppm is carry over from the previous sample, then this will mean that the measured delta value is shifted one fourth the way from the sample delta value toward the carry over delta value. It is thus appropriate to look at the concentrations of CO_2 contributed from the samples.

	CO2 (ppm)	δ^{13}C (‰)
Sample Gas	3500	-30
Background	50	-25
Mixed composition		-29.93
Shift from sample		0.07

Table 3.1: Calculation of a background influence based on equation 3.1. A 500 ppm background was considered as a small background by the analyzer, but as seen from this table, a level of only 50 ppm background may provide a significant shift in the sample delta value.

The memory effect was diagnosed by running four or five blanks (empty tin-capsule) after running a sample and watching how the concentration would evolve for the blank samples. When having memory effects, the CO_2 concentration stay elevated in the consecutive blanks. This is actually the case in figure 3.3 where the first high pulse is an actual sample followed by blanks, which still show elevated concentrations of CO_2 starting at 1800 ppm and exponentially decaying towards zero with consecutive blanks.

This exponential decay signatures that the memory effect originates from the combustion unit and not the cavity or Liaison. Memory effects from the cavity would prevent the concentration from dropping to zero between runs, this is not observed. Memory effect from a specific bag in the Liaison would show up in correlations between every third cavity injection. This is not seen either, so this memory effect has to originate from the combustion unit.

It is interesting to consider how much impact a certain background level has on a given measurement. Using the keeling equation, table 3.1 shows that a background concentration of 50 ppm deviating by 5 ‰ will cause a measured mixed value which deviates by 0.07 ‰ from the sample isotope delta value. By the manufacturer the analyzer is set to not report values for samples which produce concentrations which are lower than 500 ppm or higher than 10000 ppm. If the background level in table 3.1 is changed to 500 ppm the measured value would deviate by 0.7 ‰ from the sample value. We had the lower reporting boundary value changed such that values as low as 50 ppm would be reported. When operating with samples of unknown composition it would be advantageous that the sample values be reported regardless of the concentration, as these measurements may be the basis of quantifying how much samples should be used, or by using blank capsules verifying the background interference level from the combustion oven.

Considering background concentration levels it may be noted that the reported concentration when no capsule has been introduced to the system is between 8 and 10 ppm for a clean reactor. While the CRDS cavity is

flushed with pure nitrogen the reported concentration values drop to less than 1 ppm.

3.2.3.1 Effect of changing Oxygen flow

The largest improvement on the memory effect was achieved by increasing the amount of oxygen injected per flash combustion. The combustion module has three oxygen loops from which one can choose between three different volumes to be injected. The µ setting provides 2.5 mL pure oxygen per pulse, 5 mL is provided by the Sµ setting and 10 mL per pulse by the **M** setting.

The improvement on memory effect by changing the oxygen setting is shown in figure 3.4. At sample index 1 a capsule with 15 mg NIS-1 is combusted, and the following sample index 2 through 5 are empty tin capsules. This dummy test measurement was repeated three times for each oxygen setting to provide data confidence.

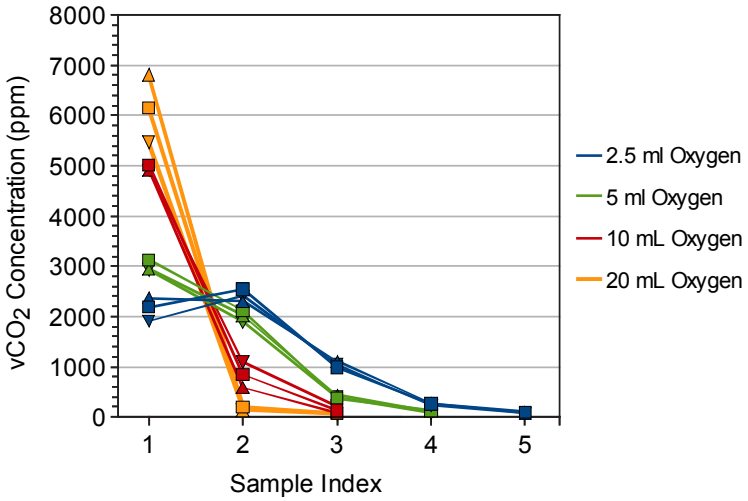

Figure 3.4: Comparison of memory for the three different oxygen settings of the combustion module. Increasing the amount of oxygen, redistributes the release of carbon and significantly decreases the memory effect for large oxygen loops.

Figure 3.4 shows how the release of CO_2 is redistributed on the following dummies. for the 2.5 ml settting, more CO_2 is released at first dummy (2500 ppm at index 2) than for the initial combustion of the sample (2000 ppm at index 1). It is not clear why this is the case but sample wrapping addressed in section 3.2.3.3 may partly explain this. Increasing the oxygen level to 5 ml, redistributes the carbon release, to decrease for each dummy i.e. at the first dummy only 2000 ppm CO_2 concentration is released while the initial combustion provides 3000 ppm CO_2 concentration. The performance

is also further enhanced as the CO_2 release at the fourth dummy (index 5) is lower than the Coordinator detection level. Finally for the 10 mL setting the combustion improves significantly for the initial combustion, releasing a CO_2 concentration of 5000 ppm, and the following dummy providing only 1000 ppm, and the CO_2 released dropping below the detection level already at the third dummy (index 4). One could argue that the CO_2 concentration is not indicative of the combustion process but the reproducibility of the profiles supports the above stated description.

Table 3.2: CO_2 Concentrations of initial combustion and when summed over the five injections in the sample dummy test. The values presented are averages with ± one standard deviation for the three repetitions at each oxygen setting.

Oxygen	CO_2 Concentration (ppm)		$\delta^{13}CO_2$ (‰)		
Setting	Sample Combustion	Integrated	Sample	Dummy 1	Dummy 2
2.5 mL	2156 ± 233	5957 ± 272	-22.15 ± 0.03	-22.15 ± 0.04	-21.1 ± 0.1
5 mL	3002 ± 111	5518 ± 227	-22.65 ± 0.07	-22.29 ± 0.08	-19.5 ± 0.6
10 mL	4941 ± 63	5923 ± 316	-22.73 ± 0.03	-21.18 ± 0.46	-9.7 ± 2.0
20 mL	6141 ± 673	6339 ± 637	-23.03 ± 0.11	-21.00 ± 1.02	-20.2 ± 6.0

It is also interesting to look at the integrated concentration over the dummy test profile for the three different oxygen settings. This is presented in table 3.2 showing that even though the CO_2 release in the initial combustion changes by more than a factor of two, the summed release is hardly altered. In table 3.2 is also shown, the $\delta^{13}CO_2$ value given by the initial combustion. This δ^{13}C goes toward lighter composition for the more complete combustion, which is a bit counter intuitive as one would expect that the lighter isotopes would be more easily released than the heavier and thus be more well represented in the more complete combustion. It is possible that this may be explained from the reaction rate being faster with the higher oxygen flow, but such a hypothesis would require further examinations.

From this test it was decided to use the 10 mL oxygen setting or higher.

3.2.3.2 Effect of adding Chromium(III)Oxide

Adding Chromium(III)Oxide in the sample may help to ensure complete sample combustion. Figure 3.5 shows data taken with the system to examine this hypothesis. Five samples were run adding different amounts of Chromium(III)Oxide to the tin sample package filled with 15 mg NIS-1. Each of the five samples were followed by a dummy test of four or five empty tin capsules. Comparing the CO_2 concentration decay in the dummy test for the different added amounts of Chromium(III)Oxide, shows no clear trend of

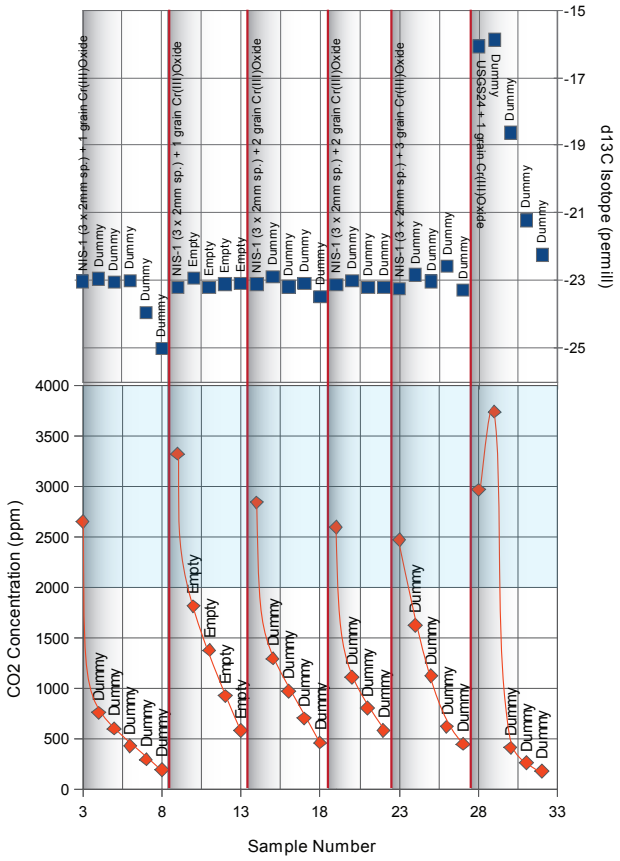

Figure 3.5: Study of memory effects when adding Chromium(III)Oxide of different amount to the tin capsules. Chromium(III)Oxide in grains of ca. 1 mm were added to ca. 10 mg of NIS-1 in quantities of one grain in Capsule 1 and 2; two grains in capsules 3 and 4; and three grains in capsule 5. The last sample contain USGS-24 with 1 grain Chromium(III)Oxide added to it. No significant change is observed for the different amounts of added Chromium(III)Oxide to NIS-1. But an enhanced memory effect is seen for the USGS-24 indicating a degradation in performance when adding Chromium(III)Oxide grains to the tin capsules.

improvement i.e. there is no significant support that adding Chromium(III)-Oxide to the packages enhances the combustion. Actually the last sample in figure 3.5 shows that when adding a grain of Chromium(III)Oxide to a package of USGS-24 provides a large memory effect, which is otherwise not experienced with the USGS-24 specimen.

3.2.3.3 Effect of sample wrapping

For the last sample shown in fiugre 3.5 the CO_2 concentration of the dummy following the sample has a higher concentration than the sample itself. This seeded the hypothesis that too much sample wrapping may shield the sample from being combusted. Meaning that the sample is only partly combusted during the first flash of oxygen.

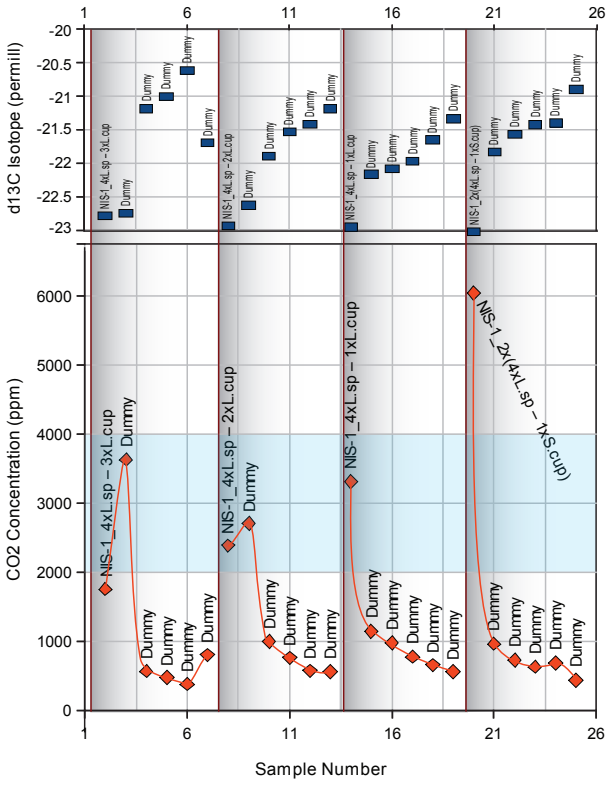

Figure 3.6: Investigation of memory effect when changing the amount of tin wrapping around the sample. The memory effect combusting 15 ± 5 *mg NIS-1 is tested for four different wrappings using five dummies after each sample. Sample 1: three 5x8 mm tin cups wrapped in layers upon each other like a Matryoshka doll. Sample 2: same as sample 1 but only two 5x8 mm tin cups. Sample 3: wrapped in single 5x8 mm tin cup. Sample 4: sample distributed into two 4x6 mm tin cups.*

The sample combustion depends on two factors: That the tin melts into the sample to provide extensive contact between sample and the high temperature from the flash combustion of the tin. Secondly: Oxygen has to be in contact with the sample for the combustion process to occur. If the package is too large or has been wrapped with too much tin, the oxygen pulse may not contribute enough time for the combustion to penetrate the whole sample. This will leave some non-combusted sample which will continue its combustion process at the following oxygen pulse, mixing the combustion products of the two samples and mixing their isotopic composition resulting in useless results.

Figure 3.6 shows the memory effect in four different tin wrappings. Notice that in the first two samples of NIS-1 an elevated concentration value appears on the following dummy, indicating that the sample is still being combusted during the combustion of the following dummy as was also the case in figure 3.4 for 2.5 mL oxygen. Wrapping the sample in multiple tincups, (as done for the first two samples) thickens the tin layer so much that the sample is not effectively combusted throughout the package until the following oxygen injection. Using only one large cup (5x8 mm) provides a better combustion as the oxygen can better access the sample. However the memory effect is still quite significant.

The last sample in figure 3.6 is wrapped into two small tin cups (4x6mm), and the total sample amount is doubled. Regardless of the sample amount being double of the other packages and actually also having less tin wrapping the memory in the following dummy is lower than for the sample being wrapped in a single large cup. This provides a much more efficient combustion as seen by the doubling in the CO_2 concentration from the sample CO_2 pulse and the concentration drop to 1000 ppm on the first following dummy. In the dummy tests presented in figure 3.6 the CO_2 concentration does not go to zero but levels out toward 250 ppm. This indicates that the reactor may also have been providing some background carbon, but the data show important indications of what may go wrong. This pre-examination also seeded the thought that distributing the sample into multiple packages may improve performance.

In further investigation of this hypothesis another wrapping test was performed, for which the results are presented in figure 3.7. It is reconfirmed here that with a too large tin capsule (9x10 mm) high concentrations of CO_2 occur in the first following dummy, almost as high as in the initial sample combustion. This indicates shielding of combustion by the larger tin capsule. Even when going from the 5x8 mm capsule to 4x6 mm some shielding effect from the larger tin capsule is seen, in terms of a slower decay of the CO_2 concentration.

When distributing the sample into two 4x6 mm tin capsules no significant effect is observed. However when distributing into four tin capsules the memory decay becomes longer again, indicating that the oxygen as a whole is consumed by the tin capsules, before the sample. It is primarily due to lag calibration that the range is restricted to the given range.

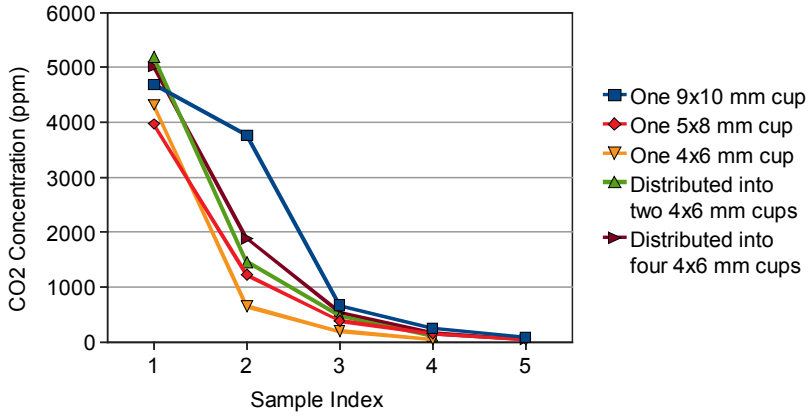

Figure 3.7: Memory effect from combustion of 15 ± 1 *mg NIS-1 for different wrappings. Index 2 through 5 are empty tin capsules.*

3.2.4 Effects of carbon amount on the delta value

In the manual for the analyzer it is stated that the carbon amount in a sample has to provide a CO_2 concentration between 2000 ppm and 4000 ppm in order to have reliable isotope measurements. It obviously requires some minimum CO_2 concentration in order to have a good absorption signal for the $^{13}CO_2$, but the upper limit is restricted by the shortening of the ring down time at the peak of the $^{13}CO_2$. The system acquired for this project is the first system to apply the new G2121-i isotopic CO_2 analyzer. This analyzer has a 25 MHz sample rate of the ring down signal, and it would thus be possible that the performance could be better for higher concentrations than in the older systems.

To investigate this, we loaded the analyzer with USGS-24 varying the amount of sample per package. As it only requires very little USGS-24 sample it was not possible to weigh the samples accurately with the available scales. The packages were therefore packed using a 1 mm dosing spoon. A total of 36 samples were made, ranging the number of scoops from 1 to 8. The change in concentration to the sample amount is plotted in figure 3.8 showing that one scoop corresponds to approximately a signal of 1000 ppm CO_2 in the

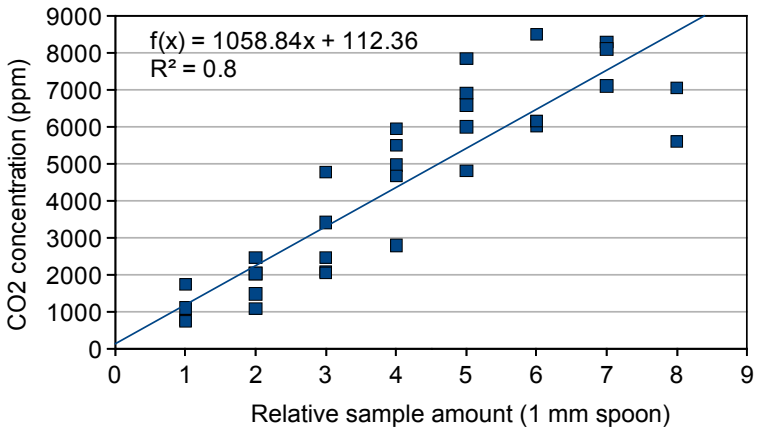

Figure 3.8: CO_2 concentration versus the number of 1mm USGS-24 scoops packed in the tin cup.

analyzer. The larger spread in concentrations at a higher number of scoops originates from the accumulated uncertainty of each scoop amount.

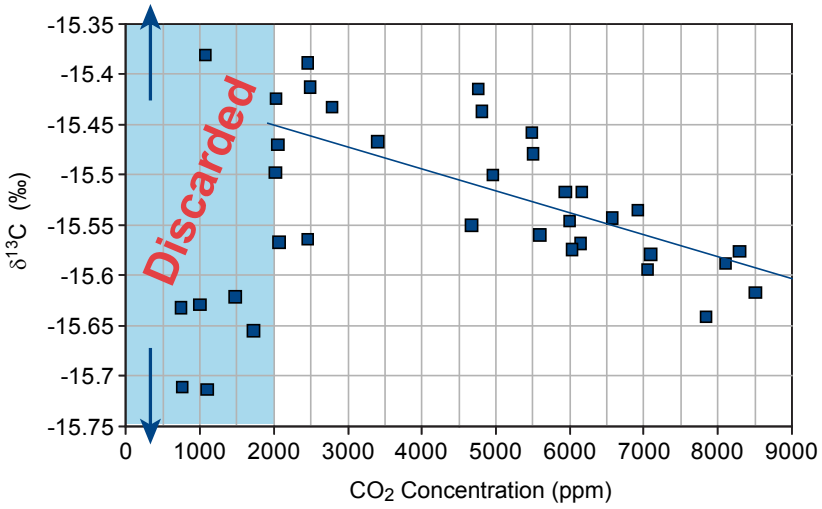

Figure 3.9: $\delta^{13}CO_2$ measurement of USGS-24 standard as measured for different amounts per tin package. Standard deviations over selected parts of this data are shown in table 3.3

The corresponding delta values versus CO_2 concentration of the 35 samples are plotted in figure 3.9. A summary of the standard deviations for selected parts of the plot is shown in table 3.3. Considering that the quoted typical precision of the analyzer is 0.2 ‰ when concentrations are kept within 2000 ppm to 4000 ppm, these data show that the analyzer may perform significantly better than this.

Figure 3.9 shows a step change in delta value at 2000 ppm which is likely to come from a change of domain for the fit to the absorption line, as the signal to noise improves. It also shows that 2000 ppm is an appropriate lower limit for the concentration. The standard deviation of the delta value for CO_2 concentrations higher than 2000 ppm is 0.07 ‰, surpassing the specified precision of 0.2‰. However when considering only the interval from 5500 ppm to 7000 ppm the standard deviation drops down to 0.02 ‰, which is remarkably good. It appears that this does not hold for the whole range from 5500 ppm to 9000 ppm because the values start drifting toward lighter isotope compositions with 0.025 ‰ pr. 1000 ppm, according to the fitted line in figure 3.9. The main result from this data is that if concentrations are kept within 3000 ppm to 7500 ppm a precision of 0.05 ppm may be expected.

Table 3.3: Standard deviations for selected parts of the data in figure 3.9.

CO_2 conc. Range (ppm)	stdev. (‰)
All data points	0.130
Above 2000	0.068
From 2000 to 6000	0.058
From 6000 to 9000	0.035
From 5500 to 7000	0.022
From 3000 to 7500	0.053

The NIS-1 samples have a TOC of 10% and from the measurement in figure 3.7 we see that 15 mg of NIS-1 provides a concentration of 4500 ppm from which we can conclude that the analyzer measures a CO_2 concentration of 3000 ppm/mg Carbon. So in order to hit within the 3000 ppm to 7500 ppm the total carbon amount in the sample should be within 1 mg to 2.5 mg.

3.2.5 CRDS precision dependence on CO_2 concentration

It is interesting to compare how the δ^{13}C precision of the combusted samples compare to laser analyzer precision. The reported delta value for a sample is based on the mean delta value of ca. 256 measurements made by the CRDS analyzer during the 8 minutes that the sample combustion product is being flushed through the cavity (the highlighted period in figure 3.3). This is not directly reported by the analyzer, so the data was re-extracted from the stored data in the folder: `DataLog_User`. For each measurement a section was manually chosen in similar range as indicated by the analyzer during operation. Based on the manual selection the mean and standard deviation was calculated for $\delta^{13}CO_2$, $^{12}CO_2$ and $^{13}CO_2$. Figure 3.10 shows the $\delta^{13}CO_2$ standard error of mean ($\sigma_{\delta^{13}CO_2}/\sqrt{256}$) for different concentrations being injected to the CRDS analyzer. These measurements were based on the USGS-24 measurements presented in the previous subsection, plus a few other samples with higher CO_2 concentration which were taken on December

16, 2010 having $\delta^{13}CO_2$ of around -23 ‰ and higher concentration.

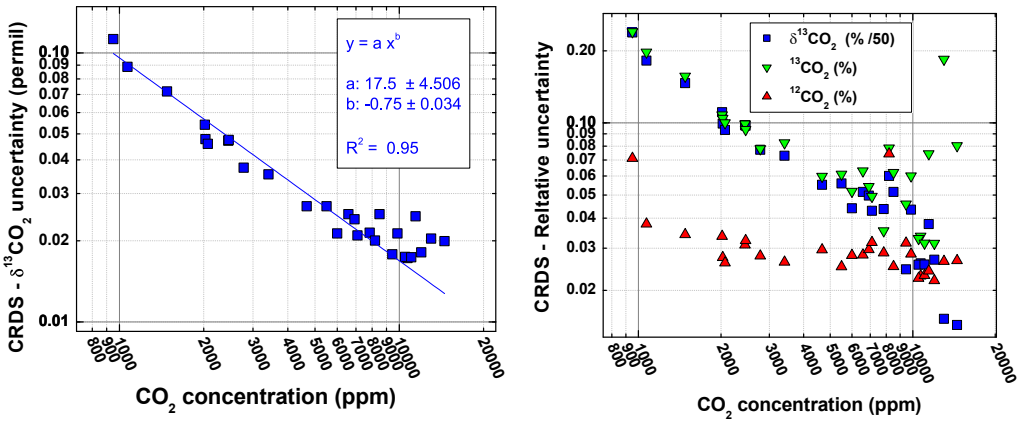

Figure 3.10: Left: Precision of the delta value recorded by the CRDS analyzer for different concentrations. Right: The delta value uncertainty is dominated by the uncertainty in $^{13}CO_2$. The correlation of the relative delta value uncertainty and the relative uncertainty in $^{12}CO_2$ and $^{13}CO_2$ is 0.32 and 0.97 respectively.

Figure 3.10 shows that at 2000 ppm the delta precision is 0.5 ‰. For concentrations lower than 2000 ppm, the uncertainty drastically increases. For values higher than 2000 ppm the uncertainty gradually improve with concentration. At 5000 ppm and above the error is lower than 0.03 ‰. This is because the delta value uncertainty is dominated by the uncertainty in the $^{13}CO_2$ as can be seen from the right plot in figure 3.10. This is to be expected as explained in section 7.2.1.

It is not clear from these measurements at which level the error is minimal, but it seems that the performance levels out around 10000 ppm. However it is certain that at concentrations exceeding 40000 ppm the precision is highly degraded. At such high concentration, the $^{12}CO_2$ concentration measurement is completely disturbed as shown in figure 3.11.

With the given setup the only way to increase the CO_2 concentration is to increase the amount of sample, which is a high price to pay if limited sample amounts are available. It is worth noting, that it is better to inject a large sample than to distribute over multiple injections, as the latter will only improve the delta value precision by one over the square root of number of samples, whereas increasing the concentration improves performance almost linearly. This assuming that the combustion processes does not decrease performance for increased amount of sample.

The concentration could also be increased by lowering the nitrogen flow, but this is obviously limited as the nitrogen acts as carrier gas from the

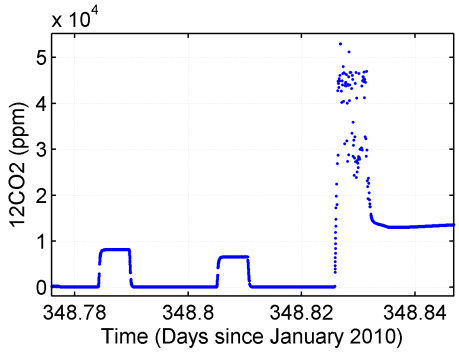

Figure 3.11: When the CO_2 concentration gets too high > 20000 ppm the low intensity of the transmitted light causes very poor performance.

combustion reactor. Finally the precision could be improved by increasing the integration time per sample, which requires that the performance is intact when lowering the gas flow through the cavity. The latter solution is also more time costly and it only improves performance by one over the square root of the integration time.

From the data in figure 3.10 and 3.9 it is concluded that the best performance in the delta value measurements by the CRDS analyzer is achieved for concentration between 6000 and 10000 ppm.

3.2.6 The carbon matrix effect on the delta value

The USGS-24 has a total carbon content of nearly 100%. This is much higher than the typical content in geological samples being around 10% to 0.05%. It is therefore interesting to see how the analyzer would respond to being diluted. Two studies were performed, one with poor mixing and one with homogenous mixing.

Non-homogenous blend of USGS-24 and Quartz For this, samples were prepared by dosing a proper amount of USGS-24 into a tin capsule and then adding highly pure quarts. For larger amounts of dilution some quarts was first added, then followed by the proper amount of USGS-24 and finally adding the remaining amount of quartz to reach desired dilution value. No significant effort to mix the quartz and carbon was made.

In Figure 3.12 shows the corresponding measurements of delta values and concentrations. The standard deviation of the $\delta^{13}C$ value stays well below 0.1 ‰ for samples diluted with 30 mg or less. For larger amounts of dilution, incomplete combustion starts to affect the measurements as seen by the lower concentrations for these measurements and the elevated CO_2 concentrations

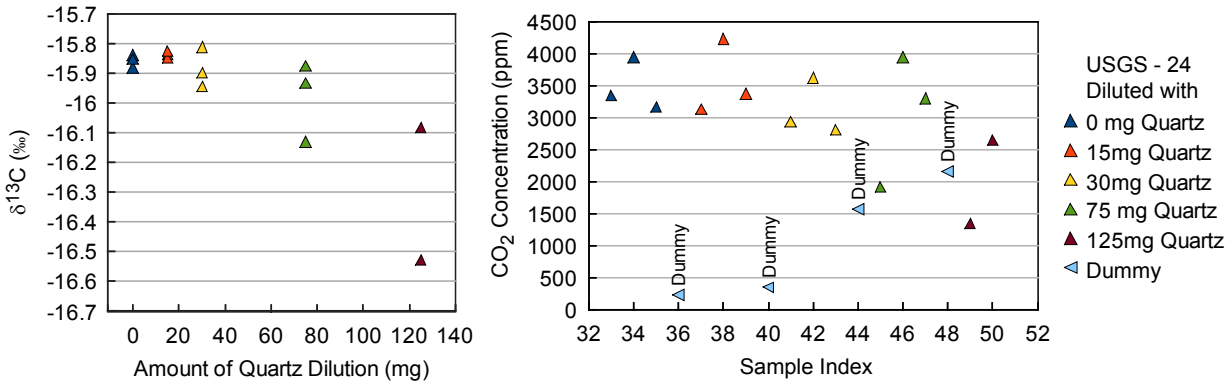

Figure 3.12: Measurements of USGS-24 diluted in different amounts of pure quartz. Left: $\delta^{13}CO_2$ vs. dilution and Right: Concentration vs. sample index.

for the interlaced dummies, see plot to the right in figure 3.12. So as long as there is less than 30 mg sample with more than 3 % carbon one may expect that the sample will be well combusted and have a delta value precision better than 0.1 ‰.

Homogenous Blend of USGS-24 and Quartz For a more accurate mixing ratio a larger volume was prepared, with respectively 10% and 1% USGS-24 diluted in Quartz of gem quality. The quartz was powdered in an agate ball mill. 1.80 g quartz powder and USGS-24 graphite was weighed out and mixed in a shaker. To produce the 1% blend, 1.80 g of the 10% mixture and 0.2 g pure USGS-24 was weighed out and also mixed in a shaker.

The delta value was measured for different sample masses on Feb. 8, 2011 providing the results shown in figure 3.13. Also shown in figure 3.13 are the data from figure 3.9 taken on Dec. 21 2010. These measurements were made with the unused reactor and 10mL Oxygen loop while the quartz diluted samples were taken with the same reactor more than 500 samples later, and using a 20 mL Oxygen loop.

The samples measured on 21/Dec/2010 have a concentration dependence of -0.02 ‰ per 1000 ppm, while the samples measured on 08-Feb-2011 all have a concentration dependence of -0.07 ‰ per 1000 ppm. The 100% USGS-24 and 10% USGS-24 fall on the same line, while the 1% USGS-24 blend is shifted by -0.28‰. The change in concentration dependence from 21-Dec-2010 to 08-Feb-2011 is either due to change in the Oxygen setting or due to wear of the reactor from the more than 500 samples run between the two sets of measurements. The undiluted samples fall essentially within the same range of delta values, indicating that system has had essentially no drift

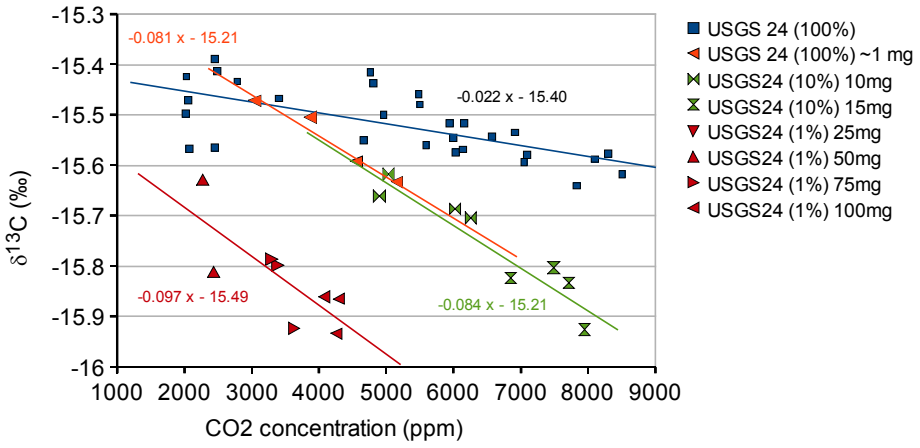

Figure 3.13: Comparison of different blending ratios of USGS-24 in pure quartz, and concentration dependence.

during the the six weeks between the two measurements.

The non homogeneous blends in figure 3.12 were taken at the end of a longer measurement series. No samples were run between these and the homogeous blend measurements in figure 3.13. Between these two runs the only changes were that the crucible inset was emptied and the Oxygen loop was increased from 10mL to 20mL. Most of the data points of the non-homogeneous blend fall within the delta values of the 1% blend around $-15.9 \pm 0.1‰$. It is likely that the lower $\delta^{13}C$ values of the non homogeneous samples are due to memory effects in the crucible, as the first samples in the homogeneous run fall within the delta values of measurements made on 21-Dec-2010.

In all three presented measurement series of USGS-24, the total carbon content was increased during the measurement. It may be that the concentration dependence originates from memory effects rather than concentration dependence. This could easily be tested repeating the measurement in reverse order.

3.2.7 Long term reproducibility

Collected in figure 3.14 are all the measurements performed on USGS-24 during the time of operation for this project.

The low delta values in the first five days are due to contamination of the combustion reactor, primarily from after having run large amounts of the NIS-1, causing a long term memory effect. For both day 38 and 39 the higher delta values are from before running 40 shale samples and the lower delta values are from after the 40 samples. Day 36 shows most of the

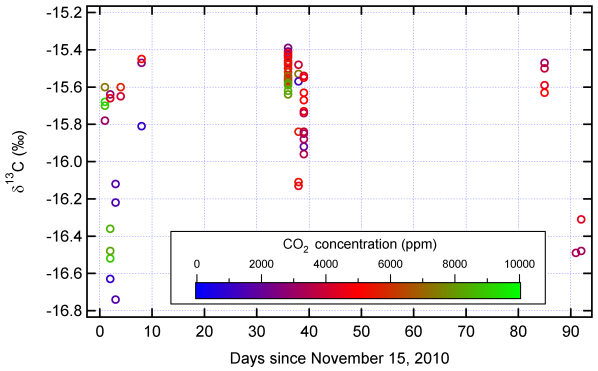

Figure 3.14: All measurements of USGS-24 taken during this project over course of time.

measurements presented in figure 3.9.

When ignoring USGS-24 measurements providing less than 2000 ppm CO_2 concentration and at most including 10 measurements from a single day the USGS-24 reproducibility is 0.63 ‰ (1-sigma).

Over the course of a day's set of measurements there is a tendency that the initial values are higher than the values taken at the end of a run. I conclude that memory effect in the combustion unit, possibly within the crucible may be the dominant factor of the observed drifts.

3.3 Measurement of the SPICE data series

To verify that the system is suitable for the geological samples, we tested the ability to reproduce a known geological sequence, and compared it to traditional mass spectrometry measurements. For this the Cambrian SPICE event present in the black shale rock core from Alum in Sweden was examined. This is a 28.9 meter thick section comprising gray to black, finely laminated mudstones with early concretionary carbonate lenses and a few primary carbonate beds. The section is fully described by Ahlberg et al. [2009].

Sample preparation The samples were prepared at the Institute of Biology, University of Southern Denmark by Tais W. Dahl. The black shale samples containing 5-15wt% organic carbon were crushed in an agate mortar to $< 0.3\mu$m particles. Powders were agitated for 2 hours in 2M hydrochloric acid to remove carbonates. Subsequently, the samples were washed in deionized water to remove any acid residuals. The samples were then dried and ground into a fine powder. Approximately 1.2 mg of carbonate-free material

containing 0.1-0.2 mg organic carbon was loaded into tin capsules, for the IRMS measurements made at SDU.

3.3.1 Initial examination samples with the CM-CRDS system

The samples were weighed out to match 1.2 mg carbon according to the reported carbon contents. Each sample was measured three times right after each other and followed by an empty tin capsule to remove memory effects for the next sample. At the beginning and end of the 50 sample carousel measurements of USGS-24 and USGS-40 standards were made to calibrate the measurements.

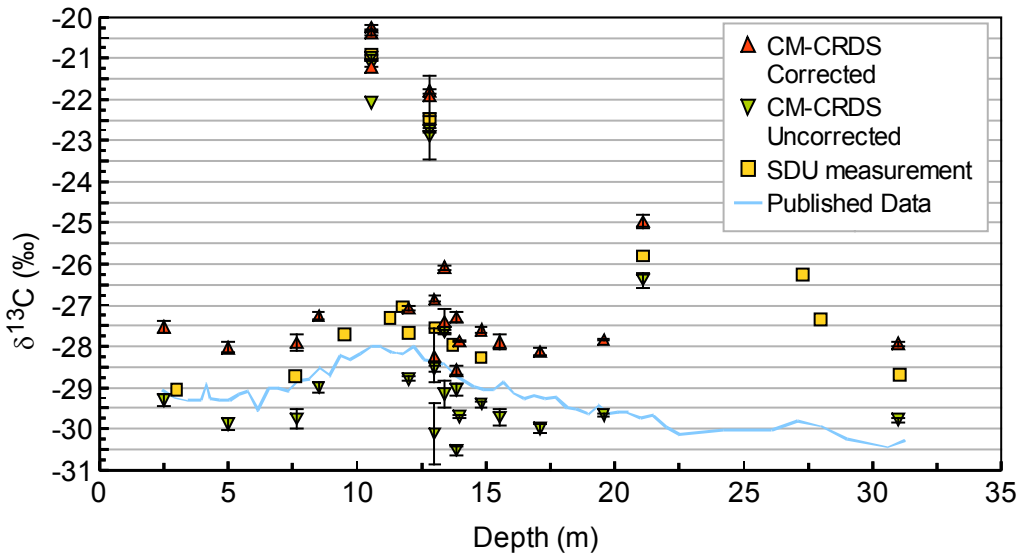

Figure 3.15: Initial measurements of the Alum SPICE excursion. Error bars indicate the $\pm 2\sigma$ standard deviation, which for many of the samples is less than 0.06 ‰. High delta values are caused by carbonates in the samples.

Figure 3.15 shows the obtained delta values from the measurements along with calibrated values described in section 3.3.2. When calibrated all data points have higher delta values than those reported by Ahlberg et al. [2009]. Some of the data points seem to follow the profile by Ahlberg et al. [2009], while others have delta values which are 3-8 ‰ higher than expected. The samples of the highest delta values at -23‰ were remeasured, and the high delta values were reproduced. Out of the 22 samples measurements, 13 samples showed a precision better than 0.05‰ (1 s.d., $n = 3$).

Mass spectrometer measurements performed at the Institute of Biology, University of Southern Denmark, also showed high delta values, so in that respect the CRDS and IRMS method agreed.

The outlying samples were examined with X-ray diffraction, which revealed large amounts of carbonates in these samples. Isotope measurement of the organic carbon is presented in section 3.3.3.

3.3.2 Calibration to standards on VPDB scale

The measurements reported by the analyzer were not calibrated to standards so calibration correction was performed in post processing. In this way it can be examined how the calibration affects the measurement values. For this two approaches were examined: recalibration using only USGS-24 and USGS-40 (2 pt. calib.) versus recalibration with USGS-24, USGS-40 and $CaCO_3$ (3 pt. calib.).

Figure 3.16 and table 3.4 show the measured calibration values and the standard reference value. Also shown are the linear fits, using either 2 point calibration or 3 point calibration. Table 3.4 shows the fit residuals for the two cases.

Table 3.4: $\delta^{13}C$ (‰) values used for recalibration of values in figure 3.15.

	VPDB	CM-CRDS	2 pt. res	3 pt. res
$CaCO_3$	1.96	4.28	-1.44	-0.14
USGS-24	-16.05	-15.765	0	0.36
USGS-40	-26.389	-28.272	0	-0.22

Using the 3 pt. recalibration applies less correction to the measured values over the whole region, but it should be expected to be less accurate at the lower delta values than if only the 2 point recalibration is used. Over the whole range from -29 ‰ to 2 ‰ the three point calibration provides less correction than the two point calibration.

Using the linear fit from figure 3.16 the measured δ_{pic} values from the Picarro analyzer were recalibrated using the formulas

$$\delta_{\text{3pt.calib.}} = 0.8735\ \delta_{\text{pic}} - 1.9175\ . \tag{3.2}$$

$$\delta_{\text{2pt.calib.}} = 0.8267\ \delta_{\text{pic}} - 3.0166\ . \tag{3.3}$$

Plotting the recalibrated values against values measured by IRMS at SDU, shows how the calibration affects the intercomparison. This is shown in figure 3.17 from which it is seen that the best agreement is given with the

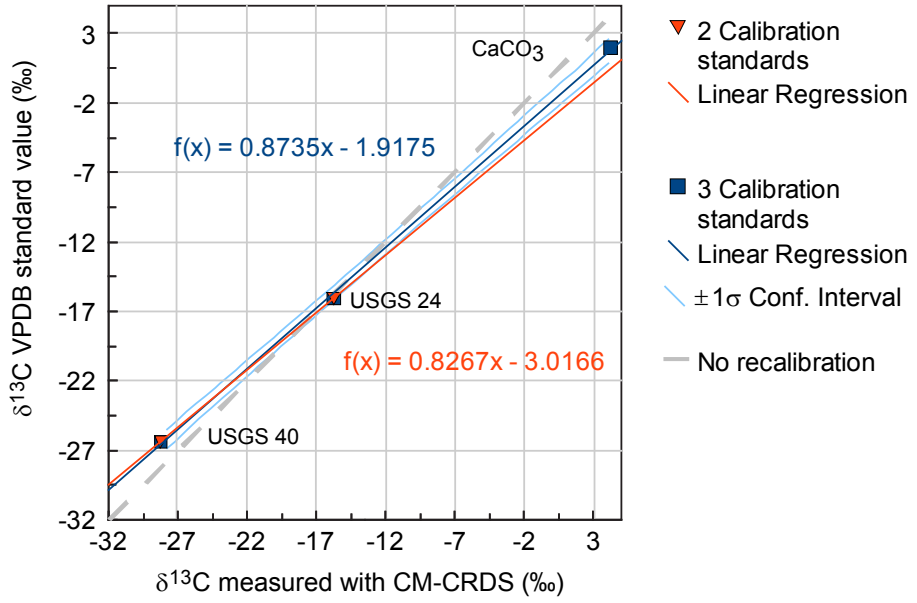

Figure 3.16: Measurements applied for the two calibrations. At low delta values below -28‰ the ±1σ confidence interval of the linear regression is greater than 0.7‰.

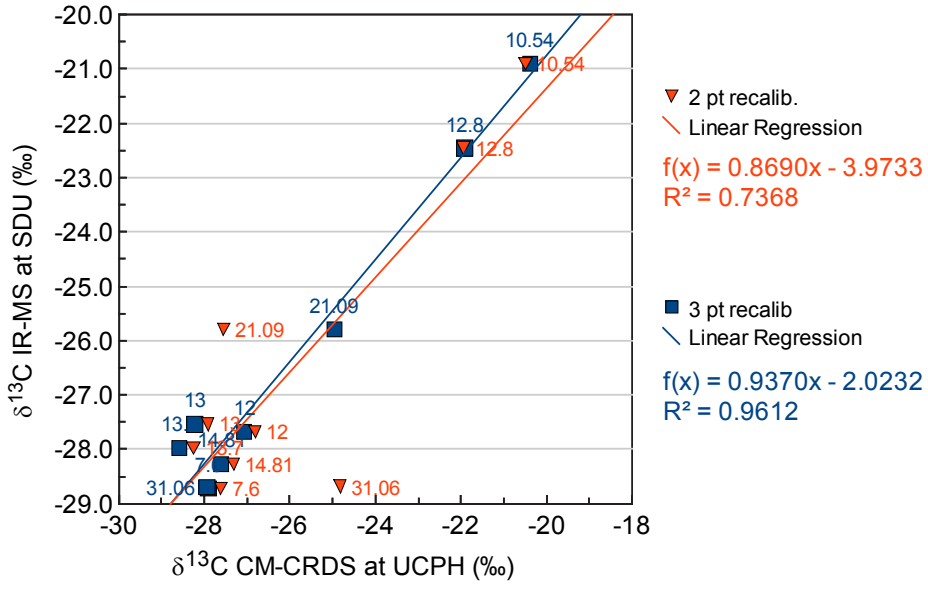

Figure 3.17: Comparison of the IRMS and CRDS measurements. The 3 pt. calibration provide a better match to the IRMS data.

3 pt. calibration. The standard deviation of the residuals change from 1.5‰ when using the two point calibration to 0.6‰ when using the three point calibration. This is not a given, as the third point ($CaCO_3$) has a delta value significantly outside the region of ther inter comparison measurements.

3.3.3 Measurements of organic carbon isotope delta values

It was concluded in section 3.3.1 that the samples contained large amounts of carbonates. To remove the carbonates the samples were heated in 10% HCl acid for an hour, followed by centrifugation in pH neutral solvent and finally dried at 60 °C for more than eight hours.

As many of the measurements presented in section 3.3.1 produced precision better than 0.05‰, it was decided to examine how the analyzer would reproduce the data set as a whole. To do this six measurement series were measured, on six different days. For each data series the whole sample set was measured making only one injecting per sample, and separating each sample by an empty capsule. The last three data series were measured in chronology with depth, while for the first three data series two of the samples were interlaced. Two of the data series 2.2 and 2.4 were performed in reverse order. No significant systematic alteration of the profile was observed for the data series measured in reverse order. The measured delta values are plotted in figure 3.18.

With the 2.0 data series, USGS-24 was run before and after the measurement for recalibration. The USGS-24 measurements showed a 0.6‰ drift over the 36 measurement, i.e. 0.016‰ per injection. Applying the USGS-24 at -16‰ to correct for values at -30‰ does not seem appropriate, so for the last five data series the sample from 2.5 m depth was measured at beginning and end of the data series. In post processing it became clear that there was no clear linear drift in the data which could be compensated for by applying these repeat measurements at start and end of the data series.

3.3.3.1 Calibration proceedure

Even though the independent measurements in the six data series showed no linear drifts, significant offsets were identified between the different measurement days. By considering the different data series as being independent, an appropriate calibration may be performed according to the following three steps.

Step 1 Find the average delta value of the measured samples at each depth.

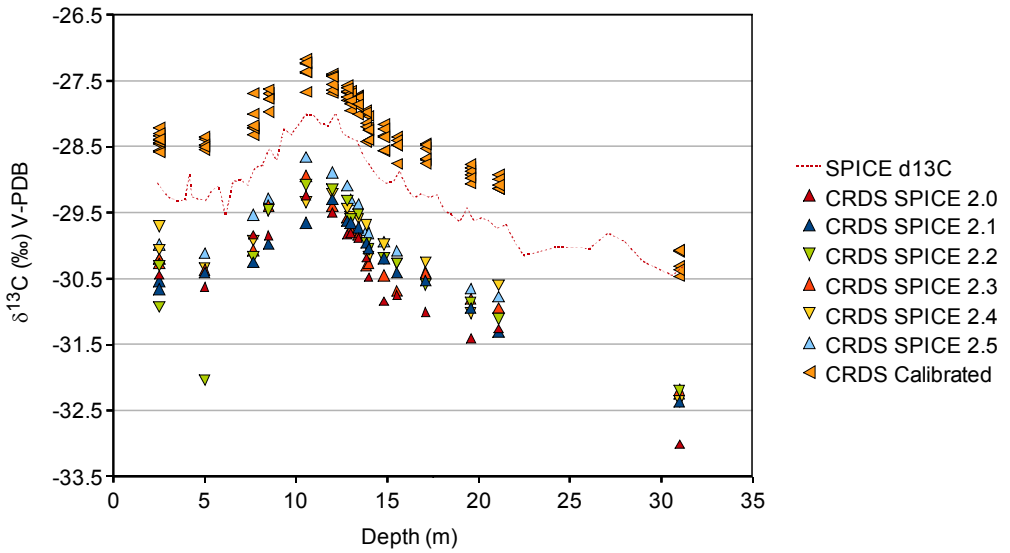

Figure 3.18: The six uncalibrated measurement series of the Alum SPICE excursion. The procedure for the calibrated data points is explained in the text. The red curve is the profile reported by Ahlberg et al. [2009].

Step 2 Find the offset to each data series which minimizes the deviation from the average values found in step 1.

Step 3 Apply the 3 pt. calibration from eq. 3.2.

In step two the different data series are considered as independent of each other. Letting $\mathbf{X}_i^j$ denotes measured delta at depth j in the data series i. Then the mean delta values $\overline{\mathbf{X}}^j = \sum_i \mathbf{X}_i^j$ can be calculated in step 1. In step two an offset x_i for each data series is found by the least square fit $\min_{x_i}\left[\sum_j \left(\mathbf{X}_i^j + x_i - \overline{\mathbf{X}^j}\right)^2\right]$.

For the calibrated measurements three of the data points were removed as the dummies indicated high levels of contamination.

3.3.4 IRMS comparison measurements

The IRMS comparison measurements were performed at the Institute of Biology, University of Southern Denmark (SDU) by Tais W. Dahl as follows:

"The samples were analyzed with a Thermo Scientific Delta V Advantage Continuous Flow Isotope Ratio Mass Spectrometer with FLASH 2000 EA

interfaced through a Conflo IV. A reference material (Atropine) was run between samples to monitor for drift of the measured isotope ratio $^{13}C/^{12}C$. A linear drift correction of -0.2‰ magnitude over the course of measurements (5 hrs) was applied to the analysis ($R^2 = 0.97$, n = 3). There was no systematic variation between obtained isotope ratios and signal intensity ($R^2 = 0.00$, n = 5). Certified reference materials with ^{13}C ranging from -45‰ to -26‰ (IVA-Sediment, IVA-Urea, IVA-Protein) were used to zero the ^{13}C scale at the Vienna PeeDee Belemnite (V-PDB). The in-run reproducibility of ATP was 0.2‰ (1 s.d.) comparable to the accuracy as determined by certified IVA standards (< 0.2‰). Precision was significantly better than this. ... a conservative estimate of the error of the mass spectrometric ^{13}C analysis is therefore 0.3‰.´´ (Tais W. Dahl).

3.3.5 Measurement results

In figure 3.19 the CRDS and IRMS measurements are plotted along with the published data by Ahlberg et al. [2009]. Figure 3.19 show that the CRDS and the two IRMS measurements provide the same delta value excursion over the profile.

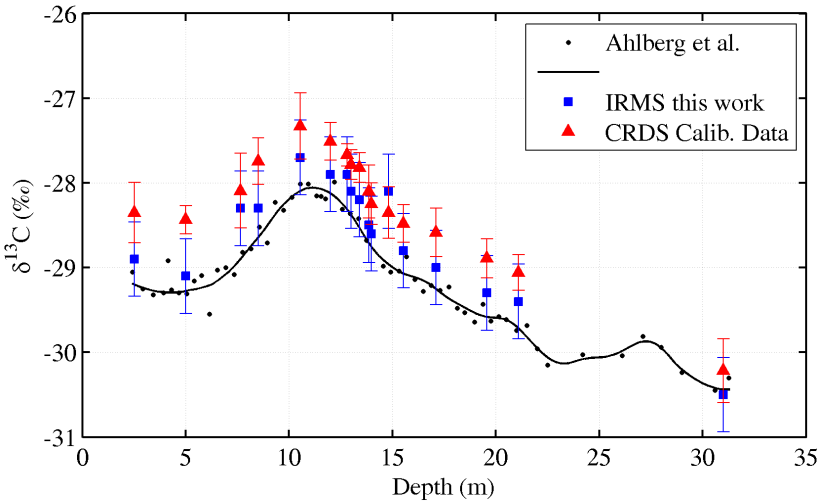

Figure 3.19: Measured $\delta^{13}C_{VPDB}$ values of the Cambrian SPICE excursion. Error bars are $\pm 2\sigma$ precision level.

To compare the profile by Ahlberg et al. [2009] with the measurements performed in this work, a smoothed interpolation curve was generated by making an interpolation spline to the Ahlberg et al. [2009] data points and smoothing with a local regression using weighted linear least squares and a

Table 3.5: $\delta^{13}C_{org}$ values of the Cambrian SPICE profile.

Depth	Ahlberg et al.	SDU	CRDS raw $\pm1\sigma$	CRDS calib. $\pm1\sigma$
2.51	-29.20	-28.9	-30.30 ±0.22	-28.35 ±0.18
5	-29.28	-29.1	-30.37 ±0.19	-28.43 ±0.08
7.65	-28.90	-28.3	-29.97 ±0.26	-28.09 ±0.22
8.5	-28.64	-28.3	-29.57 ±0.27	-27.75 ±0.14
10.54	-28.10	-27.7	-29.07 ±0.24	-27.33 ±0.20
12	-28.12	-27.9	-29.33 ±0.27	-27.51 ±0.11
12.8	-28.31	-27.9	-29.48 ±0.26	-27.67 ±0.07
13	-28.38	-28.1	-29.62 ±0.18	-27.79 ±0.09
13.4	-28.53	-28.2	-29.66 ±0.19	-27.82 ±0.09
13.85	-28.71	-28.5	-29.98 ±0.23	-28.10 ±0.16
13.97	-28.75	-28.6	-30.14 ±0.23	-28.24 ±0.12
14.81	-28.96	-28.1	-30.27 ±0.34	-28.35 ±0.15
15.53	-29.07	-28.8	-30.41 ±0.26	-28.48 ±0.11
17.1	-29.25	-29.0	-30.53 ±0.26	-28.59 ±0.14
19.57	-29.58	-29.3	-30.88 ±0.29	-28.89 ±0.12
21.09	-29.72	-29.4	-31.07 ±0.20	-29.06 ±0.11
31	-30.44	-30.5	-32.40 ±0.31	-30.22 ±0.19

2nd degree polynomial model with a 20% window. The spline values are listed in table 3.5 along with the measurement data points.

For the uncalibrated CRDS delta values the average reproducibility is 0.25‰ and for the calibrated values the average reproducibility is 0.13‰. The profile was only measured once with the IRMS system, but the accuracy was estimated to be 0.2‰ and conservatively stated as 0.3‰, showing that the CRDS method is highly compatible with IRMS. The plots in figure 3.20 compare the three data sets to each other.

On average the CRDS data are 0.66‰ higher than the Ahlberg et al. [2009] while the SDU measurements are only 0.31‰ higher. All three data sets are highly correlated with correlation factors > 0.96. The linear regressions in figure 3.20 between the three data sets show that the CRDS measurements and the IRMS from SDU have better agreement than with the Ahlberg et al. [2009] spline values. This deviation is primarily dominated by the sample value from 30m depth.

The offset between Ahlberg et al. [2009] and the SDU IRMS measurement lies within the estimated accuracy of the SDU measurements and can as such be accounted for. Ahlberg et al. [2009] do not state an accuracy of their values but mention that along with their 32 samples they measured

12 NSB-19 mean value and precision of 1.96 ± 0.02‰. Considering this it could be argued that the measurements from SDU presented here have higher accuracy as they have been calibrated to several low $\delta^{13}C$ standard values. The offset of the CRDS measurements may be accounted for by the lack of proper intercalibration between the CRDS analyzer and the mass spectrometer measurements. It is amazing that the CRDS and SDU-IRMS values only deviate by 0.35‰ being within the reproducibility of the SDU-IRMS, without any direct intercalibration.

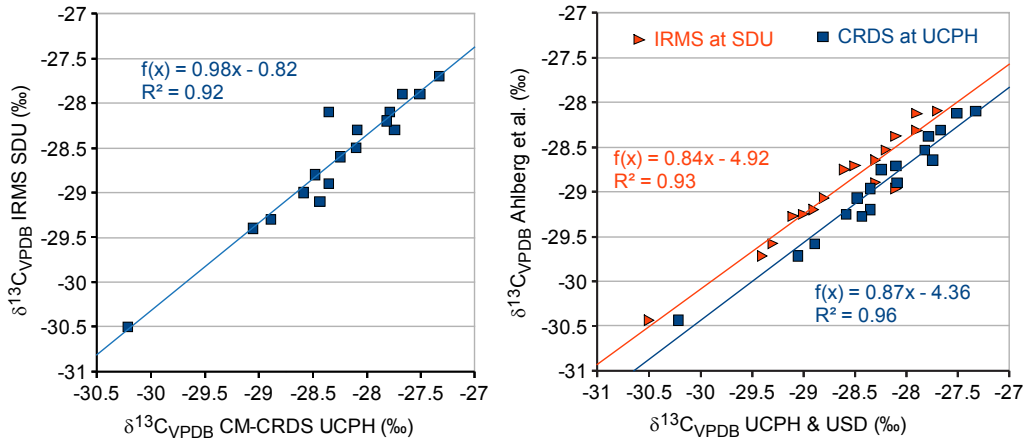

Figure 3.20: Comparison of the SPICE measurements. Left: Comparison of CRDS and IRMS measurements made in this work. Right: Comparison of measurements in this work to that reported by Ahlberg et al. [2009]. The measurements in this work have systematic better agreement to each other than to those of Ahlberg et al. [2009].

3.3.6 NordCEE internal standard-1, NIS-1??

Ca. 76 g graphite carbon isotope standard was manufactured November 10th 2010 by milling 6.9 g vein graphite from the Geological Museum collection with 69.8 g vein quartz collected at Isua, West Greenland in an agate ball mill. The vein graphite is from Lang', Upernavik Distrikt and the label is printed: Rink Nord-Grönland and numbered in ink: No 71 in the upper left corner and No 60 in the lower left corner.

3.4 Summary and outlook

3.4.1 Conclusion of system performance

Figure 3.21 plots samples which are completely combusted. For the measurements of Atropin, 30048 and the ISUA sample 01-08-07-54.18-54.21 in figure 3.21 a correlation of the delta value and the CO_2 concentration is presented. However, as the CO_2 concentration is outside the range accepted by the instrument from 2000-5000 ppm, this could be expected.

1. This study shows that a precision of 0.1 ‰ and better is achievable for rock samples using a combustion oven combined with a cavity ring down spectrometer.

2. The sample should be smaller than 30 mg and have a carbon content higher than 3 % in order to have a precision better than 0.1 ‰.

3. The combustion process is highly dependent on available oxygen and the wrapping of the samples.

4. The main drift effect in the presented CM-CRDS system appears to originate from the combustion module.

5. In advantage to IRMS, this method provides easy quantification of completeness of combustion and background levels. There is no drift from saturation like in the IRMS cups. Finally the continuous flushing of high grade nitrogen through the system provides an highly effective cleaning of the system which is not similarly possible in the ultra high vacuum of the mass spectrometer.

3.4.2 Future options for rock analysis

With the advances into mid-infrared spectroscopy analysis presented in part II new components may become measurable on a routine basis using CRDS. One component of high interest in geochemical samples is sulphur. The absorption lines shown in figure 3.22 are optional. Demonstrations of such measurements have been shown for δ^{34}S using a setup with a combustion unit, LN2 trap and direct laser absorption spectroscopy Christensen et al. [2007], with a 15 minute standard error of 0.55‰. Certainly, such a system could be improved further through the presented CRDS method.

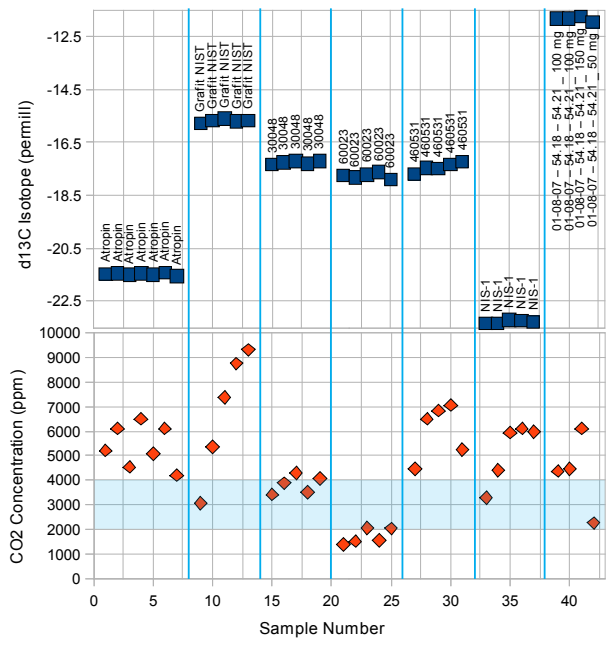

Sample	δ13C	stdev.
Atropin	-21.49	0.05
USGS 24 NIST Graphite std.	-15.69	0.07
30048	-17.25	0.06
60023	-17.77	0.11
460531	-17.44	0.18
NIS-1	-23.29	0.06
01-08-07 – 54.18 – 54.21	-11.82	0.09
$CaCO_3$ (+1.96 ‰ VPDB)	4.28	0.09

Figure 3.21: Irrespective of the samples being combusted CO_2 concentrations of higher than 4000 ppm gave great precisions of better than 0.1 ‰

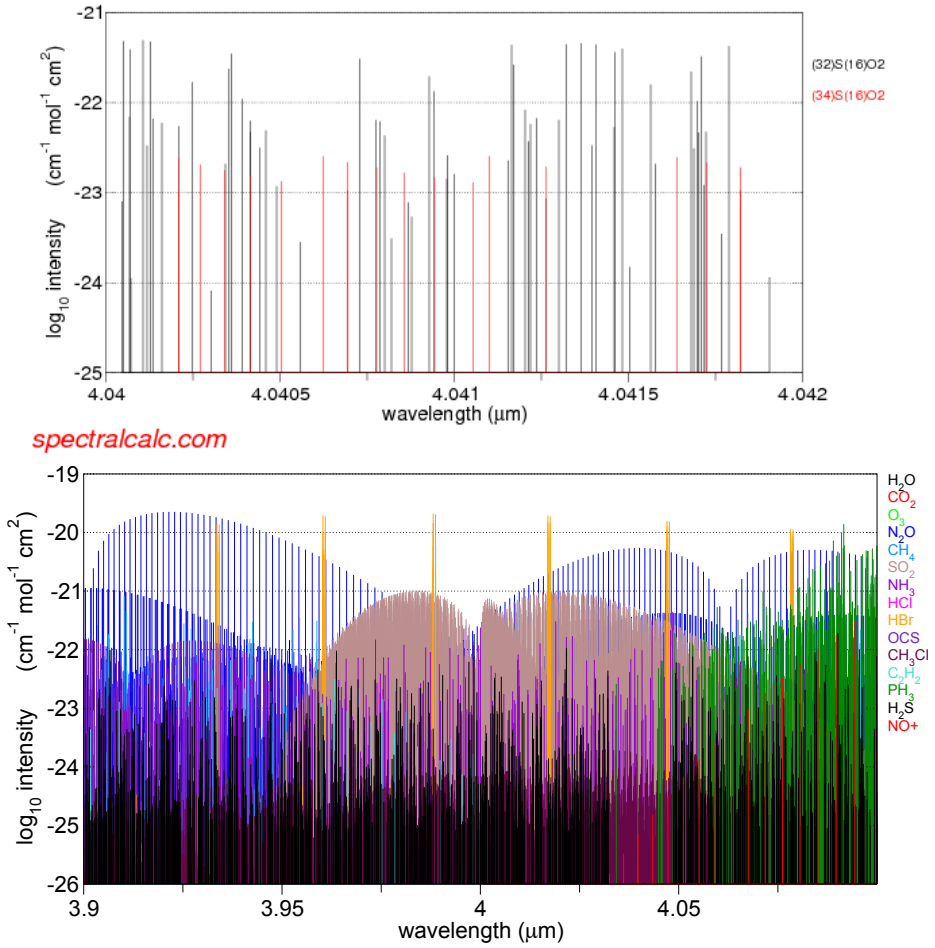

Figure 3.22: Spectral line intensities from Hitran. Right: Suitable spectral SO_2 isotope and possible interfering gases. Left: Zoom to a possible area for $\delta^{34}S$ measurements.

4 Applying CRDS to ice core samples

4.1 Motivation: climate history of N_2O

4.1.1 Archives of climate history

To understand the earth system in more recent time, polar ice-sheets have proven an invaluable archive of information on past climate, ranging back 800,000 years (BP) in Antarctica [Jouzel et al., 2007; EPICA Community et al., 2004] and 123 kyr in Greenland [North Greenland Ice Core Project, 2004]. The ice-sheets are built up by precipitating snow, accumulating layer upon layer, year after year. By drilling into the ice-sheet from the top a chronological record of information going back in time is retrieved.

A wide range of measurements are conducted on the ice cores e.g.: Crystal structure and orientation, aerosol impurities, water isotopes, and the concentrations of different atmospheric gas species in the air bubbles enclosed in the ice.

4.1.2 Ice sheets and water isotopes

The first climate record dates back 100,000 years and was obtained by measuring water isotope $\delta^{18}O$ in the ice core from Camp Century [Dansgaard et al., 1968]. Since then has numerous ice-cores been drilled in Greenland and Antarctica. Stable isotopes of water $H_2{}^{16}O$, $H_2{}^{18}O$ and HDO provide information about ocean source conditions and precipitation temperature. During transport, from the ocean evaporation site at lower latitude to the precipitation site on the ice sheet, the water isotope composition undergoes a Rayleigh distillation process. The heavier isotope falls behind in every part of the transport and have a higher condensation and evaporation temperature.

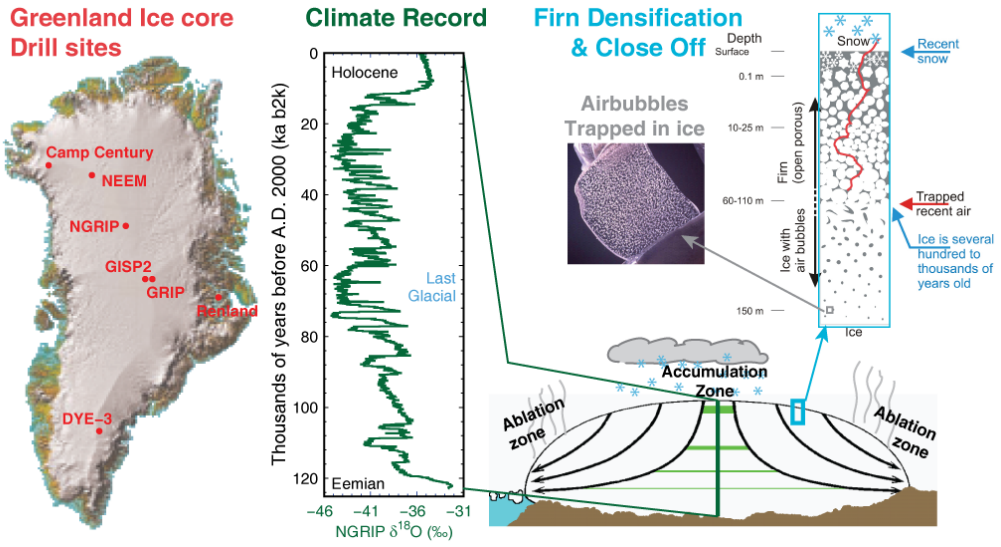

Figure 4.1: Collage of ice-core science. The map of Greenland shows important ice-core drilling sites. The climate record is the $\delta^{18}O$ record from NGRIP reproduced from Steffensen et al. [2008]. To the right a transect of an ice-sheet is sketched. The annual layers are thinned toward the bottom by the burden of overlaying ice layers. Ice is incompressible so a stretching deformation of the layers gives a net horizontal transport toward the ice margins. At the top of the ice sheet fallen snow is compressed into ice in the top 150 meters called the firn layer. During this process pockets of air are enclosed into the ice.

During evaporation in the North Atlantic from ocean to cloud, δ^{18}O becomes depleted by ca. 10‰ compared to the ocean composition [Dansgaard, 1964]. During precipitation further depletion of the cloud composition occurs as the heavy isotopes condensate more readily. Accordingly, the δ-value of both vapor and precipitate becomes increasingly negative, the more water is removed from the cloud. The variations δD and δ^{18}O is closely related to the changes in local temperature [Johnsen et al., 1989]. Variations of δ-values in ice cores provide a temperature proxy of annual cycles (in high layers) as well as glacial to inter glacial changes in temperature (in deeper layers). Figure 4.1 shows the δ^{18}O record from NGRIP. By comparing δ-values of different isotopes, additional information can often be deduced due to differences in fractionation factors. Deuterium excess defined as $d = \delta\mathrm{D} - 8\,\delta^{18}\mathrm{O}$ provide information of the evaporation conditions [Johnsen et al., 1989]. When the evaporation site is warmer than 20 °C deuterium excess becomes positive. In Greenland the deuterium excess changes by about 0.35‰/ °C of sea surface temperature change. By examination of the deuterium excess Steffensen et al. [2008] concluded that rapid climate changes can occur within 1 to 3

years.

4.1.2.1 Impurities and Aerosols

The ice cores also have other climate informations such as dustlayers from volcanoes and dessert storms. Several nondestructive methods are applied to study the impurities in the ice. With a line scanner, an optical dark field image is made along the ice core. From this physical impurities are optically visible as cloud bands on the picture, revealing dust layers among other. Electrical conductivity measurements (ECM) and dielectric profiling (DEP) are also fast non destructive method providing information about the ionic content of the ice. These methods provide information on occurrences of dust storms and volcanic eruptions [Hammer et al., 1980; Dai et al., 1991]. For further detailed knowledge of what the impurities are chemical studies has to be made which is done in high depth resolution with the continuous flow analysis system explained further below. Such systems provides data on $[SO_4^{2-}]$, $[Na^+]$, $[NO_3^-]$, $[Ca^{2+}]$, $[NH_4^+]$, and [Fe] among other [Rasmussen et al., 2006; Wolff et al., 2006; Andersen et al., 2006; Svensson et al., 2006]. These components provide knowledge and distinction of cyclonic system, volcanic eruptions, forrest fires, sea ice extent, and more [Legrand and Mayewski, 1997].

4.1.2.2 Gases

In the top ca. 150 meters of the ice sheet (called the firn layer), snow is compressed into solid ice, in a process described by the Herron and Langway [1980] model. During this process, atmospheric air is trapped in the ice in form of air bubbles) see Figure 4.1) which provide a chronological archive of atmospheric air samples back in time. The upper part of the firn is a network of porous channels which allows for air to be exchanged with the atmosphere. In the top 10 cm the dominant transport is convective while below this transport is diffusive, and at a depth of ca. 70 m to 80 m open air pores are closed off from the atmosphere see e.g. Battle et al. [1996]; Buizert et al. [2011]. The diffusion of gases in the firn layer causes a redistribution and temporal mixing of the different gas species when reaching the close off. This means that in the deep ice core, the air bubbles are younger than the surrounding ice, as well as a smoothing of the atmospheric signal is inherent. The magnitude of smoothing and age difference between gas and ice depends on accumulation rate and other temperature conditions at the site. Deeper in the ice sheet at 700 - 1000 m air bubbles disappear completely and the gases are included in the ice lattice as gas hydrates.

During glacial times greenhouse gases concentrations are generally observed to be lower than during the warmer inter-glacials, see [Schilt et al., 2010a]. In the case of CH_4, lower concentrations are mainly due to a decline in (boreal) wetland methane emissions as reflected in the decline of the inter-hemispheric methane gradient [Chappellaz et al., 1997]. In case of CO_2, the reason is mainly a higher carbon storage in the deep ocean due to reduced Southern Ocean mixing, changes in carbonate equilibrium in the ocean, and an increase in the marine biogenic fixation of CO_2 [Köhler and Fischer, 2006].

4.1.2.3 Climate History

Variations in Earth's orbital motion and rotation causes periodic changes in the insolation from the sun. The periods of eccentricity (100,000 yr), obliquity (41,000 yr) and precession (23,000 yr) have been linked to glacial-interglacial climate cycles Hays et al. [1976], but it does not explain everything. In particular the Dansgaard-Oeschger (DO) events (a ca. 1500 year temperature cycle) during the last glaciation are not clearly linked to orbital cycles. These events show an interplay between the northern and southern hemisphere [Blunier et al., 1998]. The DO-events of the northern hemisphere show rapid warming followed by slower cooling, while the southern hemisphere events show gradual increase and decrease – an interplay which can be described by a simple bi-polar see-saw model [Stocker and Johnsen, 2003]. Methane has a relatively short atmospheric life time and is well mixed in the atmosphere. This creates a rapid methane signal [Schilt et al., 2010b]during the DO-events which gives a good way of synchronizing the time scales of Antarctic and Greenland records [Blunier and Brook, 2001; EPICA Community, 2006]. It is presently believed that the bipolar-seesaw is transmitted by changes in the Atlantic meridional overturning circulation [Rahmstorf, 2002].

4.1.3 Nitrous Oxide

After CO_2 and CH_4, Nitrous Oxide is considered the most important green house gas in terms of radiative forcing, due to N_2O 's strong interference with outgoing long-wave radiation and it's Ozone depleting properties. The mixing ratio of N_2O has increased from 270 ppb (i.e. nmol/mol) in the preindustrial atmosphere to around 320 ppb today, and from 1980 have been increasing linearly by 0.26%/yr [Forster et al., 2007]. Through soil emission experiments Mosier et al. [1998] concluded that the N_2O is due primarily to an enhancement of the microbial sources associated with human agriculture.

Rockmann et al. [2003a] reported that the change in concentration since preindustrial was accompanied by a negative changes in the isotopologue

values of -1.8 ‰ for $\delta(^{15}N^{14}N^{16}O)$, -2.2 ‰ for $\delta(^{14}N^{15}N^{16}O)$, and -1.2 ‰ for $\delta(^{14}N^{14}N^{18}O)$. For the recent period since 1980 to 2003, Röckmann and Levin [2005] reported that these values continue to decrease by annual changes of -0.064 ‰/yr for $\delta(^{15}N^{14}N^{16}O)$, -0.014 ‰/yr for $\delta(^{14}N^{15}N^{16}O)$, -0.04 ‰/yr for $\delta(^{15}N_{bulk})$, and -0.02 ‰/yr for $\delta(^{14}N^{14}N^{18}O)$. These changes provide an indicator of what sources may be causing the N_2O concentration increase since the preindustrial. But to understand the changes knowledge of sinks and source contributions to the fractionation is also needed to be known.

4.1.3.1 The N_2O sources

The main source of N_2O are bacterial nitrification and denitrification processes in soil and aquatic system. An overview of sources for atmospheric N_2O is given in table 4.1. The largest amount of N_2O emission are from land at tropical latitudes, and N_2O source are found to be influenced by agriculture and fertilization. Melillo et al. [2001] deduced that the Brazilian forest soils alone contribute about 10% of total global N_2O production. Industrial sources are from nylon production, nitric acid production and fossil fuel fired plants.

Table 4.1: N_2O sources and uncertainties according to IPCC-AR4 [Forster et al., 2007].

Anthropogenic sources	N2O (TgN/yr) for 1990's	
Fossil Fuel & Industrial process	0.7	(0.2 - 1.8)
Agriculture	2.8	(1.7 - 4.8)
Biomass and Biofuel Burning	0.7	(0.2 - 1)
Human Excreta	0.2	(0.1 - 0.3)
Rivers, Estuaries & Coastal Zones	1.7	(0.5 - 2.9)
Atmospheric Deposition	0.6	(0.3 - 0.9)
Anthropogenic total	**6.7**	**(3.0 - 11.7)**
Natural Sources		
Soils under natural vegetation	6.6	(3.3 - 9)
Oceans	3.8	(1.8 - 5.8)
Atmospheric chemistry	0.6	(0.3 - 1.2)
Natural total	**11**	**(5.4 - 16)**
Total sources	**17.7**	**(8.4 - 27.7)**

The isotopes of N_2O have different isotopic signature for different sources. Oceanic and Terrestrial sources can typically be distinguished by oceanic values $\delta^{15}N > 0$ and $\delta^{18}O > 15‰$, while terrestrial $\delta^{15}N < 0$ and $\delta^{18}O < 20‰$ [Rahn and Wahlen, 2000]. From the site preferences of ^{15}N nitrification (ca. 33‰) and denitrification (ca. 0‰) in microbial processes can be dis-

Table 4.2: [a][Popp et al., 2002], [b][Dore et al., 1998] value for shallow North Pacific end-member at 80% of the net sea to air N_2O flux at station ALOHA, [c][Sutka et al., 2006], [d][Bol et al., 2003], [e][Ogawa and Yoshida, 2005] burning end members. [f]Toyoda et al. [2008] estimated average values from car exhaust.

Source	$\delta^{15}N_2O^{\alpha}$	$\delta^{15}N_2O^{\beta}$	SP	bulk	$\delta N_2{}^{18}O$
Ocean	16.1[a]	-2.2[a]	18.3[a]	7.0	14.5[b]
Terrestrial nitrification	17.9[c]	-16.0[c]	33.9[c]	0.9	11.3[c]
Terrestrial denitrification	-22.9[c]	-23.0[c]	0.1[c]	-23.0	-12.4[c]
Agricultural	-5.12[d]	-11.4[d]	6.3[d]	-8.3	10[d]
Biomass Burning	0.4[e]	-2.4[e]	2.8[e]	-1.0	25.0[e]
Automobiles	1.2[f]	-11.0[f]	12.2[f]	-4.9	43.5[f]

tinguished [Sutka et al., 2006]. Table 4.2 shows reported isotopomer and istopologue data from different sources.

4.1.3.2 The N_2O sink

The primary sink of N_2O is by photolysis in the stratosphere, accounting for 90% of the destruction through the process

$$N_2O + h\nu \rightarrow N_2 + O(^1D). \tag{4.1}$$

The rest of the N_2O destruction in the stratosphere is accounted to be lost through photo-oxidation reaction with the electronically excited oxygen atom [Stein and Yung, 2003]:

$$N_2O + O(^1D) \rightarrow N_2 + O_2 \tag{4.2}$$

$$N_2O + O(^1D) \rightarrow 2NO. \tag{4.3}$$

The NO produced in the last reaction is considered to be quickly oxidized to NO_x compounds [Ravishankara et al., 2009].

Average delta values of N_2O in troposphere is $\delta^{15}N = 7.0‰$ and $\delta^{18}O = 20.7‰$, while stratospheric ^{15}N values are enriched with $\delta^{15}N = 15‰$ and $\delta^{18}O = 12‰$ [Stein and Yung, 2003]. Based on an isotopic mass balance calculation, Kim and Craig [1993] argued for the existence of a large back flux from the stratosphere. This was necessary, in order to balance the high isotopic δ-values of the troposphere which is other-wise dominated by light sources of N_2O . This gradient in delta value was not readily understood. Through the studies of [Yung and Miller, 1997; Rahn and Wahlen, 1997; Rahn et al., 1998; Turatti et al., 2000; Johnson et al., 2001; Kaiser et al., 2002a,b, 2003] a general consensus was reached, namely that standard Rayleigh fractionation

during photolysis, describes the character of the N_2O sink, [Stein and Yung, 2003]. Blue shift of UV absorption lines of the heavier isotopes, support this conclusion and provided the theoretical predictions of fractionation between isotopomers and isotopologues of N_2O matching the empirical observations [Morgan et al., 2004].

With this understanding of the stratospheric enrichment of heavier isotopomers and isotopologues a potential method is given to differentiate between surface and stratospheric fluxes and their influences on the tropospheric N_2O concentration [Morgan et al., 2004].

The stratosphere is proposed to play an important role in observed seasonal cycles of N_2O [Nevison et al., 2004]. For example, the well-defined seasonal cycle of N_2O in the southern hemisphere has been interpreted as resulting from the net effect of seasonal oceanic outgassing of microbially produced N_2O , stratospheric intrusion of low-N_2O air and other processes [Nevison et al., 2005]. Seasonal cycles in the northern hemisphere is more complex and difficult to reconcile with seasonal variations in the northern latitude soil sources and stratospheric intrusions, [Forster et al., 2007].

4.1.3.3 N_2O link to climate history

Through studies of N_2O in ice cores we may be able to understand the past role and impact of N_2O in the atmosphere and on climate. Several ice core records have already been measured of atmospheric N_2O mixing ratios [Spahni et al., 2005; Fluckiger et al., 2004; Fluckiger, 2003; Fluckiger et al., 2002, 1999; Schilt et al., 2010a,b; Sowers, 2001] and for isotope ratios [Sowers et al., 2003, 2002; Bernard et al., 2006]. During the glaciations N_2O concentration is observed to fluctuate by large amounts (as much as 30%, [Leuenberger and Siegenthaler, 1992]) compared the the inter-glacials.

The atmospheric residence time of N_2O is 114 yr [Forster et al., 2007] (or upto 173 yr [Olsen et al., 2001]), and so N_2O signals observed in the ice cores should not be expected to vary faster than this.

N_2O isotopomer measurements may provide knowledge of in-situ production of N_2O in the ice core such as studied by Rohde et al. [2008], and may also be useful at deeper sections in the ice-cores.

Elberling et al. [2010] reported on large fast emissions of N_2O from melting permafrost at a Greenland coast site. They show that 31% of the nitrous oxide produced after thawing and rewetting a 10 cm permafrost core is equivalent to a 34 $mgNm^{-2}$ release per day to the atmosphere, which is equivalent to daily nitrous oxide emissions from tropical forests on a mean annual basis. Similar experiences of high emission of N_2O was also measured at the peat circles of the subarctic East European tundra in Russian [Repo et al., 2009].

Effects like these may also be of importance to measurements in the ice cores from Greenland as local climate effects.

Understanding of the modern N_2O budget is incomplete, in part due to the complexity of the nitrogen cycle. Availability of inexpensive automated systems to perform in field measurements of N_2O isotopomers will be crucial part to perform future detective work on N_2O for the interpretation of climatic signals.

4.2 Continuous analysis system

During the 2009 NEEM ice-core drilling field season two CRDS systems were successfully installed into the continuous flow analysis (CFA) system to measure the water isotopes and concentrations of Methane. It was planned to similarly install the N_2O isotopomer instrument described in part II into the CFA system during the NEEM 2010 field season. A diagram of the envisaged implementation is shown in figure 4.2. An automated sampling system was prepared, but eventually the N_2O isotopomer analyzer was not ready in time for the field season. The following describes circumstances for installing the N_2O analyzer in ma CFA system. Proceed to section 4.3 to read about the measurements conducted during this work.

The CFA system operates as presented by Röthlisberger et al. [2000]; Kaufmann et al. [2008], and described in short as follows. Rods of ice with a 4cm by 4cm cross section and length of 110 cm are cut from the ice core. The rod is placed vertically onto a gold coated plate which is heated in order to melt the ice-rod. The melt head is facilitated with a square knife edge, which works as to expel the melted water from the outermost part of the rod, while the inner part is collected into a drain in the center. In this way minimal contamination of the measured sampled is achieved. From the center drain the melt stream is pumped by a peristaltic pump at 14 ml/min. This melt stream contains air-bubbles originating from atmospheric air which escapes from the ice/water during and after melting. A bubble free melt stream for chemical analysis and continuous measurements of water isotoptes is created by a debubbler. To measure the water isotopes the water is flash evaporated and analyzed in a CRDS as described by Gkinis et al. [2010]. The overflow from the debubbler is a combination of water and airbubbles ca. 2:1 by volume. This stream is fed through a hydrophobic membrane separating the stream into a bubble free water stream and gas stream. The gas stream is further transfered through a 1.5 meter piece of Nafion tubing surrounded by a Helium flow, to remove excess water moisture in the gas. Finally the gas is sent into a CEAS analyzer (SARA, installed by LGGE, Grenoble) measuring

the concentrations of CH_4 and N_2O. The outlet of the CEAS instrument is connected to a CRDS CH_4 analyzer (Picarro - G1301). After the CRDS CH_4 analyzer the gas passes the vacuum pump which has provided the low pressures of the enhancement cavities, and differential pressure for transport through these. The vacuum pump is custom prepared and is highly leak tight. The exhaust of the pump is fed into a 6-port valco valve which is used to periodically provide a sample (1.5 mL every 5 minutes) into a gas chromatograph analyzing the Methane concentration. It was thus planned to collect the waste from this 6-port valve and analyze it with the N_2O isotopomer instrument described in part II. The samples would be collected over longer time periods with a liquid nitrogen trap to increase the N_2O concentration.

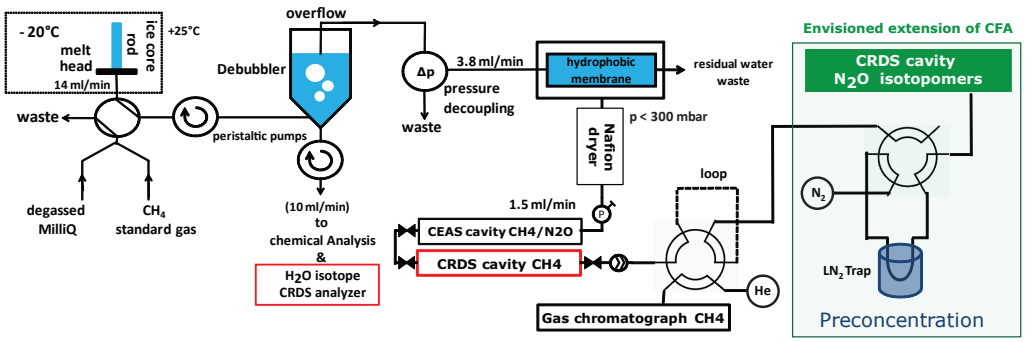

Figure 4.2: Diagram of the continuous flow analysis system installed at NEEM ice core drilling site during summer of 2010. Highlighted in red are the CRDS analyzers that were installed in the CFA system during the 2010 NEEM campaign.

The CH_4 concentration record measured during the NEEM 2010 field campaine had values corresponding to the expected values from discrete measurements. However, for N_2O the CEAS instrument measured concentrations that were much lower than expected. Rather than N_2O concentrations of 250 ppb expected for glacial values, only 60 ppb was measured, i.e. about one fourth of the expected. It was suggested that this deviation was due to N_2O being dissolved in the water stream. In the following subsection 4.2.0.4 this suggestion is supported by solubility calculations using Henry's law. In conclusion it is not expected that N_2O can be measured in the CFA system, and attention was turned toward discrete measurements presented in section 4.3.

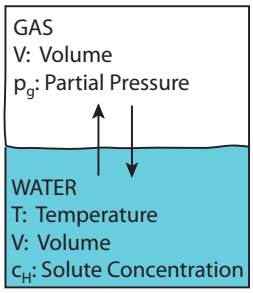

Molecule	$k_H(T_0)$ (mol kg^{-1} bar^{-1})	C_H (K)
N_2O	0.024	2800
CH_4	0.0013	1900
CO	0.00095	1600
O_2	0.0013	1700
N_2	0.0006	1700

Figure 4.3: Parameters for calculation of the temperature dependent Henry's law coefficient Dean [1992].
$T_0 = 298.15K$

4.2.0.4 Solubility of N_2O in water using Henry's law

Henry's law states that the ratio of the solute concentration in the liquid (c_aq) over the partial pressure p_g is given by the temperature dependent Henry's law constant

$$k_H = \frac{c_{aq}}{p_g} = k_H(T_0) \exp\left[-C_H\left(\frac{1}{T} - \frac{1}{T_0}\right)\right] \tag{4.4}$$

where $T_0 = 298.15$K and

$$C_H = -\frac{\mathrm{d}\left[\ln k_H(T)\right]}{\mathrm{d}(1/T)} \tag{4.5}$$

By using the ideal gas law for the molar concentration on the gas form and the density of water at given temperature k_H is represented on dimensionless form in terms of molar volume concentration in the liquid and gas phases. In figure 4.4 the solubility of Methane, Nitrogen, Oxygen and Nitrous Oxide is compared. Unlike the the first three molecular species, Nitrous oxide does have an electric dipole moment making its solubility in water much stronger than for the others.

Nitrous Oxide captured in the ice core – Several effects can perturb the distribution of N_2O in liquid and gas in the CFA system.

1. Due to the high solubility of Nitrous Oxide in water, one could expect that Nitrous Oxide is not only captured through air enclosure at the firn close off, but also has a contribution from N2O dissolved in the precipitation water. 2. On could also imagine that the N_2O is diffused from the air bubbles into the enclosing ice. 3. Finally as the CFA system melts the ice, an exchange between the liquid and gas phase of N_2O must occur.

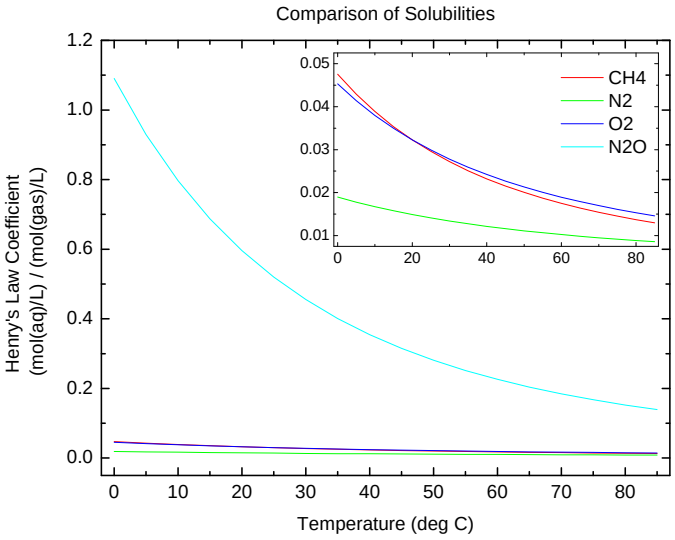

Figure 4.4: Comparison of the solubilities of N_2, O_2, CH_4 and N_2O. Notice that the solubility of N_2O is much higher than the others.

Whether effect number 2 or 3 is the dominant in the NEEM CFA could be examined by shortening the travel distance from melt-head to laser spectrometer.

One may state the question – what would it take to get a reduction factor of four for the N_2O gas concentration?

Assume that initially no N_2O was dissolved in the water. Assume further that during the CFA melting and processing time the dissolving processes reaches equilibrium. The decrease in N_2O concentration thus has to originate from dissolving processes into the water. Using Henry's law we can now determine how much water to gas volume is needed in order to decrease the N_2O gas concentration by factor 4. The Total number of N_2O molecules is conserved at all times so

$$c_{aq}(t)\ V_{aq} + p_g(t)\ V_g = 1 \tag{4.6}$$

with initial condition that at time zero all the N_2O is in the gas phase so $p_g(t_o)\ V_g = 1$. Using equation (4.4) and the initial condition we get that the remaining fraction of molecules in the gas form is given from

$$\frac{p_g(t)}{p_g(t_o)} = \frac{1}{k_H(T)\frac{V_{aq}}{V_g} + 1} \tag{4.7}$$

The amount of N_2O left in the gas phase after equilibration with the water solution is plotted in figure 4.5 for different temperatures T and volume ratios $\frac{V_{aq}}{V_g}$. Assuming a water temperature of 15 °C it would require the volume of

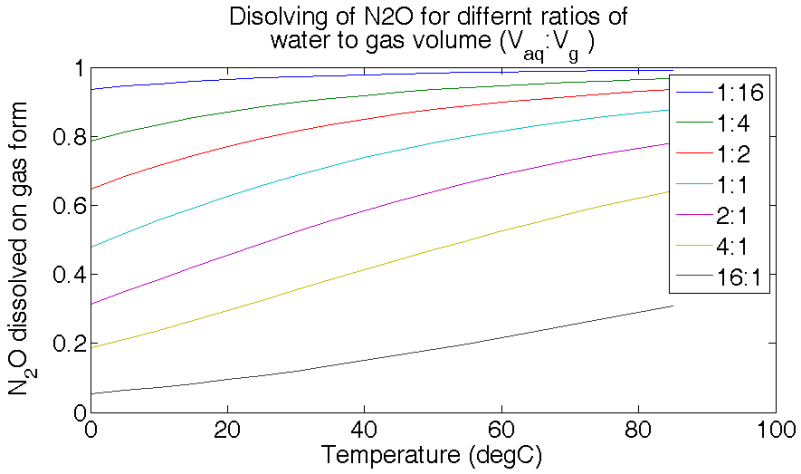

Figure 4.5: Calculation of how much N_2O will stay on gas if initially all N_2O is dissolved on gas form and then is brought to equilibration with water initially having no N_2O . The ratio of water to gas volume has to be at least 1:3 in order to account for the N_2O dilution experienced in the CFA at NEEM 2010.

the water to be at least four times that of the gas. It is worth noting that the partial pressure of N_2O would be higher, if any N_2O was dissolved in the water prior to initialization of the dissolving process between water and gas.

The volume ratio of water to air is about 2:1 in the line from the CFA debubbler and much higher between the melt head and the debubbler. Conditions for diluting the N_2O is certainly present. However it remains to be determined if the N_2O is dissolved in the water already at the melthead or if this is something occurring after the melthead during the transport to the laser spectrometers.

The dissolving of N_2O into the water can be somewhat mitigated by heating the water. However this is undesired from the chemical analysis standpoint because this enhances unwanted chemical reactions. So any heating should wait until after the CFA debubbler. At this point the volumetric ratio between water and gas is about 2:1. Thus from figure 4.5 we see that by heating the flow stream from say 0 °C to 80 °C we can improve from measuring 30% of the total N_2O conctent to measuring 70% of the total N_2O content. It should then further be noted that this process is time and temperature dependent.

4.3 CRDS measurement of discrete ice-core samples

In a collaboration with Ed Brook and Julia Rosen at Oregon State University, it has been planned to measure the ^{15}N-isotopomer δ-values of N_2O in 27 samples (of 800 g) from the Holocene section, of the Taylor Dome icecore. This section describes the extraction system that has been built for these measurements and demonstration of its operation.

Necesarry sample size for the N_2O isotopomer measurement The cavity volume is ca. 35 ml. The cavity is operated at 200 torr pressure, and an up-concentration from ca. 250 ppb to 1 ppm is desired, providing a need for ca. 40 mL of gas at STP. The ice gas content is ca. 10% i.e. a 400 mL ice core piece would be suitable for the N_2O isotopomer measurement.

Known methods for gas extractions from ice core samples There are several ways of extracting air from discrete icecore samples. Needle crusher Zumbrunn et al. [1982]; Ahn et al. [2009] and sublimation Schmitt et al. [2011] methods are high precision methods particularly suited for CO_2 which may not come into contact with liquid water phase, as this will alter the CO_2 isotope composition by chemical reactions. Although being very robust methods, these are also complex systems to set up. In another method the ice is melted in a vessel and refrozen with a -50 °C ethanol bath Chappellaz et al. [1997]. A final method applies melting of the ice sample under vacuum Chappellaz et al. [1997]; Sowers et al. [1997] a method which is best suited for component which are relatively insoluble and chemically stable in water, e.g. CH_4, O_2, N_2 and Ar. The latter two methods are more simple to implement, than the two first and more desirable from that perspective.

Despite the high solubility of N_2O in water Fluckiger et al. [1999] showed that the melt-and-refreeze method could be applied for concentration measurements, by applying a slow refreezing with a bath of -25°C. Their extraction method caused a loss of 2.32×10^{-8} ml of N_2O (STP) corresponding to a concentration correction of about 6 ppbv with a typical sample size of 40 gram of ice. For a 400 mL ice sample, needed for the CRDS analyzer, refreezing may turn out to be rather complicated to implement. The wet extraction system is not trivial either as N_2O is very soluble in water.

For this project it was decided to attempt a melt, purge and trap method using an ultra pure purge gas. The main idea being, that by continuously flushing with Nitrogen, the release of N_2O from the melted water will be improved.

4.3.1 Description of the melt & flush extraction system

A diagram of the extraction system is shown in figure 4.6 and a picture of the setup in figure 4.7. The main principle of the setup is to melt the ice sample in the melting bucket and transfer the N_2O gas to the liquid nitrogen cryogenic sample trap. Once the full sample is believed to be captured, sample trap is heated and passively expanded into the CRDS cavity. Pure nitrogen is further added to the cavity in order to reach the 200 torr, and providing the proper conditions for the spectroscopy. The system is divided into 6 sections: Sample extraction, Nitrogen carrier gas, standard gas, vacuum, and CRDS analyzer. A Syringe injection section is also indicated, which is intended for the microbial incubation samples or other, which can be handled using a syringe.

4.3.1.1 Nitrogen Carrier & N_2O standard gas

The purge gas is highly pure Nitrogen grade 6.0 i.e. 99.9999% purity. The gas is introduced to the system through a 0 to 60 psi regulator and then through a 400 ccm (Porter) flow regulator. The 3-way switching ball valve provide selection between flowing pure nitrogen or standard gas into the system through the 6-port valco valve (VICI). The 6 port valco valve allows for injection of discrete volumes of a standard determined by the volume of the standard loop (here ca. 40 ml). In position A the loop can be loaded and in position B the carrier gas may introduce the sample loop content into the system. The standard gas is delivered from a gas cylinder through a 0 to 60 psi pressure regulator. Connection to the vacuum system and shut off valves allow for evacuating the standard loop when the valco valve is in position A. The pressure gauge located in the vacuum section can be used for measuring the pressure in the standard loop during loading. All tubings are 1/8 inch stainless steel tubing.

4.3.1.2 Vacuum system

A Pfeiffer HiCube 80 Eco Turbo Drag-pump station, provides vacuum down to 2.9×10^{-4} mbar. The pump is protected from water vapor by a cold trap – a stainless steel cylinder submerged into a dry-ice ethanol bath. A diaphragm pump (KNF, N920) provides pumping for the exhaust of the extraction nitrogen carrier flow. This pump also provides rough pumping so the turbo pump does not need to be turned on and off as it may not be exposed to pressures above a few mbar. An active Pirani/capacitive transmitter (Pfeiffer, PTR26850) is used for monitoring the vacuum level when evacuating the

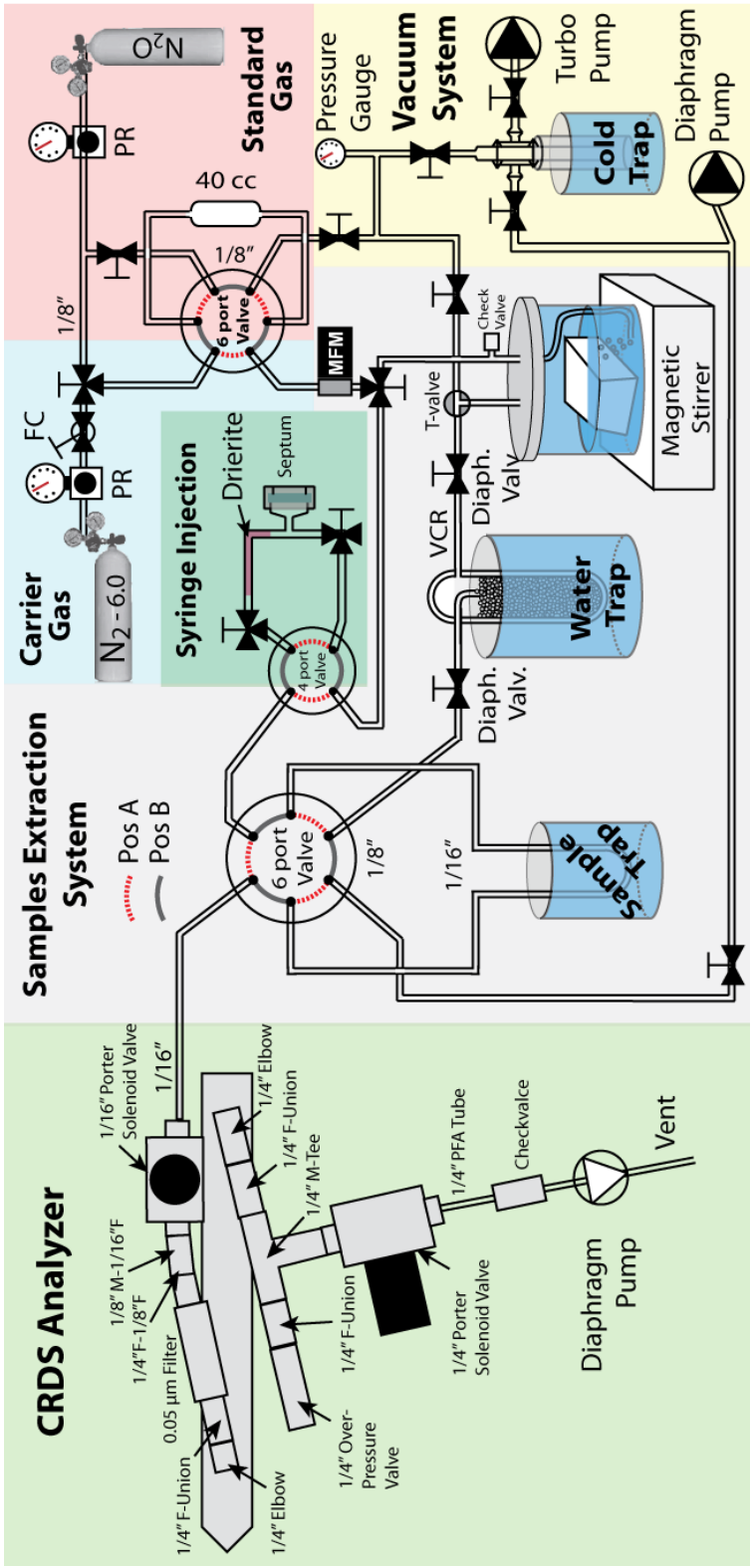

Figure 4.6: Schematic of the full gas system for biological samples, ice extraction, and injection of standards.

extraction system and for measuring the pressure in the standard loop when this is loaded.

4.3.1.3 Syringe injection

System for injecting samples with a syringe through a septum. The 3-way switching valve also provides venting of the flow line going to the CRDS analyzer, but can also be used for filling the sample loop with ambient air.

4.3.1.4 Sample Extraction

The line from the carrier gas section is connected to a mass flow meter (MFM, a Agilent Precision Gas Flow Meter) also measuring temperature and pressure. The MFM is used for monitoring the flow rate of the nitrogen flushing, as well as measuring the pressure in the melting vessel. The MFM is connected to a 3-way switching valve which connects the nitrogen (or standard) to the melting vessel or toward the sample trap and CRDS analyzer.

The melting vessel The melting vessel (see figure 4.7) top is a stainless steel flange (with a Viton gasket), which is connected to the pyrex glass bottom with a stainless steel to glass adaption. The internal volume is 3885 cm^3, which is larger than necessary, but what was available for this experiment. The top is equipped with two 1/4 inch VCR fittings making it easy to remove and insert the vessel from the setup. One fitting goes to the nitrogen supply the other to the vacuum and sampling trapping part.

The fitting toward the nitrogen is connected to the 3-way valve supplying the nitrogen for flushing. This line is also equipped with an overpressure safety check valve (5 psi cracking pressure). On the inside of the melting vessel a 1/16 in. tube is installed in order to inject the nitrogen at the bottom of the vessel, below the surface of the melt water.

The fitting toward the vacuum is connected to a 3-way port valve (Swagelok 3-way ball valve SS41GXS2-HL) which is never closed but either connects the melting vessel to the vacuum system, the water trap or both. This was chosen in order to minimize dead spaces in the line connecting the melting vessel and the sample trap. The extracted gas is transported through the 3 port valve toward the water trap.

A magnetic stirrer is installed under the melting vessel.

The water trap Is made from a stainless steel (SS) cylinder of 4 cm outer diameter and 19 cm long. At the bottom the cylinder is sealed with a SS plate welded to the cylinder. The cylinder top is capped with blank SS flange

connected to the cylinder with an ISO-KF 40 o-ring and clamp. Two 1/4 inch tubings are welted through the cap for in and outlet. The outlet 1/4 in. tube going sending gas to the sample trap, is extends to the bottom of water trap cylinder, while the inlet from the melting vessel is released right under the cap. This means that the sample has to travel down through the cold part of trap before being able to continue to the sample trap. The water trap cylinder is filled with glass beads (2 mm) to minimize volume and optimize surface area to which the water can condense. The water trap is submerged into a dry-ice ethanol mixture of -80 °C temperature. The 1/4 in. tubings connecting to the lid of the water trap have VCR fittings in order to ease the exchange of the water trap. Diaphragm valves are installed on either side of the water trap to close off when pumping or exchanging the water trap.

The sample trap From the water trap the extracted sample gas is injected to the sample trap through a 6 port-1/8" valco valve. The sample trap is connected to the valco valve in a sample injection configuration. The sample trap is a piece of 1/16" stainless steel tubing which can be submerged in the dewier with liquid nitrogen for trapping the sample. In the trapping mode the valco valve is set in the A position. On the down stream side of the sample trap the valco valve is connected to the Diaphragm pump in the vacuum section. When the sample is to be released into the CRDS cavity the valco valve is set to position B. A 1/16" tube connects the valco valve to the CRDS analyzer, which is described in section 8.2.4. The last port of the valco valve is connected to the nitrogen carrier gas 3-way switching valve, having the 4 port valco valve for the syringe injection in between. Gas from the standard gas section can be injected directly to the CRDS analyzer by leaving the 6-port valco valve in position A.

4.3.2 Measurement procedures

As sample amounts are limited and small, measurements had to be performed in a closed cavity mode. The cavity has a leak rate 0.075 torr/hr. A change in the cavity pressure changes spectroscopy conditions and may lead to drifts of the measured δ-values.

Due to very limited time only four trapping experiments can be reported here. These experiments are explained in the next four subsections. The results of these are reported in Table 4.3. In each trapping experiment the procedure for injecting the trapped sample into the CRDS analyzer is the same as explained in section 4.3.2.5.

Figure 4.7: LEFT: Picture of the extraction system and CRDS analyzer. RIGHT: Picture of blank ice being melted in the melting vessel.

4.3.2.1 Experiment with empty melting vessel

The sample loop was filled with 40 scc. of ambient air having the Standard gas valco valve in position A. Turbo pump was used to evacuate melting vessel, water trap, and all the way up to the three way valve in the carrier gas section. The valve between water trap and sample trap valco valve was closed. The sample trap valco valve was in position A and was being evacuated with the diaphragm pump. The 3-port valve at the melting vessel was then turned to only connect water trap with melting vessel. Nitrogen carrier gas was then passed into the melting vessel and the standard gas valco valve was switched to inject the 40 cc sample. The sample trap was submerged in liquid nitrogen (LN_2). When pressure in melting vessel reached 3.8 psia, all diaphragm valves were opened, starting the flushing through water and sample trap. Flushed with 100 sccm for 30 minutes. Turned off nitrogen flow with the 3-way switching valve at the MFM, and let the system evacuate with the diaphragm pump through the sample trap. The MFM pressure did not go below 1 psia. Proceeded with the sample injection procedure in section 4.3.2.5.

4.3.2.2 Experiment with bubble free ice

Bubble free ice at the center for ice and climate is produced from Milli-Q water. MQ water is in a vacuum container which is evacuated for several hours in order to remove gases from the water. The vacuum container is

then sealed and brought to freezer laboratory at a temperature of -15 °C . A heating coat is wrapped around the vacuum container and is slowly (ca. 12 hours) lifted allowing the MQ water in the container to freeze from the bottom. In this way any excess gas in the water is forced toward the top leaving frozen water ice to be gas free.

For the experiment 600 grams of bubble free ice was cut and outer surfaces removed with a band saw in a cold lab. The melting vessel had been removed from the setup by opening the VCR connections on its top. The blank ice was loaded into vessel and the lid was secured in the cold lab. It took ca. 5 minutes to bring the vessel to the setup from the cold lab, and to mount the melting vessel back into the setup. The vessel and water trap were evacuated with the turbo pump, reaching a lowest pressure of 1.2 mbar. Stopped the pumping and filled the melting vessel with 240 mbar of nitrogen. Started flushing of the system with Nitrogen through water and sample traps, evacuating with the diaphragm pump for ca. 20 minutes. Closed valves and let the ice melt. Picture of the melting blank ice is shown in figure 4.7. A hot water bath was lifted up around the melting vessel in order to increase melting speed. When possible the magnetic stirrer was turned on also to improve melting speed. The melting process took more than an hour. The 40 cc loop was filled with ambient air and was introduced to the melting vessel with the nitrogen carrier gas. Sample trap was set in position A, evacuated and lowered into LN_2. Flushed nitrogen through melting vessel, water and sample trap and evacuated with the diaphragm pump. Nitrogen was flushed at 100 sccm for 20 minutes. Pressure at the MFM stabilized at 4.7 psia. Then turned off the nitrogen flow with the three way switching valve at the MFM. and let the diaphragm pump evacuate on the system through the sample trap for 30 minutes. MFM pressure lowered to 1.8 psia and gas bubbles were still seen to be released from the 1/16" tube opening under the melt water. Proceeded with the sample injection steps in section 4.3.2.5.

4.3.2.3 Experiment with Ice core sample

A 436 gram ice core sample from the disturbed part of the Eurocore from 1989 was cleaned leaving 330 gram. The sample had large recrystallizations on the surface and a large groove[1] (see picture in figure 4.8) making the sample essentially hollow. The core was drilled without drill liquid so the external surface was not cut away, but only the large hoar crystals were removed. This only left 330 gram of sample. As with the blank ice experiment 4.3.2.2 the ice was loaded into the melting vessel in the freezer laboratory, sealed

[1]The groove origin is supposedly from a physical property measurement performed in the field before packing.

and brought to the extraction setup. After installation the melting vessel was evacuated with the diaphragm pump reaching 6 mbar vacuum within five minutes. Then opening to the turbo pump the pressure lowered to 1.9 mbar within 3 minutes. Turned off valves to vacuum pumps and introduced pure nitrogen gas into the melting vessel for flushing purposes. Nitrogen was turned off and the melting vessel re-evacuated pumping down to 2.9 mbar with the turbo pump. The 3-port valve at the melting vessel was then turned to only connect water trap with melting vessel. Then started flushing through the melting vessel, water trap, sample trap and evacuating to diaphragm pump. The nitrogen flow was 100 sccm. Sample trap valco valve was in position A and was then submerged into LN_2 for trapping of the sample when melting. A bath of hot water was raised up around the melting vessel to speed up the melting. While flushing the pressure at the MFM equilibrated at 4.7 psia. The ice was melted after 40 minutes. It was observed that lots of air bubbles would resign at the melting vessel walls under the water surface, see figure 4.8. Even when the magnet stirrer was turned on, these bubbles would stick at the walls. Used another magnetic to move the magnetic stir rod around the inside of the melting vessel popping the air bubbles. Just like cleaning a fish tank. After an hour of flushing the nitrogen was turned off with the 3-way switching valve at the MFM. This means that 6 liters of nitrogen had been flushed through the system. Proceeded with the sample injection steps of section 4.3.2.5.

Figure 4.8: Left: Eurocore ice sample in the melting vessel. Notice the large groove in the sample. Right: Air bubbles resigning on the melting vessel walls.

4.3.2.4 Experiment with Milli-Q water

This experiment was run in succession of an experiment where 500 mL of Milli-Q water was introduced to the melting vessel. The Milli-Q water was

expected to be degassed as the previous experiment had been pumping and flushing the sample with nitrogen for an extended amount of time. The diaphragm pump was used to evacuate melting vessel, water trap, and all the way up to the three way valve in the carrier gas section. The lowest pressure reached was 22 mbar. The 40 cc standard loop was filled with ambient air with the valco valve in position A. The 3-port valve at the melting vessel was turned to only connect water trap with melting vessel, and injected the 40 cc sample of ambient air. When pressure on the MFM reached 3 psia, the nitrogen was turned off, and the melting vessel was left for 15 minutes to equilibrate N_2O between gas and dilution phase. The sample trap was evacuated in position A using the diaphragm pump. The sample trap was then submerged into LN_2, and nitrogen flow was restarted flowing 100 sccm nitrogen through melting vessel, water trap, sample trap, and evacuated by the diaphragm pump. The MFM pressure equilibrated at 3.6 psia. Proceeded with the sample injection procedure in section 4.3.2.5.

4.3.2.5 Proceedure for injecting trapped sample into the CRDS cavity

The diaphragm pump in the CRDS analyzer is used to evacuate all the way up to the 3-way switching valve at the MFM. This is done while the sample is being trapped i.e. the sample trap valco valve is in position A. The 4 port valco valve is in position A at all times of this operation. During evacuation the CRDS solenoid valves are fully opened. When the pressure in the cavity reached below 5 torr (minimum reading achieved, even with inlet valve closed) the outlet CRDS solenoid valves is closed. The sample trap valco valve is then turned to B and the sample trap is heated by removal of the LN_2 bath. Upon release of the trapped sample, pressure in the cavity is usually recorded to raise by a few torr. In order to achieve proper circumstances for the spectroscopy nitrogen must be added. For this the CRDS solenoid valve is closed and then the 3-way switching valve at the MFM is turned in order to provide nitrogen toward the CRDS analyzer. The inlet solenoid valve is then slowly opened and pressure is slowly raised to 200.0 torr, at which the inlet solenoid valve is closed again. The sample is then left in the cavity until the desired amount of averaging has been performed to have a decent measurement for the N_2O isotopomer composition.

4.3.2.6 Injection of standard to CRDS

Reproducibility of the CRDS analyzer when using a closed off cavity was also tested. For this the best injection method was as follows. The CRDS

Table 4.3: Results of the four trapping experiments.

Melting vessel	Sample	N_2O conc. (ppm)	$\delta^{\alpha}N_2O$	$\delta^{\beta}N_2O$
Empty	40 scc ambient air	2.84 ± 0.003	-338 ± 3	-210 ± 3
Degassed Mili-Q water	40 scc ambient air	4.2 ± 0.007	-343 ± 6	-221 ± 5
Blank ice	40 scc ambient air	3.59 ± 0.001	-290 ± 1	-193 ± 1
330 g ice sample	EuroCore	4.0 ± 0.050	-386 ± 8	-221 ± 8

diaphragm pump was used to evacuate all the way up to the 3-way switching valve at the nitrogen carrier gas. The turbo pump was used to evacuate the standard gas sample loop with the valco valve in position A. All valves were then closed. N_2O standard gas is then injected into the tubing with the 3-way valve at the carrier gas, filling the tubing all the way to the 3-way valve at the MFM, enabling reading of the pressure. The 3-way valve at the nitrogen gas is then turned toward the nitrogen gas, diluting the standard in the tubing. Again the pressure can be read on the MFM. The 3-way valve is then closed. The valco valve is switched to B and the gas mixture expands into the evacuated 40 cc sample loop, providing a homogenization of the mixture. The 3-way valve at the MFM is then turned toward the CRDS analyzer and the gas may be injected into the cavity by slowly opening the inlet solenoid valve.

4.3.3 Measurement results and discussion

Table 4.4 provides an overview of the measured samples and standards, made with the extraction setup. All reported delta values are with respect to the reference scale described in section 10.3.2.1.

The results from the four sample trapping experiments is shown in table 4.3. In all four trapping experiments, more gas was captured than expected. A significant leak was found in the NPT fittings at the MFM. This may explain why more N_2O was found than expected. Also Technical air was used rather than high purity Nitrogen grade 6.0, which also may provide excess N_2O. The leak at the MFM was fixed before proceeding to the standard measurements presented next.

4.3.3.1 Results for standard measurements

14 Injections of standards were performed according to the proceedure in section 4.3.2.6. The concentrations and delta values for the injections are plotted in figure 4.9, where sample numbers relate to those of table 4.4. There is an apparent shift in delta values between sample number 6 and

7. After the shift in delta value the precision of the δ-values also degraded by factor of 2. Before the shift (sample 3–6.25) the minimum detectable delta values were 1.2‰ for both isotopomers and after the shift (sample 7–16) the precision degraded to 2.5‰ for both isotopomers. The precision in delta values reported in 20 second time intervals was likewise degrading from 8.7‰ to 15.8‰ for both isotopomers, as shown on the error bars in figure 4.9. Although the precision is degraded, sample to sample reproducibility of 10‰ before as well as after the shift for both isotpomers seems to be intact. The performance of the static cavity measurements was mostly worse compared to the measurement where the standard was continuously flowing through the cavity at ca. 100 sccm. Only one experiment with flowing the standard was executed and repeated flow experiments should be made for proper comparison.

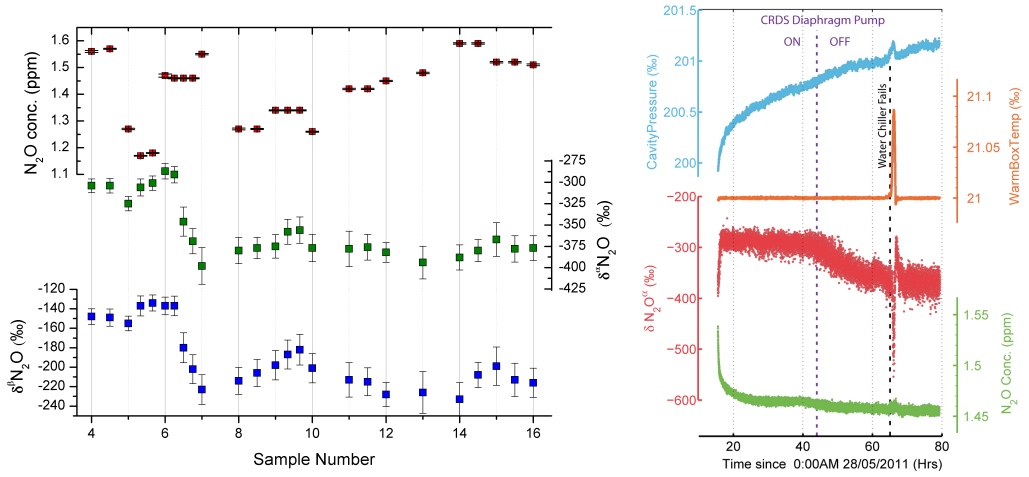

Figure 4.9: LEFT: Measured N_2O concentrations and delta values for standard gas injected in discrete portions. The standard was diluted in different amounts according to indicated in table 4.4, using the same sample numbers. RIGHT: Continous data from the measurement of sample 6 through 6.75.

The shift is concurrent with the beginning of a leak test of the cavity, executed during measurement of sample 6. For the leak test the CRDS diaphragm pump was turned off, to see if cavity pressure would start increasing faster. Continuous data from the CRDS analyzer during this test is also shown in figure 4.9. The measured cavity pressure does not show any change in the rate of pressure increase. This indicates that the dominant cavity leaks are not associated with the solenoid valves. Nor can the shift in delta values be associated with the cavity pressure. It is possible that the

finesse of the cavity degraded during the measurement, but cavity ring down measurements with pure nitrogen in the cavity (from June 4th) does not indicate evidence of this. Matters are further complicated as the water chiller operation also failed (low level of cooling liquid) during the measurement of sample 6. This was quickly fixed within an hour, but the temperature alteration may also have changed conditions for the analyzer. Investigation of the measured spectra may provide insight to the origin of the shift, but this is not investigated within the scope of this work.

4.3.4 Conclusions and outlook

An ice core gas extraction method using melt, purge and trap was built and its operation investigated. Characterization of extraction efficiency and possible fractionation was outside the scope of this work, but will be investigated in future work. It was learned that the melt and extraction took more than two hours mainly due to the melting time plus the large volume of the Melting vessel provided long gas exchange flushing time. Tests with no N_2O has to be made for both dry melting vessel and blank ice, in order to confirm that leaks and pure Nitrogen does not provide sample contamination. Further conclusion from the experiment is not possible as a significant leak at the MFM was discovered during the last measurement.

16 experiments, injecting discrete portions of standard into the cavity, showed that the minimum detectable delta value is on the order of 1‰ to 3‰ on the reference scale described in section 10.3.2.1. In the coarse of these measurements the instrument performance was observed to degrade.

Table 4.4: Data of measured samples and standards. Sample numbers having decimal values are measuements of the same sample as that of the integer by flooring the sample number. This subdivision performed due to data format and to enhance understanding of the data.

Date	Time		Sample	N_2O concentration (ppb)			$\delta^{\alpha}N_2O$ (‰)			$\delta^{\beta}N_2O$ (‰)			Sample
	start	end	number	Mean (ppm)	stdev.	min.Err.	mean	stdev.	min.Err.	mean	stdev.	min.Err.	
14/05/2011	00:00	11:00	0	2.57	2.62	0.286	-244	4.5	0.58	-116	7.83	0.75	Flowing 100% standard
20/05/2011	17:00	00:00	1	1.85	2.13	0.373	-339	9.84	2.13	-182	9.69	2.13	Dry run experiment.
21/05/2011	00:00	16:00	1.5	1.84	2.53	0.469	-339	9.75	1.69	-183	9.48	1.55	Dry run experiment.
23/05/2011	15:00	15:30	x1	2.87	17.9	3.17	-341	13.8	2.45	-212	13.8	2.42	Milli-Q water exper.
24/05/2011	11:45	13:15	x2	4.09	24.9	7.04	343	25.9	6.14	-222	27.5	4.71	Milli-Q water exper.
24/05/2011	20:00	00:00	2	3.61	7.47	1.11	-292	8.78	1.06	-195	8.96	1.15	Blank ice experiment
25/05/2011	00:00	13:45	2.5	3.59	6.41	1.26	-289	8.67	1.09	-191	10.4	1.79	Blank ice experiment
25/05/2011	16:10	17:00	x3	4.03	50.4	14.1	-355	28.4	7.67	-216	29.4	7.94	EuroCore
25/05/2011	17:30	00:00	3	2.34	3.94	0.459	-309	8.63	1.53	-164	9.05	1.61	Standard mixed with N_2
26/06/2011	00:00	10:00	3.5	2.35	2.54	0.337	-307	7.85	1.02	-166	8.2	1.02	Standard mixed with N_2
26/06/2011	19:00	00:00	4	1.56	3.61	0.361	-304	7.95	1.24	-148	8.04	1.16	Standard mixed with N_2
27/05/2011	00:00	07:00	4.5	1.57	2.02	0.287	-304	8.5	1.2	-149	8.88	1.01	Standard mixed with N_2
27/05/2011	09:00	17:00	5	1.27	2.58	0.311	-325	8.35	1.3	-155	7.58	1.32	Standard mixed with N_2
27/05/2011	19:00	00:00	5.33	1.17	1.57	0.175	-306	10	1.39	-137	10.3	1.58	Standard mixed with N_2
28/05/2011	00:00	09:00	5.66	1.18	1.62	0.195	-301	8.41	0.5	-134	8.26	0.81	Standard mixed with N_2
28/05/2011	16:00	00:00	6	1.47	5.85	0.425	-287	9.04	1.11	-137	9.07	1.53	Standard 19 psi + N2 21 psi
29/05/2011	02:00	17:00	6.25	1.46	1.7	0.11	-291	9.64	1.4	-137	10.1	1.51	Standard 19 psi + N2 21 psi
30/05/2011	00:00	16:00	6.5	1.46	1.92	0.18	-346	17.1	2.3	-180	15.3	2.27	Standard 19 psi + N2 21 psi
31/05/2011	00:30	07:45	6.75	1.46	2	0.267	-369	14.8	0.98	-202	14.8	0.746	Standard 19 psi + N2 21 psi
31/05/2011	09:40	11:00	7	1.55	2.65	0.462	-398	21.5	3.83	-223	15.2	2.11	Standard mixed with N_2
31/05/2011	19:00	00:00	8	1.27	3.34	0.426	-380	15.3	2.7	-214	13.8	2.57	Standard mixed with N_2
01/06/2011	00:00	07:00	8.5	1.27	1.88	0.286	-377	12.6	1.01	-206	14	1.43	Standard mixed with N_2
01/06/2011	08:00	17:30	9	1.34	1.84	0.212	-375	13.8	2.81	-198	15	3.04	Standard 23 psi + N2 29 psi
01/06/2011	21:10	00:00	9.33	1.34	1.94	0.14	-358	14.6	1.4	-187	14.9	1.9	Standard 23 psi + N2 29 psi
02/06/2011	00:00	07:50	9.66	1.34	1.98	0.093	-356	15.4	1.37	-182	15.7	1.74	Standard 23 psi + N2 29 psi
02/06/2011	10:30	19:00	10	1.26	1.89	0.327	-377	16	3.18	-201	15.1	2.96	Standard 25 psi + N2 30 psi
02/06/2011	21:00	00:30	11	1.42	2.67	0.327	-378	20.8	2.94	-213	17.7	3.11	Standard 30 psi + N2 25 psi
03/06/2011	00:30	07:40	11.5	1.42	2.13	0.288	-376	15	2.09	-215	14.3	1.99	Standard 30 psi + N2 25 psi
03/06/2011	08:50	10:05	12	1.45	2.05	0.123	-382	11.6	1.98	-228	12.4	1.84	Standard 30 psi + N2 25 psi
03/06/2011	11:40	16:00	13	1.48	2.56	0.347	-394	19.2	3.29	-226	21.5	3.17	Standard 30 psi + N2 25 psi
03/06/2011	21:30	00:48	14	1.59	2.64	0.473	-388	14.7	1.65	-233	17.1	3.28	Standard 30 psi + N2 25 psi
04/06/2011	00:30	14:00	14.5	1.59	2.6	0.551	-380	12.9	1.24	-208	13	1.19	Standard 30 psi + N2 25 psi
04/06/2011	22:30	01:00	15	1.52	2.49	0.564	-367	19.7	3.89	-199	19.8	4	Standard 30 psi + N2 25 psi
05/06/2011	01:00	09:00	15.5	1.52	2.44	0.468	-378	15.4	3.13	-213	17.1	3.79	Standard 30 psi + N2 25 psi
05/06/2011	12:00	16:30	16	1.51	3.19	0.679	-377	14.5	3.7	-216	15	4.04	Standard 30 psi + N2 25 psi

5

Isotopomer measurements of N_2O on microbiological respiration samples

For general introduction to N_2O please consult section 4.1.3. To understand the gobal budget of N_2O it is important to understand the natural sources. Natural production of N_2O in soil and ocean originates mainly from nitrification and denitrification of ammonia and nitrate by microbial bacteria. These processes has been observed to have different isotopomer signatures Sutka et al. [2006]. They showed that a site preferences of ca. 33‰ characteristic of nitrification and a site-preference of ca. 0‰ indicate denitrification. Further details on these relations were given by Koba et al. [2009], while recent work by Meijide et al. [2010] questions whether the relation is generally true in nature. Further investigations on these matters will be greatly simplified by continuous field deployable analyzers. This chapter presents preliminary investigations measuring the isotopomer ratios on gases from microbial incubation experiments.

Sample description and treatment The studied samples origin from the top sedimentary layer of Bøllemosen a lake in Jæregsborg Hegn ved Skodsborg. Four bottles of 117 ml volume were loaded with 2 gram of sample, (fresh with 27% moisture by mass). All samples were added easily available carbon in the form of 1 ml of glucose (in a 1g/50ml water solution) followed by 1 ml of NH_4NO_3 (in a 0.52g/100ml water solution). In two of the bottles the nitrification inhibitor Dicyandiamide was added in 1 ml portions of 0.1g DCD*/100ml solution. The bottles were incubated for 4 weeks at room temperature and then stored at 6 °C in a refrigerator.

Discrete injection setup: The setup shown in figure 5.1 was used for injecting the sample into the CRDS chamber. A three way ball valve were connected to the inlet of the cavity. The ball valve could select between a septum injection port or a pure nitrogen source. Between the cavity and the three port valve was installed a 0.05 µm pore size filter and a 1/4 inch tube filled with Drie-Rite dehumidifier.

Discrete injection procedure: The vacuum pump was used to evacuate the cavity and upstream to the septum injection port. The cavity valves were then closed. A 20 mL syringe was used to extract 15 mL of gas from the incubation bottle though the septum cap of the bottle. The syringe was then quickly injected and emptied into the septum injection port. The vacuum on the inside of the injection port would for most part suck in the sample but a little overpressure would have to be applied to inject the full sample. The sample was then admitted to the CRDS cell, slowly opening the inlet valve on the cavity. To reach sufficient cavity pressure of 200 torr, the inlet valve was closed and the three way ball valve was turned toward the pure nitrogen source providing 0.2 bar gauge pressure. The inlet valve to the cavity was then used to inject sufficient upstream gas-mixture to reach 200 torr.

The samples without the inhibitor had much higher concentrations (40-80 ppm) and greater dilution with pure nitrogen had to be made. For the injection only a few ml would be necesarry, but this sample was diluting in the cavity in steps of raising the cavity pressure with pure nitrogen, and then lowering the pressure by evacuating with the vacuum pump.

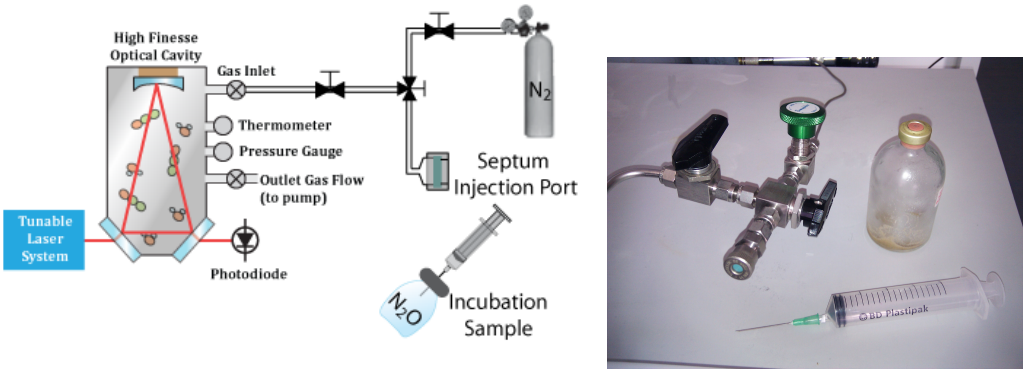

Figure 5.1: Setup diagram and picture for the injection of microbial incubation samples.

Results and discussion It was hoped to be possible to detect a difference in the isotopomer values between the nitrification inhibited and non-inhibited

incubation samples, in accordance with the theory by Sutka et al. [2006]. This turned out not to be possible as an unknown absorption feature was discovered to interfere with the absorption line of $^{15}N^{14}N^{16}O$, for the samples to which the dicyandiamide nitrification inhibitor was added. In the samples without the inhibitor, this unknown absorber was not observed.

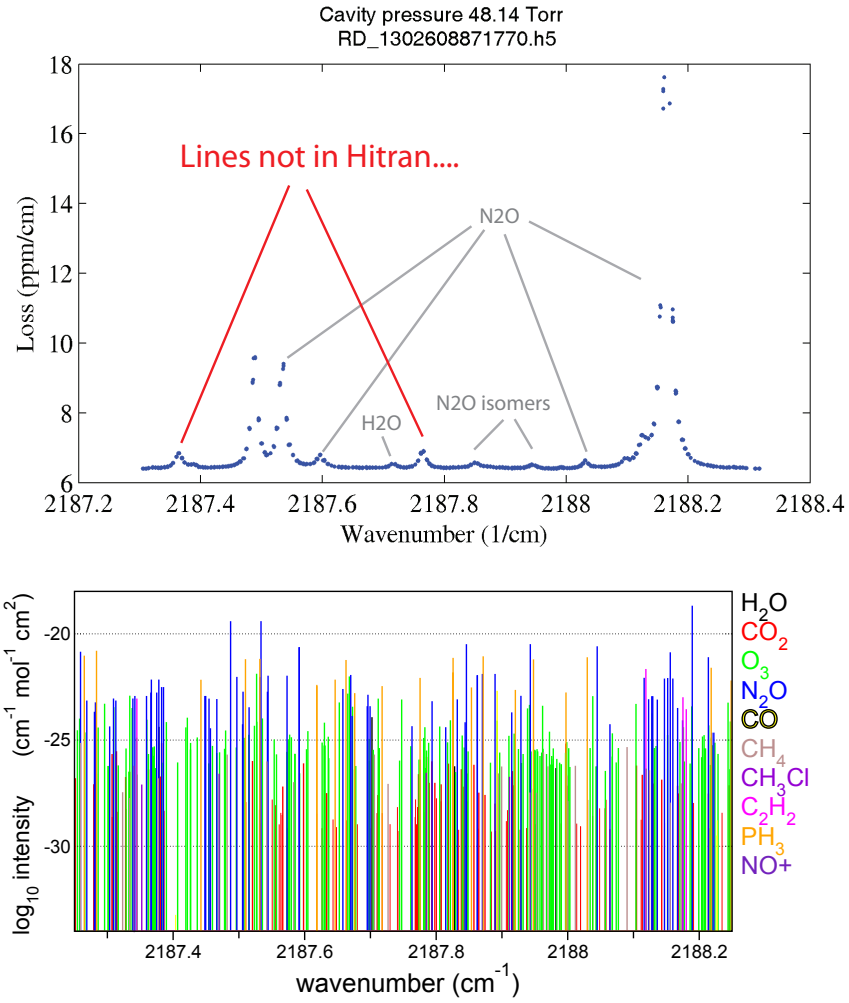

Figure 5.2: Top: Spectrum showing the absorption lines of an unknown absorber in the microbial incubation samples with added dicyandiamide nitrification inhibitor. Lower: Spectral line intensities registered in Hitran 2008.

A spectral scan of the unknown absorption line was captured with a cavity pressure of 50 torr, shown in figure 5.2. The scan has a 30MHz resolution captured in $0.005\,\mathrm{cm}^{-1}$ intervals. Below the spectrum is shown the spectral lines and their intensity in this spectral region recorded by Hitran 2008. From this it is seen that there are no lines in the Hitran database corresponding

to the observed new lines.

Examination of the new spectral feature at 50 torr shows a commencing Gaussian feature. Using a Gaussian fit it was found that the spectral line width correspond to molecular mass of ca. 30 to 35 amu, but with great uncertainty. In this mass range H_2S and NO are molecular candidates for the unknown absorber.

Time and circumstances of the analyzer prevented that a high resolution spectrum at lower pressure could be made for the un-inhibited samples. Therefore a comparison between nitrification and de-nitrification was not possible.

Outlook Many of the samples investigated by biologists also contains high concentrations of acetylene and other corrosive gases, which may damage the sensitive mirrors. The work by Yan et al. [2008] address this problem by using a prism based cavity without sensitive high reflective coatings. Such cavities may become crucial for future developments of CRDS applications within biology and chemistry.

Part II

Designing, Building and Performance Characterizing a Mid Infrared Cavity Ring-Down spectrometer for continous measurements of $\delta^{18}O$ and $\delta^{15}N$ isotopomer ratios of N_2O

The molecular absorption strength in the mid-infrared is three orders of magnitude stronger than that of the near-infrared. Improving the precision and extending the set of measurable species is the primary motivation for extending the CRDS technology into this region. Doing spectroscopy with mid-infrared lasers also opens the ability to detect a whole new range of molecular species not having significant absorption in the near-infrared. An example is the isotopes of N_2O and CO_2 illustrated by the line absorption intensities in figure 5.3. The development of an analyzer detecting N_2O isotopomers at 4.5 μm was based on the scientific reasons stated in part one, and further because optical components were accessible and of better quality at the shorter wavelength, than they would be when going beyond 5 µm. A final argument for choosing to make an analyzer for N_2O isotopomers is that these are more difficult to measure by mass spectrometry because the two 15-N isotopomers both have mass 45.

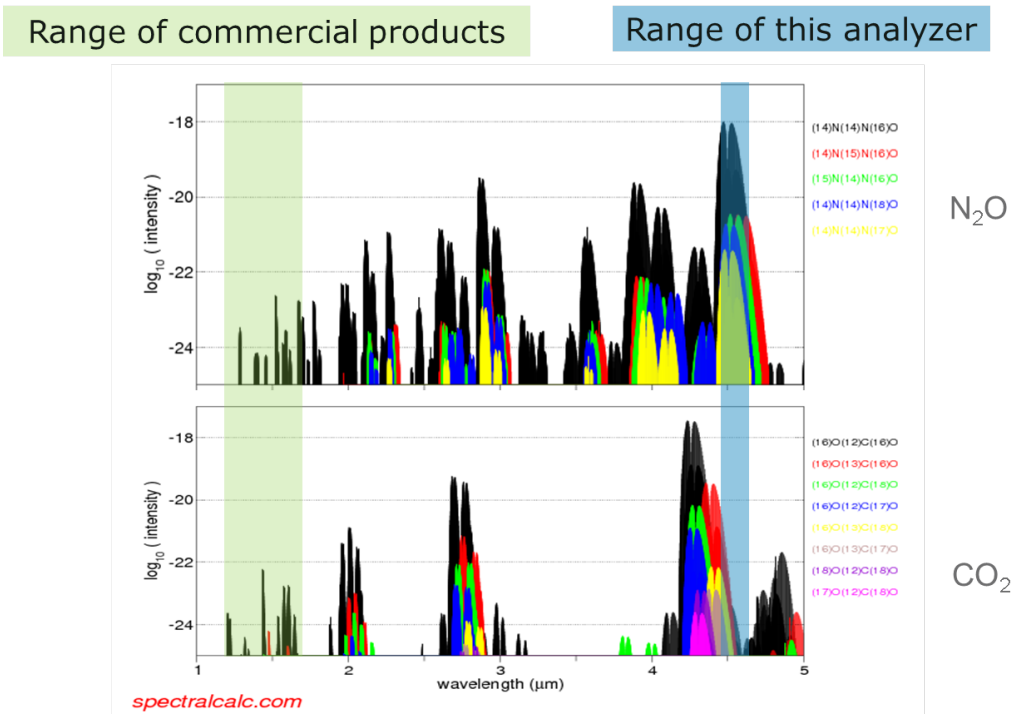

Figure 5.3: The absorption strength in the mid infrared is several orders of magnitude stronger than in the near infrared.

6 Choice of cavity enhanced method for a mid-infrared spectrometer

Since the first reporting of the CRDS method by O'Keefe and Deacon [1988], CRDS has increasingly gained attention. In 2001 a list of 196 different references for CRD measurements was drawn up by Peeters [2001]. With the advances and introduction of standardized CRDS analyzers surely this list is much longer a decade later. CRDS is not the only method applying an optical cavity for enhanced molecular absorption. A nice historical overview of the cavity enhanced methods is presented in Paldus and Kachanov [2005]; Berden and Engeln [2009]; Mikhail Mazurenka [2005]. In the following section a the fundamental properties for an enhancement cavity is given. After that section 6.2 gives a summary and comparison between the optical techniques that could be applied.

6.1 Fundamentals of cavity enhanced absorption spectroscopy

6.1.1 Transmission from an optical cavity

The optical cavity is a Fabry-Perot interferometer Hecht [2002], with two coated surfaces of high reflectivity. The intra-cavity absorption will only provide small changes to the Fabry-Perot model, but is derived in the following for completeness.

Imagine an electric wave with amplitude E_0 impinging onto the first mirror of electric coefficient reflectivity r_1 and transmission t_1. The wave will be split into two parts, a reflected and a transmitted one. The transmitted wave will continue through the cavity to be split on the second mirror of

reflectivity r_2 and transmission t_2. From here the reflected beam will bounce back and fourth between the two surfaces, decreasing its amplitude for each round trip by a fractional part[1] $r_1 r_2 e^{-2L\frac{\alpha}{2}}$ due to losses out of the mirrors and molecular absorption using Beer-Lambert's law. At the same time a fraction of the amplitude will be transmitted out of the cavity, and will contribute to either the total reflected wave or total transmitted wave, depending on the surface. The transmitted wave as well as the reflected wave is thus an infinite series of spatially overlapping beams. Assuming that the transmitted and reflected fraction is independent of the incoming amplitude, we may find the transmitted amplitude

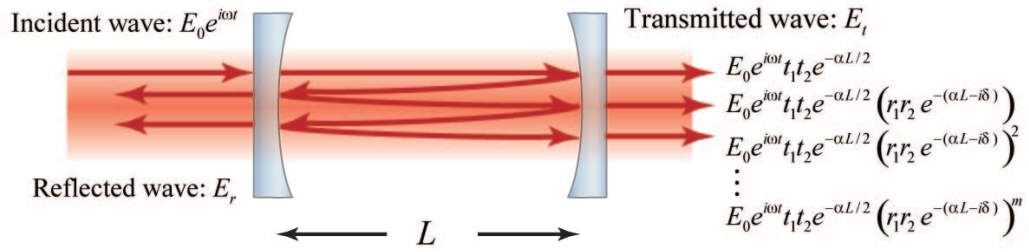

Figure 6.1: Amplitude transmission upon a given number of reflections in a Fabry-Perot cavity with inter mirror absorption.

$$
\begin{aligned}
E_t &= E_0 e^{i\omega t} t_1 t_2 e^{-\alpha L/2} + E_0 e^{i\omega t} t_1 t_2 e^{-\alpha L/2} \left(r_1 r_2 e^{-(\alpha L - i\delta)}\right) + \cdots && (6.1)\\
&+ E_0 e^{i\omega t} t_1 t_2 e^{-\alpha L/2} \left(r_1 r_2 e^{-(\alpha L - i\delta)}\right)^m + \cdots && (6.2)\\
&= E_0 e^{i\omega t} t_1 t_2 e^{-\alpha L/2} \sum_m \left(r_1 r_2 e^{-(\alpha L - i\delta)}\right)^m && (6.3)\\
&= \frac{E_0 e^{i\omega t} t_1 t_2 e^{-\alpha L/2}}{1 - \left(r_1 r_2 e^{-(\alpha L - i\delta)}\right)} && (6.4)
\end{aligned}
$$

where δ is the phase shift that the wave acquires in a round trip. Assuming that the mirrors are identical, i.e., $r_1 = r_2 = \sqrt{R_m}$ and the mirror transmittance is symmetrical $t_1 = t_2 = \sqrt{T_m}$ and the mirrors are lossless $T_m + R_m = 1$ yields the cavity transmittance

$$
\begin{aligned}
T_c &= \left|\frac{E_t}{E_0}\right|^2 = \left|\frac{T_m e^{-\alpha L/2}}{1 - R_m e^{-(\alpha L - i\delta)}}\right|^2 = \frac{T_m^2 e^{-\alpha L}}{1 + R_m^2 e^{-\alpha 2L} - 2R_m e^{-\alpha L}\cos(\delta)} && (6.5)\\
&= \frac{T_m^2 e^{-\alpha L}}{\left(1 - R_m e^{-\alpha L}\right)^2} \left(\frac{1}{1 + F\sin^2(\delta/2)}\right) && (6.6)
\end{aligned}
$$

[1]The electrical field attenuation is $\alpha/2$ because the light intensity is given by $I = |E|^2$.

where F is the coefficient of finesse given by

$$F = \frac{4R_m e^{-\alpha L}}{\left(1 - R_m e^{-\alpha L}\right)^2} \approx \frac{4R_m}{\left(1 - R_m\right)^2} \tag{6.7}$$

where the last approximation stems from $\alpha L << 1$, so the coefficient of finesse is basically equal to that of the empty cavity $\alpha = 0$.

Apart from an absorption factor, the cavity transmission is still given by the Airy function in the big parenthesis of equation (6.6) and is depicted in fig. 6.2. Two quantities are highlighted on fig. 6.2: The line width δ_{lw} and

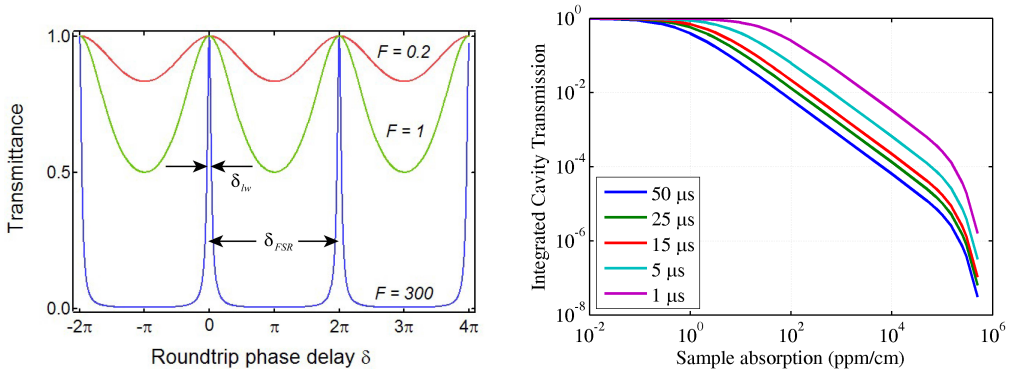

Figure 6.2: LEFT: The Airy function for different values of the coefficient of finesse F. Notice that the higher the value of F the more does the transmittance depend on the round trip phase delay δ. RIGHT: The integrated cavity mode transmission versus intra cavity transmission. The five curves correspond to cavities of different empty cavity ring down time.

the cavity free spectral range δ_{FSR}.

The cavity free spectral range (FSR) is given by the round trip phase delay being equal to an integer times 2π. The cavity round trip accumulated phase shift for a wave of vacuum frequency ν is given by $n_r(\nu)k2L + \theta(\nu) = 4\pi\nu n_r(\nu)L/c + \theta(\nu)$, where $\theta(\nu)$ is the phase shift contribution from the mirror, which only makes minor deviations and will be ignored for now. The FSR is then found from $\frac{4\pi\nu n_r L}{c} - \frac{4\pi(\nu+\mathrm{FSR})n_r L}{c} = 2\pi$ yielding

$$\mathrm{FSR} = \frac{\mathrm{c}}{2\mathrm{n_r}(\nu)\mathrm{L}} = \frac{1}{\tau_\mathrm{c}}, \tag{6.8}$$

i.e., one over the cavity round trip time τ_c. The transmitted frequencies thus constitute a frequency comb of $\nu_m = m \cdot \mathrm{FSR}$ since the free spectral range is constant.

Now turning to the line width (FWHM), it may be noted that it is equal to the empty cavity line width if the change of absorption is small within this region. Reusing that the phase delay is given by $4\pi nL\nu/c$, and that the Airy function has a maximum at $\nu = 0$ we simply solve $\frac{1}{1+F\sin^2(4\pi n_r L\nu_{\mathrm{lw}}/2c)} = \frac{1}{2}$

$$\nu_{\mathrm{lw}} = \frac{c}{2\pi n_r L}\frac{1-R_m}{|r_m|} \tag{6.9}$$

assuming empty cavity and highly reflective mirrors such that F is very large and the approximation $\sin^{-1}(1/\sqrt{F}) = 1/\sqrt{F}$ can be made.

We finally have the cavity finesse given by the free spectral range divided by the line width:

$$\mathscr{F} = \frac{\pi|r|}{1-R} \approx \frac{\pi}{1-R} \tag{6.10}$$

using that $|r| \approx 1$, so for the absorptionless cavity $\mathscr{F}^2 \approx F$. Large finesse yields a narrow transmission wavelength, which is useful in spectroscopy. But more important is that the finesse is proportional to the number of round trips $1/(1-R)$ (see (6.4)) of a transmitted light, which provides us with an effective path length Gherman and Romanini [2002]

$$L_{\mathrm{eff}} = \frac{\mathscr{F}}{\pi}2L. \tag{6.11}$$

A large value of finesse is thus desirable in order to get a long effective path length, such that a large signal to noise of the absorption is achieved.

6.1.2 Integrated cavity transmission

When increasing the molecular concentrations, intra-cavity absorption increases and the cavity ring down time thus decreases.

In equation 6.6 the transmitted power at the peak of a cavity resonance was expressed. The transmitted power also depends on the cavity line width equation 6.9. The integrated transmission can be estimated by multiplying the cavity line width by the transmission at the peak, yielding

$$T_c = \frac{T_e e^{-\alpha L/2}}{1-R_e e^{-\alpha L}} \tag{6.12}$$

when normalized to the empty cavity transmission. This expression is in good agreement with the exact ratio solution by Moosmüller et al. [2005]. Figure 6.2 shows the cavity transmission using equation 6.12 for five different mirror qualities.

The cavity transmission peak scales as $\frac{1}{\alpha^2}$ while the transmission line width scales as α, and so the integrated cavity transmission intensity of light, scales as $\frac{1}{\alpha}$ Engeln et al. [1998].

For small absorptions this expression also agrees with the Beer-Lambert expression using the effective path length:

$$T_c = \frac{I}{I_0} = \frac{1}{1 + \frac{\alpha L}{1-R}} = \frac{1}{1 + \alpha L_{\text{eff}}} \tag{6.13}$$

Transmitted power does not follow $\frac{1}{\alpha}$ at and below intra cavity absorptions that are comparable to the empty cavity loss.

6.2 Cavity enhanced spectroscopy methods

In considering the design of a mid-infrared laser spectrometer system for highly sensitive detection of trace gases the following sections will review previous methods that were developed for the visible and near-infrared optical regions. Many of these methods are now outdated due to the advances of e.g. telecommunication. But the methods could have advantages in the mid-infrared where the optical components are not as developed. The figure of merit for comparison is the noise equivalent absorption (NEA), which is the one sigma deviation precision obtainable in one second. The definition does vary a bit. van Zee et al. [1999]; Romanini and Lehmann [1993] use

$$NEA = \sqrt{\frac{2}{f_{\text{rep}}}} \frac{\sigma_{\tau,\,\text{ens}}}{c\bar{\tau}^2} = \sqrt{\frac{2}{f_{\text{rep}}}}\, \sigma_\alpha. \tag{6.14}$$

where f_{rep} is the data collection rate, $\sigma_{\tau,\,\text{ens}}$ and $\bar{\tau}$ are the standard deviation and mean of an ensemble of ring down measurements, while Bernhardt et al. [2010] use $\alpha_{\min}\sqrt{T}$ per spectral element (span/resolution) where $\alpha_{\min}$ is the minimum detectable absorption coefficient and T is the recoding time. It is important to note that $\alpha_{\min}$ is not well defined in this perspective. If $\alpha_{\min}$ is chosen as the minimum in an Allan plot, then that does not necessarily give the minimum NEA. This is because as soon as the Allan deviation starts being higher than the $1/\sqrt{T}$ averaging line, then the NEA will start to be worse than at the largest integration time, where the Allan deviation still follows the $1/\sqrt{T}$ averaging.

6.2.1 Single frequency methods

6.2.1.1 Multi pass absorption spectroscopy with QCL

Although not a cavity enhanced method - the following method should be mentioned as it has demonstrated high precision measurements. In this method, light is bounced through the samples hundreds of times but not injected through the mirrors. Nelson et al. [2002] demonstrated a NEA = $5 \times 10^{-10}\,\mathrm{cm}^{-1}\sqrt{\mathrm{Hz}}$ with a thermo electrically cooled quantum cascade laser spectrometer. It is also important to mention the pioneering and good work on N_2O isotopomer measurement done by [Waechter et al., 2008; Mohn et al., 2010; Wächter, 2007].

6.2.1.2 Cavity enhanced photo acoustic spectroscopy

Optical absorption is detected by acoustic vibrations induced in the gas. The acoustic waves are generated by modulating the light intensity with an acoustic frequency. The acoustic waves are recorded by a microphone which is typically mounted on an organ pipe surrounding the gas, to enhance sound pickup. Acoustic waves will only be generated in the gas when the light has wavelengths corresponding to the optical absorption lines of the gas. Webber et al. [2003] achieved NEA = $3.0 \times 10^{-9}\,\mathrm{cm}^{-1}\sqrt{\mathrm{Hz}}$ using a multi-pass photo acoustic system employing a laser of 500-mW power. An advantage of this method is that it is a zero-background method which increases selectivity and sensitivity, and its sensitivity scales with laser power. Without a cavity the spectral resolution is limited by the laser line width. This was compensated for by Hippler et al. [2010] who applied an optical feedback cavity method to improve the line width. With this Hippler et al. [2010] achieved a NEA = $4.4 \times 10^{-9}\,\mathrm{cm}^{-1}\sqrt{\mathrm{Hz}}$

6.2.1.3 Off-axis integrated cavity output spectroscopy

Using off-axis integrated cavity output (OA-ICOS) measurements, Engel et al. [2006] reach a per point noise-equivalent absorption sensitivity of NEA = $1.9 \times 10^{-12}\,\mathrm{cm}^{-1}\sqrt{\mathrm{Hz}}$, using a 110-cm long cavity, scanning a spectral region of 4.5 cm^{-1} at a rate of 30 Hz.

Moyer et al. [2008] demonstrated that in the mid-infrared at 6.7 µm OA-ICOS may give a NEA = $2.4 \times 10^{-11}\,\mathrm{cm}^{-1}\sqrt{\mathrm{Hz}}$, with a 2 m cavity round trip distance.

The method applies large mirrors and injects the light beam off axis such that the beam passes through the cavity N times before closing the path. In this way the effective free spectral range is divided by N. This also provides

N output beams. These are all collected on a photo detector using a large lens. In this way, it may be achieved, to have the laser on resonance at effectively all wavelengths, without changing the cavity length. The setup is very simple and requires no stabilization, as fluctuations in the cavity length increases sensitivity. The downside is, that the cavity is large inherent by the large mirrors. Resolution is limited to the line width of the laser, and performance may also be affected by drifts in laser intensity and detector sensitivity. The large cavity size is a drawback when only having limited sample amount such as for ice core samples.

6.2.1.4 Optical feedback Cavity Enhanced Absoption Spectroscopy (OF-CEAS)

Morville et al. [2005] achieved a single point NEA $= 5 \times 10^{-10}\,\mathrm{cm}^{-1}\sqrt{\mathrm{Hz}}$. This method uses a V-shaped cavity from which light internal to the cavity is allowed to feed back to the cavity. This enhances the laser to resonate with cavity whereby the line width is narrowed and coupling from laser to cavity is enhanced. Morville et al. [2005] applies an active control of the distance between laser and cavity, in order to achieve a phase matched feedback. This provides symmetric mode shapes, which allows for determination of the cavity mode spacing, and thus precise frequency designation to the data points.

6.2.1.5 CW-CRDS

CRDS with heterodyne detection He and Orr [2006] reported a noise-limited absorption sensitivity of NEA $= 5 \times 10^{-10}\,\mathrm{cm}^{-1}\sqrt{\mathrm{Hz}}$ with a rapidly swept cw CRDS scheme using optical heterodyne detection and a 4 kHz collection rate of the ring down events. The heterodyne detection provides a ring down time that is twice as long as the normal signal, but it has an undulating oscillation, which make special treatment of the signal necessary. This method is especially suited for low power lasers.

Optical feedback Cavity Ring Down Spectroscopy Motto-Ros et al. [2007] achieved single point NEA $= 2 \times 10^{-10}\,\mathrm{cm}^{-1}\sqrt{\mathrm{Hz}}$. Optical feedback is provided in a similar way as for the OF-CEAS, increasing the coupled power to the cavity and narrowing the line-width of the laser.

unlocked CRDS Applying CRDS without locking, Crosson et al. [2002] achieved a NEA $= 3.2 \times 10^{-11}\,\mathrm{cm}^{-1}\sqrt{\mathrm{Hz}}$.

Locked CRDS The periodically locked CRDS method by Martinez et al. [2006] showed a NEA $= 1.4 \times 10^{-11}\,\mathrm{cm}^{-1}\sqrt{\mathrm{Hz}}$ applying a Pound Drever Hall lock to the CRD beam and only sampling a short part of the ring down event in order to maintain the lock. In the mid-infrared at 3 µm [Halmer et al., 2005; Kleine et al., 2000] used a CdTe electro optic modulator to make a lock-in of the laser to cavity resonance before executing the CRD measurment. They denote this CRDS method cavity leak out spectroscopy (CALOS) and achieved NEA $= 7 \times 10^{-11}\,\mathrm{cm}^{-1}\sqrt{\mathrm{Hz}}$ with a 1 meter round trip cavity.

The two beam locking scheme by Spence et al. [2000] reached a NEA $= 1.0 \times 10^{-12}\,\mathrm{cm}^{-1}\sqrt{\mathrm{Hz}}$ by keeping the cavity length locked during the ring-down measurement. This was done using a mode cleaner cavity, which has different cavity properties for S and P polarization. The cavity P mode was used for locking the cavity length, while the S mode was used for the ring down measurement. Locking the laser to the resonant cavity modes also enhances the effective path length, and thus increases the measurement sensitivity.

An alternative to Pound Drever Hall locking, is the spatial mode locking schemes, presented by [Yang et al., 2004; Robins et al., 2002; Shaddock et al., 1999; Slagmolen et al., 2002].

6.2.1.6 NICE-OHMS

The highest precision presented yet is by Ye et al. reporting a sensitivity of NEA $= 1.0 \times 10^{-14}\,\mathrm{cm}^{-1}\sqrt{\mathrm{Hz}}$ over 1-s averaging time in a scheme that combines the external cavity enhancement approach with frequency-modulation spectroscopy, named NICE-OHMS (noise-immune cavity-enhanced optical heterodyne molecular spectroscopy). A frequency modulation, equal to the FSR of cavity, is used to create side bands at the neighboring cavity transmissions, one FSR away from the laser resonance. These side bands are used for Pound Drever Hall locking. Taubman et al. [2004] showed that NICE-OHMS is possible in the mid-infrared by applying current modulation to a quantum cascade laser, giving them a NEA $= 9.7 \times 10^{-11}\,\mathrm{cm}^{-1}\sqrt{\mathrm{Hz}}$.

6.2.1.7 Conclusions on single frequency methods

When leaving the near-infrared for the mid-infrared, absorption is higher because of quantum mechanics. But the trade-off is that there is also more laser intensity noise as well as increased detector noise, because the mid-infrared is closer to the Boltzmann energy, kT. In terms of optical enhancement techniques, established dielectric mirror technology means, that high finesse cavities are equally accessible in the mid-infrared, although different

optical materials have to be applied. Of the above cavity-enhanced methods WS-CRDS and ICOS stand as the best candidates for high sensitivity absorption spectroscopy in the mid-infrared.

The ICOS method requires only simple optical components. However ICOS is sensitive to fluctuation in the laser intensity, which is a major issue for QC lasers in the mid infrared. So signal/noise and hence precision will be inherently lower than for WS-CRDS.

In the case of the WS-CRDS method, the data is insensitive to laser intensity noise. Together with precision control of the pressure and temperature in the cavity, this yields an instrument with very low drift rate.

6.2.2 Broadband cavity enhanced methods

The single frequency methods presented above, are all limited to sampling a single wavelength at a time, and often these lasers have limited tuning ranges. Methods presented in the following, sample larger spectral regions simultaneously. Many of these have the advantage of sampling multiple absorption lines of the same species or interfering lines, which may be of aid to extract information on the gas composition.

6.2.2.1 Incoherent Broad band cavity enhanced spectroscopy (IBBCEAS)

Fiedler [2005]; Ruth et al. [2007] showed that an enhancement factor of 200 (mirror reflectivity $R > 0.996$) could be achieved with an incoherent light source. The absorption spectrum sends the cavity transmitted light into a Fourier transform spectroscopy or a monochromator. This method has the drawback of not providing the absolute absorption coefficient. Ventrillard-Courtillot et al. [2010] used a LED white light source and a low resolution grating-spectrometer and achieved a NEA $= 4.0 \times 10^{-9}\,\mathrm{cm}^{-1}\sqrt{\mathrm{Hz}}$.

6.2.2.2 Cavity enhanced spectroscopy using frequency combs

Advances in broadband femto-second mode locked lasers over the last decade have allowed for promising advances into high sensitivity broad band cavity enhanced spectroscopy. The mode locked femto-second laser has a spectrum, which corresponds to an ensemble of lasers with frequencies forming a uniformly spaced grid, just like the cavity transmittance spectrum. These lasers are also referred to as frequency comb lasers, due to this shape of the spectrum. The coherence property of a frequency comb makes it essentially

possible to transmit the full power of the laser, by matching the cavity transmission spectrum to the spectrum of the laser. Here follows the advances within this field.

Thorpe et al. [2006] demonstrated a broadband cavity ring down system, which simultaneously records the ring down signal from over 15 nm at 25 GHz resolution with a NEA $= 2 \times 10^{-8}\,\mathrm{cm}^{-1}\sqrt{\mathrm{Hz}}$ per channel. The ring down was recorded using a grating spectrometer to diffract the spectrum in the horizontal direction. The Cavity ring-down events were recorded by sweeping the diffracted spectrum in the horizontal direction across the camera during the cavity ring down event. The spectral resolution limits the applicability of this analyzer. It was envisioned by Thorpe and Ye [2008] that a high speed photo-detector array could substitute the moving parts. But such circuits have only been realized in a 4 detector array.

Thorpe et al. [2008]; Balslev-Clausen [2007]; Thorpe [2009]; Cossel et al. [2010] have demonstrated a method for high resolution cavity enhanced direct frequency comb spectroscopy by using a VIPA spectrometer on the cavity output. The system provided a NEA $= 2 \times 10^{-8}\,\mathrm{cm}^{-1}\sqrt{\mathrm{Hz}}$ per channel, with 800 MHz resolution over 25 nm sections, that were tunable over 200 nm.

Rather than using a VIPA, Gohle et al. [2007] showed that a vernier grid effect between frequency comb and cavity transmittance spectrum makes it possible to extract the absorption signal for each comb. This system however also uses moving parts. They achieved a NEA $= 5 \times 10^{-7}\,\mathrm{cm}^{-1}\sqrt{\mathrm{Hz}}$ for each mode of the frequency comb, spanning 4 THz per scan.

Mandon et al. [2009] achieved a NEA $= 5 \times 10^{-6}\,\mathrm{cm}^{-1}\sqrt{\mathrm{Hz}}$ per resolution unit of 1.5GHz, simultaneously covering a spectral range of $360\,\mathrm{cm}^{-1}$. This was achieved by sending a frequency comb through a high finesse cavity and recording the output spectrum with a conventional Fourier transform spectrometer. This system has also affected by the need of large moving parts, which limit acquisition speed.

Bernhardt et al. [2010] report a proof of principle method called cavity-enhanced dual-comb spectroscopy. They demonstrate a broadband cavity enhanced absorption spectroscopy method with a NEA $= 1 \times 10^{-10}\,\mathrm{cm}^{-1}\sqrt{\mathrm{Hz}}$ per channel, spanning 20 nm with 1.5 GHz resolution. This method uses two optical combs and single photo detector, i.e. no moving parts. One comb is sent through the cavity and combined with the other comb on the photo detector. By detuning one of the combs a multi heterodyne signal is recorded

on the photo-detector, from which the optical absorption spectrum can be derived by, using a Fourier transformation.

6.3 Discussion

All mentioned methods have their advantages and disadvantages. The reasons for choosing the CRDS for this work was the following: The broadband frequency comb technology is not yet available for the mid-infrared in compact automated systems. They are also expensive, so it was chosen to go with single frequency.

Of major concern was the performance of the available mid infrared lasers. In particular laser intensity was expected to be unstable and be variant when tuning the frequency. CRDS is the only method of the above mentioned which is independent of laser intensity. The on-axis cavity configuration also allows for a very small cavity volume compared to e.g. ICSO and multi-pass configurations. This is of large importance to measurements on small samples such as ice-cores. For this reason CRDS was chosen keeping open, the option of implementing a locking scheme.

7 Estimating the possible performance

This Chapter presents spectroscopic considerations on the applicable spectral lines including pressure and temperature sensitivity. Then an estimated performance and requirements for the spectrometer is treated. First a brief presentation of relevant spectroscopic features is presented.

7.1 Spectroscopic considerations for N_2O

Using the HITRAN database and assuming that pressure broadening dominates, the spectral absorption coefficient $\alpha(\nu)$ may be expressed by a Lorentzian profile

$$\alpha(\nu) = nS_{ij}g(\nu, \nu_{ij}, p, T) = \frac{nS_{ij}}{\pi} \frac{\gamma(p,T)}{\gamma(p,T)^2 + (\nu - [\nu_{ij} + p\delta(p_{\text{ref}})])^2} \tag{7.1}$$

with S_{ij} [$\text{cm}^{-1}\text{mol}^{-1}\text{cm}^2$] the line intensity for a transition between lower energy level i and upper energy level j, the normalized line profile $g(\nu, \nu_{ij}, p, T)$[1], The pressure broadened half width $\gamma(p,T)$ [cm^{-1}] at pressure p and temperature T, the spectral line transition frequency ν_{ij} [cm^{-1}], and the air pressure shift $\delta(p_{\text{ref}})$ [cm^{-1}/atm]. All these parameters are provided for the reference temperature $T_{\text{ref}} = 296$ K and pressure $p_{\text{ref}} = 1$ atm.

Line profile $g(\nu, \nu_{ij}, p, T)$ For temperatures and pressures different from the reference values, the pressure broadened half width is expressed according to

$$\gamma(p,T) = p\gamma_{\text{air}}(p_{\text{ref}}, T_{\text{ref}}) \left(\frac{T_{\text{ref}}}{T}\right)^n \tag{7.2}$$

[1] $\int_{-\infty}^{\infty} g(\nu, \nu_{ij}, p, T)d\nu = 1$

where γ_{air} [cm^{-1}/atm] is the air broadening half width and n is the coefficient of temperature dependence of air-broadened half-width. The self broadening contribution has been ignored as only trace gases are studied in this work.

At high pressures collision broadening is dominant, while at lower pressures the Doppler broadening dominates. The Doppler broadening contributed by the thermal Boltzmann velocity distribution of the molecules and the according Doppler shift experienced by the molecular ensemble provide a Gaussian line profile with a half width of

$$\gamma_D = \frac{\nu_{ij}}{c}\sqrt{\frac{8RT\ln 2}{M}} \tag{7.3}$$

where R is the ideal gas constant and M is the molar mass. Considering a light molecule such as water, the Doppler line width at 296 K is 3 MHz i.e. 0.0001 cm^{-1}. Comparison with the air-broadened half-width at different pressures is shown in table 7.3, from which it is seen that the pressure has to be below 50 Torr before the collision and Doppler line widths become comparable.

For intermediate pressures the line profile can be expressed by the Voigt profile calculated from the convolution of the Lorentzian pressure broadening and Gaussian Doppler broadening integrating overall axial velocities of the molecules

$$g(\nu) = \sqrt{\frac{M}{2\pi RT}}\frac{\gamma(p,T)}{\pi}\int_{-\infty}^{\infty}\frac{e^{-Mv^2/2RT}}{(\gamma(p,T)-\nu+\nu_{ij}v/c)^2+\gamma(p,T)^2}dv. \tag{7.4}$$

An improved model in the intermediate pressure range was given by Galatry [1961] including the narrowing of the Doppler line width due to collisional inhibition of the thermal molecular motion. The Galatry profile can be expressed as the real part of the Fourier transform Ouyang and Varghese [1989]

$$G(x',y,z) = \frac{1}{\sqrt{\pi}}\Re\left\{\int_0^{\infty}\Phi(y,z,\tau)\exp -ix'\tau d\tau\right\} \tag{7.5}$$

where x' is the dimensionless frequency separation from the line center normalized by the $1/e$ Doppler half width, y is the collision broadening parameter, z is the collision narrowing parameter, and $\Phi(y,z,\tau)$ is the correlation function

$$\Phi(y,z,\tau) = \exp\left(-y\tau+\frac{1}{2z^2}[1-z\tau-\exp(-z\tau)]\right), \tag{7.6}$$

where τ is the dimensionless time. The Voigt profile is a special case of the Galatry profile with the collision narrowing parameter $z = 0$.

In many cases the mean free path ℓ can be used, as guidance as to which regime is at hand. With the mean velocity $\bar{v}$ we have that $\bar{v}z^{-1} \cong \ell = \frac{1}{\sqrt{2}n\sigma} = \frac{k_B T}{\sqrt{2}\pi d^2 p}$. When $\ell \ll \lambda/2\pi$ a Lorentzian expression applies while for $\ell \gg \lambda/2\pi$ the Doppler regime is at hand.

Line intensity S_{ij} and temperature dependence For temperatures and pressures different from the reference values 296K the absorption line intensity can be expressed according to

$$S_{ij}(T) = \frac{A_{ij}}{8\pi c \nu_{ij}} \frac{g_j \, e^{-c_2 E_i/T}}{Z(T)} \left(1 - e^{-c_2 \nu_{ij}/T}\right) \tag{7.7}$$

where A_{ij} is Einstein's A coefficient, E_i [cm^{-1}] the lower state energy, g_j the upper state statistical weight, $c_2 = hc/k = 1.4388$ cm K the *second spectral constant* and the total internal partition function is

$$Z(T) = \sum_k g_k e^{-c_2 \, E_k/T} \tag{7.8}$$

summing over all molecular states k with statistical weights g_k [Šimečková et al., 2006]. The listed values in the HITRAN database are further corrected for the natural isotopic abundance. The temperature dependence of the partition function is listed in the Hitran - TIPS_2003 interpolation data set [Fischer et al., 2003]. For all species considered in this work the relative line intensity temperature dependence is $\approx 0.5\%$/K at 296 K.

The relative temperature dependence of the line intensity can be found by differentiation with respect to T. It is convenient to regard this temperature dependence relative to the line intensity at the reference temperature

$$\frac{1}{S_{ij}(T_{ref})} \frac{dS_{ij}}{dT}\bigg|_{T=T_{ref}} = \frac{c_2 E_i}{T^2} - \frac{\frac{c_2 \nu_{ij}}{T^2}}{e^{c_2 \nu_{ij}/T} - 1} + \frac{dZ/dT}{Z(T)} \cong \frac{c_2 E_i}{T^2} + \frac{dZ/dT}{Z(T)} \tag{7.9}$$

where ref has been omitted and the last expression applies for large ν_{ij}. The absorption lines in table 7.1 all have a relative temperature dependence in the range of 0.5%/K - 2%/K, with the highest temperature dependendence for the transitions with larger E_i.

A simple expression of the temperature dependence of isotopic delta values is also achieved when considering isotopic ratios around the standard value:

$$\frac{d\delta}{dT} \cong \frac{c_2 \Delta E}{T^2} \times 1000 \, (‰) \tag{7.10}$$

where ΔE is the difference between the lower state energy of the two isotopologue lines being considered [Bergamaschi et al., 1994]. Variations in the

delta value due to temperature fluctuations may be smaller than the variations in the individual line intensities, if the line fluctuations occur in the same direction. For the lines considered in table 7.1 the typical fluctuation is around 0.01‰/mK.

Spectral interference When considering a multiple line system, spectral features from one molecule may overlap with that of interest. Such spectral interference depends on concentrations of the two species, temperature and pressure. It may be quantified by an overlap integral. Such a quantity is highly dependent on temperature and pressure and some interference features may be compensated for by the spectroscopic fitting. A suitable quantification would therefore involve that the full fitting routine is applied.

7.1.1 Selection of spectral lines

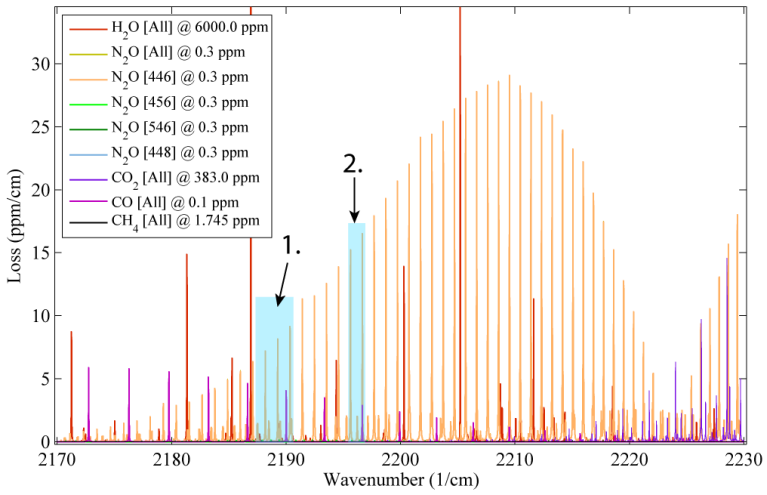

Figure 7.1: Spectrum around 4.55 µm *modeled using Hitran. The spectrum is calculated for 150 Torr and* 21 °C*. The* N_2O *isotopomer absorption lines are too small in magnitude to be seen in this figure but highlighted with blue boxes are the two spectral regions with best candidates for the isotopoloque measurements. A close-up of region 1. is shown in figure 7.2 and of region 2. in figure 7.3.*

In selecting the optimal lines for the isotopologue measurements the following important aspects should be considered: a) The line intensity strength should be large especially for the less abundant isotopologues. b) Minimal overlap with spectroscopic features of other molecules. c) The line absorption of the isotopologues should be of similar magnitude in order to achieve large dynamic range. d) Distance between spectroscopic lines of interest

should be appropriately small. e) Temperature and pressure dependence of the absorption lines minimal.

The strongest absorption lines of N_2O are found in the 4.55 µm mid-infrared optical region, as was illustrated in figure 5.3. Using the Lorentzian line profile eq. (7.1) with temperature 296 K and pressure $p = 150$ Torr the absorption spectrum highlighted in this region was modeled to provide the absorption spectrum in Figure 7.1. Applying the above mentioned selection criteria the spectral regions in figure 7.2 and 7.3 were selected. Table 7.1 summarizes the spectral parameters and temperature dependencies of the absorption lines of these selected regions.

Table 7.1: Spectral line data from HITRAN 2008.

Molecule	ν_{ij}	S_{ij}	γ_{air}	E_i	$d\delta/dT$	$\frac{dS_{ij}/dT}{S_{ij}}$
	cm^{-1}	cm^{-1}/atm	cm^{-1}/atm	cm^{-1}	‰/K	%/K
$^{14}N^{14}N^{16}O$	2187.5336	3.98E-20	0.073	840.2		1.8
$^{14}N^{14}N^{16}O$	2187.4874	3.96E-20	0.073	840.7	*	1.8
$^{14}N^{15}N^{16}O$	2187.9432	3.29E-21	0.080	65.4	12.7	0.6
$^{15}N^{14}N^{16}O$	2187.8460	3.27E-21	0.077	110.1	12.0	0.6
$^{14}N^{14}N^{16}O$	2188.0448	2.60E-21	0.084	1205.9		2.4
$^{14}N^{14}N^{16}O$	2188.1894	2.12E-19	0.070	588.8		1.4
$^{14}N^{14}N^{16}O$	2188.4835	4.19E-20	0.073	820.5		1.8
$^{14}N^{14}N^{16}O$	2188.5275	4.19E-20	0.073	820.1		1.8
$^{14}N^{15}N^{16}O$	2188.6876	3.37E-21	0.079	76.2	12.2	0.6
$^{15}N^{14}N^{16}O$	2188.7560	3.27E-21	0.078	97.2	11.9	0.6
CO	2190.0175	2.88E-19	0.056	299.8		1.0
$^{14}N^{15}N^{16}O$	2195.7618	2.73E-21	0.073	231.2	7.5	0.8
$^{15}N^{14}N^{16}O$	2195.7964	2.20E-21	0.086	22.7	10.9	0.5
$^{14}N^{14}N^{18}O$	2195.9509	1.43E-21	0.073	237.3	7.4	0.8
$^{14}N^{14}N^{16}O$	2196.2095	5.16E-20	0.078	689.6		1.6
$^{14}N^{14}N^{16}O$	2196.2364	5.16E-20	0.078	689.4		1.6
$^{14}N^{15}N^{16}O$	2196.4321	2.59E-21	0.073	251.3	7.2	0.9

For measurements of $^{14}N^{14}N^{18}O$ the absorption line at 2196 cm^{-1} is the only candidate which also offers measurements of ^{15}N isotopomers within a 1 cm^{-1}.

Considering only the isotopomers of N_2O , the spectral region at 2188 cm^{-1} is the most appropriate spectral region. For the $^{14}N^{14}N^{16}O$ measurement

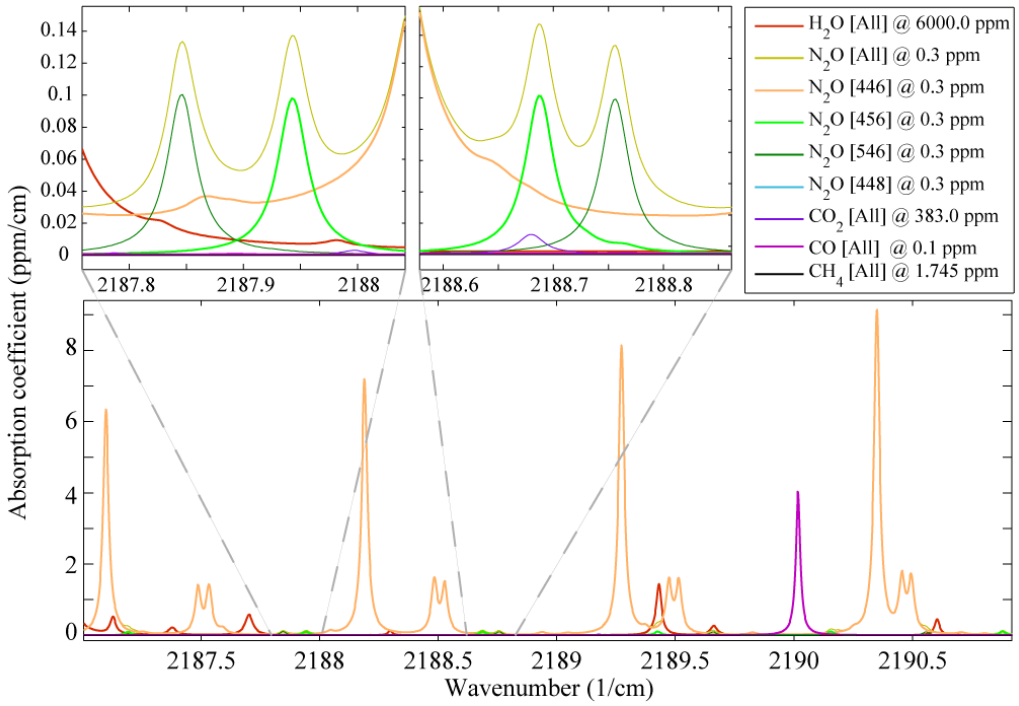

Figure 7.2: Modeled spectrum using Hitran for cell pressure of 150 Torr and temperature 21 °C. *Close-up on the spectral lines in region 1 of figure 7.1.*

three lines are available, differing by an order magnitude each. The weakest would be the best choice since its absorption is comparable to those of the isotopomers. This is advantageous for high concentrations but at low concentrations precision degrades and it may be more advantageous to choose one of the stronger lines. The delta value temperature dependence of $^{14}N^{15}N^{16}O$ for the three line strengths is: 18.7 ‰/K for weak line, 12.7 ‰/K medium strong line and 8.7 ‰/K for the strong line. So in terms of temperature dependence the strong line is most desirable and the weak line is least desirable. The medium strong line is closely spaced to another $^{14}N^{14}N^{16}O$ line of the same strength and this spectral overlap makes the fitting more difficult, which is not the case for the strong line, again making the strong line more desirable. Yet the 7 ppm/cm peak absorption of the strong line could be too strong and saturate the spectrometer. The choice of which line to choose is therefore really dependent on the spectrometer performance and the application at hand.

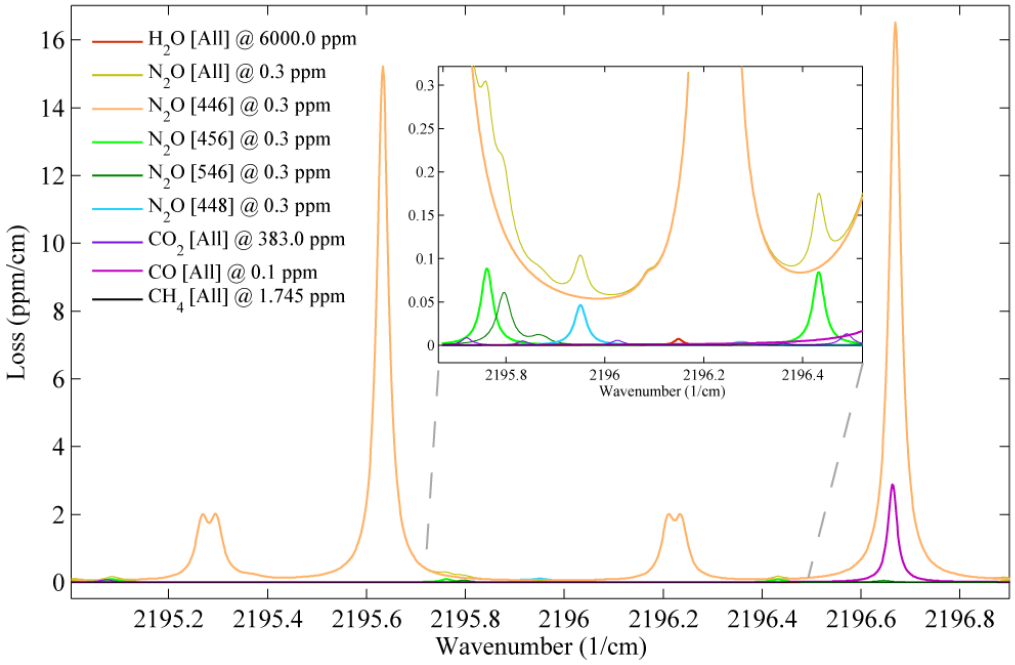

Figure 7.3: Modeled spectrum using Hitran for cell pressure of 150 Torr and temperature 21 °C. *Close-up on the spectral lines in region 2 of figure 7.1.*

7.2 Estimating precision

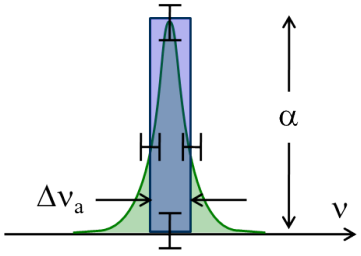

Figure 7.4: To estimate the uncertainty in the absorption peak area, the line profile can be approximated by a box, such that the area is approximated by the line width times the peak hight.

The spectrometer described below measures the molecular concentrations by measuring the absorption coefficient at a discrete number of wavelengths. By making a Galatry fit Galatry [1961] to the measurements the total line absorption is quantified and from this the molecular concentration is found through the line intensity strength.

The precision in the concentration measurement is therefore determined by the precision in simultaneously measuring the absorption coefficient and wavelength and the resolution of these. If the measurement is to be improved through long term averaging, stability of pressure and temperature must be controlled as these alters the spectral line shape.

To estimate the needed precision of the absorption coefficient and wavelength, the absorption line profile can be approximated as a simple box, as depicted in figure 7.4, i.e.

$$n = \frac{1}{S_i}\int_{-\infty}^{\infty}\alpha(\nu)d\nu \cong \frac{\alpha_i \Delta\nu_{\mathrm{a}}}{S_i}. \tag{7.11}$$

where α_i is the total line absorption, $\Delta\nu$ the absorption line width, and S_i the absorption intensity. Using this box approximation the relative concentration uncertainty σ_n can be expressed as

$$\frac{\sigma_n}{n} = \sqrt{\left(\frac{\sigma_\alpha}{\alpha}\right)^2 + \left(\frac{\sigma_{\Delta\nu}}{\Delta\nu}\right)^2} \tag{7.12}$$

where σ_α and $\sigma_{\Delta\nu}$ are the uncertainties of the absorption coefficient and wavelength. The following three subsections will address spectral region and the needed precision in wavelength and absorption coefficient.

7.2.1 Estimating required absorbance precision

The height of an absorption peak scales linearly with concentration. The uncertainty in measuring the absorption peak height is likewise linearly related to the uncertainty in the concentration. The concentration uncertainty may therefore be expressed by the sum of the absorption coefficient uncertainty at peak and baseline.

$$\sigma_n = \sqrt{\sigma_{\alpha_0}^2 + \sigma_{\alpha_{\mathrm{pk}}}^2} \times \frac{n}{\alpha_i}, \tag{7.13}$$

where α_i is the absorption peak height. Assuming that the fractional uncertainty at the peak and baseline are the same and including a total averaging time at the peak and base T_g with a ring down capture rate f_{RD} the fractional concentration uncertainty may be expressed as

$$\frac{\sigma_n}{n} = \sqrt{\frac{2}{f_{\mathrm{rd}}T_g}} \times \frac{\sigma_{\alpha_0}}{\alpha_0} \times \frac{\sqrt{\alpha_0^2 + \alpha_{\mathrm{pk}}^2}}{\alpha_i} \tag{7.14}$$

$$\rightarrow \sqrt{\frac{2}{f_{\mathrm{RD}}T_g}} \times \frac{\sigma_{\alpha_0}}{\alpha_0} \times \begin{cases} 1 & \alpha_i \gg \alpha_0 \\ \sqrt{2}\frac{\alpha_0}{\alpha_i} & \alpha_i \ll \alpha_0 \end{cases} \tag{7.15}$$

Assumed is also that there are no significant drifts so the error average down as $1/\sqrt{N}$, where N is the number of captured ring downs.

The uncertainty in delta value $\delta^{15}\mathrm{N} = \left(\frac{R}{R_{\mathrm{std}}} - 1\right) \times 1000‰$, when considering ratios $R = R_{\mathrm{std}}$ only depends on the uncertainty of the measured ratio $R = [^{15}N]/[^{14}N]$ given by

$$\sigma_{\delta^{15}\mathrm{N}} = \sqrt{\left(\frac{\sigma_{[^{15}N]}}{[^{15}N]}\right)^2 + \left(\frac{\sigma_{[^{14}N]}}{[^{14}N]}\right)^2} \times 1000‰ \tag{7.16}$$

When measuring multiple lines we must take into account that different lines to be sampled and that this may include idle time when tuning from one absorption line to the other. A sequence denote the sampling of a number of groups, where each group is the absorption data collected at a single absorption line. The group time designates the amount of time spent to collect data at a given absorption line and the sequence time will denote the time spent in total for all groups in the sequence including the transition time between groups.

Previous work in the mid-IR by Halmer et al. [2005] demonstrate an empty cavity ring down time of 32 µs, and a shot to shot noise of 0.17% with a 1 m round trip cavity length. Assuming the same mirror quality as in [Halmer et al., 2005][2] but applying half the cavity length (0.5 m) and a shot to shot noise of 0.15%, provides an effective path length of 9000 meters. A precision estimate for the envisioned cavity is shown in table 7.2 calculated on basis of the above equations, applied to an ambient N_2O concentration of 330 ppb. The group and sequence times are determined from typical values of the near-infrared CRDS analyzer.

Table 7.2 shows that with a data point reported every 10 seconds the following precisions is expected, 0.2 ppb for N_2O concentration, 2.8‰ for $\delta^{15}\mathrm{N}$ and with 5 minutes averaging an N_2O precision of 12 ppt and $\delta^{15}\mathrm{N}$ precision of 0.5‰ is predicted.

7.2.2 Estimating the required wavelength precision

In order that the precisions in table 7.2 are achieved the precision in wavelength must match the precision in absorption measurements as stated in equation 7.12.

The necessary wavelength precision depends on the absorption line width, which depends on the gas pressure in the cavity cell. According to the

[2]The mirrors used by Halmer et al. [2005] were purchased from Los Gatos Inc. a manufacturer of ICOS system, and a competitor to Picarro Inc. durinng the time of this work - an ironic coincidence.

Table 7.2: Predicted performance for the analyzer. A sequence of 10 seconds is a assumed. A sequence is set to take 10 seconds.

		N_2O	^{15}NNO	$^{14}N_2^{18}O$	Units
Molecular Absorption	α_i	1.55	0.08	0.05	ppm/cm
Peak Absorption	$\alpha_{\rm pk}$	3.75	2.28	2.25	ppm/cm
Cavity Absorption	α_0	2.2	2.2	2.2	ppm/cm
Shot to Shot	$\frac{\sigma_\alpha}{\alpha}$	0.15%	0.15%	0.15%	
Ring Down Rate/2	$f_{\rm RD}$	150	150	150	RD/sec
Group Time per sequence	T_g	1	3	3	sec/seq
Total Integration Time		5.0	5.0	5.0	min
Group Integration Time		30.0	90.0	90.0	sec
Concentration		330	1.19	1.08	ppb
Min. Detectable (per seq.)		0.113	0.003	0.005	ppb
Min. Detectable (5 min.)		12.14	0.59	0.86	ppt
Isotope δ precision (per seq.)			2.82	4.46	‰
Isotope δ precision (5 min.)			0.52	0.81	‰

HITRAN database the typical air-broadening half widths are around 0.075 cm^{-1} atm^{-1}. Table 7.3 shows the corresponding line widths at different pressures.

For proper comparison with the absorption precision, we must consider the single shot precision of the molecular absorption peak height. Given as for the absorption precision calculation above, a 0.15 % shot to shot noise, an empty cavity absorption of $\alpha_0 = 2.2$ ppm/cm, and a molecular absorption peak height of $\alpha_{pk} = 1.4$ ppm/cm, provides a relative precision of the peak height measurement of 0.45%. The shot to shot precision in wavenumber required to match the corresponding precision in absorption, is shown in table 7.3 at different pressures.

Table 7.3: The typical air-broadening half width is about $0.075\,\mathrm{cm}^{-1}/\mathrm{atm}^{-1}$. *Below are shown the FWHM absorption line widths, at the different pressures. The last two columns list the corresponding 0.45% precision values for these line widths.*

Cavity Pressure	FWHM Line Width		Frequeny Precision 0.45%	
(torr)	(1/cm)	(GHz)	(1/cm)	(MHz)
760	0.150	4.50	0.00068	20.34
200	0.039	1.18	1.8E-04	5.35
140	0.028	0.83	1.2E-04	3.75
100	0.020	0.59	8.9E-05	2.68
50	0.010	0.30	4.5E-05	1.34
25	0.005	0.15	2.2E-05	0.67

It must be emphasized that this is the necessary wavenumber precision of the individual ring downs measured. Even if the laser line width is larger than this required precision, it may still be possible to achieve the required wavenumber precision either by high speed averaging of the laser wavenumber to locate the center frequency or by utilizing the much narrower line width of the passive high finesse cavity. This will be addressed further in the analysis of the laser and cavity in the following sections.

7.2.3 Precision of ring down measurements

One way of improving the performance on the isotope measurements is to increase the concentration. This approach is optically limited by the decrease in the cavity ring down time and transmitted light.

Figure 7.5 shows how the signal to noise ratio of the ring down amplitude is related to the relative ring down noise (shot to shot noise). For each point on the curves in figure 7.5 one thousand cavity decays were simulated according to:

$$V(t) = V_0 \exp^{-t/\tau} + \epsilon(t) \tag{7.17}$$

where V_0 is the ring down amplitude and $\epsilon(t)$ a gaussian pseudo-random noise signal. An exponential least square fit was applied to each simulated decay and the relative standard deviation of the fitted decay times was calculated as the ring down shot to shot noise. It was assumed that the detector samples at 20 MHz.

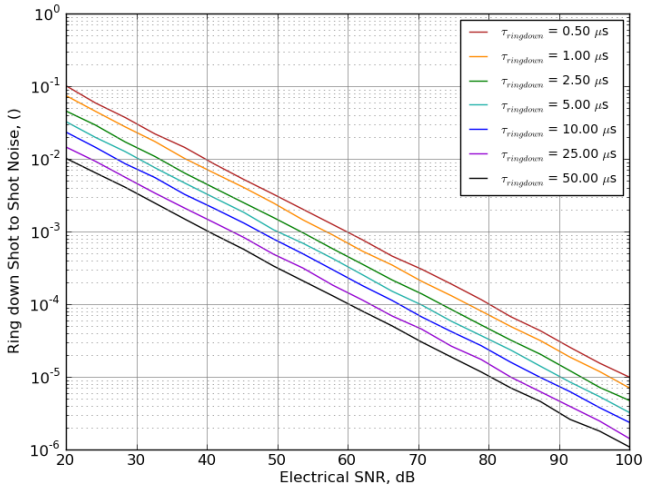

Figure 7.5: Simulation of amplitude noise impact on the fitted cavity ring down noise.

The simulation in figure 7.5 is in good agreement with the expression by van Zee et al. [1999]

$$\frac{\sigma_\alpha}{\alpha} = \frac{2\sigma_{\mathrm{V,tech}}}{V_0}\sqrt{\frac{2\Delta t}{\tau}}. \tag{7.18}$$

Where $\sigma_{\mathrm{V,tech}}$ is the technical noise and Δt the sampling interval. The technical noise $\sigma^2_{\mathrm{V,tech}} = \sigma^2_{\mathrm{digit}} + \sigma^2_{\mathrm{pd}}$ is the quadratic sum of the digital noise $\sigma_{\mathrm{digit}} = V_{\mathrm{d}}/2^N$ (where V_{d} is the dynamic range of the acquisition card and N is the number of bits) and the amplified photodiode noise $\sigma_{\mathrm{pd}} = G \times R_\lambda \times NEP \times \sqrt{B}$ (where G (V/A) is the transimpedance gain, R_λ $(A/W)$the responsivity, NEP $(\mathrm{W}/\sqrt{\mathrm{Hz}})$ is the noise equivalent power, and B (Hz) is the photo-detector bandwidth Motto-Ros et al. [2007].

A change in ring down time from 15 µs to 0.5 micro seconds causes the shot to shot noise to degrade by a factor of five. Assuming that the amplitude of the ring down is unchanged, the precision in N_2O concentration and delta values (table 7.2) also degrade by a factor of five, as these are linearly related according to equation 7.15 and 7.16. This means that the relative precision in concentration scales as $\sqrt{n}$. Performance improves as $\sqrt{n}$ as long as the ring down rate does not change and the ring down trigger level can remain unchanged. The rule of thumb is, that with a ring down time of 5 µs and a signal to noise ratio of 3000 (70 dB) one should expect a shot to shot noise of 0.01%.

The expression in equation (7.18) is suitable for digitization and electrical noise contributions. When these noises are low the shot noise limit is reached where $\sigma_V = \sqrt{2eV_0\Delta f/R_\lambda}$ and the shot to shot noise can be expressed as

$$\frac{\sigma_\alpha}{\alpha} = \sqrt{\frac{\alpha ec}{R_\lambda I_0}} = \sqrt{\frac{\alpha 2e\Delta f}{V_0}}. \tag{7.19}$$

where R_λ is the responsivity of the detector and I_0 is the intensity of light on the detector at the start of the ring down, and Δf the measurement bandwidth [Romanini and Lehmann, 1993; Lehmann, 1996]. So in the shot noise limit the performance only improve by $\sqrt{V_0}$ rather than V_0 as in the above case.

The transmitted intensity may decrease so much that the transmitted amplitude demands a lower threshold. This corresponds to both decreasing the SNR and changing to a corresponding lower ring down in figure 7.5. In section 6.1.2 it was shown that the transmitted power is proportional to $\frac{1}{\alpha}$. So if the sample concentration is so large that a lowering of the threshold is needed, then the relative noise (eq. 7.18) will increase according to $\sqrt{\alpha^3}$ and accordingly as $\sqrt{n^3}$ i.e. the concentration increase will cause impaired performance.

8 Description of final Mid-IR CRDS prototype analyzer

The system consists of two 19 inch rack mountable boxes and an external diaphragm pump. The optics box (height 6U, W × H × D = 37×28×58 cm) contains all optics and driver electronic boards and data acquisition cards. The host box (height 5U, W × H × D = 44 × 23 × 62 cm) contains host computer, laser driver, water chiller, and AOM driver.

8.1 The Host Box

Serves as organizer for the larger necessary components which cannot fit into the optics box. The host box contains the laser controller box, host computer, water chiller, RF circuits for the AOM, and DC power supplies.

Figure 8.1: Picture of the mid infrared cavity ring down N_2O analyzer. On the table are the optics box and to the left the vacuum pump. Under the table the host box is located.

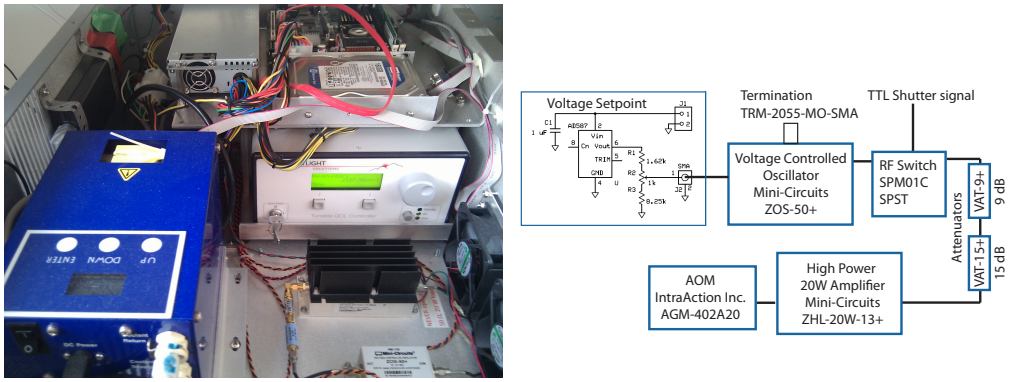

Figure 8.2: Left: Picture of the Host box interior seen from the front. Right: Schematic of the RF circuits.

The host computer board has an 2.4 GHz Intel Core2Duo processor with 1 GB RAM and a 160GB hard disk, running windows XP. The software running the analyzer is written in Python and C++. A 500W DC power supply provides power for the host computer and to the electronics in the optics box. The water chiller is a compact 160W Air-Cooled Liquid Recirculating Chiller (Oasis, Solid State cooling system) and controlled by the host computer through an RS-323 connection.

RF circuit A voltage control is used to set the RF frequency of a voltage controlled oscillator (VOC, a Mini-Circuits ZOS-50+). The RF signal from the VOC goes through a RF Switch (SPM01C SPST, Mid-Atlantic RF Systems Inc.) which is controlled by a TTL signal from the Engine board, in the optics box. The output of the switch is attenuated by 24dB (Mini-Circuits, VAT-15+ and VAT-9+ coupled in series), and amplified with a 20W amplifier (Mini-Circuits, ZHL-20W-13+) from where it is connected to the AOM in the optics box via a coaxial cable.

8.2 The Optics Box

The optics box is built from 3 mm aluminum walls, covered on the inside with 2 cm thick polystyrene insulation plates. The front can be removed in order to access for building and optical alignment and the top is a lid with hinges in the back, which can be turned open, by ca. 105 deg. Electronic boards are mounted under the lid. An optical breadboard (12" by 18") made from aluminum is mounted at the bottom of the box, on shock and vibration absorbing supports. All connections electrical, gas and water are connected

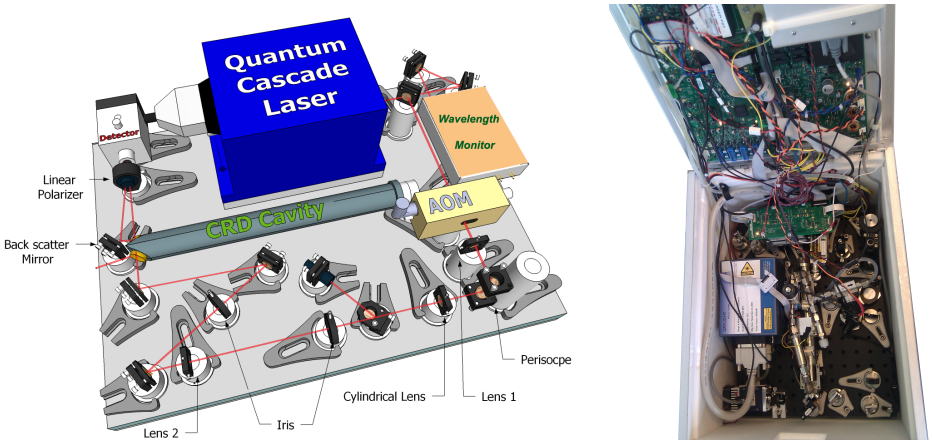

Figure 8.3: Left: Schematic of the optical layout. Right: Picture of the interior of the optics box.

through a panel in the back.

8.2.1 Thermal Control system

Under the optics breadboard is mounted a commercial cold plate through which cooling water flows, from the water chiller. This serves as to provide general cooling of the optics box. The cooling water is further connected in series through the AOM, Laser and cold plate cooler to provide cooling for the heat dissipated within these. The water chiller is set at 16 °C . The water temperature is stable to within 0.2 °C . To stabilize temperature further a cold plate cooler (Thermo electric cooling (TEC) assembly with a peltier element, grill, and fan) mounted under the lid in the optics box, circulates the air inside the optics box. A digital PID loop locks the temperature measured in the wavelength monitor at 21 °C to within 0.001 °C .

8.2.2 Optical Elements

Unless otherwise stated the optical parts are mounted on New Focus 1 inch pedestal posts for stability. All mirrors are 0.5" diameter with protected gold coatings, mounted on New Focus tiny mirror mounts.

The laser is a External cavity Quantum Cascade laser (Daylight Solutions Inc., 21045-MHF-) with >100mW output power, 30MHz line width, and 80 cm^{-1} tuning range around 2200 cm^{-1}. The laser is mounted to the breadboard on top of a 1" aluminum block giving an initial beam height of 2.5 inches.

Beam paths: Emerging from the laser, the beam is split in two beams by a 99% high reflective coating on a fused silica substrate mounted at 45° to the beam. The transmitted beam is directed into the wavelength monitor by two mirrors. The reflected beam goes toward the ring down cavity.

From the beam splitter (BS) the beam passes the following in sequence: At 8" from BS an Germanium crystal AOM (IntraAction Corp. model AGM-402A20) run with a frequency of 40MHz and having a divergence angle 58.2 mrad = 3.33 degrees to the first order beam. At 9.5" from BS a Spherical Lens (ZnSe, f=196 mm at 4.55 µm, ROC=281.2 mm, Diameter=8mm), and at 12" from BS a periscope which lowers the beam height to 1.5" and changes Polarization to vertical.

In distances from the periscope the beam passes at 2" a cylindrical Lens (ZnSe, f=225 at 4.55 µm, ROC = 315.9mm, Diameter = 8mm), at 6" from periscope an adjustable Iris to block all other than the 1 order beam from the AOM. At 10" from periscope a spherical Lens (ZnSe, f=147mm at 4.55 µm, ROC=209.9mm, Diameter = 8 mm). At 11", 18" and 25" from periscope mirrors are reflected upon. The first and last of these three mirrors are conveniently used for aligning the beam into the cavity located at 26" from the periscope. The beam transmitted through the cavity is passed through a linear polarizer (ThorLabs, LPMIR050) and detected with a DC coupled MCT detector (Vigo, PVI-3TE-6) having a 20MHz bandwidth. A mirror is located at the cavity output mirror and oriented at 90° to this, facing the detector. This mirror directs light which is backscattered in the cavity onto the same detector lowering the ring down noise. All the ZnSe lenses have surface qualities of 40/20 scratch/dig and are AR coated for 4.2 µm to 4.9 µm.

The cavity has three mirrors which are glued to a stainless steel body. The body is made from a 1 inch diameter rod with a 88° cut at one end where the input and output coupling mirrors are glued onto the cavity. At the other end of the rod a high reflective concave mirror is mounted to the body via a piezo electric (PZT) assembly. The PZT assembly consists of a Zerodur membrane which constrains the motion of the piezoelectric bender. The mirror is glued onto the center of the Zerodur structure and this is glued onto a stainless steel spacer (a short hollow tube) which is glued onto the cavity body. The body is hollowed by drilling to provide the beam path for the laser. The cavity round trip distance is ca. 48.5 cm. The input and output coupling mirrors have flat surfaces with AR coatings toward the outside and HR toward the inside. The concave mirror has a 1m ROC. The mirrors manufactured by LohnStar Inc. have Silicon substrates and their

effective reflectivity is 99.989%.

The wavelegnth monitor The CuW baseplate is mounted onto an stainless steel plate with stainless steel screw fastened clamps. The stainless steel plate is screwed onto a pedestal post. A stainless steel cover shields the wavelength monitor optics from air temperature fluctuation in the optics box. Custom amplifier boards with AD converters are soldered directly onto the wavelength monitor detectors to lower pickup noise. These two boards are connected to the wavelength monitor engine board which is mounted over the wavelength monitor and connected to the mother board under the lid via a 16 pin ribbon-wire.

8.2.3 Electronic elements

Except for the wavelength monitor board and a pressure sensor board, the remaining electronic boards of the optics box are mounted under the lid. These are the TEC controller for the ring down detector (Vigo, STCC-04), an optional pre-amplifier also for the ring down detector, and a humidity sensor (Toradex Inc., Oak Sensor) connected to the host computer by USB. A custom PZT driver board for the laser providing 0 V – 100 V with a 16 bit resolution.

The last two boards are identical to those used in the Picarro G2000 platform, which are custom modified for this analyzer.

The Logic board operates as a high speed control unit, including data acquisition and processing. This board is connected to the host computer by USB. An 500 MHz FPGA card (Xilinx, Spartan XC3S1000) controls temperature PID loops, pressure, laser, and transfer of acquired data to the Host computer. The logic board provides shutter signal for the laser and AOM and also collects the ring down signals at either 10 MHz or 25 MHz by choice. A Floating-Point Digital Signal Processor (Texas instruments, TMS320C6713B-300) uses the measured ring down signal to calculate the decay rate for each individual ring downs. The logic board also controls the other boards, which are connected by 8, 16 and 32 bin ribbon cables.

The Engine Board provides power and control signals for the cavity piezo (0V-200V), input and output sample valves, and thermo electric cooler. All are controlled with 16 bit resolution.

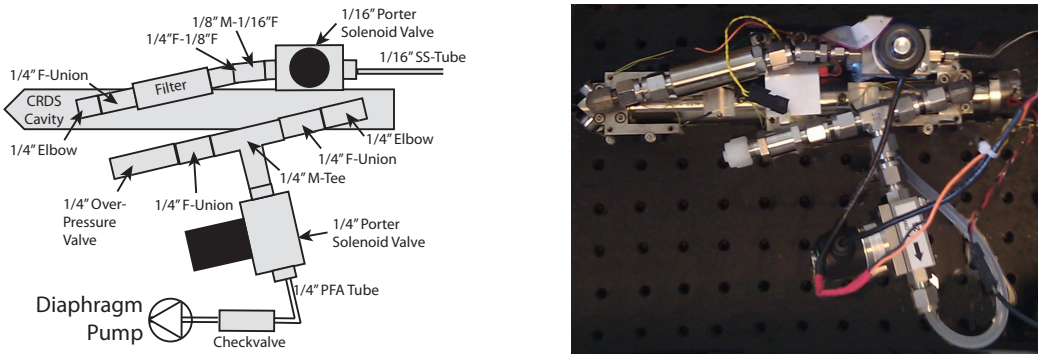

Figure 8.4: Configuration of the gas delivery and vacuum system.

8.2.4 Vacuum system

Samples are introduced to the analyzer through a 1/16" stainless steel tubing. This is connected to a 1/16" solenoid valve (Porter) controlling the injection flow rate. From this the sample passes a particle filter (Mykrolis, WG2FT1SS2) Leaving less than 0.03 particle/liter that are greater than 0.01 µm. The sample enters the optical cavity at the end of the two flat mirrors. The pressure is measured with a pressure sensor (GE, NPC-1220), and thermistors mounted on the outside of the cavity body provide temperature measurements. The gas exits the cavity at the Piezo end of the cavity onto a male Swagelok Tee provide which is connected to an overpressure valve to prevent more than 10 psi overpressure. The last arm of the tee is connected to a 1/4" solenoid valve (Porter) which is connected to a four head diaphragm pump (KNF, N 84.4 ANDC) through a directional flow valve. This provides pressure control with a typical precision of 0.02 torr, at 200 torr.

8.2.5 Software and data treatment

The cavity ring down profile is fitted by the fast exponential fitting algorithm byHalmer et al. [2004], and optionally followed by one or multiple iterations of the Levenberg-Marquardt algorithm. For the multi line spectral Galatry fitting algorithm by Ouyang and Varghese [1989] is applied, implemented in the Picarro software. A special mode for the analyzer called *FSR mode hopping* was created for this spectrometer applying broad laser frequency tuning, sweeping several cavity FSR to collect spectral absorption data. Most of the software was based upon that of the Picarro near-infrared analyzers.

9 Analysis of components in the system

9.1 Factors that constrain the design

Unlike the near-infrared optics – applied for telecommunication, mid-infrared technology is far less advanced. In particular polarization maintaining fibers and passive optical isolators are presently not available. The lack of polarization maintaining fibers rules out the possibility of distributing the system into individual submodules. This requires that all the optics are placed on a common robust baseplate in order to preserve beam alignment.

Passive optical isolators for mid-ir are not commercially available and are only demonstrated with low performance. Quantum Cascade lasers are in general very sensitive to optical feedback, making optical isolation a crucial desire. An Acousto Optical Modulator (AOM) was chosen in order to comply with this need as well as fulfill the need for a sub-microsecond optical on/off switch. In future instrumentation the QCL may be exchanged with DFB lasers which provide fast switching. .

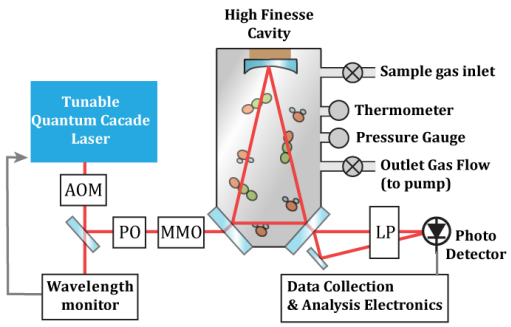

Figure 9.1: Diagram of the analyzer components analyzed in this chapter. Abbreviations are explained in the text.

A diagram of the components in the system is shown in figure 9.1, the key parts being: A Quantum Cascade Laser, a wavelength monitor, optical mode matching optics (MMO), a polarization controller (PO), an acousto optic modulator (AOM), a high finesse optical cavity, a back scatter mirror, a linear polarizer, and a ring down photo detector. Analyses of these components will be given in the following sections.

The analyzer was developed in several steps. First a basic table top setup using regular optical mounts and open cavity and no wavelength monitor. Next mirrors were mounted on a cavity body and the system was integrated in a temperature controlled environment. The wavelength monitor was implemented and the system was integrated with the electronics from the NIR Picarro products. Then steps toward building the system, where all optics would be glued to a compact rugged base plate, was attempted but this was eventually abandoned. And then finally the design described in the previous chapter was settled. Pictures of the different stages are shown in figure 9.2

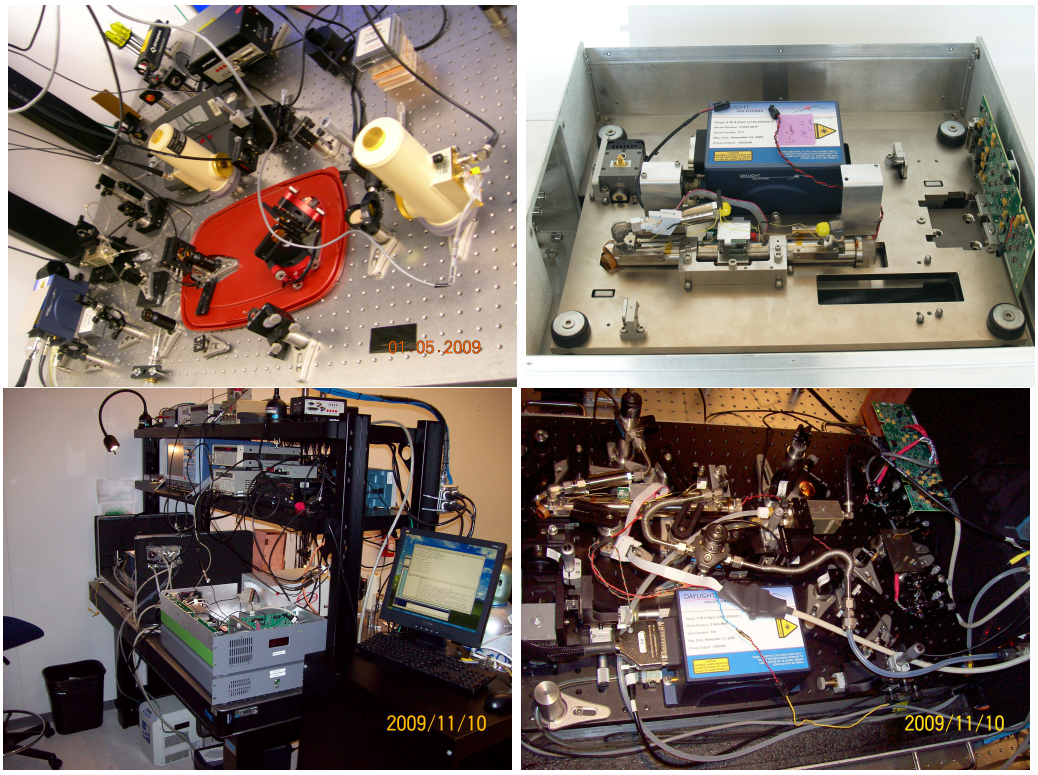

Figure 9.2: TOP LEFT: Basic setup using free standing mirror optics and liquid nitrogen cooled detectors. TOP RIGHT: Attempted solution for gluing all optics onto a single rugged base plate. BOTTOM: System in temperature isolated environment including wavelength monitor and integration with NIR analyzer electronics.

9.2 Laser performance

In the characterization of the laser: the power spectrum, frequency noise, tunability and accuracy were examined.

The laser is an External Cavity - Quantum Cascade Laser (EC-QCL) with a frequency selective optical readout provided by a diffraction grating in a Littrow configuration as schematically shown in figure 9.3.

The laser frequency can be changed in three different ways. Through the QCL chip by controlling frequency and temperature and through the grating angle. The laser from Daylight Solutions has three ways of controlling the laser frequency: the coarse tuning with the stepper motor regulated by the laser controller, a piezo (PZT) fine tuning which is controlled by a 0 V to 100 V input through a Triax connection in the laser house and an AC-current control provided through a SMA connection also in the laser house. The two first controls change the laser frequency by changing the grating angle. The AC-current is a modulation input, which has limited operation as to AC modulate the laser current.

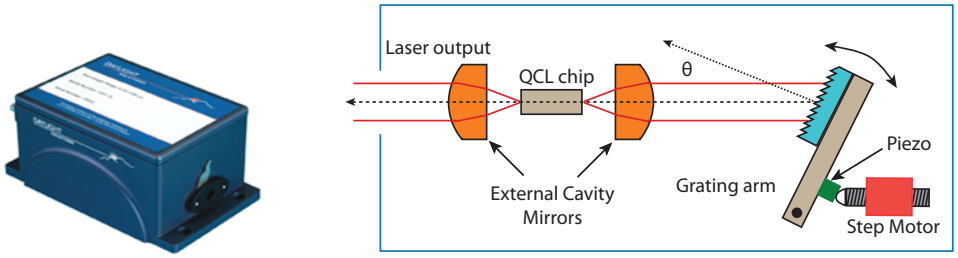

Figure 9.3: LEFT: a picture of the laser. RIGHT: Diagram of the internal laser configuration, with a linear external cavity and the optical grating for tuning the laser frequency, either by stepper motor or piezo.

9.2.1 Laser power spectrum

Figure 9.4 shows the typical tunability and power spectrum of the Quantum Cascade laser (QCL) manufactured by Daylight Solutions Inc. Using the laser controller the current was set at a designated value and then the coarse tuning was used to trace the power spectrum. The laser power was measured using a Ophir power meter. In june 2009 the laser was turned around the manufacturer for realignment because the laser had started to mode hop see section 9.2.2. When returned the laser output power was 50% higher, and tuning range reduced. Figure 9.4 resembles a typical power spectrum.

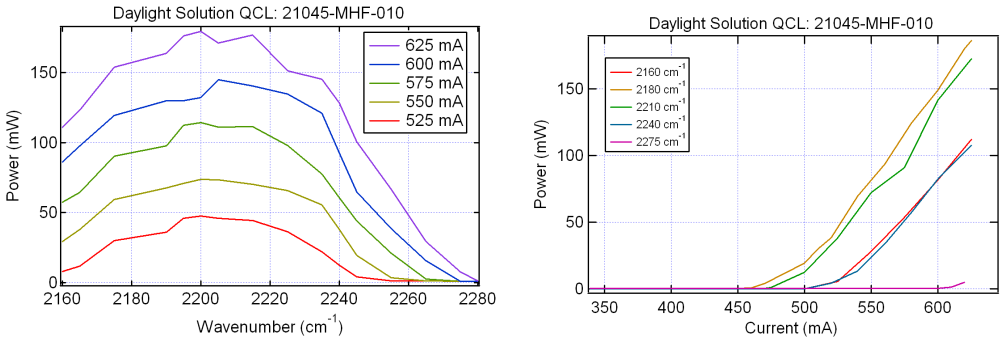

Figure 9.4: Power spectrum for different current settings of the 21045-MHF-010 laser when received in Jan. 2009. The laser has very broad tuning ability of more than 100 cm^{-1}.

9.2.2 Laser Mode Hopping

As mentioned in the previous section occurrence of mode hopping in the laser 21045-MHF-010 was detected. Rather than using a ophir thermal power sensor the beam was attenuated using one or more pieces of fused silica wedges and using a MCT photodetector cooled with liquid nitrogen. A function generator using a sinusoidal sweep function was amplified to make a 0 to 100 Volt amplitude using a ThorLabs PZT driver. The Function generator and the MCT detector were connected to an oscilloscope. Figure 9.5 shows the output power as the frequency is tuned using the pzt. A 100 V sweep corresponds to ca. 1 (1/cm).

The laser has an internal power fluctuation which originates from its own cavity. In figure 9.5 this fringe pattern is undisturbed for the low 530 mA current setting, while discontinuities occur for higher currents 540 mA and 560 mA. The discontinuity corresponds to the laser suddenly changing to a different frequency. Also the pzt voltage at which the discontinuity occurs depend on the direction of the sweep. This discontinuous switching back and forth in frequency is the common characteristic of mode hopping.

By programming the laser controller, the laser grating can be made to sweep the frequency continuously over the full tuning range. The controller provides a TTL signal to indicate the start and stop time of the sweep. This was used to convert the oscilloscope time into a wavenumber scale. In figure 9.6 this method was used to capture the power spectrum before and after the laser was realigned by the manufacturer.

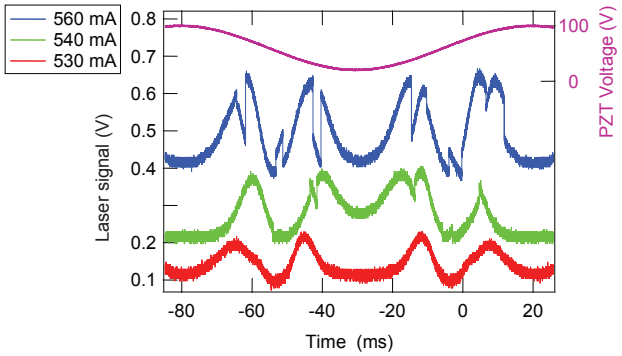

Figure 9.5: Tuning the laser frequency using the pzt input. Imperfect alignment causes the laser to have output power fluctuations due to internal etaloning. Applying 530 mA current to the QCL ensures that a clean etalon fringe is traced. For a QCL current of 540 mA and 560 mA sudden jumps in the fringe pattern occurs. The jumps get stronger for higher currents. The jumps change timing depending on the sweep direction.

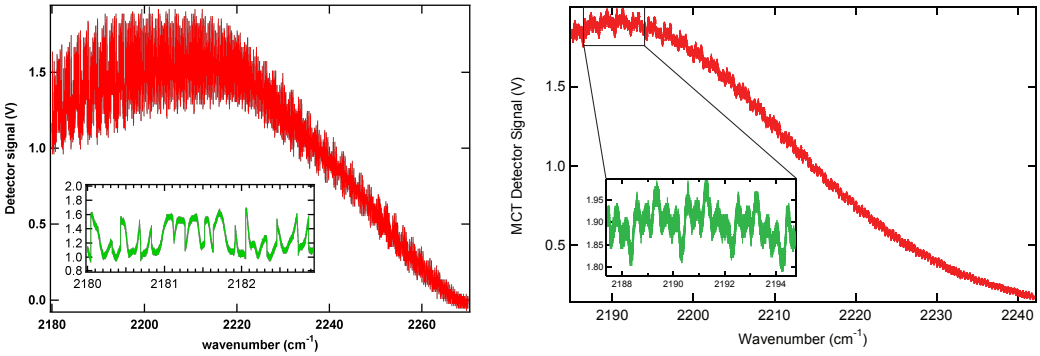

Figure 9.6: Laser output Left: with mode hopping before realignment, Right: After realignment without mode hopping. Notice that the laser etalon fringe amplitude is much smaller after the realignment, and discontinuities are no longer present.

9.2.3 Laser frequency noise

The laser line width is of great importance to how well the laser can be coupled to the high finesse cavity, see section 6.1.

To diagnose the laser line width the setup in figure 9.7 was used. Changes in laser frequency were converted by the ZnSe etalon, into voltage changes in the MCT 2 detector. In order to separate laser intensity fluctuations from frequency fluctuations a reference intensity has to be measured which was done by the MCT 1 detector.

Emerging from the laser a half–wave plate rotates the polarization from P to S. The beam is then split by a Fused Silica wedge. The transmission through the fused silica wedge is much higher than the reflected power so another Fused Silica wedged provides additional attenuation. The reflected beam goes through a 3 mm ZnSe etalon corresponding to a 20 GHz FSR.

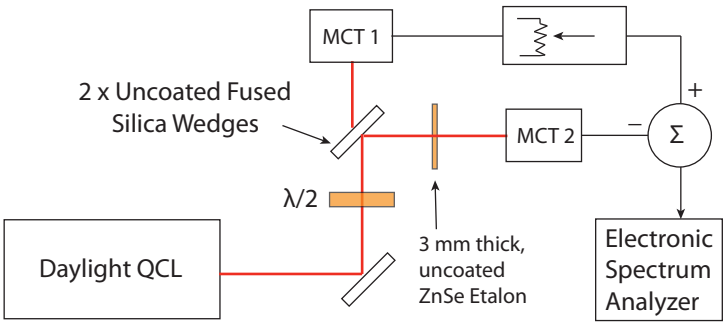

Figure 9.7: Setup for the measurement of the laser frequency noise presented in figure 9.8.

The QCL was tuned to 2220.0 cm^{-1} and the current set at maximum value. To minimize the FM to AM coupling, the laser was tuned to a local power peak using the pzt control. By changing the Etalon angle the signal was adjusted to half the midpoint of the fringe side. The signals were adjusted to equal using a SRS preamplifier, and the difference was passed to an electronic spectrum analyzer (ESA). At low frequencies significant pickup noise is present. So to distinguish this from the laser noise the ESA measurement was made with the laser *on* and laser *off* (baseline). The setup does not completely eliminate intensity noise and should be considered an upper limit.

The voltage excursion is converted to frequency as follows: The etalon fringe can be expressed as a sinusoid $V(\nu) = V_A \sin(\frac{2\pi\nu}{\mathrm{FSR_E}})$, and by Taylor expansion at 0 giving the following relation

$$\Delta\nu = \frac{\mathrm{FSR_E}}{V_A 2\pi}\Delta V \tag{9.1}$$

where V_A is the etalon fringe amplitude and $\Delta\nu$ is the excursion in frequency and ΔV excursion in detector voltage signal. The Etalon has $\mathrm{FSR}_E = 20\,\mathrm{GHz}$ and the etalon fringe amplitude is $V_A = 0.375\,\mathrm{Vpk}$. The strongest noise is contributed at 200 Hz with a signal power of $P_s = -54.6\,\mathrm{dBm}$. This corresponds to a signal amplitude of $\Delta V = 2 \times \sqrt{0.1 \times 10^{P_s/10}} = 3.75 \times 10^{-4}$ Vpp. So according to equation (9.1) the frequency excursion is 6.46 MHz. Following this calculation the frequency excursion plots in figure 9.8 were constructed from the ESA measurements.

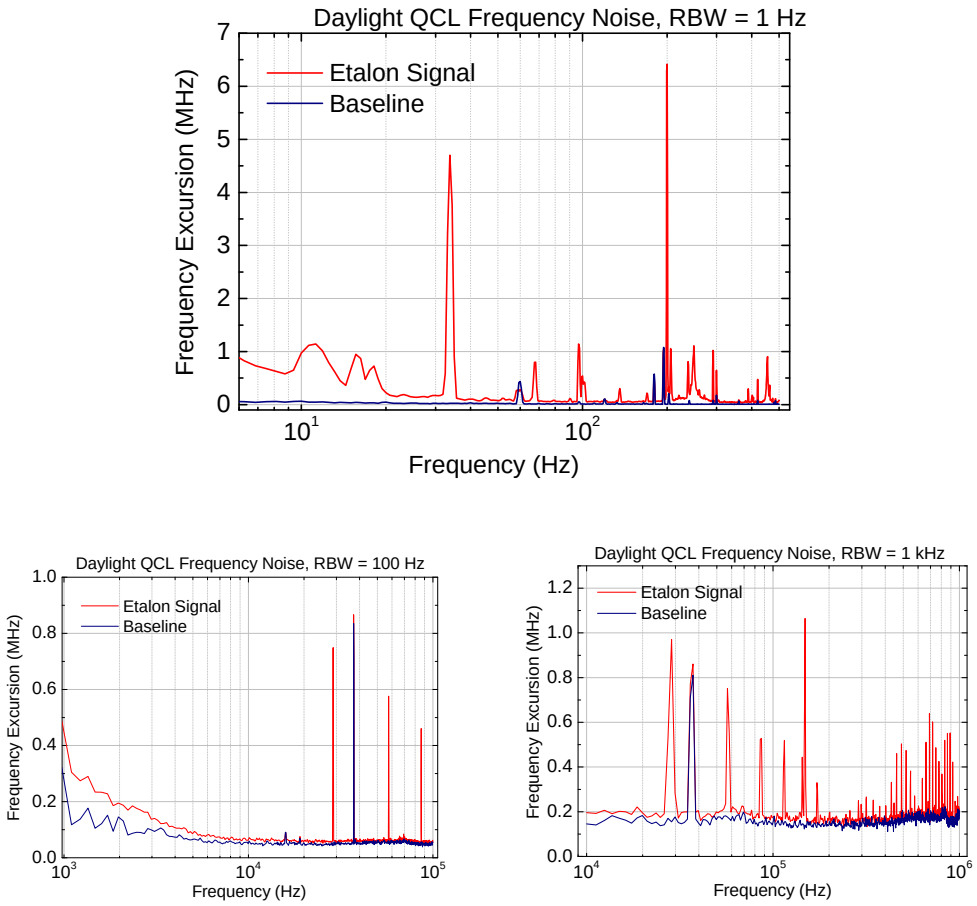

Figure 9.8: Low frequency noise spectrum taken with the setup shown in figure 9.7. Notice the strong noise signal at 30 Hz and 200 Hz, the magnitude of the higher frequency is much weaker.

It can be seen that there are strong peaks at 33 Hz and its higher harmonics. The strongest noise contribution is contributed from the 200 Hz

frequency, which is clearly not a pickup in the detectors. Adding up the peak contributions gives a line width of ca. 15 MHz depending on how these are added, which is comparable to the 30 MHz line width specified by the vendor.

9.2.3.1 Tuning ability of the laser

The scheme for collecting data points for spectral fitting depends on the abilities of the laser frequency tuning control. In the Picarro near-infrared system a feedback loop to the DFB laser current is used to lock the laser frequency to the cavity mode. In order that this scheme is applicable with the QCL, the laser must have suitable tuning response characteristics. To examine this, a step function was applied to the laser pzt control and the etalon transmission was recorded. The laser signal showed a distinct undulated damped oscillator response, shown in figure 9.9. The ringing cannot be assigned to the piezo driver as this has a response time of only 10 µs, also shown in figure 9.9. The damping signal has a carrier frequency of ca. 240 Hz which coincides with the 200 Hz frequency noise signal in figure 9.8. This supports that the primary noise of the laser at 200 Hz may originate from mechanical resonances of the laser grating arm.

The 0 to 100 Volt PZT input signal provides a laser tuning range of 2.3 cm^{-1}. With a full 16 bit resolution at this voltage range will correspond to a 1.1 MHz digital resolution.

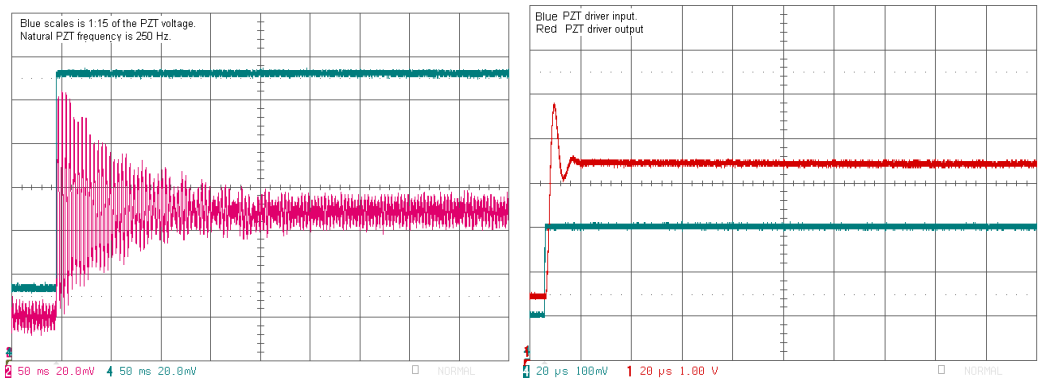

Figure 9.9: Response of the laser to a step function change in the laser piezo voltage.

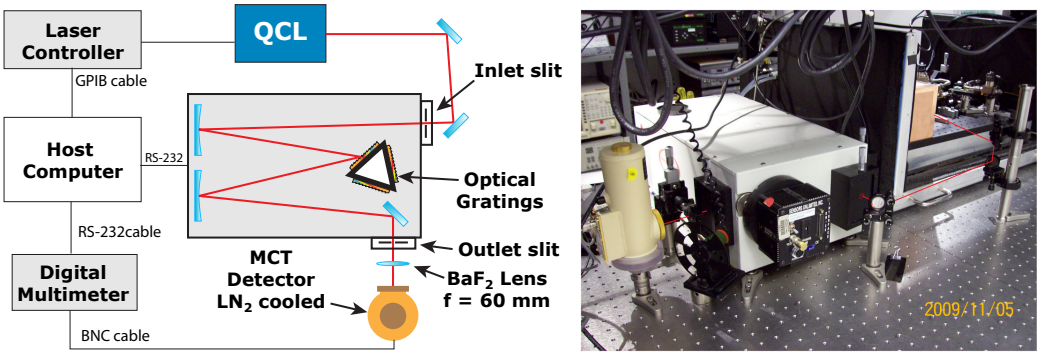

Figure 9.10: Interferometer setup to study the coarse tunning ability of the laser.

9.2.4 Accuracy of the laser coarse setting

The laser has an internal spectrometer, which is used to convert the laser controller coarse tuning input in order to perform accurate tuning of the laser grating. The linearity and reproducibility of the coarse tuning is of great importance to how the system can be booted and how the laser can be broadly tuned to absorption species several wavenumbers apart.

To quantify the precision of the laser coarse tuning a 0.5 m – Acton SpectraPro-500i grating monochromator was used for comparison. A schematic and picture of the setup is shown in figure 9.10. The grating was equipped with three gratings 300, 600, 1200 g/mm of which only the 300 g/mm grating could be used for the 4.5 µm wavelength.

A co-aligned visible diode laser, was used to make the initial alignment through the monochromator. The grating provided only very weak reflection, so a chopper was used to identify the beam on the detector. The input and output slit was adjusted in order to optimize the transmitted intensity. The resolving power of the monochromator is proportional to the number of grooves illuminated on the grating. To utilize this, the input slit was fully opened while the output slit was closed as much as the detector signal would allow. To determine the laser signal on the detector, a chopper was used to on/off intensity on the oscilloscope. Once aligned the laser was swept across the monochromator transmission line using the laser PZT, showing an approximate line width of 0.15 cm^{-1} much broader than the laser line width and tuning ability. I.e. the monochromator must be applied by scanning the laser across the monochromator transmission line. A python program was written to control the laser, monochromator, and measuring the transmitted laser intensity using an Agilent 34401A, 6.5 Digit Multimeter. The program instructs the monochromator to a set of wavelengths. For each set point

of the monochromator, the laser is tuned 3 nm in steps of 0.02 nm across the transmission line of the monochromator, recording the profile using the multimeter. A least squares gaussian fit is made to the transmission profile from which the monochrometor transmission peak position is determined in terms of laser set point. Figure 9.11 shows the monochromator set point versus laser determined set point as determined from the scan.

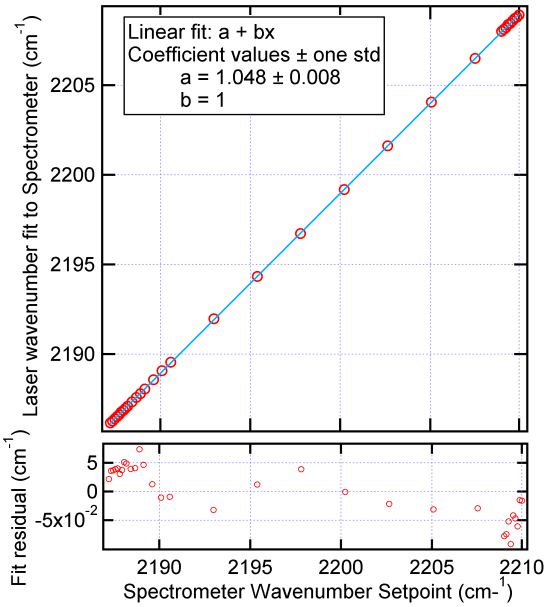

Figure 9.11: Tuning agreement between the internal spectrometer of the laser and the Acton SpectraPro-500i.

In figure 9.11 a linear fit through the monochromator set point versus corresponding laser value is made keeping the slope fixed at 1. By keeping the slope fixed, an offset of 1.05 cm^{-1} is apparent and over the 20 cm^{-1} the frequency diverges by 0.1 cm^{-1}.

The Laser specification claims unidirectional accuary of $\pm 0.5\,cm^{-1}$ with a unidirectional repeatability of 0.02 cm^{-1}, which is confirmed to within the accuracy of the monochromator being ± 0.2 nm and ± 0.05 nm, corresponding to $\pm 0.1\,cm^{-1}$ and $\pm 0.024\,cm^{-1}$. The laser tuning repeatability is only indirectly confirmed in terms the created traces. For a real repeatability measurement, the above measurement should have been repeated enough to provide sufficient statistics. However for this, a more accurate monochromator would have been required. For the analyzer design the important conclusion is that the laser coarse setting is sufficiently accurate to hit within one half of the

analyzer wavelength monitor as will be treated in the following section.

9.2.5 Beam shape properties

In order to achieve an efficient coupling to an external cavity, the properties of the laser beam shape has to be of high quality.

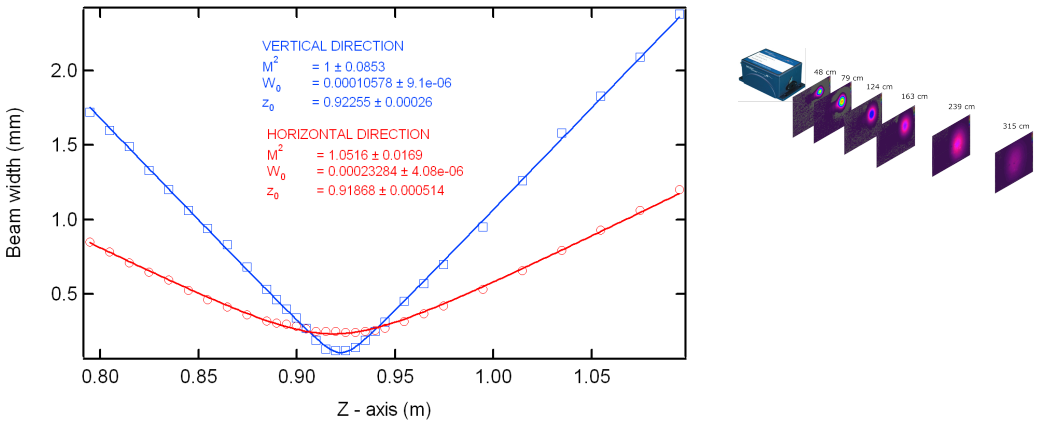

Figure 9.12: Results from razor blade measurements of the laser beam profile behind a 12.7cm focal lens. Solid curves are the curve fits of beam radius expression eq. 9.2, provided by the shown fitting parameters given in meters. Right: A Spiricon pyrocam III infrared camera was used to take pictures of the beam profile at several distances

Measurement of the beam profile was performed by razor blade measurements. A ZnSe lens of focal length 12.7 cm was placed 77.47 cm from the laser head. At 117 cm from the laser head a 1 inch diameter ZnSe lens of 5 cm focal length was placed, focusing the beam onto an optical power-meter located at 122 cm from the laser. A two axis linear translation stage with microtometers of 0.01 mm resolution was used to perform razor blade measurements by finding the 10% - 90% clipping diameter D_c from which the electrical field gaussian beam radius is calculated as $w = 0.7805 D_c$ according to Siegman et al. [1991]. The beam radius was measurmed in both horizontal and vertical direction at numerous distances behind the first ZnSe lens, results shown in figure 9.12. From this set of laser distances and beam radii a least square fit was made to the beam radius expression

$$w(z) = \sqrt{W_0^2 + \left(M^2 \frac{\lambda}{\pi W_0} (z - z_0) \right)^2} \tag{9.2}$$

finding the beam quality factor M^2, the beam waist w_0 and position of waist z_0 along the beam path parameterized by z having its origin at the output

of the laser Siegman [1990]. The fitted values for the horizontal and vertical beam profile of the 21045-MHF-010 laser are shown in figure 9.12.

The beam is elliptical and the beam quality parameter M^2 is close to one for both axes and Gaussian beam propagation is expected. Using ABCD matrix calculations, the beam width may be propagated back through the lens to provide the beam parameters emerging from the laser. For the horizontal axis the waist radius is 0.6654 mm, located 41.7 cm away from the laser with a Rayleigh range of 7.598 cm. For the vertical axis the waist radius is 0.4238 mm, located 14.25 cm away from the laser with a Rayleigh range of 3.082 cm.

9.3 The optical cavity

A ring-shaped cavity configuration shown in figure 9.13 has been used in this work. It was developed for mode cleaning of high power lasers for application in laser interferometer gravitational wave observations Willke et al. [1998]. This design has several advantages in comparison to a linear cavity. The following advantages were noted by Zare et al. [1999].

The greatest advantage of the ring shaped cavity is that the 45° input angle highly reduces optical feedback to the laser. As the line width cavity is typically much narrower than that of the laser only a small fraction of the incident light is injected into the cavity, while the majority is reflected by the input mirror. In linear cavities this will be reflected back toward the laser causing increased noise in frequency tuning, mode oscillation stability and power output. "The excess laser noise leads in turn to unstable laser-resonator coupling, increased baseline noise, and reduced absolute sensitivity for absorption measurement"Zare et al. [1999].

The ring resonator has traveling wave boundary conditions, which provides a uniform light intensity in the cavity. A linear cavity has standing wave boundary condition, providing a non-uniform laser power which may cause sample burning and non-uniform sample excitations. These effects are greatly reduced in the ring resonator.

The ring resonator also provides mode separation of S (Sagittal) and P (Parallel) polarization. According to the Fresnel equations S-polarized light has a π-phase shift at any reflection, while the P-polarization has π phase shift only for angles of incidence greater than Brewster's[1] angle and zero phase shift for smaller angles of incidence. The phase difference of the two polarizations in one cavity round trip is therefore $\phi_P - \phi_S = \pi$, when the

[1]Brewster's angle: $\theta_B = \arctan(n_t/n_i) \geq 45°$ where $n_t < n_i$ are the index of refractions of the incident medium i and transmitted medium t.

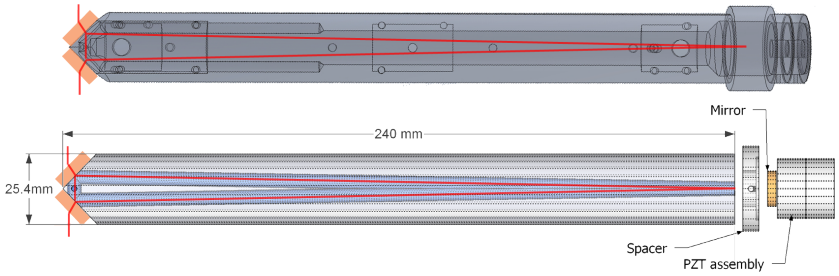

Figure 9.13: TOP: Design of the optical cavity applied in this work and in the standard Picaro G1000 products. The two mirrors to the left are flat mirrors for input and output coupling. They have anti reflective coatings on surface toward outside of cavity and High reflective coatings on the surface toward the inside of the cavity. The mirror to the right is a spherical concave mirror with a 1 meter radius of curvature. BOTTOM: Design with reduced internal volume advantageous for small samples. This design was not conducted in this work. The optical round trip distance is ca. 48 cm, depending on the choice of spacer.

angles of incidence are smaller than Brewster's angle. Resonance frequency of the two polarizations are therefore shifted by a half free spectral range with respect to each other, and such that resonance of the P-polarization is located midway between any two contiguous resonances of the S-polarization and vice versa Saraf et al. [2007]. When including the HR coatings of the phase shift difference, may be different than π and thus the S-polarization need not be exactly shifted by one FSR. The reflection of the two polarizations differ also according to the Fresnel equations Hecht [2002]. At the flat mirrors at the near 45° angle of incidence the reflection of the S-polarization is significantly higher than for the P-polarization. The highly reflective coatings of the mirrors are therefore optimized for the S-polarization at the given angle of incidence.

The difference in mirror reflectivity for the two polarizations transfer into the availability of a high and low Finesse cavity within the same configuration. This provides the ability to address strong and weak spectral lines with the same cavity by having a detection system distinguishing the S and P polarization. This can be achieved using two detectors after the cavity where a polarizing beam splitter is used to split the polarizations onto each detector.

If any disadvantage to the ring resonator, it is that more mirrors are required than in a linear cavity and it is more difficult to align.

Table 9.1: Calculated properties of the designed cavity for mirrors providing 5 µs *and 10* µs *ring down times with a cavity roundtrip distance of 0.49 m.*

Cavity ring down time	10.0	5.0	µs
Effective path length	6000	3000	m
Average Mirror Reflectivity	99.995%	99.989%	-
Cavity FSR	612	612	MHz
Cavity Finesse	38468	19234	-
Cavity Linewidth	16	32	kHz

9.3.1 Cavity properties

In order that an empty cavity ring down time of 10 µs is achieved, it is required that in the total round trip losses (including mirror transmission) are smaller than 160 ppm for a roundtrip distance of 48.6 cm. Characteristic properties of such a cavity is shown in table 9.1.

Cavity Clipping For the envisioned application to ice core samples (or other biologial samples) the inside cavity volume is crucial to the needed amount of sample. This provides a desire to make the cavity as small as possible. A proposal for such a cavity is shown in figure 9.13. The minimization of the internal volume is dependent on design but ultimately limited by the beam diameter. Loss due to clipping from an aperture (the cavity body) is given by Siegman [1986] p. 666:

$$\text{Clipping Loss } = e^{-\frac{2a^2}{w^2}} \tag{9.3}$$

where a is the aperture radius and w the electrical beam width. For simplicity of production and adaptability with available building tools it was chosen to use the stainless steel cavity body used in the near-infrared products by Picarro. For this cavity the minimum internal aperture was to be 4.5 mm diameter. The beam diameter for the eigenmode of the cavity of 48 cm roundtrip length and a mirror of 1 m radius of curvature is $w = \sqrt{\lambda L/\pi\sqrt{R/L}} = 0.85$mm using p. 499 Milonni and Eberly [1988]. Using eq. 9.3 the clipping losses are found to be 0.9 ppm which is insignificant compared to the total losses of 160 ppm for the 10 µs CRDT requirement.

9.3.2 Transverse Electrical Mode structure

A common struggle for cavity ring down systems, is mode beating with higher order transverse electromagnetic modes (TEM_{mn}) [Huang and Lehmann,

2007]. The choice of cavity length and radius of curvature chosen for the concave mirror governs the structure of the higher order modes. This choice is crucial to the performance, as seen in the following considerations.

The mode structure of the higher order transverse electrical modes of a linear cavity can be calculated from the formula by Kogelnik and Li [1966], which is widely referenced in optical literature. However, the three mirror cavity has odd reflection symmetry in the parallel plane. This means that for TEM_{mn} modes, where the parallel mode m is an odd number, has to travel around the cavity twice in order that the polarizations of the modes match up again. The round trip phase requirement can be written as [Barriga et al., 2005]:

$$\frac{L}{\lambda} - 2(m+n+1)\arctan\left(-\sqrt{g}\right) - \pi\frac{((1-(-1)^m)}{2} = 2\pi q \qquad (9.4)$$

where q, m, n are positive integer indicies, L is the round trip optical path length, and $g = \sqrt{1 - L/R}$ is the cavity stability factor, as the cavity by symmetry is similar to a linear cavity made from a flat mirror and a curved mirror with the radius of curvature R separated by the distance $L/2$. A factor of -1 has been extracted from the $\sqrt{g}$ according to Kogelnik and Li [1966]. The second term in equation 9.4 is related to the Gouy phase and the third is related to the symmetry of the higher order modes. By a rewriting of equation 9.4 the resonance frequencies of the TEM_{mn} are expressed, in terms of the free spectral range $FSR = c/L$, as

$$\nu_{q,m,n} = q\,FSR + \frac{FSR}{\pi}(m+n+1)\arctan\left(-\sqrt{g}\right) + \frac{FSR}{2}\frac{(1-(-1)^m)}{2}. \qquad (9.5)$$

Coupling of energy from the TEM_{00} to higher order TEM_{mn} may occur due to missalignment or difference in the beam shape of the incoming beam and the shape of the cavity TEM_{00} eigenmode. However even if these are perfectly matched, coupling to the higher order TEM_{nm} may still occur due to scattering points on the mirrors. This coupling is related by the spatial overlap of the TEM_{00} and the higher order TEM_{mn} mode Paschotta [2006] at the mirror. Suppression of the higher order modes can also be achieved by introducing an aperture in the cavity as the higher order TEM_{mn} in general has larger beam diameter than the TEM_{00}. Yet, the cavity design should be such that the frequency difference between the TEM_{00} and higher order TEM_{nm} modes should at least be larger than the line width of the laser especially for lower values of m and n. In this way simultaneous excitation of TEM_{00} and higher order TEM can be minimized.

For NIR systems the laser line width is typically a few MHz while for the QCL in this work, it is 40 MHz. This increases the requirement on the

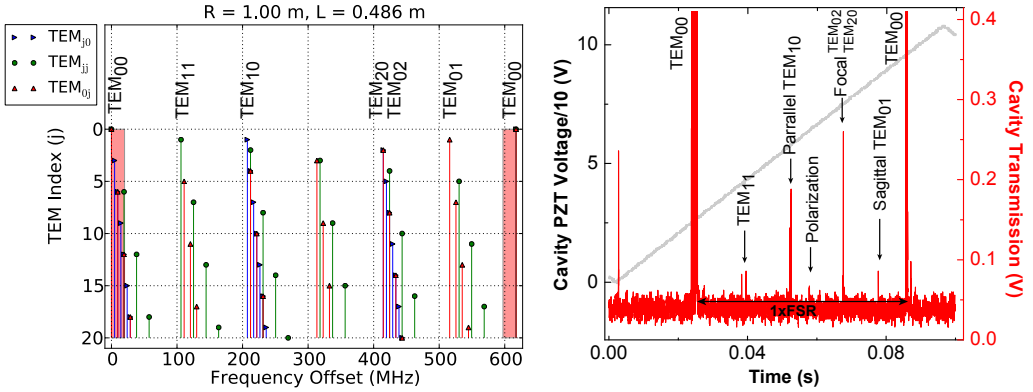

Figure 9.14: LEFT: Cavity mode structure calculated according to equation 9.5. Red fill Zones at the TEM_{00} indicates the 20 MHz laser half line width. RIGHT: Measured cavity transmission trace, by sweeping the cavity resonance frequencies by 1.4 FSR.

mode spacing of the cavity. Figure 9.14 shows TEM_{mn} frequencies calculated according to equation 9.5.

Also shown in figure 9.14 is the measured cavity transmission trace for a cavity with a 1 m radius of curvature mirror. In the trace the location of the three most dominant higher order modes are labeled, according to which adjustments they are most sensible to during building and alignment. Indicated with Polarization is the location of the TEM_{00} mode of the other polarization. These are shifted by ca. a half FSR. During building and mode matching the coupling to these modes is minimized such that the transmission for these modes is suppressed to less than 2.5% of the detector range.

Cavities using different mirror curvatures was also built. In particular did only one cavity achieve a ring down time great than 10 µs which was built with a mirror having 0.5 m radius of curvature. But, calculating the mode structure from this cavity showed much greater overlap with the fundamental cavity mode, which was also reflected in the measured shot to shot noise of this cavity. To make the ring down time longer it was also considered to make a longer cavity. This has further advantages e.g. that the FSR is shorter, and a much better decoupling from the higher order TEM will be achieved especially for $L \approx 60$cm and around $L \approx 80$cm.

9.3.2.1 Temperature and Pressure influence on mode stability

For schemes where the cavity is kept fixed, pressure and temperature changes could have an impact on the mode structure. Changes in the mode frequen-

cies $\nu_m = c/\lambda_m = m \times c/nL$ are found by differentiation

$$\frac{d\nu_m}{dT} = \frac{d\nu_m}{dL}\frac{dL}{dT} = \frac{c}{n\lambda_m} \times \frac{dL}{dT} = \frac{c}{2n\lambda_m} \times \alpha_T. \tag{9.6}$$

where the factor of 1/2 arises from the cavity body being half the length of the optical round trip distance. For stainless steel Invar the thermal expansion coefficient is $\alpha_T = 1.5 \times 10^{-6}\mathrm{K}^{-1}$, yielding thermal dependence of the mode frequency of ca. $50\,\mathrm{MHz\,K^{-1}}$. Contributions from changes in the index of refraction are insignificant. With the thermal stability of a few mK, thermal fluctuations have no influence on the cavity mode.

With respect to pressure changes differentiation yields

$$\frac{d\nu_m}{dT} = \frac{d\nu_m}{dn}\frac{dn}{dp} = \frac{-c}{\lambda_m\, n^2}\frac{dn}{dp} \approx 25\,\mathrm{MHz/Torr} \tag{9.7}$$

where the pressure dependence of n to first order is $dn/dp = 37.5\,\mathrm{MHz/Torr}$ page 10–252 Lide [2005]. With the typical pressure stability $\lesssim$ 10 mTorr the mode stability with respect to pressure fluctuations is 0.25 MHz. This value should be compared to table 7.3 stating frequency precision required at different pressures, from which it is seen that below 50 Torr they are comparable in magnitude.

9.3.3 Cavity mirrors

The requirement for the mirrors is that their reflection R is great enough to ensure the desired ring down time may be achieved. Using $R = \sqrt[3]{1 - \mathrm{FSR}/\tau}$ as the average mirror reflectivity per mirror for a given ring down time it is found that for τ =10 µs the reflectivity is 99.995% while for τ =5 µs the reflectivity is $R = 99.989\%$. Complementary to the reflectivity is transmission T and absorption loss A such that energy is conserved by $T + R + A = 1$. This means that the mirror losses cannot exceed the residual of the mirror reflection, i.e. 50 ppm for τ =10 µs and 110 ppm for τ =5 µs. Surface roughness of the mirrors also contribute to losses due to scattering away from the specular direction of the TEM_{00} and may as such be regarded as a contribution to mirror absorption. For a given smooth surface roughness σ_r the total integrated scattering loss (TIS) is calculated from Vorburger et al. [1993]; Harvey and Fender [1982]

$$\mathrm{TIS} = \frac{P_{\mathrm{scat}}}{P_{\mathrm{tot}}} = \left(4\pi\sigma_r \cos\theta_i/\lambda\right)^2 \tag{9.8}$$

where θ_i is the angle of incidence, and lambda the wavelenght of the light. The cosine factor is a correction for the decreased effective roughness when

the beam is not at normal incidence. Again the performance of the flat mirrors with a 45° angle of incidence surpasses that of the curved mirror with near normal angle incidence, as was the case for the reflection mentioned in the previous section. Using equation 9.8 we can calculate the maximum allowed surface roughness for a given ring-down, being 2.5 nm for τ =10 µs and 3.8 nm for τ =5 µs for the normal angle of incidence. If the mirror absorption losses are known this should be subtracted and the surface roughness must be correspondingly smaller.

The above considerations are the limiting case where the necessary transmission has been disregarded.

For the electrical field, the expression for cavity transmission reads in a similar way, as for the linear cavity with transmission t_1, t_2 through the input and output mirror and a optical round trip distance $L = L_1 + L_2 + L_3$ where L_1 is the distance between the input and output mirror. The electrical field of the output beam is then expressed by

$$E_t = E_i(t)t_1t_2e^{-\alpha L_1/2}\sum_{m=0}^{\infty}\left(r_1r_2r_3e^{-\alpha(L)/2+i\phi}\right)^m \tag{9.9}$$

$$= \frac{E_i(t)t_1t_2e^{-\alpha L_1/2}}{1-r_1r_2r_3e^{-\alpha L/2+i\phi}} \tag{9.10}$$

where $E_i(t) = E_0e^{i\omega t}$ expresses the electric field at the cavity input and ϕ the round trip phase delay. With $R_m = r^2$ we realize that $R = R_m^{3/2}$ provides the same expression for the cavity transmission as for a linear cavity. So the power transmitted by the cavity is

$$T = \frac{T_m e^{-\alpha L_1}}{(1-Re^{-\alpha L/2})^2} \times \frac{1}{1-\frac{4Re^{-\alpha L/2}}{(1-Re^{-\alpha L/2})^2}\sin^2(\phi/2)}. \tag{9.11}$$

As the cavity mirror losses are dominated by the curved back mirror, the power transmitted through the cavity is determined by the transmission of the flat imput mirrors. It is worth designing the HR coating of the flat mirrors such that the reflection matches that of the curved mirror, because in this way the transmitted power through the cavity may be optimized.

The high-reflective mirror surface is achieved by coating the surface with layers of alternating index of refraction and each layer with ca. $\lambda/4$ thicknesses with λ being the wavelength of the light for which high reflection is achieved. A description of quarter stacks is presented in most introductory books on optics e.g. [Hecht, 2002]. It should be noted that the final reflectivity increases with larger difference between the index of refraction of the two coating materials. When designing mirror coatings considerations to crystal

structure must also be made as the two materials may have poor adhesion to each other. In such case additional gluing layers may be needed between the $\lambda/4$ layers. So the detailed design of the mirrors was performed by the vendors. For the input and output coupling mirror an anti reflective coating was applied to the outer surface of the mirror, the design of which is much less restrictive.

Mirrors studied in this work As it was mentioned in the introduction, optical technology of the mid-infrared is not nearly as developed as for the near-infrared. This partly due to the limited number of materials that provide good transparency in the mid-infrared region. Availability of high reflective coatings turned out to be the largest obstacle for this project. Actually there was no company that had a standard product or method for high reflective coatings in the 4.5 µm mid-infrared. Only four of the companies addressed were willing to consider producing such mirrors and in all four cases it was on a development basis. These companies were II-VI Infrared, Research Electro-Optics, Inc. (REO), Advanced Thin Film, Inc. (ATF), and LohnStar Optics. Of these companies only ATF and LohnStar had past experience in producing mid-infrared coatings. A short summary of the mirrors and performance follows here.:

Laser Power Optics: This company has not existed for several years, but Picarro Inc. was in possession of Mid-IR mirrors from earlier studies in the mid-IR. These mirrors were manufactured in 2004 or earlier and were designed for 4.9 µm. Flat mirrors and mirors with ROC of 1 and 0.5 meters was a available. Further specifications of these mirrors were not know, but examinations by II-VI-infrared lead to believe that these had coatings with ThF_4 and ZnSe layers. The transmission was measured to be 120 ppm for the flat mirrors and the longest ring down measured was ca. 10 µs corresponding to an average mirror reflectivity of 99.994%. The power transmitted through the assembled cavity was measured to ca. 1 µW. Although this met the desired ring down time the shot to shot noise performance could not be met, because this mirror had a 0.5 meter ROC and this provide high order mode interference as explained in the previous section. Using 1 meter ROC mirrors the best ring down time achieved was 8 µs but the transmission was only few micro watts so additional electronic amplification of the signal was necessary. The signal amplification increases the amplitude noise and trigger delay providing a shot to shot noise performance of 0.4% with the built setup, but typically worse (ca. 1%) when integrated with the analyzer electronics, primarily due to the preamplifier.

II-VI-infrared: Two sets of coatings were examined Batch # 100 using Ge and ZnSe layers produced for all three mirrors and using ZnSe substrates. Second batch # 170 was only new coatings of back mirrors using Ge and ThF_4 layers. For the # 100 batch the transmission through the flat mirrors was 65 ppm on the P polarization, which was so low that good CRD measurements were only achieved for P polarization. The longest τ achieved was < 1 µs. Substituting the back-mirror with the # 170-batch Ge-ThF_4 coated improved performance even though the transmission through these were measured to be twice that of the # 100-batch. Using # 170-batch back mirror $\tau = 1.5\mu$s was achieved. The manufacturer specified the surface roughness as $\leq$ 3.5nm. This corresponds to TIS $\approx$ 95ppm corresponding to a 5µs ring down time. High quality polishing of ZnSe is difficult as it is a polycrystalline material. These mirrors had grain sizes of ca. 75 µm which could provide additional scattering. As mentioned the cavity transmission was too low for CRD measurements on the S polarization but using mirrors from Laser Power Optics as the flat mirrors this was possible and with the # 170-Batch as back mirror a 5 µs ring down time was achieved. In conclusion the losses of these mirrors were too large to achieve the desired performance.

LohnStar: For these mirrors a Si substrate was used. This is a monocrystalline structure which allows for polishing of much smaller surface roughness ($<$ 1Å Teichert et al. [1995] on 10 µm scale) than ZnSe. With these mirrors a ring down time of 5.25 µs ($R = 99.989\%$) was a achieved and more importantly the transmission through the cavity was much higher than for any of the other mirrors, enough to saturate the detector. The ring down shot to shot noise provided with these mirrors was better than 0.2% with the analyzer electronics.

9.3.4 The piezo assembly

The PZT assembly see figure 9.13 is a custom design by Picarro Inc. The assembly provides a travel of 6.4 µm per 100 V (ca. 8.7 MHz/V in the 0.5 m cavity) and typically enough to deliver a sweep of more than 2 FSR at $\lambda = 4.5$ µm.

The cavity mirror is mounted to the PZT assembly with a small spacer, made from Fused Silica. When the mirror substrate is made from a material which is transparent to the applied wavelength this may lead to the occurrence of interference from the beam reflected at the mounting surface, e.g. as the change in refractive index from e.g. ZnSe to Fused Silica causes large reflection. This reflection is fed back into the cavity and may cause a sinusoidal interference modulation of the empty cavity loss when tuning the

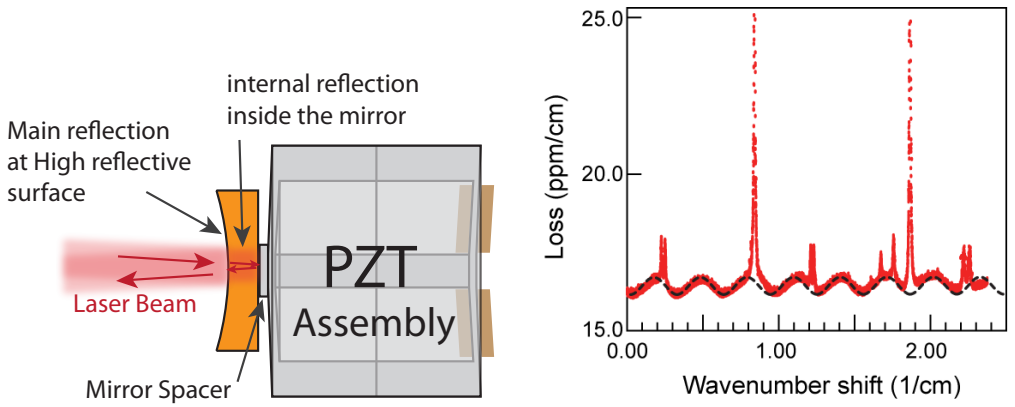

Figure 9.15: LEFT: Design of the PZT assembly. Indicated is the intra mirror reflection which may cause an interference signal in the cavity loss as shown to the right. RIGHT: Absorption spectrum showing sinusoidal baseline indicated with black dashed line. The origin of this is the reflection from the (rear) mounting side of the curved mirror.

wavelength of the laser as shown in figure 9.15. This origin was confirmed by the interference period corresponding to the mirror thickness and in measurements with a thinner mirror, the period was seen to become correspondingly longer.

This problem is easily solved by either making an index matching transition to the mirror spacer, or by choosing a mirror substrate which absorbs the applied wavelength. For the mid-ir this could be Fused Silica or BK7 etc.

In the final design, the scheme for collecting spectra keeps the cavity length fixed while the laser frequency is in a spectroscopic window, which was chosen due to the poor frequency control of the laser. This means that only a discrete frequency grid with points spaced by one cavity FSR is sampled. When multiple absorption lines are being sampled their peak will in general not be sampled within one such FSR grid. To sample the peaks of multiple lines it is therefore require that the length of the cavity is changed, such that the cavity FSR grid matches the different peak frequencies. Such a scheme requires that the cavity PZT is able to reproduce the desired wavelength with a precision meeting the requirements chosen from table 7.3. The 16 bit digital resolution corresponds to 0.02MHz but the PZT driver usually has substantial noise and further piezo's typically have large hysteresis and the piezo travel is certainly not linear with voltage. The real precision can only be confirmed with high resolution spectroscopy e.g. by using near IR or visible light and even then it is most likely to change over time as the piezo gets used. This has not been done.

9.3.5 Linear polarizer for detection of the S-mode

The cavity finesse for the P polarization is much smaller than that for the S polarization. Any slight missalignment of the cavity or mode matching will result in a strong power signal being emitted from the cavity with P polarization even if the cavity input beam is perfectly S-polarized. When sweeping the cavity or laser, this transmitted signal with P-polarization will usually be much stronger than that transmitted with S-polarization. The transmitted S- and P- polarization can then only be distinguished by their ring down time, as this is much shorter for the P polarization (typically a factor of five for cavities in this project).

The only way to ensure that the system will only trigger on the S polarization is to use a linear polarizer after the cavity, to suppress the power with P polarization reaching the detector.

A ThorLabs LPMIR050 linear thin film polarizer was used, which was measured to have a 60% peak transmission at 4.5 µm and the extinction ratio was specified at 10^4.

9.4 The ring down detector

The ring down detector is a (HgCdZn)Te[2] Vigo detector PVI-3TE-6 with a MIPDC-F-20 built-on preamplifier. The wavelength cutoff is 6 µm, the detectivity of this detector is 8.7×10^{10} cmHz$^{1/2}$/W. The responsivity is > 1.5 A/W and has a rise time ca. 10ns which provides a cutoff frequency of ca. 16 MHz. Detectors with shorter wavelength cutoff were available but the rise time of these was longer giving a cutoff frequency lower than 8 MHz, being slower than the sampling rate of the acquisition card. The preamplifier provides a transimpedance gain of 1.8×10^4 V/A at 50 Ω load and has a cutoff frequency of 20 MHz. This provides a minimum detectable power of 5.3 nW. The responsivity for the combined system is 6.4×10^4 V/W, providing a noise equivalent voltage of 0.3 mV. Having a 2 V swing this applies a S/N ratio of ca. 6000.

Detectors covering a longer wavelength region were also available, but their detectivity was an order of magnitude smaller.

9.5 The back scatter mirror

Scattering of light from the optical surfaces within the ring-down cavity couples light between the forward traveling wave (the “forward” wave), which

[2] also known as (MCT) detector.

is initially coupled into the cavity by the mode-matching optics and travels counter-clockwise in Figure 9.1, and a backward traveling wave (the "back scatter wave"), which travels clockwise in Figure 9.1. The forward wave exits the ring-down cavity through the primary cavity output, and goes directly to the ring-down detector. The backward wave exits the ring-down cavity through the input mirror going back toward the laser, which may be used for optical feedback. It also exits through the output mirror but not in the direction of the ring-down detector.

Energy circulating in the "back scatter" wave is not observed by the ring-down detector, and therefore appears as a time-dependent distortion of the measured (forward wave) ring-down signal. This can adversely affect the accuracy of the computation of the ring-down time. The excitation of the back scatter wave always has the same resonant frequency as the forward wave. Yet the time response of the back scatter wave is not simply proportional to the forward wave. The energy in the back scatter wave depends on the time history of the forward wave, in particular on how the cavity fills up with light (which is in general a noisy, chaotic process due to the broad line-width of the laser). It is in theory possible to correct the computed ring-down time for this distortion by using a second detector to measure the time dependence of the back scatter wave, which has been implemented in earlier systems. In the presented solution, a novel and simpler method was demonstrated, by using a single mirror to direct the back scatter beam through the linear polarizer and onto the ring-down detector.

Figure 9.16 shows a comparison of system performance with and without applying the back scatter beam to the ring-down detector. The system was first optimized for the ring-downs while blocking the back scatter beam. The back scatter beam was then unblocked. The mirror mount of the back scatter beam was adjusted to optimize the performance. The data in figure 9.16 was then taken in conjunction of each other, blocking and unblocking the back scatter beam. By applying the back scatter beam the shot to shot performance improved by more than a factor of 20 from 1% to 0.04%. It is important to note that the full beam of both forward and backward output should be captured on the photodetector. Performance may appear better e.g. by a configuration as shown in figure 9.16 but when frequency swept it is observed that the noise and baseline exhibit an interference behavior. In this setup spacial limitations made it impossible to incorporate the focusing lens to properly focus both forward and back scatter beam.

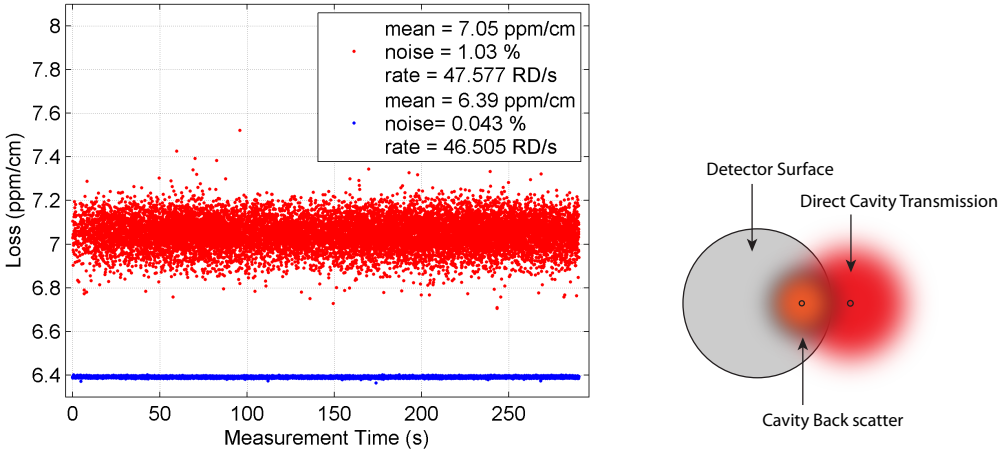

Figure 9.16: LEFT: Two time series of ring down measurements, comparing with and without applying the back scatter wave. RIGHT: Balancing of the power from forward and back ward waves can give seemingly better performance.

9.5.1 Optical mode matching to cavity

In order that high power from the laser beam is coupled into the cavity it is required that the spatial beam shape entering the cavity matches that of the cavity eigenmode. The topic of this section is to describe how this is achieved. The procedures described apply not only when building the analyzer, but also for the cavity building station.

The profiling of the beam emerging from the laser was described in section 9.2.5. Calculation of the cavity eigenmode and propagation of Gaussian beams through optical elements is widely explained through literature Milonni and Eberly [1988]; Siegman [1986]. Calculating the eigenmode of the cavity (using $L = 0.486$m and 1 m mirror ROC) and knowing the beam profile, the task is then to find the proper optical elements and their positions such that the beam from the laser is converted to match into the cavity. This is a nonlinear problem, and there is no straightforward optimization method for solving this problem. Every optical element in the beamline has to be taken into account, and given that the beam emerging from the laser is elliptical, the mode matching is further complex as optical components making the beam spherical have to be introduced at appropriate positions.

To solve this problem a Mathematica program[3], with the graphical user

[3]The original code by Sebastian Bange was modified for solving the problem of this project. Original code was collected from: http://freenet-homepage.de/sbange/university/mathematica/mathematica.html.

interface provided by the 'manipulate' function was used to adjust positions and properties of the optical elements introduced into the beam line.

To evaluate the quality of a mode matching configuration, the electric field coupling coefficients for mismatch of waist axial position and waist size calculated according to Anderson [1984], were used:

$$\text{Waist Size :} \qquad \frac{w_0'}{w_0} - 1 \tag{9.12}$$

$$\text{Transverse position :} \qquad \frac{\lambda z_0'}{2\pi w_0^2} \tag{9.13}$$

where w_0' is the laser beam waist size in the cavity and z_0' is the beam waist position relative to the waist position of the cavity eigenmode having waist w_0. Squaring the coupling coefficients in 9.13 provides the power loss to the higher order modes. The coupling coefficients would have to be smaller than 0.3% in order that misalignment losses to higher order modes are smaller than 10 ppm. Losses to higher order modes may also cause interference in the ring down signals so preferentially the coupling coefficients are lower than 0.1%.

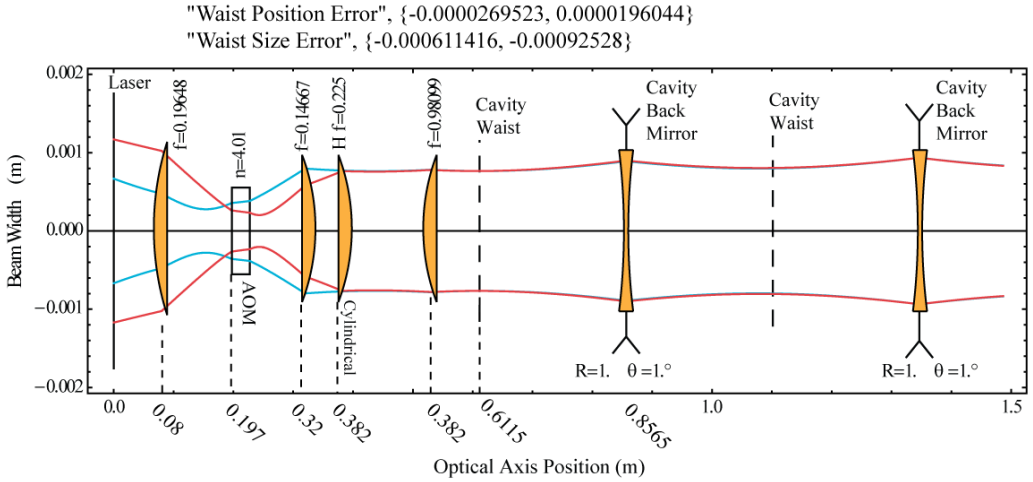

Figure 9.17: ABCD matrix calculation of the beam width as going through the chosen mode matching optics. Blue is the vertical (P) profile while red is the horizontal (S) profile.

Shown in figure 9.17 is an ABCD calculated solution for the mode matching. The following considerations were taken into account when doing the layout:

In order to minimize the analyzer footprint, minimal distance between laser and the cavity is desired, while keeping the physical mounting realistic,

and also providing sufficient freedom to perform the actual alignment. The physical layout of the optics is shown in figure 8.3.

The mode matching between any two spherical cavities can be achieved using just two lenses. However as the laser beam in this project is elliptical, additional optical elements are needed. Several options are possible in making the beam spherical. One is to focus the beam through a small circular aperture, but this method requires that quite a bit of laser power is absorbed. Another is to use anamorphic prism pairs. For this work it was chosen to use a single cylindrical lens and two spherical lenses, as sufficient means of obtaining the mode matching. This has a few disadvantages compared to using anamorphic prism pairs, as the focal length can only be designed for a specific configuration because the focal length of the lens is fixed. Further it is difficult to align because the position on the beam axis has to be found accurately.

Included in the mode matching calculation is also the AOM through which the beam will focus without a too small waist as the AOM was designed for semi large beams. The AOM is 3 cm thick but has an index of refraction of ca. 4, so the optical path length of the AOM is 12 cm. The AOM could not be placed closer than 10 cm from the laser, as reflections from its surface would then provide optical feedback to the laser.

In the original design it was planned to glue the optics onto a plate of low thermal expansion in order to assure minimal vibrational and thermal sensitivity to the alignment. In order that alignment would still be possible after gluing of the optics, it was decided in the design to include a thick parallel plate for the adjustment of the beam position plus a weak lens to adjust the input angle just before the cavity. This lens was also included, being of 1 m focal length. The index of refraction of the parallel plate and input mirror was neglected in the calculation.

The design of focal lengths and positions for the required optical elements were decided by starting at the laser and applying the optical elements piece by piece toward the cavity progressively shaping the beam to the eigen mode going into the cavity. Several iterations had to be made in order to find the right combination and order of the elements, while also being physically realistic. Once the optical elements had been decided a fine tuning of their positions was made in order to confirm that the obtainable coupling losses could be better than 1 ppm.

The optical line in the final analyzer deviates to some extent from the configuration shown in figure 9.17, because it was decided to use mirror mounts instead of gluing the optics. Alignment was therefore easier to do using two planar mirrors.

9.5.1.1 Polarization Optics

In order to achieve the highest finesse possible for the cavity, the polarization has to be linear in the sagittal direction. Coming out of the laser the polarization is linear but in the P direction. A 90° change of the polarization is therefore necessary. The AOM has the highest efficiency for the P-polarization (with respect to acoustic wave vector) so the polarization should not be changed until after the AOM. Change of the polarization was attempted in two ways: using a $\lambda/4$–plate or using a periscope. For the scheme of gluing the optics onto a single rugged plate, using a $\lambda/4$–plate would be the best option. A Cadmium thiogallate ($CdGa_2S_4$) $\lambda/4$–waveplate acquired from Altechna showed fine conversion of the polarization. However as the final analyzer was designed under the conditions of the low transmission ZnSe mirrors (see section 9.3.3), all unnecessary loss of power had to be avoided. Since gluing of the mirrors was also not pursued using a telescope turned out to be the best option.

9.6 Optical switch

As the chosen quantum cascade laser does not have the capability of fast optical switching of the output, a form of switch had to be implemented. Two possible choices are blocking the beam by means of a mechanical actuator or by means of an acousto optical modulator. The expected ring down time is around 10 μs and lower. Preferably the shutter is able to shut off the beam power in 0.1 μs, on demand, and with less than 0.4 μs delay.

Mechanical Switch The typical beam width ($1/e$ radius of the field) is 1 mm. The shutting time is determined by the speed of the shutting element v_{sh} and width of the laser w according to

$$\tau_{sh} = \frac{2w}{v_{sh}}, \tag{9.14}$$

multiplying by 2 to get the diameter. Given that the typical beam width is $w = 1$ mm, the shutter speed would have to be 20 km/s in order to ensure that the fall time is faster than 0.1 µs. Further improvement of the shutter speed may be achieved by focusing the beam and letting the actuator block the beam at the waist. If the beam is collimated with a width of 1 mm and we use a lens of focal length $f = 2.5$ cm, the diffraction limited beam waist would then be $w_0 = \frac{\lambda f}{\pi w_1} = 35.8\mu$m. Correspondingly an average shutter speed of 358 m/s would be needed.

9.6.0.2 The AOM as an optical switch for the MIR region

An AOM consists of an optical crystal and a piezo electric transducer. An electric RF modulator drives the transducer to produce sound waves in the crystal, which form a diffraction grating by the alternation in index of refraction between compressed and rarefied regions see fig. 9.18. Using the right configurations, up to 80% may be deflected into the first order beam. When the RF modulation is switched off, the optical grating will disappear and no diffraction will occur, leaving all the light in the first order beam. The RF modulation can be stopped almost instantaneously, leaving the acoustic wave propagation as the dominant delay of switching. The acoustic speed in the crystals is typically on the order of several km/s fulfilling the above mentioned speed requirement for the shutter. The grating structure appear static to the light passing the AOM, even though the acoustic wave are traveling waves. Because the speed of light is 5 orders of magnitude faster than the speed of sound. With the applied AOM a shutter delay of ca. 0.5 µs

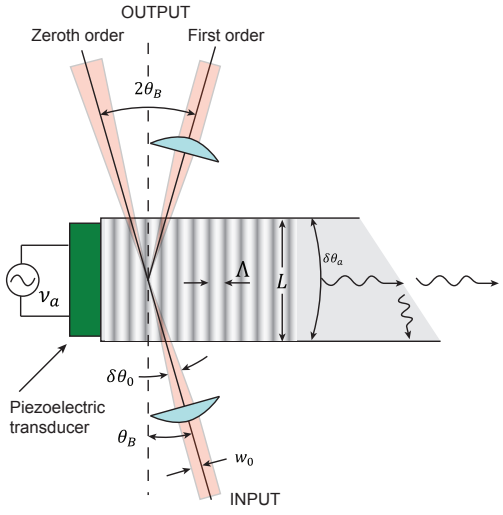

Figure 9.18: Typical configuration for an acousto optic modulator.

9.6.1 Improvement of shutter delay by use of laser AC input

The only direct current input to the laser is AC modulation input. During some line width experiments, where the AC current was modulated, it was discovered that a square pulse input causes laser to temporarily turn off. Using the SRS-DG535 pulse delay generator output to apply a 0V to 4V step

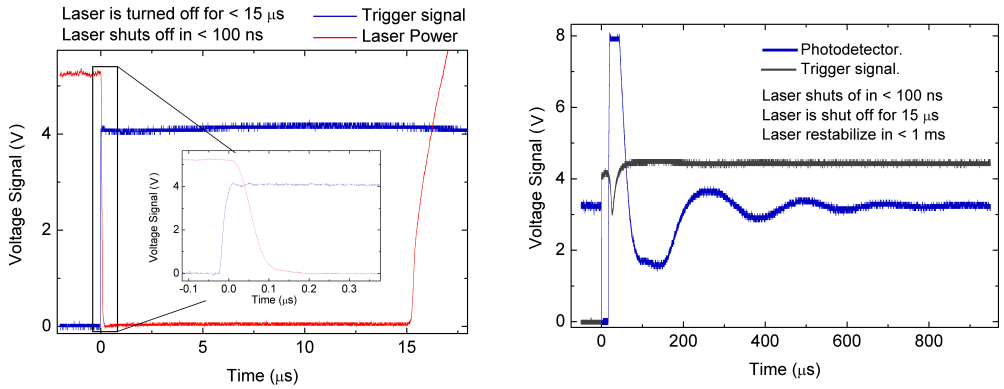

Figure 9.19: Shutter performance by applying a voltage step to the laser current modulation input.

increase with 50 Ω impedance into the AC input of the laser, caused the laser power to be turned off in less than 100 ns as shown in Figure 9.19. This was measured with the PVI-6-TE3 detector at full laser power attenuated with fused silica pieces. The laser stays off for 15 µs upon which it turns back on. The power then re-stabilizes within 1 ms. If a smaller voltage step is applied the laser will stay off for a shorter amount of time, but also reestablish power level faster. It is expected that the wavelength is also perturbed during this operation but examinations of this was not performed, though it could easily be done with an etalon setup.

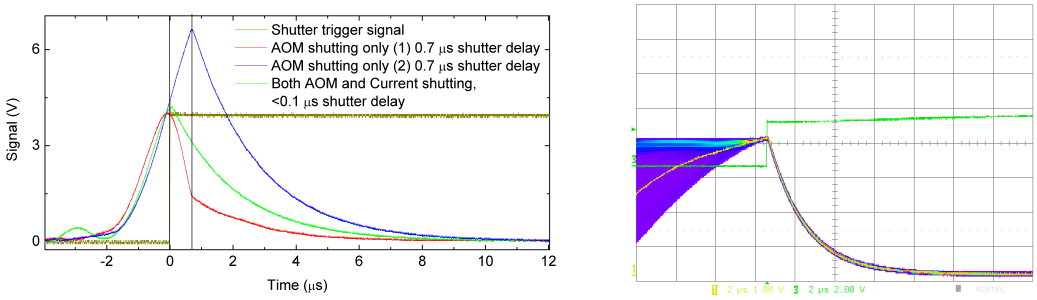

Figure 9.20: LEFT: Comparison of the shutter delay using only an AOM and including the laser AC input shutter method. RIGHT: Oscilloscope persistence measurement when only using the AC current input as shutter. Performance is highly improved.

Applying the AC shutting technique into the cavity build system using the SRS-DG535 as trigger, readily improved the ring down noise performance compared to only using the AOM. Measured from the shutter trigger step signal, a 0.7 µs delay was measured for the AOM to shut off the light. Here

the predominant delay is acoustic travel from transducer to beam in the AOM crystal. When the AC current shutter is used the light is turned off in 0.1 µs. The delay in the SRS-DG535, from threshold is reached to output trigger signal is generated, is also ca. 100 ns, so in total shut off takes 200 ns from threshold is reached. When only applying the AOM as laser shutter the 0.5 µs delay is long enough to make mode beating occur between the light of different frequencies being filled into the sweeping cavity. This creates interference in the ring down signal which causes large variations in the ring down amplitude at the time at which the laser turns off (see red and blue curve in figure 9.20).

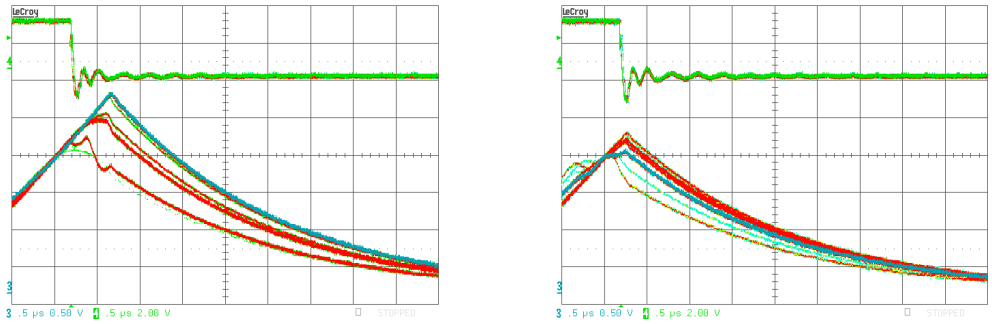

Figure 9.21: Comparison between laser power shutting method, using the analyzer electronics. LEFT: Using only the AOM. RIGHT: Using AOM and Laser AC current input. With the shorter shutting delay the large modulations are removed from RD signal. remark: Trigger signal is inverted.

The oscilloscope persistence setting provides a quick and simple method for examining ensembles of ring downs. Figure 9.21 shows a comparison between only using the AOM shutter and including the laser AC input, when using the Picarro G1000 electronics as trigger source for the laser. It was found that the Picarro G1000 electronic trigger delay from reach of threshold was 200 ns i.e. twice that of the SRS-DG535. It was also found that the impedance was not as well matched as for the SRS-DG535. This is seen in the trigger step signal as larger oscillations at the step corners. This may cause that the laser was not turned off as efficiently with the Picarro electronics. This is interpreted as the cause of the larger spread in amplitude at laser shut off compared to the persistence plot when using the SRS-DG535 as trigger for the AC shutter.

9.6.1.1 Optical feedback when omitting the AOM

If the AOM is removed from the beam path, optical feedback from cavity to laser is permitted. This was an advantage with the high absorption mirrors

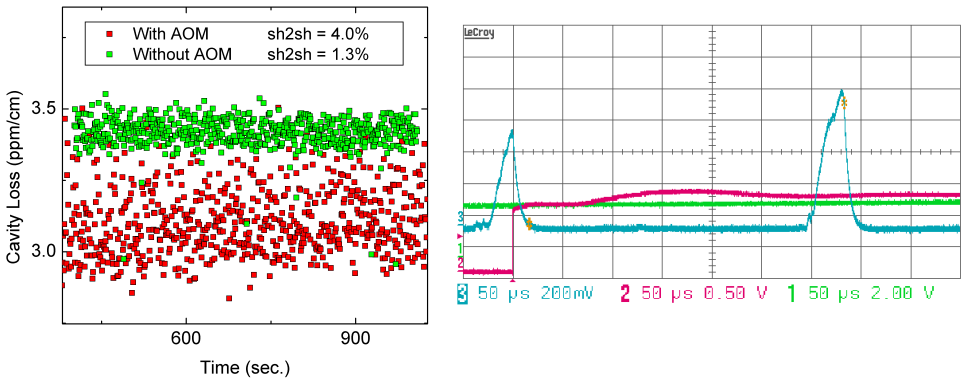

Figure 9.22: LEFT: Ring down measurements comparing performance with optical feedback (without AOM) and without optical feedback (with AOM). RIGHT: Ring down trace measured without the AOM in the optical beam. Undesired cavity transmission is seen after 100 µs *and full cavity transmission after* 300 µs.

as a much larger transmission signal could be obtained. With the AC shutter method it was possible to examine the ring down performance without the AOM. Examinations of this were made with a cavity using a 0.5 m radius of curvature back mirror and a ca. 10 µs ring down time. Results from this are shown in Figure 9.22. The laser is only turned off for 15 µs but to measure the 10 µs ring down time a measurement time of 50 µs or more is suitable. However, as seen on figure 9.22 light transmitted through the cavity will typically not be observed for more than typically 100 µs. This is because the laser frequency is detuned away from the cavity resonance, when the step is applied to the AC current input. A set of ring down measurements was performed using this configuration and it was compared to measurements on the same cavity for which the AOM was included. It was found, that without the AOM better performance was achieved, possibly due to higher cavity transmission. But without the AOM several undesired outliers was observed which probably originated from ring downs where the laser had reentered resonance before the end of the fitting window.

Regardless of these intriguing results, omitting the AOM was abandoned as there was no way of being sure that the AC shutter method would guarantee the laser to stay off for longer than 15 µs. Surely if the laser *was* able stay off longer, further studies with optical feedback would be of great interest.

9.7 Wavelength Monitor

In section 7.2.2 it was pointed out that precise measurements of the laser frequency, at the moment of the ring down measurement, are crucial to the

obtainable performance. In short when a spectral point lies on the side of an absorption peak, an error in the measured wavelength $\delta\lambda$ is equivalent to an error in the ringdown time τ, of $\delta\lambda$ multiplied by the slope (derivative) on the side of the spectral peak, $\partial\tau/\partial\lambda$. The typical Air-broadened half-width of the rotation-vibrational transitions of N_2O in the mid-infrared is about 1 GHz and the required precision over this range has to be about 5 MHz as stated in table 7.3 for cell pressure of 200 Torr. Preferably this precision is better in order to be neglectable to the spectral measurement and to enable measurements at lower pressures.

9.7.1 Principle of the wavelength monitor

To understand the operation of the wavelength monitor, first consider a simple single-beam, low finesse etalon arrangement. The etalon will reflect a portion of the power and transmit the remainder of the single incident beam. The ratio of the power in the reflected beam to the power in the transmitted beam is a sinusoidal function of the wavelength (actually the optical frequency) of the incident beam (assuming it is monochromatic), where the sinusoidal period is the free spectral range of the etalon. Either of the functions shown in Figure 9.23 is an example of this ratio. This single-beam arrangement works well provided that the laser tunes only over a range where the sinusoidal signal, of the power ratio, has a substantially non-zero slope, the highlighted segments on the functions in figure 9.23.

The single-beam arrangement has wavelength regions with the power ratio slope being too close to zero (near the maxima and minima) to be useful to determine the wavelength. Increasing the free-spectral range of the etalon (by decreasing its thickness) is one way to increase the range of usable slope, but this simultaneously decreases the slope in that usable segment, reducing the ability of the etalon to resolve closely spaced wavelengths.

This problem can be circumvented by having two Etalon signals with the same free spectral range (FSR) being 90 degrees out of phase. This provides that one of the ratio signals will always have a significant slope. Such a configuration can be achieved using a single Etalon, and two input beams aimed at the Etalon at different angles, see figure 9.23. This wavelength monitor is a key component of the Picarro analyzers, and is described in their patents Tan [2007, 2008b,a]. The design had to be substantially modified to be applicable for the mid-infrared, but the operation is essentially the same.

A choice of Etalon thickness and material has to be made. Coating of the Etalon surface may also be necessary in order that the Etalon has the proper Finesse for a good Etalon fringe signal. These decisions should be made

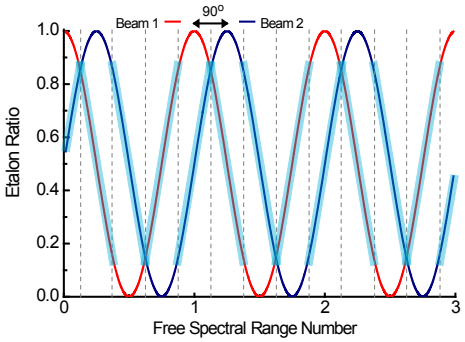

Figure 9.23: The power ratio interference signals. (Wavelength monitor schematic, is left out). Highlighted in blue are the usefull sections of the etalon signals.

taking account of which precision is necessary for the spectrometer. However precision of the wavelength monitor depends not only on the Etalon but also on the noise of the detectors.

9.7.2 Operation

The transmitted and reflected intensity of a Fabry-Perot is given by

$$I_R = I_0 \frac{F sin^2(\varphi/2)}{1 + F \sin^2(\varphi/2)} \tag{9.15}$$

$$I_T = I_0 \frac{1}{1 + F \sin^2(\varphi/2)} \tag{9.16}$$

where I_R, I_T and I_0 are the reflected, transmitted and incident intensities respectively and

$$F = \frac{4R}{(1-R)^2} \tag{9.17}$$

$$\varphi = 2\pi \frac{2\ell}{\lambda} \sqrt{n^2 - \sin^2\theta} = 2\pi \frac{\nu}{\mathrm{FSR}} \sqrt{1 - \frac{\sin^2\theta}{n^2}} \tag{9.18}$$

where R is the Etalon surface reflectivity, and φ is the round trip phase change by a beam with wavelength λ approaching at an angle of θ onto an Etalon of thickness ℓ and index of refraction n.

The resonance frequencies of a beam hitting an Etalon at a small angle is expressed by

$$\nu_m = m \left(\frac{c}{2n\ell \cos\theta} \right), \qquad m = 1, 2, 3, \cdots \tag{9.19}$$

and the free spectral range as

$$\mathrm{FSR} = \frac{c}{2n\ell\cos\theta} \tag{9.20}$$

where θ is the internal angle and ℓ the Etalon thickness Milonni and Eberly [1988]. For the wavelength monitoring it is desired that the Etalon FSR is much smaller than the optical wavelength in order to provide an accurate wavelength measurement. This means that m is a large number and thus that the resonance frequency ν_m for the two beams can be significantly different while their FSR remain essentially the same.

In order to generate a useful sinusoidal signal which has a simple relation to frequency the ratio

$$S_i \equiv \frac{I_R}{I_T} - \frac{F}{2} = F\sin^2\left(\frac{\varphi}{2}\right) - \frac{F}{2} = -\frac{F}{2}\cos\varphi \tag{9.21}$$

is used. In the case that the angles of incidence of the two beams are exactly $\pi/2$ out of phase

$$S_1 \approx -\frac{F}{2}\cos\left(2\pi\frac{\nu}{\mathrm{FSR}}\right) = -\frac{F}{2}\cos(\phi) \tag{9.22}$$

$$S_2 \approx -\frac{F}{2}\cos\left(2\pi\frac{\nu}{\mathrm{FSR}} + \frac{\pi}{2}\right) = \frac{F}{2}\sin(\phi) \tag{9.23}$$

where FSR has been approximated to the free spectral range at normal incidence. This approximation will be very accurate for small angles of incidence and small frequency variations. From these two signals a frequency may be obtained as

$$\frac{S_2}{S_1} = -\tan\phi = -\tan\left(2\pi\frac{\nu}{\mathrm{FRS}}\right) \tag{9.24}$$

and therefore

$$\nu = -\frac{\mathrm{FSR}}{2\pi}\arctan\frac{S_2}{S_1}. \tag{9.25}$$

This only provides the frequency to within one FSR of the Etalon. In order to know the accurate wavelength it is necessary to have another means of measuring the laser frequency to within 1/4 of the Etalon FSR.

One ambiguity of the wavelength measurement remains, namely to which free spectral range the particular measured wavelength belong. This ambiguity has to be resolved by having a different way of knowing the laser frequency which is precise and accurate to within the free spectral range of the wavelength monitor. The simplest solution for this is obtained if the tuning properties of the laser provide the required accuracy. The QCL has a tuning repeatability of $0.02\,\mathrm{cm}^{-1} = 600\,\mathrm{MHz}$, which is more than plenty

to resolve the 50 GHz free spectral range of the etalon. This repeatability is even enough to resolve an FSR of 10 GHz as studied in appendix B. The smaller FSR would provide higher precision as addressed in the next section, yet it was chosen to use a 50 GHz (1.66cm^{-1}) FSR as it was not certain at the time of this decision, how the laser should be operated during a spectral scanning, and for this a 50 GHz provide more flexibility.

9.7.2.1 Alignment angles and sensitivity

The two beams approaching the Etalon have the same frequency. In order that the resonance frequencies of the two beams are shifted by 1/4 of an FSR their phase must differ by $pi/2$. A Taylor expansion of equation 9.18 gives

$$\varphi \approx 2\pi \frac{2n\ell}{\lambda}\left(1 - \frac{\theta^2}{2n^2}\right) \tag{9.26}$$

with which the phase difference is expressed as

$$\Delta\varphi = \varphi_1 - \varphi_2 = \frac{2\pi\ell}{n\lambda}\left(\theta_2^2 - \theta_1^2\right). \tag{9.27}$$

By setting the phase difference equal to $\pi/2$ as required above, it is obtained that

$$\theta_2 = \sqrt{\frac{n\lambda}{4\ell} + \theta_1^2} \tag{9.28}$$

This expression provides the angle of incidence for beam 2 which ensures that the resonance is shifted by 1/4 of an FSR with respect to that of beam 1 for any input angle of this[4]. For an input angle of 3.5° for beam 1 onto a 50 GHz Etalon made from ZnSe the angle of incidence for beam 2 will be 4.4°.

The relation between a variation in the phase difference $\delta\Delta\varphi$ and corresponding variation in the angle of incidence $\delta\theta_2$ can be found by differentiation of equation (9.27) giving

$$\delta\theta_2 = \left(\frac{\partial\Delta\varphi}{\partial\theta_2}\right)^{-1}\delta\Delta\varphi = \left(\frac{\lambda n}{4\pi\ell\theta_2}\right)\delta\Delta\varphi. \tag{9.29}$$

From this a change in the phase difference $\delta\Delta\varphi$ of 1 degree corresponds to a change of θ_2 of 33 arc seconds, for the above configuration with beam 1 at 3.5° angle of incidence.

[4]A negative solution also exists corresponding to the two beams approaching the Etalon from opposite directions with respect to the normal of incidence. Such a configuration should not be chosen because it is more sensitive to the laser pointing stability.

9.7.2.2 Thermal influence on the wavelength spectrometer

By differentiating equation (9.19) with respect to temperature we may find the Etalon resonance sensitivity to temperature

$$\frac{\mathrm{d}\nu_m}{\mathrm{d}T} = \frac{mc}{2}\frac{\mathrm{d}}{\mathrm{d}T}\left(\frac{1}{n}\cdot\frac{1}{\ell}\right) = \frac{c}{2\lambda_m}\left(\alpha_T + \frac{1}{n}\frac{\mathrm{d}n}{\mathrm{d}T}\right) \tag{9.30}$$

This shows that noise from thermal expansion is independent of the Etalon thickness. Table 9.2 shows this Etalon thermal drift for 50GHz configurations for five appropriate optical materials for the Mid-IR, and compared to BK7 a typical material used in the near-infrared. From the thermal drifts calculated in table 9.2 it is concluded that the temperature of the Etalon needs to be stable to within 1 mK in order that the corresponding shifts in frequency are on the order of 1MHz.

Table 9.2: Properties of optional optical materials N. Nikogosyan [1997], and the corresponding drift in measured frequency calculated according to : $\frac{dn}{dt}\frac{c}{\lambda^2(n+\alpha_T)}$.

	BK7	**CaF2**	**BaF2**	**ZnSe**	**Si**	**Ge**	
Wavelength	1.55E-06	4.57E-06	4.57E-06	4.57E-06	4.57E-06	4.57E-06	m
Index	1.501	1.404	1.454	2.431	3.428	4.018	-
Reflectance	4.01	2.82	3.42	17.40	30.06	36.18	%
F	0.17	0.12	0.15	1.02	2.46	3.55	
Signal Amplitude	14.8	10.7	12.8	50.5	71.1	78.0	%
Length	2.000E-03	2.100E-03	2.100E-03	1.234E-03	8.600E-04	7.400E-04	m
FSR	5.00E+10	5.09E+10	4.91E+10	5.00E+10	5.09E+10	5.04E+10	Hz
dn/dT	1.700E-06	-7.400E-06	-1.630E-05	5.340E-05	1.620E-04	3.960E-04	K-1
α_T	7.100E-06	**1.890E-05**	**1.840E-05**	7.500E-06	2.400E-06	5.800E-06	K-1
Thermal Drift	-797	-447	-236	-967	-1630	-3425	MHz/K
	-0.027	-0.015	-0.008	-0.032	-0.054	-0.114	cm^{-1}/K

9.7.3 Measurements with Wavelength monitor

In a preliminary setup the etalon and steering mirrors were placed on a CuW plate while the detectors were mounted on 2 way translation stages. Half ball Sapphire lenses of 6 mm focal length were mounted in front of the detectors to ensure full capture of the beam power. The beam splitter is located on a separate mirror mount. A picture of this setup in the final stage is shown in figure 9.26. Figure 9.24 shows the four detector signal while sweeping the laser piezo from 0 Volt to 100 Volt at 0.8 Hz, the corresponding signal ratios I_R/I_T are also shown as a function of wavelength and in a quadrature-like plot. The laser wavenumber scale is deduced from the data in figure 9.25.

The detector signals are not pure sinusoidal curves because the laser power itself has an etalon effect, as seen in the laser power spectrum in figure 9.6.

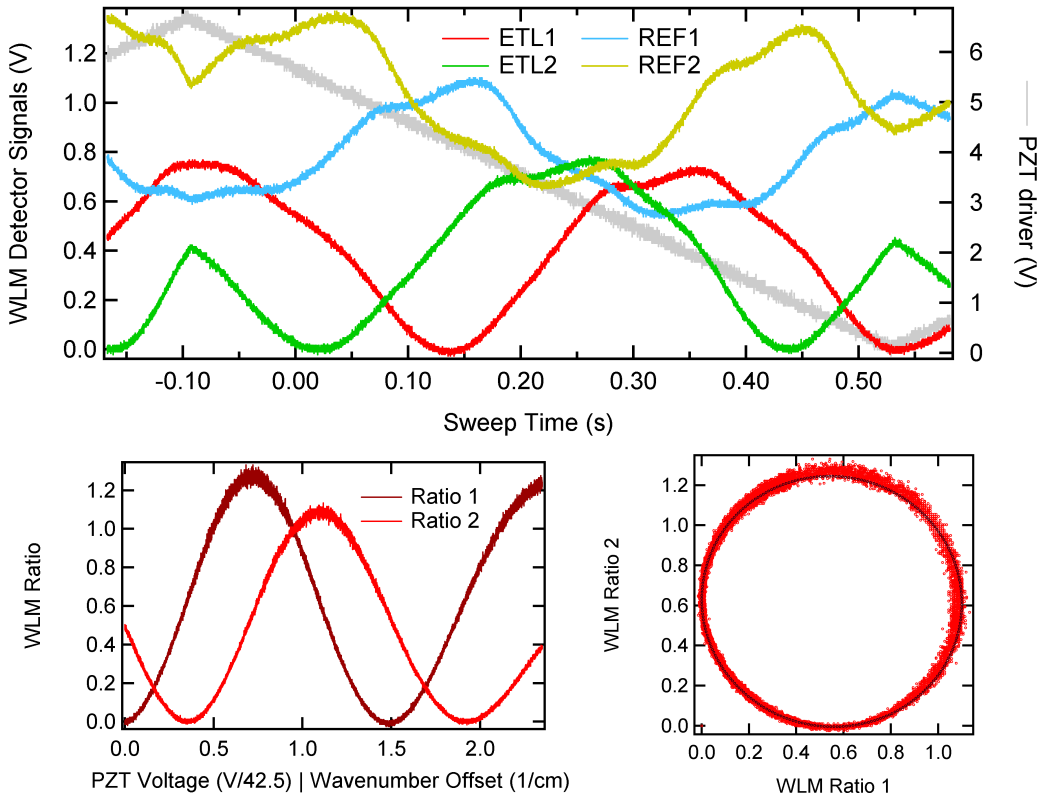

Figure 9.24: TOP: Measured detector signals from the four detectors when sweeping the laser frequency with the piezo from 0 to 100 V. BOTTOM: Corresponding ratio plots for the two etalon signals.

In the ratios I_R/I_T this laser power effect is negligible, and the sinusoidal shape is more pronounced. The ratio plot in figure 9.24 also shows that the applied PZT voltage does not provide a linear conversion to frequency, as the sinusoid gets more stretched at higher voltages. Comparing up slope and down slope voltage also shows pronounced hysteresis. Performing sinusoidal fit to each signal gives that their phase difference is 95°.

9.7.3.1 Scanning the full laser tuning range

Figure 9.25 shows the wavelength monitor measurements over a broader range of wavenumbers. This data was generated by connecting the wavelength monitor to the Picarro G1000 wavelength monitor board. A python program was used collect the detector signals. First the dark currents were measured. The laser was then tuned in steps of 0.03cm^{-1} from 2185 cm^{-1} to 2215 cm^{-1}. For each step the detector signals were recorded and subtracted

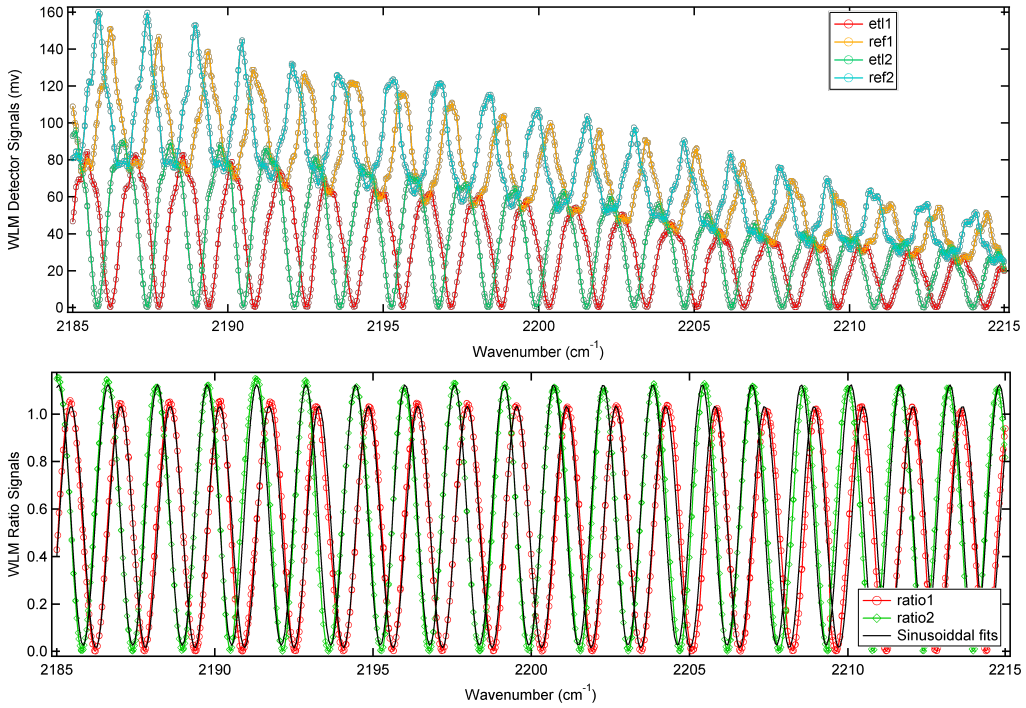

Figure 9.25: Detector signals and Ratios, when stepping the laser frequency with the controller. The quadrature plot for this measurement is shown in figure 9.26

by the respective dark currents, and the wavenumber was read from the laser. During the measurement the temperature was controlled to within 0.6 °C .

As the laser wavenumber is tuned toward higher wavenumbers the laser intensity drops, yet the ratios I_R/I_T (also shown in figure 9.25) keeps their amplitude. Performing a sinusoidal fit yields an Etalon FSR of 1.5645 ± 0.00026 cm^{-1} (46.935 GHz±7.8 MHz)[5] and a phase difference of 92° between the two signals. The FSR reported here is with respect to the one reported by the laser.

Figure 9.26 shows a plot of ratio against ratio from which it is seen that the ellipse becomes more circular toward larger wavenumbers, which may reside from nonlinearities of the parameters in equation 9.28.

A full frequency performance test of the wavelength monitor could not be made, as the precision proceeded that of the available spectrometer used in section 9.2.4. Ideally a wave-meter for the mid-infrared would be used to calibrate the wavelength monitor over the full range of its operation. The following section provides analysis and estimate of the wavelength monitor

[5]± indicate 1 sigma fit residuals

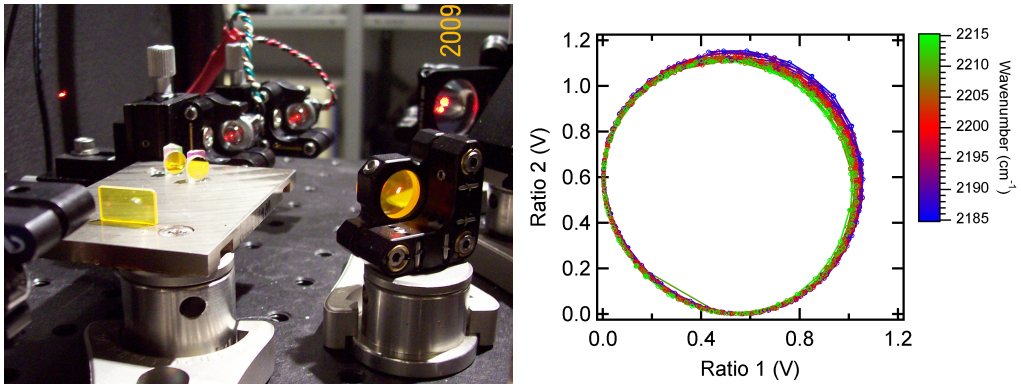

Figure 9.26: Left: A setup for a wavelength monitor. Right: The quadrature data for the full range tuning measurements in figure 9.25.

precision.

9.7.3.2 Wavelength monitor precision

The main components governing the precision of the wavelength monitor is the etalon material, thickness and surface qualitiy and the detector performance. Larger reflectivity of the Etalon provides a larger signal in transmission and reflectivity. Equation (9.1) provides a crude performance estimate for an Etalon. Expressed in terms of the detector currents

$$\delta\nu = \frac{\mathrm{FSR_E}}{2\pi}\frac{\delta i_D}{i_A} \tag{9.31}$$

where $i_A/\delta i_D$ is the signal to noise ratio of the detector currents. The signal amplitude i_A is given by the maximum of the Etalon reflection (eq. 9.16) $F/(1+F)$. Assuming that the Etalon is made from ZnSe and using the reflectivity at normal incidence this is ca. 50%.

Detector noise Used in the wavelength monitor was an uncooled Mercury cadmium telluride (MCT, (HgCdZn)Te) model PVI-5 from Vigo. This detector has a detectivity $D^* = 3.00 \times 10^9$ cmHz$^{1/2}$/W, Responsivity 1.3 A/W, Bandwidth 10MHz and Area 1mm^2. This provides a minimum detectable current of 0.14 µA. The linearity of the detector was measured by connecting the photo diode directly to an ammeter, and measuring the current for different applied laser powers. [6]From this measurement the data in figure 9.27 was obtained, showing that light intensities should stay below ca.

[6]To get reasonable photo power the beam from the laser body was reflected of from a BaF_2 flat at 45° The transmission from this flat was used to measure the power with a

100 µW in order to ensure detector linearity. Letting 150 µA be the current at maximum Etalon transmission, the Etalon signal amplitude is 75 µA giving a signal to noise ratio of 531. Finally the frequency precision $\delta\nu$ can be estimated for different Etalon FSR's giving values shown in figure 9.27. The performance could be improved by a factor of 2 choosing a smaller detector area of 0.2 mm.

The detectors are strongly dominated by Johnson noise. Assuming a shunt resistor of 100 Ω the Johnson noise will be $\delta i = \sqrt{4k_BT/R} = 40$ nA. In comparison the measured dark current of 4.5 µA provides a shot noise $\delta i = \sqrt{2ei_{\text{dark}}\Delta f} = 3.7$ nA, which is an order of magnitude lower.

A better performance could in theory be obtained by choosing a smaller detector area but this complicates alignment and collection of the full beam power.

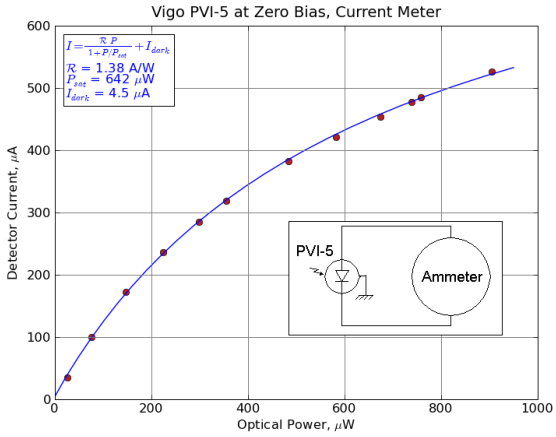

FSR (GHz)	$\delta\nu$ (MHz)
5	1.50
12.5	3.75
25	7.49
50	14.99
100	29.97
150	44.96

Figure 9.27: Left: Linearity measurement of the PVI-5 MCT detector. Right: Table of $\delta\nu = \text{FSR}_\text{E}/(2\pi\text{SNR})$*, for the signal to noise ratio* $\text{SNR} = 531$.

power meter. The reflection from the BaF_2 flat was reflected on another BaF_2 flat and then applied onto the Photodetector. Using the index of refraction for BaF_2 at 4.5 µm the laser power measured with the power meter was calculated into the power applied onto the photo diode.

10 Characterization of analyzer performance

This chapter presents data demonstrating the performance of the analyzer measurements of N_2O concentration and isotopomer ratios. Presented first are spectroscopic measurements performed with the analyzer. A spectral fitting routine was only generated for measurements of the N_2O concentration and the two ^{15}N isotopomers. The performance of the concentration and isotopomer ratio measurements is presented in the last section of this chapter. In the following the minimum of the Allan deviation (using a sliding interval, see appendix A) is applied to determine the minimum obtainable sensitivity and the optimal averaging interval, unless otherwise stated. In the following Allan plots both the consecutive interval and sliding interval calculated Allan deviations are plotted.

10.1 Performance of cavity ring down measurements

Proceedure: Figure 10.1 shows the cavity ring down performance of the system. This measurement was performed by keeping the cavity fixed and detuning the laser frequency by 800 MHz with a sawtooth signal at a sweep-rate of 110MHz/ms. 50000 ringdowns were collected over the coarse of 11.6 minutes. The cavity pressure was set at 200 torr and was flushed with technical air at ca. 50 sccm.

Results and discussion: This ring down dataset shows a mean loss of 6.39 ppm cm^{-1} with a 1σ noise of 2.18 ppb cm^{-1} and a linear drift of -0.34 ppb cm^{-1}/min collected at a rate of 72 Ring downs per second. Leaving an optimal averaging time of 14 seconds with a minimum detectable absorption

of 0.08 ppb cm^{-1}. The measured drift in absorption loss is likely to originate from thermal drift so the a linear correction has been applied to generate the data plotted in figure 10.1. The thermal drift of the Etalon during the measurement was 0.0015 °C which accounts for -0.12 MHz/min using values of table 9.2. The rest of the drift may come from a larger temperature drift in the optics box, exterior to the wavelength monitor.

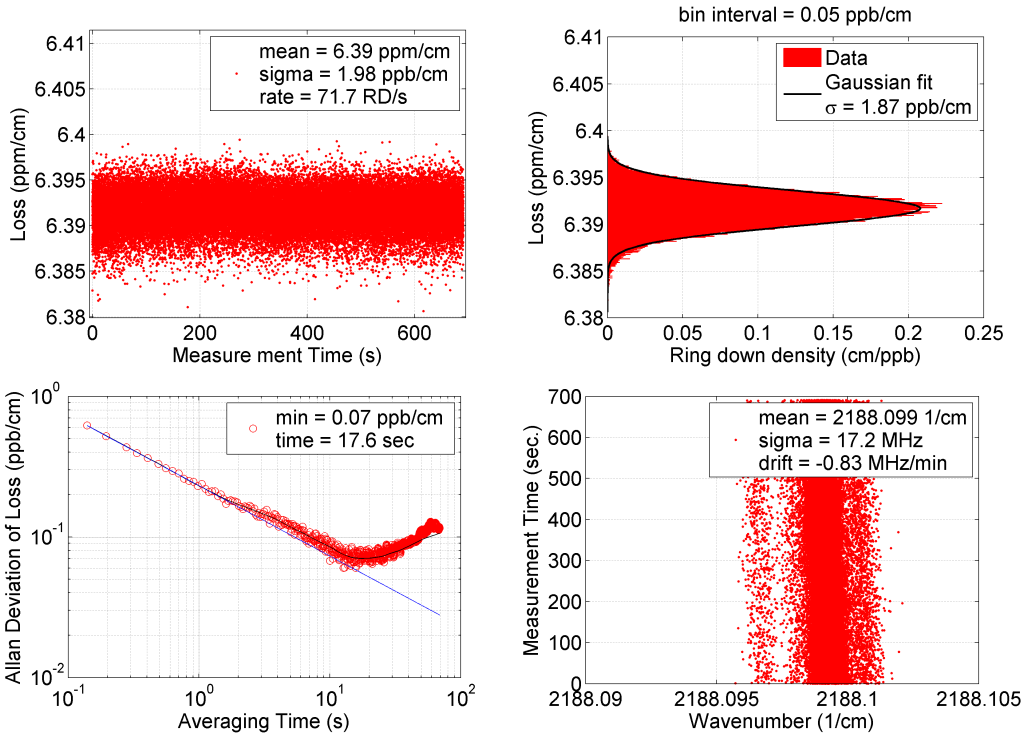

Figure 10.1: Ring Down performance of the presented analyzer. Cavity filled with technical air at 200 torr and 21 °C . The NEA is $2.3 \times 10^{-10}\mathrm{cm}^{-1}/\sqrt{\mathrm{Hz}}$ *UpperLeft: Plot of 50000 consecutive loss measurements. Upper Right: Histogram of the loss measurements. Lower Left: Allan deviation plot showing that minimum detectable absorption is* $7 \times 10^{-11}\mathrm{cm}^{-1}$. *Blue line shows the slope for* $1/\sqrt{\tau}$. *Lower Right: Measured wavenumber of the laser at the time of the ring down.*

Applying a linear correction provide a mean loss of 6.39 ppm/cm with a 1σ noise of 1.98 ppb/cm corresponding to a 0.031% shot to shot noise. With this approach the Allan deviation average down for 18 seconds obtaining a minimum detectable absorption of 0.07 ppb cm^{-1}. I.e. the linear correction does not have big influence on the performance, and thus higher order effects must be at play. The histogram in figure 10.1 shows a nearly gaussian distribution with slightly higher density in the arm of lower loss values. From the Allan variance plot of figure 9.2 the data is seen to average according to $1/\sqrt{\tau}$

(Indicated with blue line) for values of τ less than 10 seconds. Inspecting the precision of the individual a Levenberg-Marquardt fit of the ring downs, showed a 0.03% fit uncertainty (w. ring-down sampled at 10 MHz, and SNR of 2000). This is in good agreement with the estimate in section 7.2.3. This also indicates that the ring-down noise is limited by the detector.

The spread in the recorded wavelength is 17.2 MHz. This spread is on the order of magnitude of the laser line width. The wavelength monitor may be able to record the wavelength to higher precision, but timing at which the ring down is triggered may be at a stochastic time during which the laser is on resonance with the cavity, leaving the laser line width as the dominant uncertainty contributor.

The noise equivalent absorption at one second of averaging is $2.3 \times 10^{-10}\mathrm{cm}^{-1}/\sqrt{\mathrm{Hz}}$ as given by the 1 second Allan deviation. This is a factor of 3 worse than the results obtained by Halmer et al. [2005], but considering that their cavity is 5 times longer, the results presented here show potential to surpass the precision of Halmer et al. [2005]. Comparing to the OA-ICOS presented by Moyer et al. [2008] the results presented here is still an order of magnitude worse. It should be noted that both works by Halmer et al. [2005]; Moyer et al. [2008] use liquid nitrogen cooled detectors and lasers.

10.2 Measured absorption spectra

10.2.1 Spectral scan from 2163 cm^{-1} to 2235 cm^{-1}

The spectrum in figure 10.2 demonstrates the broad tuning ability of the analyzer. This spectrum was taken at an early stage of the development using the p-polarization of the cavity. The scan is performed tuning the laser in steps of 0.03 cm^{-1} using the laser controller coarse setting and keeping the laser pzt fixed at zero. The cavity is swept one full cavity FSR at a rate of 100 Hz to obtain frequent resonance. For each wavenumber step point of the laser, 100 ring downs were measured and averaged to provide the absorption data points in figure 10.2. The typical uncertainty in the 100 ring downs is 1% to 4% providing a standard error of mean of ca. 0.2% for each datapoint in Figure 10.2. The ring downs were collected with a 16 bit, 25 MHz electronic aqcuisition card (GaGe), and the ring down threshold was adjusted from 2 Volt to 0.1 Volt to accommodate for large absorptions. The cavity contains ambient air at 1 bar pressure at 21 °C but with no pressure or temperature control. The spectrum was sampled twice comparing a Liquid cooled detector (gray dots) with the TEC Vigo detector (red line). No significant difference is observed in the performance of the two measurements as other factors were

likely limiting the performance. This measurement was not redone with the final analyzer as it would require further FPGA programming and was not of priority. On figure 10.2 it should be noticed that an increased baseline noise

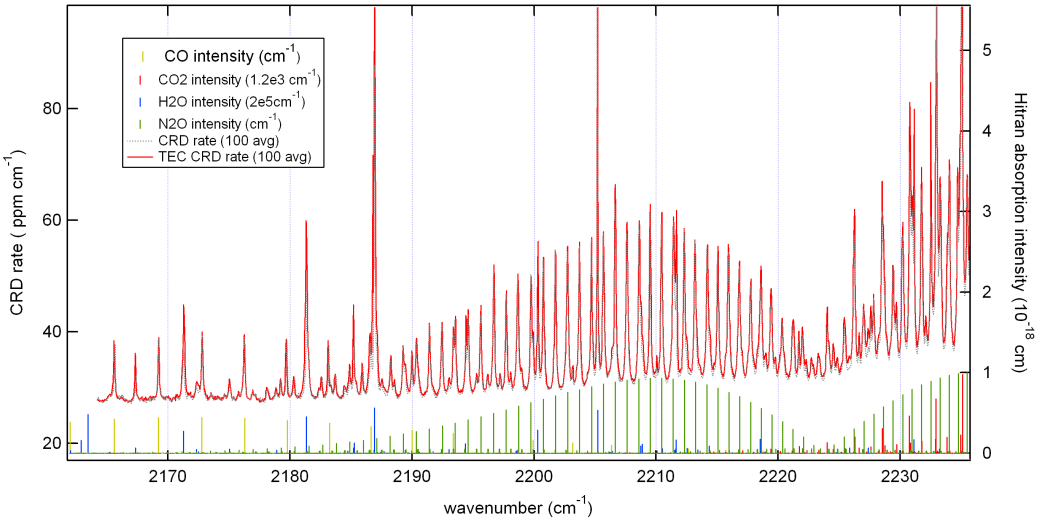

Figure 10.2: Absorption spectrum acquired using cavity ring down spectroscopy. Resolution is on the order of 50 MHz with a sampling interval of 900 MHz. At each step 100 ring downs are averaged. Absorption features are well identified from the spectral line intensities of Hitran plotted at the bottom.

is present below 2180 cm^{-1} and toward 2230 cm^{-1} and beyond absorption from $^{13}CO_2$ becomes very dominant. Beyond 2240 cm^{-1} it was practically not possible to measure the spectrum due to large absorption from CO_2.

10.2.2 Spectra of carbon monoxide

It has previously in literature been noted that measurements of Carbon Monoxide isotopologues showed larger fluctuations than would be expected from the precision of the analyzer Wächter [2007]. In this work it was observed that also the concentration itself of CO fluctuate by large amounts also on short timescales. This is supported by the spectroscopic data shown in Figure 10.3. The figure shows a sequence of 10 spectra taken in 18 second intervals plotted in different colors. Each spectrum contains a 1000 ring down measurements, sampled at 150 MHz frequency spacing.

Results and discussion These measurements show that the CO absorption line at 2190 cm^{-1} has a peak height variation of 0.7 ppm/cm full range

(i.e. $> 10\%$, and stdev $= 0.28$ ppm/cm i.e. 4%) observed within seconds. In comparison the N_2O peak height is stable to within 0.5%. This peak height fluctuation was also observed for higher pressures and under static cavity conditions i.e. no flow. In terms of the the ambient CO concentration of 100 ppbv this fluctuation correspond to 10 ppbv. The fluctuation was also observed at different cavity pressures, ranging from 50 torr to 400 torr. With the high cavity pressure shown in figure 10.3 it can be excluded that the spectral variation is based on poor wavelength targeting.

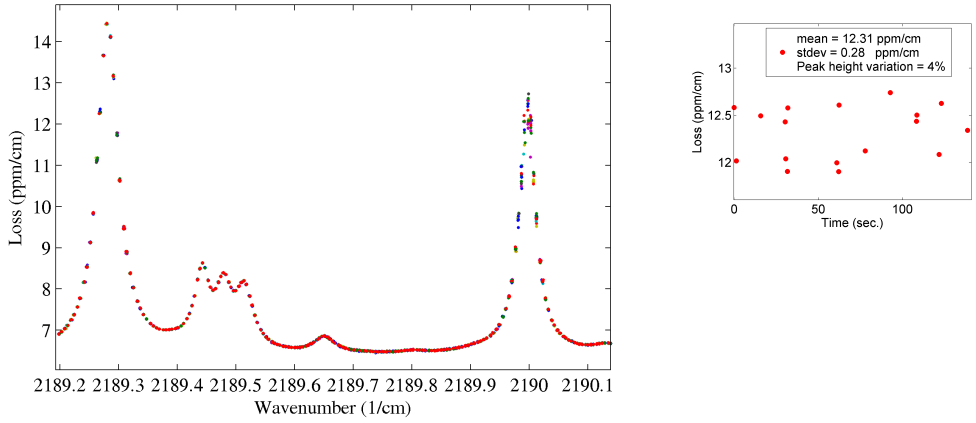

Figure 10.3: Left: Absorption spectrum of N_2O and CO sampled over 150 seconds. Right: Measurements of the CO peak absorption as a function of time. Notice the fluctuation is higher than 4%

The CO concentration fluctuation is not likely to origin from diffusion effects as N_2O is not seen to have a similar fluctuation. The variation is not likely to origin from thermal fluctuations either as these CO lines has a smaller thermal sensitivity than the neighboring N_2O lines as seen from table 7.1. Speculations have been made, that CO has large adsorption interaction with stainless steel surfaces, which the cavity body is made from. If adsorption is the source of the concentration fluctuation, applying a coating to the inside of the cavity body, will be essential in order to obtain high precision measurements of CO. Further investigations on long term changes (in terms of hours) would have to be measured to make further conclusions. This was not possible within the time span of the presented work.

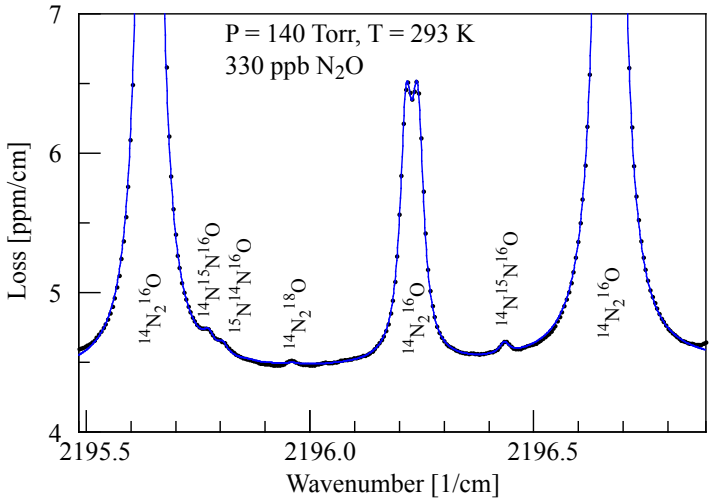

Figure 10.4: Measured spectrum of $^{14}N_2^{18}O$.

10.2.3 Spectra of N_2O isotopologues

The spectral scans of N_2O isotopologues in figure 10.4 and 10.5 are collected by the same procedure as for the Carbon monoxide. Each spectrum contains 1000 ring down measurements, sampled at 150 MHz frequency spacing. Each of the two plots are generated by averaging 50 spectra. The spectral resolution is ca. 20 MHz. The blue line through the data points has been generated by fitting the spectrum with galatry functions applying data from Hitran 2008.

Results and discussion Figure 10.4 shows the spectrum of $N_2{}^{18}O$ at 2196 cm^{-1} for atmospheric concentration of N_2O . The spectrum was collected at a pressure of 140 Torr. The isotopologue lines of $N_2{}^{18}O$ at 2195.95 cm^{-1} and $^{14}N^{15}N^{16}$ at 2196.43 cm^{-1} are reasonably well resolved, but higher concentrations would be needed in order to achieve valuable precision. For biogeoscience knowledge of bulk $\delta^{15}N$ would also need to be measured in order to provide scientific relevance. However, a much lower pressure would be needed in order to spectroscopically resolve the $^{15}N_2O$ isotopomers absorption lines in this region. This cannot be achieved wiht the presented analyzer.

In the spectral region at 2187.9 cm^{-1} the isotopomer absorption lines are separated by 0.1 cm^{-1} rather than 0.3 cm^{-1}. The spectrum shown in figure 10.5 was used to calibrate the wavelength monitor for the positions of the absorption lines, however during operations it was found that poor wavelength targeting required that the pressure should be set at 200 Torr to

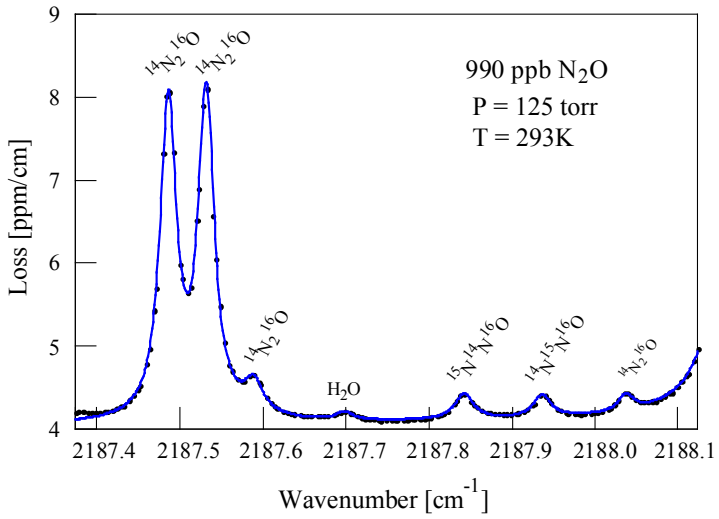

Figure 10.5: Measured fine scan of the spectral region applied for the continuous N2O isotopomer measurements.

optimize performance.

10.2.3.1 Spectral fitting for N_2O isotopomers ratios

Proceedure Figure 10.6 show the sampled spectrum during continuous operation. A sequence of four groups collect data for the three isotopologue lines. For each group the cavity length is kept fixed and the laser is tuned collecting absorption data in wavenumber intervals of $0.02\,\mathrm{cm}^{-1}$. The absolute value of the wavenumbers being collected is determined by the length of the cavity which is controlled by a feed back loop from the fitter optimizing cavity piezo voltage to target the peak of the desired absorption peak. The average wavenumber measured at the target wavelength and the distance to the neighboring measurement points spaced by the cavity FSR (designated the value $0.02\,\mathrm{cm}^{-1}$) is used to designate high precision wavenumber scale. A full sequence is typically captured in 16 seconds, combined by four groups being:

Group 1 collects 150 ring downs from $2187.41\,\mathrm{cm}^{-1}$ to $2187.77\,\mathrm{cm}^{-1}$ sampling the N_2O double peak and the water line.
Group 2 zooms into the double peak to improve statistics of the peak height. 150 ring downs is sampled from $2187.505\,\mathrm{cm}^{-1}$ to $2187.565\,\mathrm{cm}^{-1}$.
Group 3 zooms onto $^{15}N^{14}N^{16}O$ collecting 200 ring downs from $2187.79\,\mathrm{cm}^{-1}$ to $2187.91\,\mathrm{cm}^{-1}$.
Group 4 zooms onto $^{14}N^{15}N^{16}O$ collecting 200 ring downs from $2187.87\,\mathrm{cm}^{-1}$

to 2188.03 cm^{-1}.

Using the average ring down for each cavity resonance, the spectrum in figure 10.6 is typically measured. The green line through the measurement points is the Galatry fit through the datapoints, for which the residuals EW shown in the lower plot of Figure 10.6. The fit residual is less than 50 ppb cm^{-1} over the full range and less than 8 ppb cm^{-1} at the isotopomer peaks. It is worth noting that from equation 7.16 and using peakheights table 7.2 the peak height error of the less abundant isotopologue (height 80 ppb cm^{-1}) is 12.5‰/(ppb cm^{-1}) given that this is the dominant error. Using this an error of 8 ppb/cm corresponds to an error of 100‰ in the δ-value. However if the fitting error is systematic the spectral fit from consecutively captured spectra may still be much better.

10.3 N_2O measurements

10.3.1 Performance of N_2O concentration measurements

For ambient concentration measurements, figure 10.7 shows a measurement over the course of four days. A data point is recorded every 16.5 seconds. The concentration is recorded as 325 ppb ± 0.6 ppb (1σ). The minimum of the Allan deviation is 0.068 ppb, at an averaging interval of 12 minutes. On a 5 minute average the precision is 0.1 ppb (1σ). For measurements of higher concentration it was found that the relative precision is 0.14% for concentrations within the range from 0.3 ppm to 4 ppm. Above 4 ppm the relative degrades increases rapidly.

10.3.2 Performance of δ^{15}N-N_2O isotopomer measurements

10.3.2.1 Reference for reported delta values

It was not possible within this work to establish suitable isotopomer standards with N_2O concentration levels of 1 ppm. Thus no full calibration of the analyzer was performed. To give a proxy of the performance all isotope values were calculated relative to the peak height ratios found in the ambient air at the Picarro factory before shipment to Copenhagen. These ratios are $^{14}N^{15}N^{16}O$; $R_\alpha = 0.072196$ and for $^{15}N^{14}N^{16}O$; $R_\beta = 0.082604$. These ratios are large compared to those of atmospheric nitrogen $R = 0.00367$. To estimate the deviation from the delta value calculated from atmospheric nitrogen we can apply the Hitran database values for the absorption strengths to calculate the corresponding concentration ratios: $R_\alpha = 0.006$ and $R_\beta = 0.00682$.

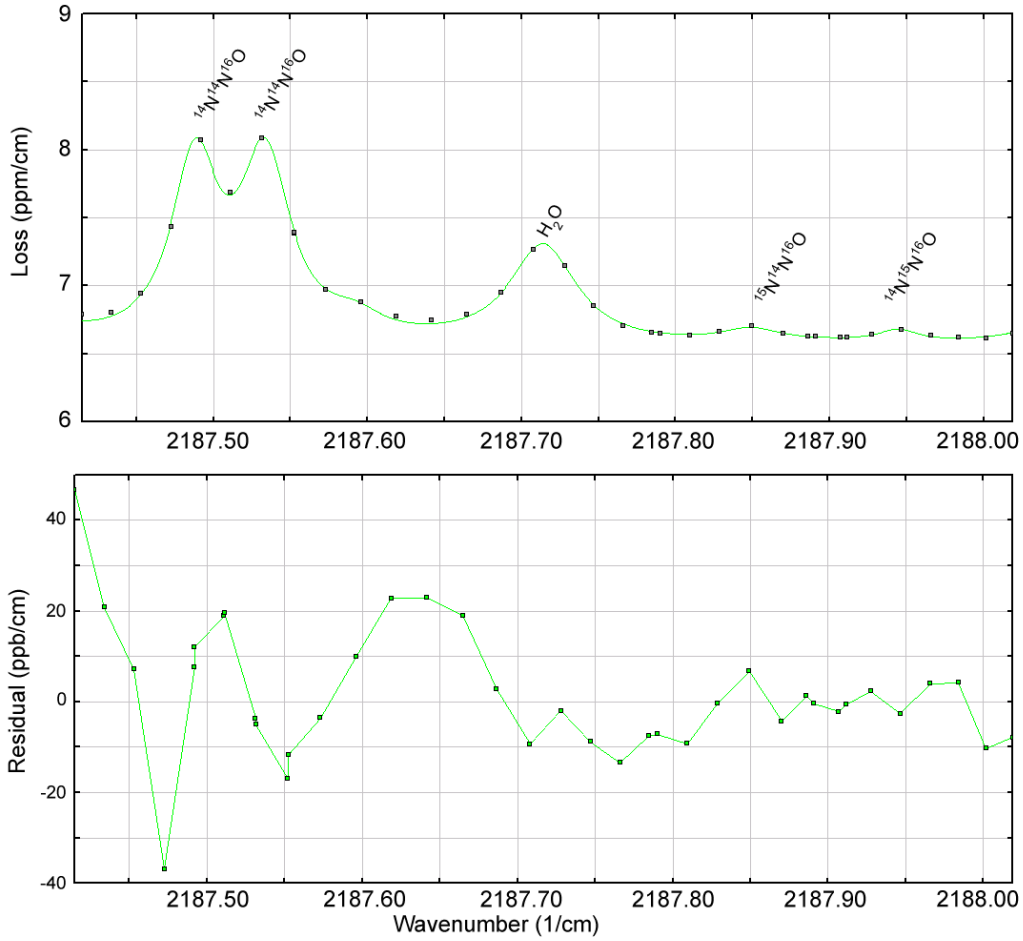

Figure 10.6: Spectral data collecting during normal operation of the analyzer. The analyzer multicomponent Galatry fit to the spectral lines is shown with the green line and in the plot below the corresponding fitting residual is shown.

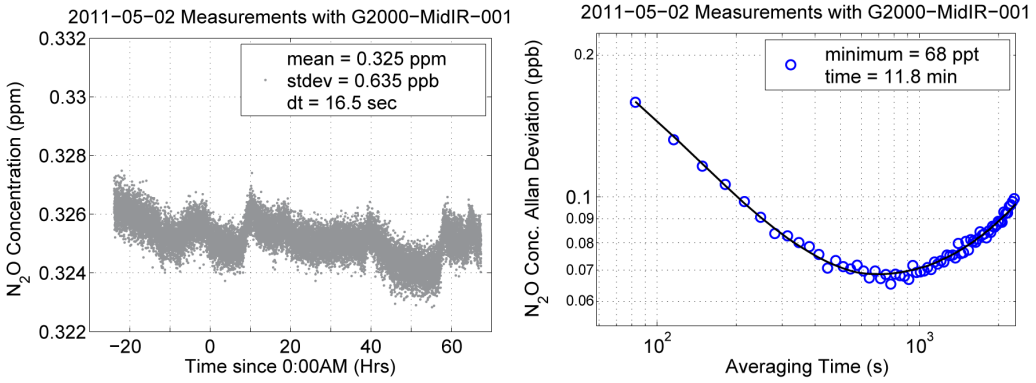

Figure 10.7: 90 Hours of measurements, on sample of ambient n2o concentration.

The concentration ratios only deviate by a factor of two from that of atmospheric nitrogen. It is therefore reasonable to expect that the delta precision obtained from the peak height ratios relative to ambient air at Picarro lies within a factor of two from the equivalent precision in delta value with respect to atmospheric air.

Circumstances of the analyzer were changed during the shipment but the isotopic δ-values were still measured relative to the peak height ratios measured at Picarro.

To the bio-geo-science literature the relevant delta values are relative to the ^{15}N ratio of atmospheric nitrogen. The system should be calibrated relative to two or more N_2O gases with known isotopomer composition in order to make measurements on the atmospheric nitrogen scale. This was not achieved in this work.

Figure 10.8 shows isotope measurements at ambient N_2O concentrations. The datapoints are reported at 16 second intervals, with a delta value precision of 12‰ to 14‰ for both isotopomers. Figure 10.9 shows measurements taken for a gas of 1ppm N_2O concentration. For the 1 ppm concentration, data points are also collected at 16 second intervals. With the elevated concentration, precision of the isotopomers improve, to better than 5‰. This measurement was run with a zero flow cavity condition, by closing both valves. During the measurement the cavity pressure was observed to linearly increase by 12 torr over the coarse of the 7 hours of measurements. This drift was also apparent in the isotopomer measurement and a linear correction was applied to provide the shown data.

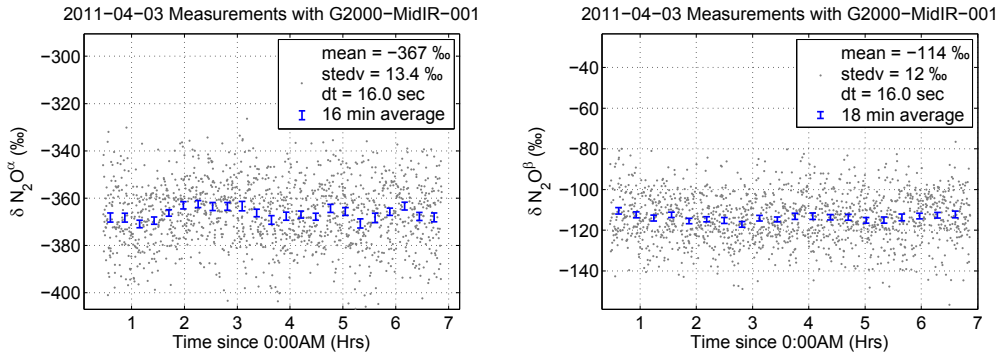

Figure 10.8: N_2O isotopomer measurements at ambient ca. 330 ppb concentrations. Blue error bars indicate the 1σ standard error of mean over the averaging interval.

Figure 10.10 shows the Allan variance for the four data series as shown in figure 10.8 and 10.9. For the first 20 minutes all four Allan deviations are seen to follow the $1/\sqrt{\tau}$ (indicated with blue solid line). Beyond this a systematic error is seen to degrade the averaging performance. For the ambient

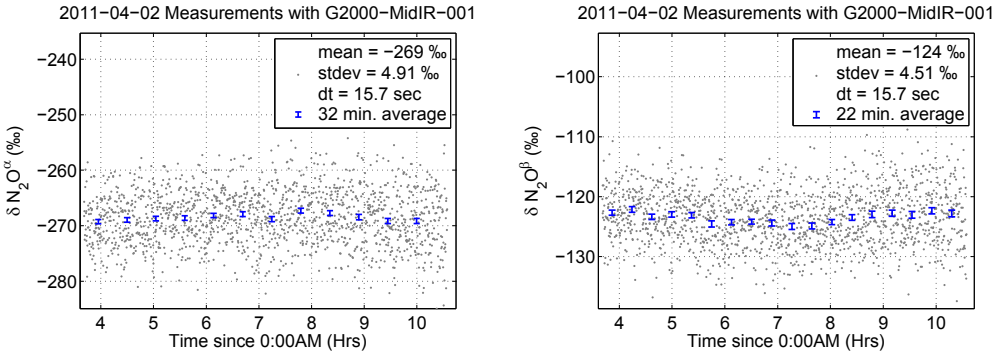

Figure 10.9: N_2O isotopomer measurements at 1 ppm N_2O concentration. Blue error bars indicate the standard error of mean over the averaging interval.

concentration 0.3 ppm the minimum Allan deviation is reached at 1‰ with 100 minutes of averaging. With a 1ppm N_2O concentration the minimum Allan Deviation is reached with 70 minutes of averaging with a minimum detectable δ-value of 0.5‰ for both isotopomers. With an averaging time of 5 minutes the Allan deviation is below 1.5‰ but it takes 10 minutes of averaging to reach below 1‰.

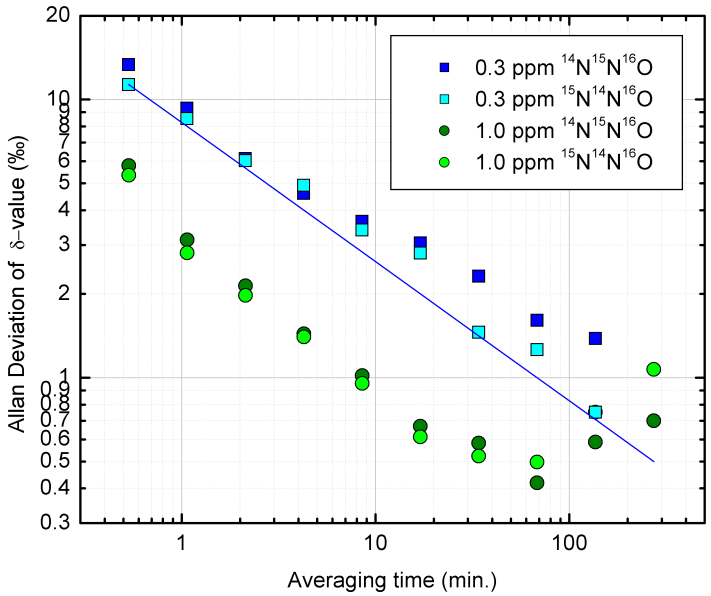

Figure 10.10: Allan deviation for measurements at 0.3 ppm and 1 ppm N_2O concentration.

11

Summaries, conclusions & outlooks

In this thesis we introduced new applications of CRDS measurements for biogeoscience, and demonstrate the capabilities in terms of replacing IRMS measurements with CRDS.

11.1 Development of a novel mid-infrared CRDS spectrometer and its applications

In this work a novel and fully automated, mid-infrared cavity ring down spectrometer, was designed, built and applied to biogeoscientific measurements. This fully operational CRDS analyzer performs automated measurements on N_2O concentrations and isotopomer ratio measurements on the rare species of $^{14}N^{15}N^{16}O$ and $^{15}N^{14}N^{16}O$. At ambient concentrations of N_2O (i.e. ca. 320 ppb concentration) the analyzer provides continous datapoints in 17 second time intervals with a 1σ precision 0.6 ppb for the N_2O concentration and ca. 12‰ for the two isotopomers. With extended averaging times Allan variance analysis provides that a minimum detectable N_2O concentration of 68 ppt is reached in 11.8 minutes, while the minimum detectable isotopomer δ-value of 1‰ is reached within 100 minutes.

At elevated N_2O concentrations of 1 ppm the precision improves significantly for the isotopomer measurements providing a precision better than 1‰ in 10 minutes and a minimum detectable δ-value of $\leq$ 0.5‰ averaging over 70 minutes for both isotopomers.

In terms of absorption benchmark this analyzer has a NEA = $2.3 \times 10^{-10}\text{cm}^{-1}/\sqrt{\text{Hz}}$, which is an order of magnitude short of the cavity enhanced absorption spectroscopy by Moyer et al. [2008]. However considering the cell volume, this analyzer may still be the best suited instrument for measure-

ments with small availability of sample. In terms of absorption benchmark this analyzer has a NEA $= 2.3 \times 10^{-10} \mathrm{cm}^{-1}/\sqrt{\mathrm{Hz}}$, which is an order of magnitude short from the cavity enhanced absorption spectroscopy by Moyer et al. [2008]. However considering the cell volume, this analyzer may still be the best suited instrument for measurements with small availability of sample.

Experiments with trapping of discrete samples in the CRDS cell were applied, giving an average precision of 1.2‰ for both isotopomers with N_2O concentrations between 1 and 2 ppm. The reproducibility of these measurements was 10‰. Application to real samples was also investigated. A melt, purge and trap extraction system for ice core measurements was built and tested on a real ice core sample. However, a full characterization of performance was not possible within the scope of this work. Microbial Nitrification and de-nitrification processes was also addressed. Samples of lake sediments from Bøllemosen in Denmark were bottled and added with glucose, plus the nitrification inhibitor Dicyandiamide, and incubated for 4 weeks at 21°C. Measurements of the N_2O from the headspace of these bottles showed occurrence of absorption lines not reported in the Hitran 2008 database. From measurements of carbon monoxide absorption lines, high speed concentration variations of (ca. 10 %) were observed with the system.

11.1.1 Future perspective for the mid-infrared CRDS analyzer

The here presented mid-infrad analyzer was the the prototype development for the commercial N_2O isotopomer analyzer being launched by Picarro Inc. in August 2011. The design of the final commercial analyzer was based on suggested improvements recommended by this work. These recommendations were to: make the cavity longer, exchange the laser with a narrow band DFB-QCL, improve mirrors, apply cooling to the wavelength monitor detectors, and improve the thermal control of the optical environment. Another improvement worth mentioning could be implementation of optical-feedback to improve cavity transmission. Such a system could also open for higher spectral resolution by applying a fast feedback control from wavelength monitor to cavity length. This could make the precision of wavelength monitor the limiting confinement.

This work is not only the basis for a new product, but actually for a whole new line of products operating in the mid-infrared. These analyzers will give accessibility to whole range of relevant components that is not detectable with near-infrared spectroscopy.

In the applications to microbial nitrification and de-nitrification experi-

ments, the developed analyzer provide ideal circumstances, for studying dynamics of the microbial processes. This is so, due to the continuous operation of the CRDS analyzer. Such measurements of dynamics could be conducted in the lab as well as in the field in the natural environment of the source.

11.2 Measurements of δ^{13}C in rocks

This work studied the application of the novel Picarro CM-CRDS system for measurements of $\delta^{13}C_{VPDB}$ in rock samples. It was shown that a precision of 0.1 ‰ and better is achievable for kerogen and graphitic rock samples, by this combination of a flash combustion oven followed by a cavity ring down spectrometer. The sample should be smaller than 30 mg and have a carbon content higher than 3 % in order to have a precision better than 0.1 ‰. The combustion process is highly dependent on available oxygen and the wrapping of the samples.

It was found that rocks containing more than 0.5% TOC provide effective combustion and sufficient yield of CO_2 to obtain analytical precision of the Carbon 13/12 ratio. It was found that 1 mg of carbon correspond to a CO2 concentration of 3000 ppm in the laser spectrometer. The instrument is stated to have a δ^{13}C precision of 0.1‰ when CO_2 concentrations are within the range 2000 ppm to 4000 ppm (0.6 mg to 1.3 mg Carbon). Measurements of USGS-24 graphite standard was made which show that the best precision may be achieved with concentrations ranging from 3000 ppm to 7500 ppm (1 mg to 2.5 mg Carbon) providing a precision of 0.05‰ in δ^{13}C. Large memory effects was observed in the combustion unit in some experiments. We have worked to optimize Oxygen flow and sample packaging to alleviate this problem. This study show that total sample mass of less than 75 mg and a 20 mL oxygen pulse for flash combustion effectively eliminate memory effects in the combustion unit.

Measurements of several kinds of geological samples was also made, among these experiments on δ^{13}C measurements of carbonates. Powdered carbonates were mixed with quartz powder and find a precision of these measurements better than 0.1‰. Work on inter comparison measurements with mass spectrometric measurements, of samples straddling the SPICE isotopic excursion in a Cambrian Alum shale stratigraphic section, was also presented. These measurements showed an average agreement of 0.3‰ without using common calibration standards.

Experiments tuning the the parameters of the CRDS system, in terms of injected sample concentration or averaging time, precision of < 0.03‰ was achieved by the analyzer. The main drift effect in the presented CM-CRDS

system was concluded to originate from the combustion module. An advantage of CRDS compared to IRMS, is that the CRDS method provides a simple quantification of the combustion, in terms of completeness, and background levels, due to the Liaison collection system. Finally the continuous flushing of high grade nitrogen through the system provides an highly effective cleaning of the system which is not similarly possible in the ultra high vacuum of the mass spectrometer.

In conclusion it was found that the CM-CRDS system is a suitable solution for the $\delta^{13}C$ of the Isua rock cores. The system consumables is only pure oxygen and nitrogen which is cheaper than for He used with IRMS systems.

11.2.1 Future perspectives

The major source of drifts in the studied CM-CRDS was concluded to be incomplete combustion of the samples. Future projects could address improvements of the combustion process. Automatic adjustment of the CO_2 concentration injected to the CRDS could also be implemented in the future to make the packaging of samples easier. One could also imagine system integrating CRDS with laser ablation. For such kind of a system careful consideration to particle filtering should be made.

With the advent of the mid-infrared CRDS systems, new components become accessible. Combining mid-infrared systems with a combustion module could provide a high precision analyzer for isotopes of SO_2 and N_2O.

Bibliography

Ahlberg, P., Axheimer, N., Bascook, L. E., Eriksson, M. E., Schmitz, B., and Terfelt, F. (2009). Cambrian high-resolution biostratigraphy and carbon isotope chemostratigraphy in Scania, Sweden: first record of the SPICE and DICE excursions in Scandinavia. *Lethaia*, 42(1):2–16.

Ahn, J., Borook, E. J., and Howell, K. (2009). A high-precision method for measurement of paleoatmospheric CO_2 in small polar ice samples. *Journal of Glaciology*, 55, no. 191:499–506.

Andersen, K. K., Svensson, A., Johnsen, S. J., Rasmussen, S. O., Bigler, M., Rothlisberger, R., Ruth, U., Siggaard-Andersen, M.-L., Peder Steffensen, J., Dahl-Jensen, D., Vinther, B. M., and Clausen, H. B. (2006). The Greenland Ice Core Chronology 2005, 15-42 ka. Part 1: constructing the time scale. *Quaternary Science Reviews*, 25(23-24):3246–3257.

Anderson, D. Z. (1984). Alignment of resonant optical cavities. *Appl. Opt.*, 23(17):2944–2949.

Appel, P. W. U., Rollinson, H. R., and Touret, J. L. R. (2001). Remnants of an Early Archaean (>3.75 Ga) sea-floor, hydrothermal system in the Isua Greenstone Belt. *Precambrian Research*, 112(1-2):27 – 49.

Balslev-Clausen, D. (2007). Broad band cavity enhanced direct frequency comb spectroscopy – applied to Molecular beams & Trace gas detection. Master's thesis, University of Copenhagen.

Barriga, P., Zhao, C., and Blair, D. (2005). Optical design of a high power mode-cleaner for AIGO. *General Relativity and Gravitation*, 37:1609–1619.

Battle, M., Bender, M., Sowers, T., Tans, P. P., Butler, J. H., Elkins, J. W., Ellis, J. T., Conway, T., Zhang, N., Lang, P., and Clarket, A. D. (1996). Atmospheric gas concentrations over the past century measured in air from firn at the South Pole. *Nature*, 383(6597):231–235.

Berden, G. and Engeln, R., editors (2009). *Cavity Ring-Down Spectroscopy Techniques and Applications*. Wiley.

Bergamaschi, P., Schupp, M., and Harris, G. W. (1994). High-precision direct measurements of $^{13}CH_4/^{12}CH_4$ and $^{12}CH_3D/^{12}CH_4$ ratios in atmospheric methane sources by means of a long-path tunable diode laser absorption spectrometer. *Appl. Opt.*, 33(33):7704–7716.

Bernard, S., Rockmann, T. R., Kaiser, J., Barnola, J. M., Fischer, H., Blunier, T., and Chappellaz, J. (2006). Constraints on N_2O budget changes since pre-industrial time from new firn air and ice core isotope measurements. *Atmospheric Chemistry and Physics*, 6:493–503.

Bernhardt, B., Ozawa, A., Jacquet, P., Jacquey, M., Kobayashi, Y., Udem, T., Holzwarth, R., Guelachvili, G., Hansch, T. W., and Picque, N. (2010). Cavity-enhanced dual-comb spectroscopy. *Nat Photon*, 4(1):55–57.

Blunier, T. and Brook, E. J. (2001). Timing of Millennial-Scale Climate Change in Antarctica and Greenland During the Last Glacial Period. *Science*, 291(5501):109–112.

Blunier, T., Chappellaz, J., Schwander, J., Dallenbach, A., Stauffer, B., Stocker, T. F., Raynaud, D., Jouzel, J., Clausen, H. B., Hammer, C. U., and Johnsen, S. J. (1998). Asynchrony of Antarctic and Greenland climate change during the last glacial period. *Nature*, 394(6695):739–743.

Bol, R., Toyoda, S., Yamulki, S., Hawkins, J. M. B., Cardenas, L. M., and Yoshida, N. (2003). Dual isotope and isotopomer ratios of N_2O emitted from a temperate grassland soil after fertiliser application. *Rapid Communications in Mass Spectrometry*, 17(22):2550–2556.

Brenninkmeijer, C. A. M. and Rockmann, T. (1999). Mass spectrometry of the intramolecular nitrogen isotope distribution of environmental nitrous oxide using fragment-ion analysis. *Rapid Communications in Mass Spectrometry*, 13(20):2028–2033.

Buizert, C., Martinerie, P., Petrenko, V. V., Severinghaus, J. P., Trudinger, C. M., Witrant, E., Rosen, J. L., Orsi, A. J., Rubino, M., Etheridge, D. M., Steele, L. P., Hogan, C., Laube, J. C., Sturges, W. T., Levchenko, V. A.,

Smith, A. M., Levin, I., Conway, T. J., Dlugokencky, E. J., Lang, P. M., Kawamura, K., Jenk, T. M., White, J. W. C., Sowers, T., Schwander, J., and Blunier, T. (2011). Gas transport in firn: multiple-tracer characterisation and model intercomparison for NEEM, Northern Greenland. *Atmospheric Chemistry and Physics Discussions*, 11(5):15975–16021.

Canfield, D. E., Rosing, M. T., and Bjerrum, C. (2006). Early anaerobic metabolisms. *Philosophical Transactions of the Royal Society B: Biological Sciences*, 361(1474):1819–1836.

Chappellaz, J., Blunier, T., Kints, S., Dällenbach, A., Barnola, J.-M., Schwander, J., Raynaud, D., and Stauffer, B. (1997). Changes in the atmospheric CH_4 gradient between Greenland and Antarctica during the Holocene. *J. Geophys. Res.*, 102(D13):15987–15997.

Christensen, L. E., Brunner, B., Truong, K. N., Mielke, R. E., Webster, C. R., and Coleman, M. (2007). Measurement of Sulfur Isotope Compositions by Tunable Laser Spectroscopy of SO_2. *Analytical Chemistry*, 79(24):9261–9268.

Cossel, K., Adler, F., Bertness, K., Thorpe, M., Feng, J., Raynor, M., and Ye, J. (2010). Analysis of trace impurities in semiconductor gas via cavity-enhanced direct frequency comb spectroscopy. *Applied Physics B: Lasers and Optics*, 100(4):917–924.

Crosson, E. R., Ricci, K., Richman, B., Chilese, F., Owano, T., Provencal, R., Todd, M., Glasser, J., Kachanov, A., Paldus, B., Spence, T., and Zare, R. (2002). Stable Isotope Ratios Using Cavity Ring-Down Spectroscopy: Determination of $^{13}C/^{12}C$ for Carbon Dioxide in Human Breath. *Anal. Chem.*, 74:2003–2007.

Czerwinski, F., Richardson, A. C., and Oddershede, L. B. (2009). Quantifying Noise in Optical Tweezers by Allan Variance. *Opt. Express*, 17(15):13255–13269.

Dai, J., Mosley-Thompson, E., and Thompson, L. G. (1991). Ice Core Evidence for an Explosive Tropical Volcanic Eruption 6 Years Preceding Tambora. *J. Geophys. Res.*, 96(D9):17361–17366.

Dalrymple, G. B. (2001). The age of the Earth in the twentieth century: a problem (mostly) solved. *Geological Society, London, Special Publications*, 190(1):205–221.

Dansgaard, W. (1964). Stable isotopes in precipitation. *Tellus*, 16(4):436–468.

Dansgaard, W., Johnsen, S. J., Möller, J., and Langway, C. (1968). Oxygen isotope analysis of an ice core representing a complete vertical profile of a polar ice sheet. *ISAGE Symposium*, –:9394.

de Groot, P. A. (2009). *Handbook of Stable Isotope Analytical Techniques Vol. 2*. Elservier.

Dean, J. (1992). *Lange's Handbook of Chemistry*. McGraw-Hill, Inc.

Dore, J. E., Popp, B. N., Karl, D. M., and Sansone, F. J. (1998). A large source of atmospheric nitrous oxide from subtropical north pacific surface waters. *Nature*, 396(6706):63–66.

Elberling, B., Christiansen, H. H., and Hansen, B. U. (2010). High nitrous oxide production from thawing permafrost. *Nature Geoscience*, Advance Online Publication:–.

Engel, G. S., Drisdell, W. S., Keutsch, F. N., Moyer, E. J., and Anderson, J. G. (2006). Ultrasensitive near-infrared integrated cavity output spectroscopy technique for detection of CO at 1.57 μm: new sensitivity limits for absorption measurements in passive optical cavities. *Appl. Opt.*, 45(36):9221–9229.

Engeln, R., Berden, G., Peeters, R., and Meijer, G. (1998). Cavity enhanced absorption and cavity enhanced magnetic rotation spectroscopy. *Review of Scientific Instruments*, 69(11):3763–3769.

EPICA Community, M. (2006). One-to-one coupling of glacial climate variability in Greenland and Antarctica. *Nature*, 444:195–198.

EPICA Community, M., Augustin, L., Barbante, C., Barnes, P. R. F., Barnola, J. M., Bigler, M., Castellano, E., Cattani, O., Chappellaz, J., DahlJensen, D., Delmonte, B., Dreyfus, G., Durand, G., Falourd, S., Fischer, H., Fluckiger, J., Hansson, M. E., Huybrechts, P., Jugie, R., Johnsen, S. J., Jouzel, J., Kaufmann, P., Kipfstuhl, J., Lambert, F., Lipenkov, V. Y., Littot, G. V. C., Longinelli, A., Lorrain, R., Maggi, V., Masson-Delmotte, V., Miller, H., Mulvaney, R., Oerlemans, J., Oerter, H., Orombelli, G., Parrenin, F., Peel, D. A., Petit, J. R., Raynaud, D., Ritz, C., Ruth, U., Schwander, J., Siegenthaler, U., Souchez, R., Stauffer, B., Steffensen, J. P., Stenni, B., Stocker, T. F., Tabacco, I. E., Udisti, R., van de Wal, R. S. W., van den Broeke, M., Weiss, J., Wilhelms, F., Winther, J. G., Wolff, E. W.,

and Zucchelli, M. (2004). Eight glacial cycles from an Antarctic ice core. *Nature*, 429(6992):623–628.

Fiedler, S. E. (2005). *Incoherent broad-band cavity-enhanced absorption spectroscopy*. PhD thesis, Technical University of Berlin.

Fischer, J., Gamache, R., Goldman, A., Rothman, L., and Perrin, A. (2003). Total internal partition sums for molecular species in the 2000 edition of the HITRAN database. *Jour. Quant. Spec. Rad. Trans.*, 82:401–412.

Fluckiger, J. (2003). *Nitrous oxide and methane variations covering the last 100,000 years: Insight into climatic and environmental processes*. PhD thesis, University of Bern.

Fluckiger, J., Blunier, T., Stauffer, B., Chappellaz, M., Spahni, R., Kawamura, K., Schwander, J., Stocker, T. F., and DahlJensen, D. (2004). N_2O and CH_4 variations during the last glacial epoch: Insight into global processes. *Global Biogeochemical Cycles*, 18(1):–.

Fluckiger, J., Dallenbach, A., Blunier, T., Stauffer, B., Stocker, T. F., Raynaud, D., and Barnola, J. M. (1999). Variations in atmospheric N_2O concentration during abrupt climatic changes. *Science*, 285(5425):227–230.

Fluckiger, J., Monnin, E., Stauffer, B., Schwander, J., Stocker, T. F., Chappellaz, J., Raynaud, D., and Barnola, J. M. (2002). High-resolution Holocene N_2O ice core record and its relationship with CH_4 and CO_2. *Global Biogeochemical Cycles*, 16(1):–.

Forster, P., Ramaswamy, V., Artaxo, P., Berntsen, T., Betts, R., Fahey, D., Lean, J. H. J., Lowe, D., Myhre, G., Prinn, J. N. R., Raga, G., Schulz, M., and Dorland, R. V. (2007). *Climate Change 2007: The Physical Science Basis. Contribution of Working Group I to the Fourth Assessment Report of the Intergovernmental Panel on Climate Change*, chapter Changes in Atmospheric Constituents and in Radiative Forcing, pages 130–217. Cambridge University Press, Cambridge, United Kingdom and New York, NY, USA.

Galatry, L. (1961). Simultaneous effect of doppler and foreign gas broadening on spectral lines. *Phys. Rev.*, 122(4):1218–1223.

Gherman, T. and Romanini, D. (2002). Mode locked cavity enhanced absorption spectroscopy. *Optics Express*, 10:1033.

Gkinis, V., Popp, T. J., Johnsen, S. J., and Blunier, T. (2010). A continuous stream flash evaporator for the calibration of an IR cavity ring-down spectrometer for the isotopic analysis of water. *Isotopes in Environmental and Health Studies*, 46(4):463–475.

Gohle, C., Stein, B., Schliesser, A., Udem, T., and Hänsch, T. W. (2007). Frequency comb vernier spectroscopy for broadband, high-resolution, high-sensitivity absorption and dispersion spectra. *Physical Review Letters*, 99(26):263902.

Halmer, D., von Basum, G., Hering, P., and Mürtz, M. (2004). Fast exponential fitting algorithm for real-time instrumental use. *Review of Scientific Instruments*, 75(6):2187–2191.

Halmer, D., von Basum, G., Hering, P., and Mürtz, M. (2005). Mid-infrared cavity leak-out spectroscopy for ultrasensitive detection of carbonyl sulfide. *Opt. Lett.*, 30(17):2314–2316.

Hammer, C. U., Clausen, H. B., and Dansgaard, W. (1980). Greenland ice sheet evidence of post-glacial volcanism and its climatic impact. *Nature*, 288(5788):230–235.

Harvey, J. E. and Fender, J. S. (1982). Specifying surface finish and scattering tolerances of conical optical elements. *Opt. Eng.*, 21:983.

Hays, J. D., Imbrie, J., and Shackleton, N. J. (1976). Variations in the earth's orbit: Pacemaker of the ice ages. *Science*, 194(4270):pp. 1121–1132.

He, Y. and Orr, B. (2006). Detection of trace gases by rapidly-swept continuous-wave cavity ringdown spectroscopy: pushing the limits of sensitivity. *Applied Physics B: Lasers and Optics*, 85(2):355–364.

Hecht, E. (2002). *Optics*. Addison Wesley.

Herron, M. M. and Langway, Jr., C. C. (1980). Firn densification: an empirical model. *Journal of Glaciology*, 25:373–385.

Hippler, M., Mohr, C., Keen, K. A., and McNaghten, E. D. (2010). Cavity-enhanced resonant photoacoustic spectroscopy with optical feedback cw diode lasers: A novel technique for ultratrace gas analysis and high-resolution spectroscopy. *The Journal of Chemical Physics*, 133(4):044308.

Huang, H. and Lehmann, K. (2007). Noise in cavity ring-down spectroscopy caused by transverse mode coupling. *Opt. Express*, 15(14):8745–8759.

Johnsen, S. J., Dansgaard, W., and White, J. W. C. (1989). The origin of Arctic precipitation under present and glacial conditions. *Tellus B*, 41B(4):452–468.

Johnson, M. S., Billing, G. D., Gruodis, A., and Janssen, M. H. M. (2001). Photolysis of nitrous oxide isotopomers studied by time-dependent hermite propagation. *The Journal of Physical Chemistry A*, 105(38):8672–8680.

Jouzel, J., Masson-Delmotte, V., Cattani, O., Dreyfus, G., Falourd, S., Hoffmann, G., Minster, B., Nouet, J., Barnola, J. M., Chappellaz, J., Fischer, H., Gallet, J. C., Johnsen, S., Leuenberger, M., Loulergue, L., Luethi, D., Oerter, H., Parrenin, F., Raisbeck, G., Raynaud, D., Schilt, A., Schwander, J., Selmo, E., Souchez, R., Spahni, R., Stauffer, B., Steffensen, J. P., Stenni, B., Stocker, T. F., Tison, J. L., Werner, M., and Wolff, E. W. (2007). Orbital and millennial Antarctic climate variability over the past 800,000 years. *Science*, 317(5839):793–796.

Kaiser, J., Brenninkmeijer, C. A. M., and Rockmann, T. (2002a). Intramolecular $N-15$ and $O-18$ fractionation in the reaction of N_2O with $O(D-1)$ and its implications for the stratospheric N_2O isotope signature. *Journal of Geophysical Research-Atmospheres*, 107, no. D–14(D14):4214.

Kaiser, J., Röckmann, T., Brenninkmeijer, C. A. M., and Crutzen, P. J. (2003). Wavelength dependence of isotope fractionation in N_2O photolysis. *Atmospheric Chemistry and Physics*, 3(2):303–313.

Kaiser, J., Rockmann, T., and Brenninkmeijer, C. A. M. (2002b). Temperature dependence of isotope fractionation in N_2O photolysis. *Phys. Chem. Chem. Phys.*, 4(18):4420–4430.

Kaufmann, P. R., Federer, U., Hutterli, M. A., Bigler, M., Schupbach, S., Ruth, U., Schmitt, J., and Stocker, T. F. (2008). An improved continuous flow analysis system for high-resolution field measurements on ice cores. *Environ. Sci. Technol.*, 42:21.

Kim, K.-R. and Craig, H. (1993). Nitrogen-15 and Oxygen-18 Characteristics of Nistrous Oxide: A Global Perspective. *Science*, 262:1855.

Kleine, D., Dahnke, H., Urban, W., Hering, P., and Mürtz, M. (2000). Real-time detection of $^{13}CH_4$ in ambient air by use of mid-infrared cavity leak-out spectroscopy. *Opt. Lett.*, 25(21):1606–1608.

Koba, K., Osaka, K., Tobari, Y., Toyoda, S., Ohte, N., Katsuyama, M., Suzuki, N., Itoh, M., Yamagishi, H., Kawasaki, M., Kim, S., Yoshida, N.,

and Nakajima, T. (2009). Biogeochemistry of nitrous oxide in groundwater in a forested ecosystem elucidated by nitrous oxide isotopomer measurements. *Geochimica et Cosmochimica Acta*, 73(11):3115 – 3133.

Kogelnik, H. and Li, T. (1966). Laser beams and resonators. *Appl. Opt.*, 5(10):1550–1567.

Köhler, P. and Fischer, H. (2006). Simulating low frequency changes in atmospheric CO_2 during the last 740, 000 years. *Climate of the Past*, 2(2):57–78.

Legrand, M. and Mayewski, P. (1997). Glaciochemistry of polar ice cores: A review. *Rev. Geophys.*, 35(3):219–243.

Lehmann, K. K. (1996). Ring-down cavity spectroscopy cell using contiuous wave excitation for trace species detection.

Leuenberger, M. and Siegenthaler, U. (1992). Ice-age atmospheric concentration of nitrous oxide from an Antarctic ice core. *Nature*, 360(6403):449–451.

Lide, D. R., editor (2005). *CRC Handbook of Chemistry and Physics, 86th Edition*. Taylor & Francis.

Mandon, J., Guelachvili, G., and Picqué, N. (2008). Efficient two-comb fourier spectroscopy. 2008.

Mandon, J., Guelachvili, G., and Picque, N. (2009). Fourier transform spectroscopy with a laser frequency comb. *Nature Photonics*, 3(2):99–102.

Mandon, J., Guelachvili, G., Picqué, N., Druon, F., and Georges, P. (2007a). Femtosecond laser fourier transform absorption spectroscopy. *Opt. Lett.*, 32(12):1677–1679.

Mandon, J., Sorokin, E., Sorokina, I. T., Guelachvili, G., and Picqué, N. (2007b). Infrared frequency combs and supercontinua for multiplexing high sensitivity spectroscopy. 2007.

Manhes, G., Allègre, C. J., Dupré, B., and Hamelin, B. (1980). Lead isotope study of basic-ultrabasic layered complexes: Speculations about the age of the earth and primitive mantle characteristics. *Earth and Planetary Science Letters*, 47(3):370 – 382.

Martinez, R. Z., Metsälä, M., Vaittinen, O., Lantta, T., and Halonen, L. (2006). Laser-locked high repetition rate cavity ringdown spectrometer. *J. Opt. Soc. Am. B*, vol. 23, no. 4:727–740.

Meijide, A., Cardenas, L. M., Bol, R., Bergstermann, A., Goulding, K., Well, R., Vallejo, A., and Scholefield, D. (2010). Dual isotope and isotopomer measurements for the understanding of N_2O production and consumption during denitrification in an arable soil. *European Journal of Soil Science*, 61(3):364–374.

Melillo, J. M., Steudler, P. A., Feigl, B. J., Neill, C., Garcia, D., Piccolo, M. C., Cerri, C. C., and Tian, H. (2001). Nitrous oxide emissions from forests and pastures of various ages in the Brazilian Amazon. *J. Geophys. Res.*, 106(D24):34179–34188.

Mikhail Mazurenka, e. a. (2005). Cavity ring-down and cavity enhanced spectroscopy using diode lasers. *Annu. Rep. Prog. Chem., Sect. C,*, 101:100–142.

Milonni, P. W. and Eberly, J. H. (1988). *Lasers*. Wiley-Interscience.

Mohn, J., Guggenheim, C., Tuzson, B., Vollmer, M. K., Toyoda, S., Yoshida, N., and Emmenegger, L. (2010). A liquid nitrogen-free preconcentration unit for measurements of ambient n_2o isotopomers by *qclas*. *Atmospheric Measurement Techniques*, 3(3):609–618.

Mojzsis, S. J., Arrhenius, G., McKeegan, K. D., Harrison, T. M., Nutman, A. P., and Friend, C. R. L. (1996). Evidence for life on earth before 3,800 million years ago. *Nature*, 384:55 – 59.

Moosmüller, H., Varma, R., and Arnott, W. P. (2005). Cavity ring-down and cavity-enhanced detection techniques for the measurement of aerosol extinction. *Aerosol Science and Technology*, 39:30–39.

Morgan, C. G., Allen, M., Liang, M. C., Shia, R. L., Blake, G. A., and Yung, Y. L. (2004). Isotopic fractionation of nitrous osxide in the stratosphere: Comparison between model and observaions. *Jour. Geophys. Res.*, 109:D04305.

Morville, J., Kassi, S., Chenevier, M., and Romanini, D. (2005). Fast, low-noise, mode-by-mode, cavity-enhanced absorption spectroscopy by diode-laser self-locking. *Applied Physics B: Lasers and Optics*, 80:1027–1038.

Mosier, A., Kroeze, C., Nevison, C., Oenema, O., Seitzinger, S., and van Cleemput, O. (1998). Closing the global N_2O budget: nitrous oxide emissions through the agricultural nitrogen cycle. *Nutrient Cycling in Agroecosystems*, 52(2):225–248.

Motto-Ros, V., Morville, J., and Rairoux, P. (2007). Mode-by-mode optical feedback: cavity ringdown spectroscopy. *Applied Physics B: Lasers and Optics*, 87:531–538.

Moyer, E., Sayres, D., Engel, G., St. Clair, J., Keutsch, F., Allen, N., Kroll, J., and Anderson, J. (2008). Design considerations in high-sensitivity off-axis integrated cavity output spectroscopy. *Applied Physics B: Lasers and Optics*, 92(3):467–474.

N. Nikogosyan, D. (1997). *Properties of optical and Laser-related materials a handbook*. Joh Wiley & Sons Ltd.

Nelson, D., Shorter, J., McManus, J., and Zahniser, M. (2002). Sub-part-per-billion detection of nitric oxede in air using a thermoelectrically cooled mid-infrared quantum cascade laser spectrometer. *Appl. Phys. B*, 75:343 – 350.

Nevison, C. D., Keeling, R. F., Weiss, R. F., Popp, B. N., Jin, X., Fraser, P. J., Porter, L. W., and Hess, P. G. (2005). Southern Ocean ventilation inferred from seasonal cycles of atmospheric N_2O and O_2/N_2 at Cape Grim, Tasmania. *Tellus B*, 57(3):218–229.

Nevison, C. D., Kinnison, D. E., and Weiss, R. F. (2004). Stratospheric influences on the tropospheric seasonal cycles of nitrous oxide and chlorofluorocarbons. *Geophys. Res. Lett.*, 31(20):L20103–.

North Greenland Ice Core Project, M. (2004). High-resolution record of Northern Hemisphere climate extending into the last interglacial period. *Nature*, 431:147–151.

Ogawa, M. and Yoshida, N. (2005). Nitrous oxide emission from the burning of agricultural residue. *Atmospheric Environment*, 39(19):3421 – 3429.

O'Keefe, A. and Deacon, D. A. G. (1988). Cavity ring-down optical spectrometer for absorption measurements using pulsed laser sources. *Review of Scientific Instruments*, 59(12):2544–2551.

Olsen, S. C., McLinden, C. A., and Prather, M. J. (2001). Stratospheric N_2O; NO_y system: Testing uncertainties in a three-dimensional framework. *J. Geophys. Res.*, 106(D22):28771–28784.

Ouyang, X. and Varghese, P. L. (1989). Reliable and efficient program for fitting Galatry and Voigt profiles to spectral data on multiple lines. *Appl. Opt.*, 28(8):1538–1545.

Paldus, B. A. and Kachanov, A. A. (2005). An historical overview of cavity-enhanced methods. *Can. J. Phys.*, 83:975–999.

Paschotta, R. (2006). Beam quality deterioration of lasers caused by intracavity beam distortions. *Opt. Express*, 14(13):6069–6074.

Peeters, R. T. H. (2001). *Cavity Enhanced Absorption Spectroscopy.* PhD thesis, Katholieke Universiteit Nijmegen.

Picqué, N., Girard, V., Jacquemet, M., Fearrenq, R., and Guelachvili, G. (2007). Kilometric path lengths in infrared absorption with time resolved fourier transform spectroscopy. 2007.

Popp, B. N., Westley, M. B., Toyoda, S., Miwa, T., Dore, J. E., Yoshida, N., Rust, T. M., Sansone, F. J., Russ, M. E., Ostrom, N. E., and Ostrom, P. H. (2002). Nitrogen and oxygen isotopomeric constraints on the origins and sea-to-air flux of N_2O in the oligotrophic subtropical North Pacific gyre. *Global Biogeochem. Cycles*, 16(4):1064–.

Rahmstorf, S. (2002). Ocean circulation and climate during the past 120,000 years. *Nature*, 419(6903):207–214.

Rahn, T. and Wahlen, M. (1997). Stable isotope enrichment in stratospheric nitrous oxide. *Science*, 278(5344):1776–1778.

Rahn, T. and Wahlen, M. (2000). A reassessment of the global isotopic budget of atmospheric nitrous oxide. *Global Biogeochemical Cycles*, 14(2):537–543.

Rahn, T., Zhang, H., Wahlen, M., and Blake, G. A. (1998). Stable isotope fractionation during ultraviolet photolysis of n_2o. *Geophysical Research Letters*, 25(24):4489–4492.

Rasmussen, S. O., Andersen, K. K., Svensson, A. M., Steffensen, J. P., Vinther, B. M., Clausen, H. B., Siggaard-Andersen, M.-L., Johnsen, S. J., Larsen, L. B., Dahl-Jensen, D., Bigler, M., Röthlisberger, R., Fischer, H., Goto-Azuma, K., Hansson, M. E., and Ruth, U. (2006). A new greenland ice core chronology for the last glacial termination. *J. Geophys. Res.*, 111(D6):D06102–.

Ravishankara, A. R., Daniel, J. S., and Portmann, R. W. (2009). Nitrous oxide (N_2O): The dominant ozone-depleting substance emitted in the 21st century. *Science*, 326(5949):123–125.

Röckmann, T. and Levin, I. (2005). High-precision determination of the changing isotopic composition of atmospheric N_2O from 1990 to 2002. *J. Geophys. Res.*, 110(D21):D21304–.

Repo, M. E., Susiluoto, S., Lind, S. E., Jokinen, S., Elsakov, V., Biasi, C., Virtanen, T., and Martikainen, P. J. (2009). Large N_2O emissions from cryoturbated peat soil in tundra. *Nature Geoscience*, 2(3):189–192.

Robins, N. P., Slagmolen, B. J. J., Shaddock, D. A., Close, J. D., and Gray, M. B. (2002). Interferometric, modulation-free laser stabilization. *Optics Letters*, vol. 27, No. 21:1905.

Rockmann, T., Kaiser, J., and Brenninkmeijer, C. A. M. (2003a). The isotopic fingerprint of the pre-industrial and the anthropogenic N_2O source. *Atmospheric Chemistry and Physics*, 3:315–323.

Rockmann, T., Kaiser, J., Brenninkmeijer, C. A. M., and Brand, W. A. (2003b). Gas chromatography/isotope-ratio mass spectrometry method for high-precision position-dependent N-15 and O-18 measurements of atmospheric nitrous oxide. *Rapid Communications in Mass Spectrometry*, 17(16):1897–1908.

Rohde, R. A., Price, P. B., Bay, R. C., and Bramall, N. E. (2008). In situ microbial metabolism as a cause of gas anomalies in ice. *Proceedings of the National Academy of Sciences*, 105(25):8667–8672.

Romanini, D. and Lehmann, K. (1993). Ring-down cavity absorption spectroscopy of the very weak hcn overtone bands wiht six, seven and eight stretching quanta. *J. Chem. Phys.*, 99 (9):6287.

Rosing, M. T. (1999). ^{13}C-Depleted Carbon Microparticles in > 3700-Ma Sea-Floor Sedimentary Rocks from West Greenland. *Science*, 283(5402):674–676.

Rosing, M. T., Bird, D. K., Sleep, N. H., Glassley, W., and Albarede, F. (2006). The rise of continents–an essay on the geologic consequences of photosynthesis. *Palaeogeography, Palaeoclimatology, Palaeoecology*, 232(2-4):99 – 113.

Rosing, M. T. and Frei, R. (2004). U-rich Archaean sea-floor sediments from Greenland - indications of > 3700 Ma oxygenic photosynthesis. *Earth and Planetary Science Letters*, 217(3-4):237 – 244.

Röthlisberger, R., Bigler, M., Hutterli, M., Sommer, S., Stauffer, B., Junghans, H. G., and Wagenbach, D. (2000). Technique for continuous high-resolution analysis of trace substances in firn and ice cores. *Environmental Science & Technology*, 34(2):338–342.

Rothman, L., Gordon, I., Barbe, A., Benner, D., Bernath, P., Birk, M., Boudon, V., Brown, L., Campargue, A., Champion, J.-P., Chance, K., Coudert, L., Dana, V., Devi, V., Fally, S., Flaud, J.-M., Gamache, R., Goldman, A., Jacquemart, D., Kleiner, I., Lacome, N., Lafferty, W., Mandin, J.-Y., Massie, S., Mikhailenko, S., Miller, C., Moazzen-Ahmadi, N., Naumenko, O., Nikitin, A., Orphal, J., Perevalov, V., Perrin, A., Predoi-Cross, A., Rinsland, C., Rotger, M., Simecková, M., Smith, M., Sung, K., Tashkun, S., Tennyson, J., Toth, R., Vandaele, A., and Vander Auwera, J. (2009). The HITRAN 2008 molecular spectroscopic database. *Journal of Quantitative Spectroscopy and Radiative Transfer*, 110(9-10):533–572.

Ruth, A. A., Orphal, J., and Fiedler, S. E. (2007). Fourier-transform cavity-enhanced absorption spectroscopy using an incoherent broadband light source. *Applied Optics*, 46:3611–3616.

Saad, N. (2010). *Combustion Module for CM-CRDS by Costech*. Picarro Inc., 480 Oakmead Parkway Sunnyvale, CA 94085 - USA.

Saraf, S., Byer, R. L., and King, P. J. (2007). High-extinction-ratio resonant cavity polarizer for quantum-optics measurements. *Appl. Opt.*, 46(18):3850–3855.

Schidlowski, M. (1988). A 3,800-million-year isotopic record of life from carbon in sedimentary rocks. *Nature*, 333(6171):313–318.

Schilt, A., Baumgartner, M., Blunier, T., Schwander, J., Spahni, R., Fischer, H., and Stocker, T. F. (2010a). Glacial-interglacial and millennial-scale variations in the atmospheric nitrous oxide concentration during the last 800,000 years. *Quaternary Science Reviews*, 29:182–192.

Schilt, A., Baumgartner, M., Schwander, J., Buiron, D., Capron, E., Chappellaz, J., Loulergue, L., Schüpbach, S., Spahni, R., Fischer, H., and Stocker, T. F. (2010b). Atmospheric nitrous oxide during the last 140,000 years. *Earth and Planetary Science Letters*, 300(1-2):33 – 43.

Schmitt, J., Schneider, R., and Fischer, H. (2011). A sublimation technique for high-precision measurements of $\delta^{13}CO_2$ and mixing ratios of CO_2 and

N_2O from air trapped in ice cores. *Atmospheric Measurement Techniques Discussions*, 4(2):1853–1892.

Schopf, J. and Packer, B. (1987). Early Archean (3.3-billion to 3.5-billion-year-old) microfossils from Warrawoona Group, Australia. *Science*, 237(4810):70–73.

Schopf, J. W. (1994). Disparate rates, differing fates: tempo and mode of evolution changed from the Precambrian to the Phanerozoic. *Proceedings of the National Academy of Sciences*, 91(15):6735–6742.

Shaddock, D. A., Gray, M. B., and McClelland, D. E. (1999). Frequency locking a laser to an optical cavity by use of spatial mode interference. *Opt. Lett.*, 24(21):1499–1501.

Siegman (January 1990). New developments in laser resonators. In *Presented at Conference on Laser Resonators SPIE/OE LASE '90, Los Angeles.*

Siegman, A. E. (1986). *Lasers.* University Science Books.

Siegman, A. E., Sasnett, M. W., and Jonhnston Jr., T. F. (1991). Choice of clip levels for beam width measurements using knife-edge techniques. *IEEE Journal of Quantum Electronics*, vol. 27, no. 4.:1098– 1104.

Slagmolen, B. J. J., Shaddock, D. A., Gray, M. B., and McClelland, D. E. (2002). Frequency stability of spatial mode interference (tilt) locking. *IEEE Journal of Quantum Electronics*, vol. 38, no. 11:1521.

Sowers, T. (2001). N2O record spanning the penultimate deglaciation from the Vostok ice core. *Journal of Geophysical Research-Atmospheres*, 106(D23):31903–31914.

Sowers, T., Alley, R. B., and Jubenville, J. (2003). Ice core records of atmospheric N_2O covering the last 106,000 years. *Science*, 301(5635):945–948.

Sowers, T., Brook, E., Etheridge, D., Blunier, T., Fuchs, A., Leuenberger, M., Chappellaz, J., Barnola, J. M., Wahlen, M., Deck, B., and Weyhenmeyer, C. (1997). An interlaboratory comparison of techniques for extracting and analyzing trapped gases in ice cores. *Journal of Geophysical Research-Oceans*, 102(C12):26527–26538.

Sowers, T., Rodebaugh, A., Yoshida, N., and Toyoda, S. (2002). Extending records of the isotopic composition of atmospheric N_2O back to 1800 AD from air trapped in snow at the South Pole and the Greenland Ice Sheet Project II ice core. *Global Biogeochemical Cycles*, 16, no. 4(4):1129.

Spahni, R., Chappellaz, J., Stocker, T. F., Loulergue, L., Hausammann, G., Kawamura, K., Fluckiger, J., Schwander, J., Raynaud, D., Masson-Delmotte, V., and Jouzel, J. (2005). Atmospheric methane and nitrous oxide of the late Pleistocene from Antarctic ice cores. *Science*, 310(5752):1317–1321.

Spence, T. G., Harb, C. C., Paldus, B. A., Zare, R. N., Willke, B., and Byer, R. L. (2000). A laser-locked cavity ring-down spectrometer employing an analog detection scheme. *Rev. Sci. Instr.*, vol. 71, no. 2:347 – 353.

Steffensen, J. P., Andersen, K. K., Bigler, M., Clausen, H. B., Dahl-Jensen, D., Fischer, H., Goto-Azuma, K., Hansson, M., Johnsen, S. J., Jouzel, J., Masson-Delmotte, V., Popp, T., Rasmussen, S. O., Rothlisberger, R., Ruth, U., Stauffer, B., Siggaard-Andersen, M.-L., Sveinbjornsdottir, A. E., Svensson, A., and White, J. W. C. (2008). High-resolution greenland ice core data show abrupt climate change happens in few years. *Science*, 321(5889):680–684.

Stein, L. Y. and Yung, Y. L. (2003). Production, isotopic composition, and atmospheric fate of biologically produced nitrous oxide. *Annual Review of Earth and Planetary Sciences*, 31(1):329–356.

Stocker, T. F. and Johnsen, S. J. (2003). A minimum thermodynamic model for the bipolar seesaw. *Paleoceanography*, 18(4):1087–.

Sutka, R. L., Ostrom, N. E., Ostrom, P. H., Breznak, J. A., Gandhi, H., Pitt, A. J., and Li, F. (2006). Distinguishing nitrous oxide production from nitrification and denitrification on the basis of isotopomer abundances. *Appl. Environ. Microbiol.*, 72(1):638–644.

Svensson, A., Andersen, K. K., Bigler, M., Clausen, H. B., Dahl-Jensen, D., Davies, S. M., Johnsen, S. J., Muscheler, R., Rasmussen, S. O., Rothlisberger, R., Peder Steffensen, J., and Vinther, B. (2006). The Greenland ice core chronology 2005, 15-42 ka. Part 2: comparison to other records. *Quaternary Science Reviews*, 25(23-24):3258–3267.

Tan, S. M. (2007). Wavelength measurement method based on combination of two signals in quadrature, us0195328 patent.

Tan, S. M. (2008a). Calibration of frequency monitors having dual etalon signals in quadrature, us0137089 patent.

Tan, S. M. (2008b). Wavelength measurement method based on combination of two signals in quadrature.

Taubman, M. S., Myers, T. L., Cannon, B. D., and Williams, R. M. (2004). Stabilization, injection and control of quantum cascade lasers, and their application to chemical sensing in the infrared. *Spectrochimica Acta Part A: Molecular and Biomolecular Spectroscopy*, 60(14):3457 – 3468.

Teichert, C., MacKay, J. F., Savage, D. E., Lagally, M. G., Brohl, M., and Wagner, P. (1995). Comparison of surface roughness of polished silicon wafers measured by light scattering topography, soft-x-ray scattering, and atomic-force microscopy. *Applied Physics Letters*, 66(18):2346–2348.

Thorpe, M. and Ye, J. (2008). Cavity-enhanced direct frequency comb spectroscopy. *Applied Physics B: Lasers and Optics*, 91:397–414.

Thorpe, M. J. (2009). *Cavity-Enhanced direct frequency comb spectroscopy.* PhD thesis, University of Colorado.

Thorpe, M. J., Balslev-Clausen, D., Kirchner, M. S., and Ye, J. (2008). Cavity-enhanced optical frequency combspectroscopy: application to human breathanalysis. *Opt. Express*, 16(4):2387–2397.

Thorpe, M. J., Moll, K. D., Jones, R. J., Safdi, B., and Ye, J. (2006). Broadband cavity ringdown spectroscopy for sensitive and rapid molecular detection. *Science*, 311:1595.

Toyoda, S., Yamamoto, S., Arai, S., Nara, H., Yoshida, N., Kashiwakura, K., and Akiyama, K. (2008). Isotopomeric characterization of N_2O produced, consumed, and emitted by automobiles. *Rapid Communications in Mass Spectrometry*, 22(5):603–612.

Turatti, F., Griffith, D. W. T., Wilson, S. R., Esle, M. B., Rahn, T., Zhang, H., and Blake, G. A. (2000). Positionally dependent ^{15}N fractionation factors in the UV photolysis of N_2O determined by high resolution FTIR spectroscopy. *Geo. Res. Lett.*, 27, No. 16:2489–2492.

van Zee, R. D., Hodges, J. T., and Looney, J. P. (1999). Pulsed, single-mode cavity ringdown spectroscopy. *Applied Optics*, Vol. 38, No. 18:3951 – 3960.

Ventrillard-Courtillot, I., Sciamma OBrien, E., Kassi, S., Méjean, G., and Romanini, D. (2010). Incoherent broad-band cavity-enhanced absorption spectroscopy for simultaneous trace measurements of NO_2 and NO_3 wiht a LED source. *Applied Physics B: Lasers and Optics*, 101:661–669.

Vorburger, T. V., Marx, E., and Lettieri, T. R. (1993). Regimes of surface roughness measurable with light scattering. *Appl. Opt.*, 32(19):3401–3408.

Šimečková, M., Jacquemarta, D., Rothmana, L. S., Gamacheb, R. R., and Goldmanc, A. (2006). Einstein A-coefficients and statistical weights for molecular absorption transitions in the HITRAN database. *Jour. Quant. Spec. Rad. Trans.*, 98:130–155.

Wächter, H. (2007). *Infrared Laser-Spectroscopic Determination of Isotope Ratios of Trace Gases*. PhD thesis, ETH Zürich.

Waechter, H., Mohn, J., Tuzson, B., Emmenegger, L., and Sigrist, M. W. (2008). Determination of N_2O isotopomers with quantum cascade laser based absorption spectroscopy. *Opt. Express*, 16(12):9239–9244.

Webber, M. E., Pushkarsky, M., and Patel, C. K. N. (2003). Fiber-amplifier-enhanced photoacoustic spectroscopy with near-infrared tunable diode lasers. *Applied Optics*, 42:2119.

Werle, P., Mücke, R., and Slemr, F. (1993). The limits of signal averaging in atmospheric trace-gas monitoring by tunable diode-laser absorption spectroscopy (tdlas). *Applied Physics B: Lasers and Optics*, 57:131–139.

Werner, R. A., Rothe, M., and Brand, W. A. (2001). Extraction of CO_2 from air samples for isotopic analysis and limits to ultra high precision $\delta^{18}O$ determination in CO_2 gas. *Rapid Communications in Mass Spectrometry*, 15(22):2152–2167.

Willke, B., Uehara, N., Gustafson, E. K., Byer, R. L., King, P. J., Seel, S. U., and R. L. Savage, J. (1998). Spatial and temporal filtering of a 10-W Nd:YAG laser with a Fabry–Perot ring-cavity premode cleaner. *Opt. Lett.*, 23(21):1704–1706.

Wolff, E. W., Fischer, H., Fundel, F., Ruth, U., Twarloh, B., Littot, G. C., Mulvaney, R., Röthlisberger, R., de Angelis, M., Boutron, C. F., Hansson, M., Jonsell, U., Hutterli, M. A., Lambert, F., Kaufmann, P., Stauffer, B., Stocker, T. F., Steffensen, J. P., Bigler, M., Siggaard-Andersen, M. L., Udisti, R., Becagli, S., Castellano, E., Severi, M., Wagenbach, D., Barbante, C., Gabrielli, P., and Gaspari, V. (2006). Southern Ocean sea-ice extent, productivity and iron flux over the past eight glacial cycles. *Nature*, 440(7083):491–496.

Yan, W., Chen, Y., Chen, H., Krusen, C., and Woods, P. (2008). Development and applications of continuous-wave cavity ring-down spectroscopy. *International Journal of Thermophysics*, 29(5):1567–1577.

Yang, W., Joshi, A., Wang, H., and Xiao, M. (2004). Simple method for frequency locking of an extended-cavity diode laser. *Appl. Opt.*, 43(29):5547–5551.

Yung, Y. L. and Miller, C. E. (1997). Isotopic fractionation of stratospheric nitrous oxide. *Science*, 278(5344):1778–1780.

Zare, R. N., Martin, J., Paldus, B. A., and Xie, J. (1999). Ring resonant cavities for spectroscopy. *US Patent*, US05912740:.

Zumbrunn, R., Neftel, A., and Oeschger, H. (1982). CO_2 measurements on 1-cm^3 ice samples with an IR laserspectrometer (IRLS) combined with a new dry extraction device. *Earth and Planetary Science Letters*, 60(2):318 – 324.

A

Allan deviation

The typical figure of merit used for the stability of a signal in laser absorption spectroscopy is the Allan Deviation. This provides information for how well a data set average down within an increasing averaging window/time. A set of measurement points $\{x_n | n = 1 \cdots N\}$ is sampled within a time t_N. It is assumed that the data acquisition rate is effectively constant within a measurement interval time $dt = t_N/N$. A time interval $\tau < t_N$ for averaging will then contain $p = \tau/dt$ data points. The full data set is divided into consecutive sections $A_i(p)$

$$\underbrace{x_1 \cdots x_p}_{A_1(p)} \underbrace{x_{p+1} \cdots x_{2p}}_{A_2(p)} \underbrace{x_{2p+1} \cdots \cdots}_{\cdots} x_N \tag{A.1}$$

and the arithmetic mean is calculated for each:

$$A_n(p) = \frac{1}{p} \sum_{i=1+p(n-1)}^{pn} x_i, n = 1 \ldots m \tag{A.2}$$

Finally the Allan variance is calculated according toWerle et al. [1993]

$$\sigma_A^2(\tau) = \frac{1}{2(m-1)} \sum_{i=1}^{m-1} [A_i(p) - A_{i+1}(p)]^2 \tag{A.3}$$

For a white noise signal the Allan plot has a slope of -1 in a double logarithmic plot, while for a linear drift the slope is +2. The minimum of the Alan variance gives minimum obtainable sensitivity in real experiments.

Overlapping Allan Variance For long averaging intervals the calculated Allan variance becomes very uncertain. One can give up the statistical inde-

pendence of the time intervals, and use a sliding interval instead

$$\underbrace{x_1 x_2 \cdots x_p}_{A_1(p)} \underbrace{x_{p+1} x_{p+2} \cdots x_{2p}}_{A_1'(p)} x_{2p+1} x_{2p+2} \cdots\cdots x_N \tag{A.4}$$

$$x_1 \underbrace{x_2 \cdots x_p x_{p+1}}_{A_2(p)} \underbrace{x_{p+2} \cdots x_{2p} x_{2p+1}}_{A_2'(p)} x_{2p+2} \cdots\cdots x_N \tag{A.5}$$

from which the Allan Variance is found according to Czerwinski et al. [2009]

$$\sigma_A^2(\tau) = \frac{1}{2(N+1-2p)} \sum_{i=1}^{N+1-2p} [A_i(p) - A_i'(p)]^2. \tag{A.6}$$

This expression has a statistical error defined, by the standard error of the mean

$$\mathrm{SE}_{\sigma(\tau)} = \sqrt{\frac{p}{N}} \sigma_A(\tau), \tag{A.7}$$

which is smaller than that of the non sliding formulation.

B

Measurements with a 4 mm ZnSe Etalon

Measurement with the isobox setup using the.

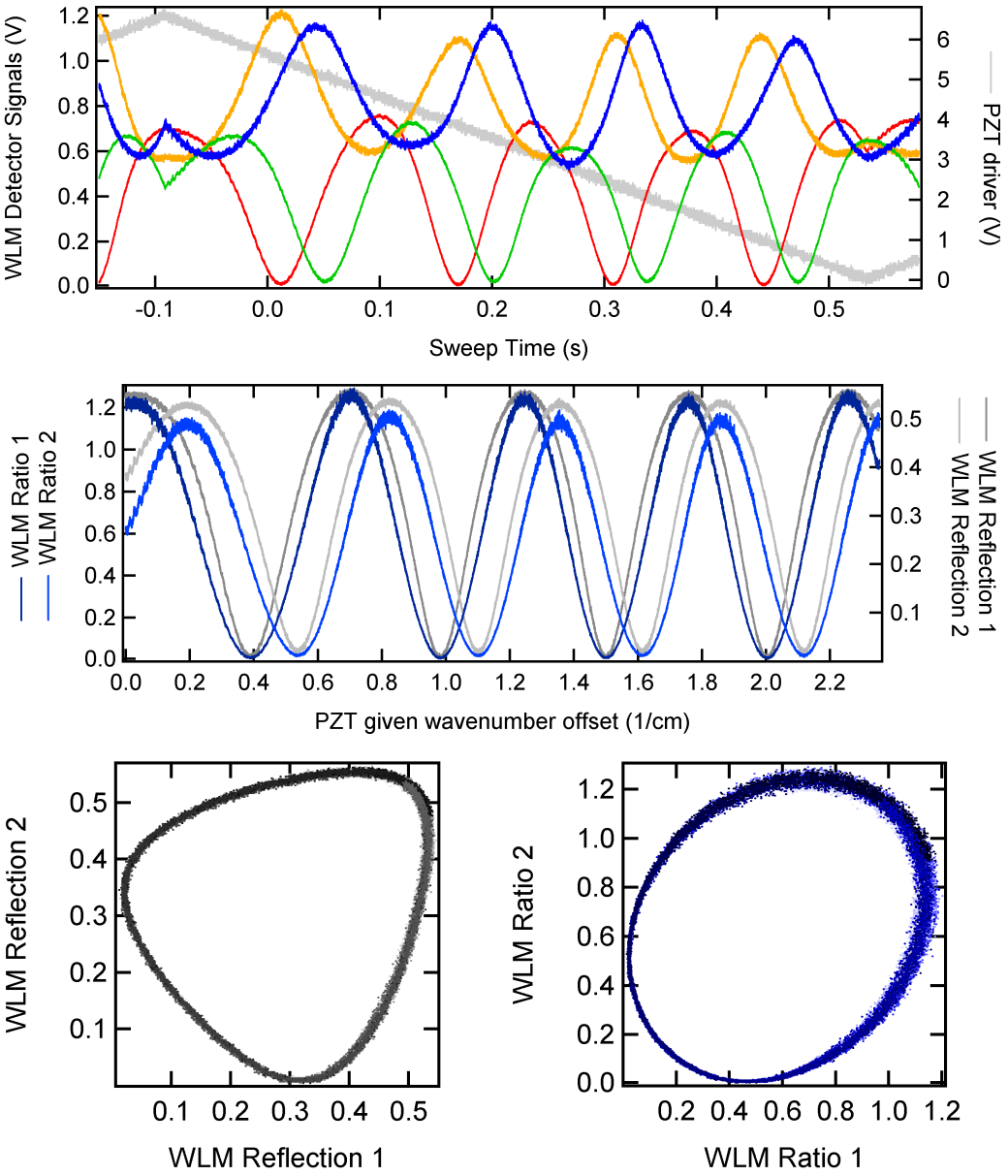
WLM Detector Signals (V)
PZT driver (V)
Sweep Time (s)
WLM Ratio 1
WLM Ratio 2
WLM Reflection 1
WLM Reflection 2
PZT given wavenumber offset (1/cm)
WLM Reflection 2
WLM Reflection 1
WLM Ratio 2
WLM Ratio 1